Spinning Black Hole Pairs: Dynamics and Gravitational Waves

Rebecca Grossman

Submitted in partial fulfillment of the
requirements for the degree of
Doctor of Philosophy
in the Graduate School of Arts and Sciences

Columbia University

2011

Abstract

Spinning Black Hole Pairs: Dynamics and Gravitational Waves

Rebecca Grossman

Black hole binaries will be an important source of gravitational radiation for both ground-based and future space-based gravitational wave detectors. The study of such systems will offer a unique opportunity to test the dynamical predictions of general relativity when gravity is very strong. To date, most investigations of black hole binary dynamics have focused attention on restricted scenarios in which the black holes do not spin (and thus are confined to move in a plane) and/or in which they stay on quasi-circular orbits.

However, spinning black hole pairs in eccentric orbits are now understood to be astrophysically equally important. These spinning binaries exhibit a range of complicated dynamical behaviors, even in the absence of radiation reaction. Their conservative dynamics is complicated by extreme perihelion precession compounded by spin-induced precession. Although the motion seems to defy simple decoding, we are able to quantitatively define and describe the fully

three-dimensional motion of arbitrary mass-ratio binaries with at least one black hole spinning and expose an underlying simplicity. To do so, we untangle the dynamics by constructing an instantaneous orbital plane and showing that the motion captured in that plane obeys elegant topological rules.

In this thesis, we apply the above prescription to two formal systems used to model black hole binaries. The first is defined by the conservative 3PN Hamiltonian plus spin-orbit coupling and is particularly suitable to comparable-mass binaries. The second is defined by geodesics of the Kerr metric and is used exclusively for extreme mass-ratio binaries. In both systems, we define a complete taxonomy for fully three-dimensional orbits. More than just a naming system, the taxonomy provides unambiguous and quantitative descriptions of the orbits, including a determination of the zoom-whirliness of any given orbit. Through a correspondence with the rational numbers, we are able to show that all of the qualitative features of the well-studied equatorial geodesic motion around Schwarzschild and Kerr black holes are also present in more general black hole binary systems. This includes so-called zoom-whirl behavior, which turns out to be unexpectedly prevalent in comparable-mass binaries in the strong-field regime just as it is for extreme mass-ratio binaries.

In each case we begin by thoroughly cataloging the constant radius orbits

which generally lie on the surface of a sphere and have acquired the name "spherical orbits". The spherical orbits are significant as they energetically frame the distribution of all orbits. In addition, each unstable spherical orbit is asymptotically approached by an orbit that whirls an infinite number of times, known as a homoclinic orbit. We further catalog the homoclinic trajectories, each of which is the infinite whirl limit of some part of the zoom-whirl spectrum and has a further significance as the separatrix between inspiral and plunge for eccentric orbits.

We then show that there exists a discrete set of orbits that are geometrically closed n-leaf clovers in a precessing *orbital plane*. When viewed in the full three dimensions, these orbits do not close, but they are nonetheless periodic when projected into the orbital plane. Each n-leaf clover is associated with a rational number, q, that measures the degree of perihelion precession in the precessing orbital plane. The rational number q varies monotonically with the orbital energy and with the orbital eccentricity. Since any bound orbit can be approximated as near one of these periodic n-leaf clovers, this special set offers a skeleton that illuminates the structure of all bound orbits in both systems, in or out of the equatorial plane. A first significant conclusion that can be drawn from this analysis is that all generic orbits in the final stages

of inspiral under gravitational radiation losses are characterized by precessing clovers with few leaves, and that no orbit will behave like the tightly precessing ellipse of Mercury.

We close with a practical application of our taxonomy beyond the illumination of conservative dynamics. The numerical calculation of the first-order (adiabatic) approximation to radiatively evolving inspiral motion in extreme mass-ratio binaries is currently hindered by prohibitive computational cost. Motivated by this limitation, we explain how a judicious use of periodic orbits can dramatically expedite both that calculation and the generation of snapshot gravitational waves from geodesic sources.

Contents

List of Figures

Acknowledgments

This work would not have been possible without the support of many people along the way. In no particular order, I would like to thank them for their contributions, large and small.

My seventh grade math teacher, Linda Adams, was the first math teacher to foster and encourage my love of math. It is because of her steadfast confidence in my potential that I persevered through and excelled in my high school math classes.

For more than a decade now, Reshmi Mukherjee and Tim Halpin-Healy have been continuous sources of encouragement, counsel, instruction, opportunity and patience, both during my time at Barnard as an undergraduate and throughout my tenure as a graduate student at Columbia. They have each left an indelible mark on me as a scientist and educator, and I cannot thank them enough for the interest they have taken in my development as both.

The administrative staff at both the Barnard and Columbia Physics departments handled all things logistical with skill and professionalism while I was a student. From making sure I got paid to helping me in the final throes of the defense, I am indebted to Molly Gill, Randy Torres, Joey Cambareri, Nicole Griggs, Lalla Grimes, Rasma Mednis, Lydia Argote, and John T. Carr III.

I have also been fortunate to have been exposed to an exceptional group of peers with whom I have stayed up all night working on problem sets and from whom I have learned more than books and classes could ever have taught me. Thank you Ben Geller, Aliza Hakimian, Britt Reichborn-Kjennerud, Simon Judes, Mina Fazlollahi, Guillaume Plante, Tatia Engelmore, Adam Brown, Azfar Adil, Jake Hofman, Seth Caughron, Mark Cooke, Jamie Rollins and Alex Stone.

Among this ensemble, Gabe Perez-Giz must be singled out. Gabe has not only been my peer, but also my collaborator, teacher, mentor, best friend and confidant. There are many moments in a P.hD. program that tax one's tolerance of the intolerable and test one's determination to finish. Gabe has the unique distinction of having been there to buoy me through every one of those moments, as he has been in all aspects of my life and as he is for so many others. Thank you, Gabe, for being the rock in the past decade of my life.

I want to thank my five committee members, Szabi Marka, Jeremy Dodd, Eduardo Ponton, Tim Halpin-Healy and Janna Levin, who graciously dedicated their time to my thesis.

And to my advisor, Janna Levin. You raised me through my physics adolescence and we both survived to talk about it. You showed me what it means to be a physicist, how to conduct research and importantly how research doesn't really start until the paper writing commences.

From my earliest memory, my parents, Harry and Luba Grossman, have always been my greatest support structure and biggest fans. Even before I knew how to read, they gave me math workbooks to "play" with. And when I took my first physics class sophomore year of college and called them hysterical because I didn't know how to do any of the first problem set on projectile motion, they worked out the first few problems with me until I understood what I was doing and could do the rest of the problem set alone. Their faith in me is unwavering, their love is unconditional and they have shown me that there is no limit in what life has to offer. Thank you mom and dad – in the truest sense of that expression.

for halu

Chapter 1

Introduction

1.1 The 2-body problem in General Relativity

Beginning in 1905 with the publication of the theory of special relativity (SR) [1], and throughout the next decade with the development of general relativity (GR) [2; 3], Einstein fundamentally changed our concepts of space, time and the "gravitational force." Prior to Einstein, the prevailing theory of gravity was Newton's, which explained gravity as a force

$$\mathbf{F}_{\rm grav} = \frac{Gm_1m_2}{r^2}\hat{\mathbf{r}} \tag{1.1}$$

between masses. The default state of motion was a constant velocity straight line, and gravitational forces caused celestial bodies to deviate from that default. In contrast, GR states that in the absence of non-gravitational influences, there is no such deviation. Particles simply follow potentially complex looking geodesics of the background spacetime geometry, a geometry encoded in the metric tensor $g_{\mu\nu}$.

Philosophically, Einstein's point of view is simpler: what we previously attributed to a gravitational force is actually Newton's first law of motion at work in a curved spacetime. But computationally, GR is a nightmare. The Einstein equation

$$R_{\mu\nu} - \frac{1}{2}Rg_{\mu\nu} = 8\pi T_{\mu\nu} \tag{1.2}$$

states that the metric on the LHS[1] is sourced by the combined energy-momentum tensor $T_{\mu\nu}$ of particles and fields on the RHS. $T_{\mu\nu}$, however, depends on

[1]The Ricci tensor $R_{\mu\nu}$ and Ricci scalar R depend on higher powers of both the metric

the distribution of those particles and fields over spacetime. Consequently, as matter moves along geodesics, those geodesics change. The problem of motion in GR is therefore inseparable from the much more difficult problem of solving for the geometry globally at every instant.

The difference between Newton's and Einstein's perspectives is especially apparent in the gravitational 2-body problem. In Newtonian gravity, it is trivial to write the resulting orbits in closed form. But in GR, the problem cannot be solved analytically. Fortunately, gravity is weak even in most astrophysical situations, and we can determine the motion of the two bodies in a binary using equation (1.1), possibly with small corrections. But when gravity is strong and equation (1.1) fails, one has no choice but to solve not a 2-body problem but a 1-spacetime problem with a 2-body source term.

1.2 Astrophysical context: black hole binaries

This is precisely the situation in binary systems composed of two black holes (BHs) in a close orbit. BH binaries are an important astrophysical source of gravitational waves (GWs) and are interesting not only to relativists and astrophysicists but also to the community devoted to GW physics and efforts at GW detections. One way to characterize these systems is by the total mass and mass ratio of the constituents. Binaries composed of BHs of masses in the $\sim 10^1 - 10^3 M_\odot$ range will emit GWs that fall in the frequency sweet spot of the four existing ground-based GW detectors: GEO600 [4], LIGO [5], TAMA 300 [6] and VIRGO [7]. While merger rate predictions for such BH binaries vary from a few events per year on the low end to more optimistic predictions of a few tens of events per year, there is no dispute that ground-based GW detectors should be able to observe the GW emission from such BH binaries [8; 9; 10; 11].

BH binaries with widely different masses are also expected to occur in nature. A galactic supermassive BH with a mass $\sim 10^5 - 10^7 M_\odot$ may at times capture a companion[2] $\sim 10^1 - 10^2 M_\odot$ BH into a bound orbit. As the system radiates energy and angular momentum into GWs, the orbit of the companion will decay until it eventually falls into the central black hole.

and its various derivatives with respect to spacetime coordinates, so that equation (1.2) is a system of coupled nonlinear PDEs for the metric components $g_{\mu\nu}$.

[2]The companion could also be some other stellar mass compact object (i.e. a neutron star or white dwarf).

The GWs emitted by such extreme mass-ratio inspirals (EMRIs) will have a frequency range that future space-based GW observatories[3] will be optimized to detect ($\sim 10^{-5} - 10^{-1}$ Hz, with an optimal frequency of $\sim 10^{-2}$ Hz). The estimated detection rate for extreme mass ratio binaries again varies widely depending on the model used and lies somewhere between 10 and 1000 events per year [13; 14; 15; 16].

As suggested earlier, the spacetime around two orbiting BHs eludes analytic description. To understand how both the motion and the emitted GWs will look, one must resort to solving equation (1.2) over all spacetime on a computer. This approach, called numerical relativity (NR), has matured over the past several years, and it has been used successfully to simulate the inspiral and merger of BH binaries. While NR has made impressive breakthroughs [17; 18; 19; 20; 21; 22; 23], especially in resolving the final plunge of a black hole pair, NR is so computationally expensive that it is out of the question to use it to simulate earlier stages of the inspiral, let alone to systematically explore the inspiral dynamics over different ranges of BH parameters and orbital initial conditions.

1.3 Approximating motion in BH binaries

Instead the inspiral phase of the motion is handled with some sort of analytic or semi-analytic approximation method. All such methods artificially separate the problem of determining motion from the problem of determining the geometry in which the motion takes place. In order to get traction analytically, they take an approach that is philosophically more Newtonian. First, they treat the spacetime as fixed. Then, they attribute the deviation of the motion from geodesics of that spacetime not to an evolving metric but instead to fictitious forces.

Such quasi-relativistic approximation methods aim to reproduce the true dynamics to some accuracy. In this work, we focus on two such formalisms that are widely used: (1) the post-Newtonian (PN) expansion, and (2) the test particle limit.

[3] NASA has recently withdrawn financial support for the planned LISA mission, which may still fly in a leaner form (called ELISA or "LISA light") funded entirely by the European Space Agency. If funded, ELISA will still have specifications that allow it to detect GWs from EMRIs [12].

1.3.1 The post-Newtonian (PN) expansion

Conceptually, in a PN expansion, we pretend that we are in flat (Euclidean) space and try to reproduce relativistic dynamical effects by adding fictitious forces to the usual Newtonian force. Those forces are introduced at various orders in the expansion parameter, which is the square of the ratio of the orbital velocity to the speed of light, $\left(\frac{v}{c}\right)^2$. Terms in the PN expansion are labeled by the order in $\left(\frac{v}{c}\right)^2$ at which they enter the expansion: 2.5PN terms enter at $\left(\frac{v}{c}\right)^5$, 3PN terms go like $\left(\frac{v}{c}\right)^6$, and so forth. Whole integer PN terms are conservative, while half-integer PN terms are dissipative and are responsible for removing the orbital energy and angular momentum the system should lose to gravitational radiation.

The PN expansion is constructed under the assumptions of a weakly gravitating and slowly moving source. However, as two black holes get closer to merger, those assumptions break-down – the BHs can reach orbital velocities of $\sim 0.5c$ – and the system may require many higher order terms in the approximation in order to converge [24]. Unfortunately, the terms in each successive order of the expansion are difficult to derive. Moreover, moving to each successive order adds pages to the equations of motion and offers little analytical transparency. Therefore, in deciding how far to carry the PN expansion, a balance must be struck between physical accuracy and algebraic manageability.

The expansion in most widespread use today contains terms up to order 3PN. Actually, two different types of PN expansions (worked out separately by two different groups) are both widely used, and their dynamical predictions have been shown to agree [25; 26]. The first type expands the Einstein equations (1.2) directly in powers of $\frac{v}{c}$ [27; 28]. The second type is built on the Hamiltonian formulation of GR by Arnowitt-Deser-Misner (ADM) [29] and instead expands the Hamiltonian in powers of $\frac{v}{c}$ [30; 31]. In this work, we opt to use the Hamiltonian formulation up to order 3PN.

1.3.2 The test particle limit

The second approximation method we discuss is applicable only to extreme mass-ratio systems. The PN expansion contains the mass ratio of the binary as a free parameter, so in principle it can be applied to BH systems of arbitrary masses. That approximation has been compared to NR simulations of comparable mass binaries in nearly circular orbits [24]. In this restricted regime,

the 3PN approximation seems to work reasonably well, at least insofar as its predictions of where the last stable circular orbit before the plunge phase lies and what the gravitational waveforms emitted during those last several orbital cycles will look like [24].

For extreme mass-ratio systems, NR simulations of are not yet stable[4], so the PN expansion cannot be tested against a fully relativistic radiative simulation in this case. However, in the non-radiative case, there is an exact model with known solutions – geodesic motion in the Schwarzschild and Kerr spacetimes – against which the conservative 3PN dynamics can be compared. Such comparisons have only been performed in a limited sense (e.g. comparing predictions of the radius of the last stable circular orbit), and the 3PN predictions of even that simple value are poor.

Luckily, the extreme mass-ratio can be modeled with a different scheme. In this case, we can treat the small BH as a test particle and the large BH as the sole source of the spacetime geometry. In GR, that geometry will be the Schwarzschild metric, or, more realistically, the Kerr metric if the central BH has spin. Using the Kerr metric as our background, we can then use black hole perturbation theory to find how the addition of a small companion distorts that spacetime [32; 33]. The small distortion of that spacetime due to the lighter companion is reinterpreted as a radiation reaction field that causes the companion to trace an accelerated (non-geodesic) trajectory in the Kerr or Schwarzschild background. This method also naturally predicts the forms of the GWs produced, since by construction GWs can be viewed as simply distortions of the background spacetime.

Like the PN expansion, BH perturbation theory adds terms of progressing orders in a small parameter, which in this case is the mass ratio rather than v/c. Unlike the PN expansion, the BH perturbation theory technique is more relativistic, in that the zeroth order description is already highly relativistic (Kerr geodesic motion) rather than Newtonian. Thus, the expectation is that far lower orders in such an expansion will need to be kept in order to obtain a highly accurate representation of the relativistic motion and the GW emission from EMRI systems.

[4]Such simulations have difficulty simultaneously resolving the widely separated size scales of both the central BH and the companion BH.

1.4 Conservative dynamics of BH binaries

Besides being more tractable, approximation methods have the helpful feature that they can separate conservative and dissipative parts of the dynamics. NR cannot do this – it solves the Einstein equations directly, and since merger and GWs are inherent to those equations, the effects of radiation cannot be "turned off", so to speak. But both the PN expansion and the test particle limit with BH perturbation theory can do so, and while dissipative dynamics is what is relevant to the astrophysics of BH mergers and to GW physics, the conservative dynamics also merits study in its own right.

There are several reasons for this. First, the conservative dynamics will already contain rich features that are different from what is expected in non-relativistic systems. Second, until the very late stages of the inspiral, when the rate of radiation becomes large, the dissipative dynamics can be envisioned as a transit through various non-dissipative orbits. Thus, understanding the conservative dynamics helps us to frame the different features we expect a BH binary system to exhibit as it evolves toward merger, features that will be encoded in the GWs it emits. Third, understanding the non-radiative dynamics predicted by both the PN expansion and the test particle limit is a good test bed for understanding the limits of validity of the former.

1.4.1 The status quo: planar motion with low eccentricity

Unfortunately, even though a thorough understanding of the conservative dynamics of black hole pairs is essential, the full richness of those dynamics remains largely unexplored. Granted, equations of motion exist for both the PN and test particle formalisms that can be integrated numerically for any initial conditions. This is not the same, however, as a complete organization of the range of qualitative phenomena that can occur within each formalism. To date, such qualitative organization of the conservative dynamics has been scant and not systematic. There has been more thorough investigation of the dynamics, however, in two situations in which the analysis is greatly facilitated.

The first such situation is planar motion in the test particle limit. In standard GR textbooks [34; 35; 36], the first discussion presented of relativistic motion is geodesic (test particle) motion in the Schwarzschild spacetime produced by a nonspinning black hole. Mathematically, this is the simplest

possible relativistic binary since it is really a 1-body problem (that of the test particle) in a fixed spacetime with no radiation. A fairly complete catalog of Schwarzschild geodesic motion is available from such texts. Recently, a topological taxonomy based on features of *periodic orbits* in Ref. [37] also added new insight into test particle dynamics. The addition of spin to the central black hole in the Kerr case means the motion is no longer confined to a plane unless the position and velocity of the orbiting particle both begin in the equatorial plane. In this scenario, symmetry confines the motion to that plane, even in the Kerr case, and the taxonomy of [37] provides similar insights.

The second situation is motion of comparable mass black holes that is both planar and nearly circular. Although pairs of comparable, stellar mass BHs are significant candidates for a first direct detection with LIGO, their detectable gravitational radiation would be emitted from nearly circular orbits – at least that was the refrain. This has led to a preferential focus on quasi-circular inspiral motivated by considerations of long-lived binaries that begin with a modest eccentricity that is gradually shed as angular momentum is lost to GWs. A fair assessment of known astrophysics, the belief that this is the only important channel for BH binary formation discouraged analyses of eccentric orbital dynamics in favor of the simpler analysis of circular orbits. Quasi-circular, planar motion of BHs with comparable masses are also the systems easiest to simulate with numerical relativity, which is another reason why the focus has for so long been on this restricted type of motion.

1.4.2 The importance of spin and eccentricity

Unfortunately, it is increasingly apparent that both of the aforementioned assumptions – planar motion and nearly vanishing eccentricity – are astrophysically too restrictive, whether taken alone or together. Planar motion only holds exactly for binary systems in which neither BH spins. But in a compact object binary, at least one object will spin, probably substantially [38]. Such spinning binaries cannot remain confined to a plane and trace out elaborate orbits in 3D. This will certainly be the case in EMRIs, since the spins of galactic supermassive BHs are expected to be substantial [38].

Likewise, comparable mass BH binaries formed by tidal capture in dense star clusters, such as globular clusters, do not conform to the quasi-circular story [39]. As one BH scatters with another in a dense region, a burst of radiation is emitted on close encounter. Some subset of these encounters will

leave the pair bound in a highly eccentric orbit that merges too quickly to circularize. Estimates conclude that as many as 30% of multi-black hole systems will retain eccentricities > 0.1 as their waves sweep into the LIGO bandwidth [40]. Most recently, a new source of eccentric mergers was predicted to have a substantial detection rate [41]. Black hole/black hole scattering in galactic nuclei would similarly lead to tidal captures and highly eccentric, short-lived black hole binaries with 90% entering the LIGO bandwidth with eccentricities > 0.9 [41]. These competitive sources for a first detection by Advanced LIGO [41] are further motivation to study binary BH dynamics more systematically [42; 43; 44].

1.5 Organization of thesis and publication history

This thesis is a step toward improving our knowledge of eccentric spinning BH binaries. Our technique is to extend the tools mentioned above that have yielded so much analytical insight in the Schwarzschild and equatorial Kerr test particle cases. It will turn out that the same methods, including the taxonomy based on periodic orbits, can be extended to simplify the description of seemingly complicated eccentric 3D motion in both the PN system with spinning black holes and for nonequatorial Kerr geodesic motion. The key to extending those tools is the identification and construction of an instantaneous orbital plane into which the 3D motion can be projected. Surprisingly, all the qualitative features present in Schwarzschild test particle motion also manifest themselves in that orbital plane, in both the PN and Kerr systems. In the PN system, however, while all the qualitative features persist (an important finding), the distribution of those features over orbital parameters of the system is not always quantitatively accurate, so our analysis also furnishes a new way to test the limits of validity of the PN expansion.

The document is organized as follows. In Chapter 2, we summarize the salient features of Schwarzschild and equatorial Kerr geodesic motion. That chapter is over 90% review of material found in both GR texts and in Levin and Perez-Giz [37], while some is unpublished original work, including the details of a pseudo-effective potential formulation of equatorial Kerr motion that we generalize in Chapter 5. Chapters 3 and 4 and then Chapter 5 generalize the dynamics work of [37] to the post-Newtonian and extreme mass-ratio systems, respectively. Chapters 3 and 4 are based on work done with Professor

Janna Levin in two papers [45; 46] that detail the dynamics of orbits in the 3PN system with spin and show that in this system, orbits projected into the orbital plane qualitatively mimic those of the Schwarzschild and equatorial Kerr systems. Chapter 5 extends the use of the orbital plane to generic Kerr orbits and details the dynamics of that system by similarly describing periodic orbits in that system. That chapter is based on work with Professor Janna Levin and Gabe Perez-Giz in [47].

The upshot of showing that the Schwarzschild tools can be extended to these more elaborate systems will be to extract a better dynamical understanding of varying approximations of the dynamics, some of which are genuinely informative about what will happen in nature and some of which instead reveal limitations of the approximation methods themselves. A better understanding of both those things is crucial to any attempts to decipher astrophysical information about compact binaries from future observation of gravitational waves.

As a practical application of our technique beyond illumination of the dynamics, Chapter 6 shows how the aforementioned periodic orbits in the generic Kerr system can be used to speed up the calculation of inspiraling orbits and GWs from extreme mass-ratio systems, at least at first-order. Currently, such calculations are prohibitively expensive to perform in bulk. In joint work with Professor Janna Levin and Gabe Perez-Giz in [48], we showed that periodic orbits can be leveraged to accelerate this calculation by an order of magnitude or more.

Finally, Chapter 7 summarizes our conclusions and offers thoughts for future work.

Chapter 2

Fiducial examples: planar motion in Schwarzschild and Kerr

The goal of this chapter is to summarize timelike geodesic dynamics in both the Schwarzschild geometry and Kerr equatorial geometry. In both cases, motion is confined to a plane. This chapter is compiled from standard GR textbooks [34; 35; 36], a recent paper by Levin and Perez-Giz [37] and some original unpublished work. The objective is to review a nice set of existing visual and analytic tools for organizing the conservative (non-radiating) motion when the spacetime does not evolve and the motion is planar. This is a prelude to chapters 3, 4 and 5 where we will show how to generalize it even when the motion of our binaries ceases to be planar.

2.1 The geodesic equations in the Schwarzschild metric

We begin with the Schwarzschild metric in spherical polar coordinates and dimensionless units where $(G = c = 1)$. The central black hole mass M and the test particle mass μ have been appropriately absorbed into the coordinates to ensure dimensional correctness and is equivalent to setting $M = \mu = 1$. The

metric in this form is

$$\begin{aligned} ds^2 &= -d\tau^2 \\ &= \left(1-\frac{2}{r}\right)dt^2 - \left(1-\frac{2}{r}\right)^{-1} dr^2 - r^2 d\theta^2 - r^2\sin^2\theta d\varphi^2 \quad , \end{aligned} \tag{2.1}$$

where τ is proper time, t is coordinate time and r, θ and φ are spherical polar coordinates.

The geodesic equations

$$\frac{d^2x^\lambda}{dt^2} = -\Gamma^\lambda_{\mu\nu}\frac{dx^\mu}{dt}\frac{dx^\nu}{dt} \quad , \tag{2.2}$$

where $\Gamma^\lambda_{\mu\nu}$ are the Christoffel connections and defined by

$$\Gamma^\lambda_{\mu\nu} = \frac{1}{2}g^{\lambda\sigma}\left(\partial_\mu g_{\nu\sigma} + \partial_\nu g_{\sigma\mu} - \partial_\sigma g_{\mu\nu}\right) \quad , \tag{2.3}$$

are the equations of motion (EOM) for the system. However, solving for the motion directly from the geodesic equations is cumbersome because (2.2) yields four coupled second-order differential equations. Instead, we exploit the symmetries of the Schwarzschild geometry to determine simplified equations of motion.

The Schwarzschild geometry is invariant under time translations and two angular rotations. These symmetries lead to a conserved energy (E), z-component of the angular momentum (L_z), and a total angular momentum magnitude (L). Because L and L_z are both conserved, a geodesic is confined to a fixed inclination, ι, where $\cos\iota = \frac{L_z}{L}$. Therefore, all Schwarzschild motion is confined to a plane. Further, because of the spherical symmetry there is no preferred equatorial plane. So we are always free to choose the equatorial plane to coincide with the plane of motion of a geodesic. That choice of equatorial plane is equivalent to choosing $\theta = \frac{\pi}{2}$. We will always make that choice because it greatly simplifies the mathematical overhead in solving for the dynamics in this system.

We can find the coordinate representation of the conserved quantities directly from $K_\mu u^\mu =$ constant, where u^μ is the particle's four-velocity and K_μ is a Killing vector satisfying Killing's equation $\bigtriangledown_{(\mu}K_{\nu)} = 0$ ($\bigtriangledown_\mu$ denotes a covariant derivative and the parentheses indicate that we take the symmetric

part). In light of the conventions above, we find that

$$E = \left(1 - \frac{2}{r}\right)\frac{dt}{d\tau} \tag{2.4a}$$

$$\begin{aligned} L_z &= L \\ &= r^2 \frac{d\varphi}{d\tau} \quad . \end{aligned} \tag{2.4b}$$

Equations (2.4) can be rearranged to furnish the EOM for t and φ (the EOM for θ, of course, is $d\theta/d\tau = 0$).

To get the remaining radial EOM we contract the 4-velocity and see from the metric in equation 2.1 that

$$g_{\mu\nu}\frac{dx^\mu}{d\tau}\frac{dx^\nu}{d\tau} = -1 \quad , \tag{2.5}$$

which yields

$$\begin{aligned} -1 = &\left(1 - \frac{2}{r}\right)\left(\frac{dt}{d\tau}\right)^2 - \left(1 - \frac{2}{r}\right)^{-1}\left(\frac{dr}{d\tau}\right)^2 - r^2\left(\frac{d\theta}{d\tau}\right)^2 \\ &- r^2\sin^2\theta\left(\frac{d\varphi}{d\tau}\right)^2 \quad . \end{aligned} \tag{2.6}$$

Plugging equation 2.4 into equation 2.6 and simplifying we obtain

$$-E^2 + \left(\frac{dr}{d\tau}\right)^2 + \left(1 - \frac{2}{r}\right)\left(\frac{L^2}{r^2} + 1\right) = 0 \quad . \tag{2.7}$$

We can see from the radial EOM, equation (2.7), that the radial motion can be mapped to a classical 1D effective potential V_{eff}. We now turn to a description of the effective potential formulation of Schwarzschild motion.

2.2 V_{eff} formulation

Just as in the Newtonian 1-body problem, equation (2.7) contains only the orbital coordinate r and its velocity $\dot{r}$. Additionally, the terms containing the constant parameters E and L can be isolated in such a way that we can rearrange equation (2.7) into the form

$$\frac{1}{2}\left(\frac{dr}{d\tau}\right)^2 + V_{\text{eff}} = \mathcal{E}_{\text{eff}} \quad , \tag{2.8}$$

in exact analogy to what is done for the radial motion in the Newtonian 1-body problem. Rearranging (2.7) into the form (2.8), we find that for the Schwarzschild system,

$$V_{\text{eff}} = \frac{1}{2} - \frac{1}{r} + \frac{L^2}{2r^2} - \frac{L^2}{r^3} \quad , \tag{2.9}$$

and

$$\mathcal{E}_{\text{eff}} = \frac{1}{2}E^2 \quad . \tag{2.10}$$

It is important to note that a clear effective potential formulation is possible in the Schwarzschild system because the EOM for r, equation (2.7), has no coupled E-L terms. The separability of E and L allows us to put all E dependencies in the $\mathcal{E}_{\text{eff}}$ term and all L dependencies in the V_{eff} term [1]. It is a direct result of this E-L separability in (2.7) that the orbital dynamics of the Schwarzschild system can be formally described by the effective potential in exactly the same way that an effective potential is used in Newtonian dynamics.

We thus have (up to initial conditions) a two-parameter family of orbits, each orbit in the family specified by its E and L. Because those two parameters are separable in (2.8), our method for determining the allowed orbits is as follows. We choose an L and, for that value of L, we can plot V_{eff} as a function of r from equation (2.9). From this plot, we immediately see what the allowed orbits are for that L. This procedure is identical to the analogous one in the effective potential description in Newtonian dynamics.

While the radial motion in the Schwarzschild geometry can be expressed in terms of the familiar effective potential technique of Newtonian mechanics, the actual effective potential of Schwarzschild is different from Newton. In the Newtonian case, there are only two qualitatively different categories of V_{eff} curves in terms of their shapes: one for $L = 0$, which has no extremum and slopes down to negative infinity as r drops, and one for all other L that contains a single minimum and an angular momentum barrier on the left that approaches infinity as $r \to 0$. In contrast, the Schwarzschild V_{eff} admits five qualitatively distinct shapes of curves, depending on the value of L. Figure 2.1 shows the five categories of V_{eff} curves allowed by the Schwarzschild metric,

[1] The separability of E and L comes from the spherical symmetry of the Schwarzschild metric, which is reflected in the fact that there are no coordinate cross-terms. As we will see in the next section this does not hold for the Kerr geometry.

from which we can discern at a glance various qualitative categories of possible Schwarzschild orbits, summarized in Table 2.1.

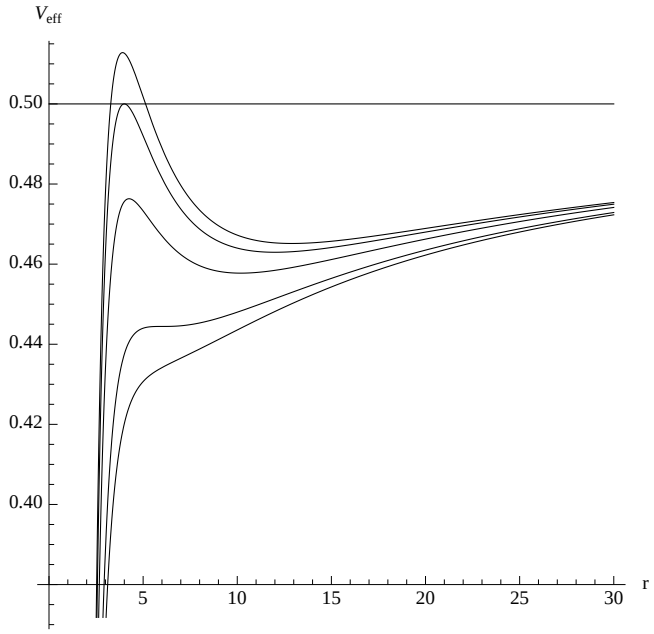

Figure 2.1: The highest curve has an $L = 4.1$. The next highest curve has an $L = L_{ibco} = 4$ where the unstable circular orbit is marginally bound with $E = 1$. The middle curve has $L = 3.8$. The second lowest curve has an $L = L_{isco} = \sqrt{12}$ where the stable and unstable circular orbits have merged producing a saddle point. And the lowest curve has $L = 3.3$.

Two of the five curves are boundary cases or critical cases which divide the allowed orbit classification into three regimes. The L value for each of the two boundary cases is given a special name, $L_{ibco} = 4$ and $L_{isco} = \sqrt{12}$, where *ibco* stands for innermost bound circular orbit and *isco* stands for innermost stable circular orbit. These boundary L values are named such because L_{ibco} is the largest L value for which there is a bound ($E \leq 1$) unstable circular orbit and L_{isco} is the smallest L value for which there is a stable circular orbit (or, rather, for which there are any circular orbits). More specifically, for all $L > L_{ibso}$, there is only one bound circular orbit and it is stable and there exists the possibility of scattering orbits, and for all $L < L_{isco}$ there are no circular orbits and the only allowed orbits are plunging. In Figure 2.1, $L = L_{ibco}$ is the second highest curve and $L = L_{isco}$ is the second lowest curve. For all

$L_{isco} < L < L_{ibco}$, there exist two bound circular orbits, one stable and one unstable. We *define* the strong-field as the regime in which we have a bound unstable circular orbit, i.e. the regime in which $L < L_{ibco}$.

2.3 Summary of possible motions

We summarize all the dynamical features of the allowed orbits in the Schwarzschild geometry in Table 2.1, which is broken up according to the five different L regimes. The subscript s in Table 2.1 means stable circular orbit and the subscript u means unstable circular orbit.

While a true effective potential modeled on the Newtonian system[2] also provides velocity information about a test particle in orbit at a position not on the curve, that aspect of the effective potential is not necessary for us to organize the dynamics as in Table 2.1.

2.4 Circular orbits revisited

As evident from V_{eff} in Figure 2.1, each fixed L admits $0, 1$ or 2 circular orbits, depending on that L value. We can summarize the constant r, circular orbits in the following way. To find the E and L values of the circular orbits, we take equation (2.7) and solve for $\ddot{r}$. We can then solve for E_{circ} and L_{circ} by simultaneously solving $\dot{r} = \ddot{r} = 0$ for E and L. We find that

$$E_{circ}(r) = \frac{r-2}{r^{\frac{1}{2}}\sqrt{r-3}} \tag{2.11a}$$

$$L_{circ}(r) = \frac{r}{\sqrt{r-3}} \quad . \tag{2.11b}$$

Figure 2.2 shows a plot of E_{circ} vs r and L_{circ} vs r. Looking at the L_{circ} vs r plot, we see that for a given L, there are always two circular orbits until you hit a minimum L value for which there is only one circular orbit. Then for all $L < L_{min}$ there are no circular orbits. The minimum L value is that of

[2]While the Schwarzschild effective potential allows for different types of orbits than those possible in a Newtonian potential, the Schwarzschild effective potential otherwise works just like a Newtonian potential in terms of the identification of circular orbits (extrema of the potential) and the identification of turning points for eccentric orbits (intersection of $\mathcal{E}_{\text{eff}} =$ constant lines with the potential.

	Plunge	**Scatter**	**Bound**	**Circular**
$L < L_{isco}$	All orbits plunge.	None	None	None
$L = L_{isco}$	All orbits plunge except one; $r = r_{circ}$ and $E = E_{circ}$	None	None	One stable circular orbit at the r and E of the saddle point.
$L_{isco} < L < L_{ibco}$	Orbits with $r < r_u$ or $E > E_u$ plunge.	None	All orbits with $E_s < E < E_u$ and $r > r_u$ are bound.	One stable and one unstable, both bound. $r_s > r_u$ and $1 > E_u > E_s$.
$L = L_{ibco}$	Orbits with $r < r_u$ or $E > E_u = 1$ plunge.	None	All orbits with $r > r_u$ and $E_s < E < E_u$ are bound.	One stable and one unstable. $r_u < r_s$ and $E_u > E_s$.
$L > L_{ibco}$	Orbits with $r < r_u$ or orbits with $E > E_u$ plunge.	Orbits with $1 < E < E_u$ and $r > r_u$ scatter.	Orbits with $E_s < E < 1$ and $r > r_u$ are bound.	One stable and one unstable. $r_u < r_s$ and $E_s < 1 < E_u$.

Table 2.1: The above table shows what types of orbits are allowed for a given L in the Schwarzschild geometry.

the *isco* and its value corresponds to L_{isco} in Table 2.1. If we now look at the E_{circ} vs r graph we can see that there is also a minimum value in the energy of circular orbits and the E_{min} occurs at the same r value as does L_{isco}. So the *isco* is the circular orbit with both the lowest energy and the lowest angular momentum.

For all $L > L_{isco}$, we obtain two circular orbits. The smaller radius one always has a higher energy, and there is no upper bound to that energy. At a certain L, the energy of the smaller radius circular orbit reaches $E = 1$. For

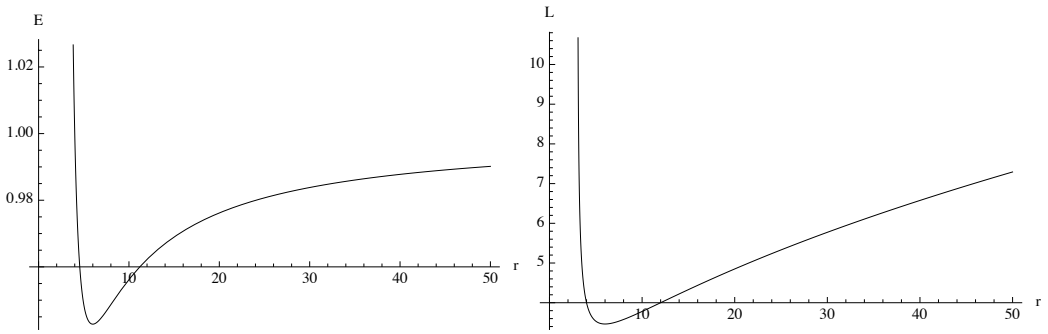

Figure 2.2: Left: Shows a plot of E vs r for circular Schwarzschild orbits. Right: Shows a plot of L vs r for circular Schwarzschild orbits.

any $L > L(E = 1)$, the energy of that circular orbit becomes $E > 1$, making that orbit unbound (able to reach radial infinity). The L value corresponding to a circular orbit with $E = 1$ is L_{ibco}.

If we continue to investigate the properties of the circular orbits, we find that all circular orbits produced with $r < r_{isco}$ are unstable and $r > r_{isco}$ are stable. This matches the dynamical features we can read off the V_{eff} plot in figure 2.1. All circular orbits have $\frac{\partial V_{\text{eff}}}{\partial r} = 0$. Stable circular orbits further have $\frac{\partial^2 V_{\text{eff}}}{\partial r^2} > 0$, while unstable circular orbits have $\frac{\partial^2 V_{\text{eff}}}{\partial r^2} < 0$. The boundary case – the *isco* – has $\frac{\partial^2 V_{\text{eff}}}{\partial r^2} = 0$. If we compare the r, L and E values of the circular orbits that we read from the different V_{eff} curves in figure 2.1, we see that those values match the values on the E_{circ} and L_{circ} vs r graphs of Figure 2.2.

Investigating the orbital dynamics using the equations of motion, we discover all the properties layed out in Table 2.1. While less visually direct than the effective potential method described in Section 2.1, this method is still a correct way of realizing the orbital dynamics of the Schwarzschild system.

2.5 Homoclinic orbits

The separatrix orbit, also called a homoclinic orbit [49; 50; 51], is a particularly important orbit for the dynamical analysis of our system because it marks, for a given L, the boundary between orbits that are bound and those that plunge. For all L such that $L_{isco} < L < L_{ibco}$, the unstable circular orbit is bound. There also exists a bound orbit with the same energy as the unstable circular

orbit that is not circular. The left panel of Figure 2.3 shows an effective potential for such an L with a dotted line indicating the non-circular orbit with the same energy as the unstable circular orbit.

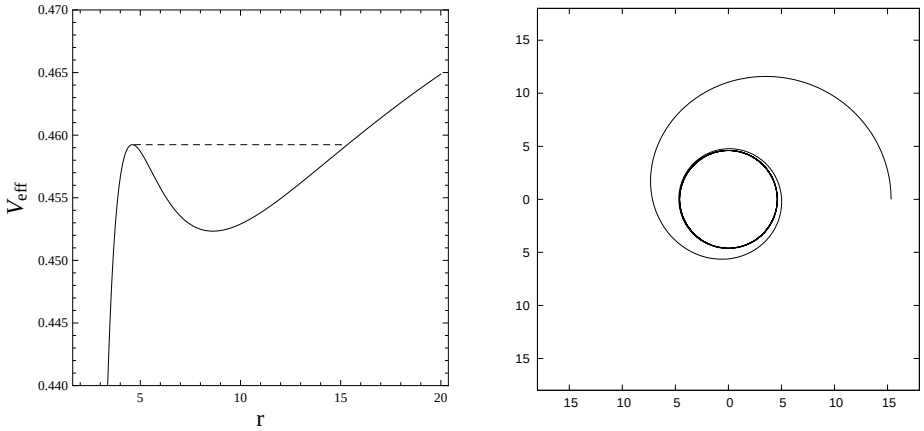

Figure 2.3: Left: An effective potential for $L_{isco} < L < L_{ibco}$ with $L = 3.636619$. The dotted line has an energy $E = 0.958373$, the energy of the unstable circular orbit and the associated homoclinic orbit. Right: The homoclinic orbit with $L = 3.636619$ and $E = 0.958373$.

This separatrix orbit has an apastron larger then the radius of the unstable circular orbit and a periastron equal to the radius of the unstable circular orbit. Unlike with a typical bound orbit, which has a finite radial period, it takes an infinite amount of time for the dashed orbit to reach that periastron, and during that time, it whirls quasi-circularly in azimuth an infinite number of times as it approaches the unstable circular orbit. Because it approaches the same circular orbit in the infinite future and past, this orbit is called homoclinic (heteroclinic orbits approach two different recurring orbits in the infinite future and past). The right panel of Figure 2.3 shows the appearance in physical space of the same homoclinic orbit identified on the effective potential.

2.6 Zoom-whirl orbits

A homoclinic orbit is the infinite whirl limit of a more general class of orbits that exist in the strong field called zoom-whirl orbits. It was generally believed that zoom-whirl orbits only existed energetically very near the homoclinic

orbit. But that belief turns out not to be true, and zoom-whirl behavior is in fact prevalent in the strong field even at energies closer to that of the stable circular orbit [37].

While most GR textbooks highlight the distinction between Newtonian and relativistic motion with a discussion of the perihelion precession of Mercury, which is described as the slow precession of the Keplerian ellipse, this type of orbit only exists in the weak field. As it turns out, there are no slowly precessing ellipses in the strong field. Periastron advance can be severe and the orbit can execute tight nearly circular whirls before zooming out again to apastron. This behavior has been known for a while and is termed "zoom-whirl". While not every orbit in the strong field is a zoom-whirl orbit, this behavior is common.

The top two panels of Figure 2.4 show the same single zoom-whirl orbit. For visual ease, the top left panel has been evolved for a shorter amount of time to see more clearly both the zoom and whirl phases of the orbit. The top right panel has been allowed to evolve for a longer time to show the pattern the orbit traces out. The bottom panel of the figure shows the corresponding effective potential picture with a dotted line indicating the energy of this orbit. Notice that even though this energy is a good bit below that of the unstable circular orbit, it nonetheless exhibits zoom-whirl behavior.

2.6.1 Orbital frequencies

Because all Schwarzschild orbits execute planar motion in the equatorial plane, they are restricted to radial and azimuthal motion. From the effective potential picture of Figure 2.1, we immediately see that all bound non-plunging, non-scattering orbits are periodic in the radial direction and move between an apastron (r_a) and periastron (r_p). We can therefore define a radial period T_r and radial frequency ω_r,

$$\begin{aligned} T_r &= \frac{2\pi}{\omega_r} \\ &= 2\int_{r_p}^{r_a} dr \frac{d\tau}{dr} \quad , \end{aligned} \tag{2.12}$$

where $\frac{d\tau}{dr}$ is found from equation (2.7)[3].

[3]We have chosen to define the period and frequency in terms of proper time, τ. We can also define corresponding periods and frequencies for coordinate time t or for any other choice of time coordinate.

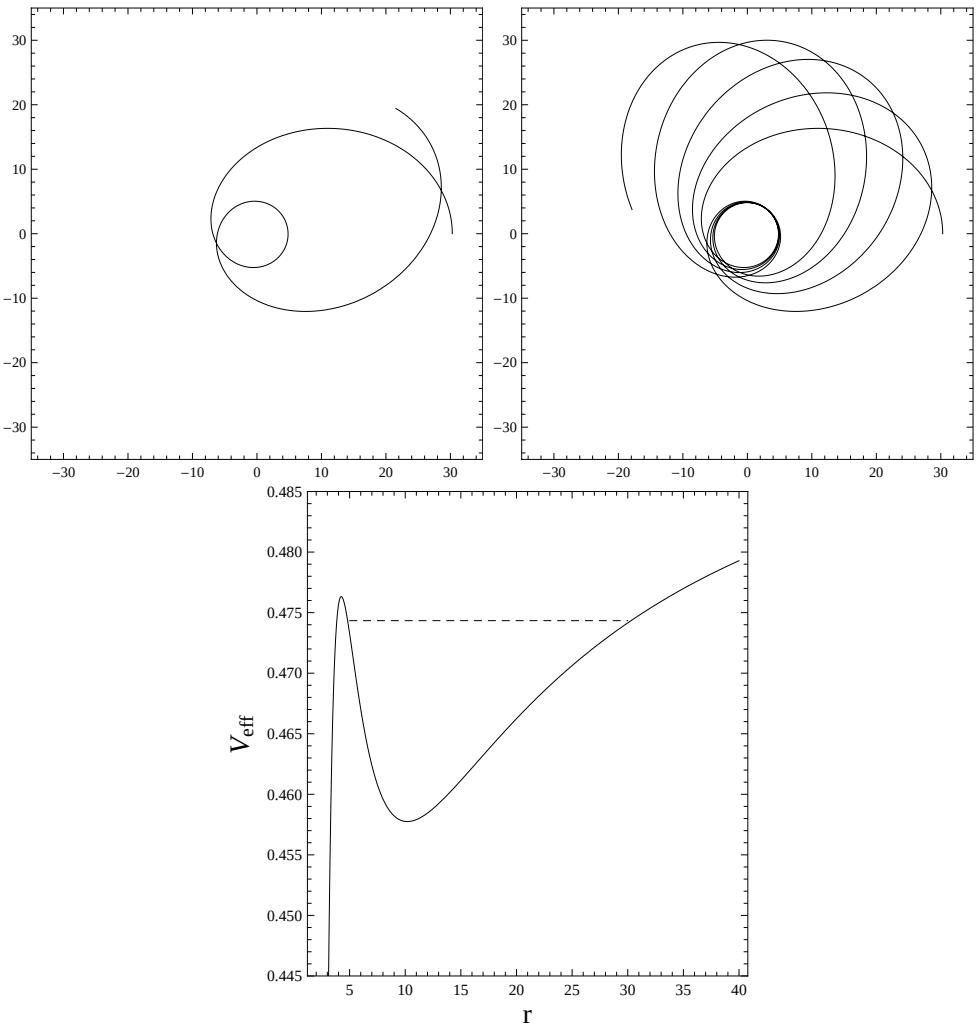

Figure 2.4: Top: The top two plots show the same generic orbit for different amounts of time in the Schwarzschild spacetime exhibiting zoom-whirl behavior with orbital parameters $E = 0.974$ and $L = 3.8$. Bottom: The effective potential for orbits with $L = 3.8$. The dotted line indicates an energy of $E = 0.974$.

From the φ EOM, equation 2.4b, we see that azimuthal motion depends only on the radial coordinate and constants. Therefore, because the radial motion is periodic, the azimuthal velocity must also be periodic over a radial

cycle. We therefore define an azimuthal frequency

$$\begin{aligned}\omega_\varphi &= \frac{1}{T_r}\int_0^{T_r} d\tau \frac{d\varphi}{d\tau} \\ &= \frac{\Delta\varphi}{T_r}\end{aligned} \tag{2.13}$$

as the average value of the azimuthal velocity over one radial period. The quantity $\Delta\varphi$ above represents the total amount of azimuth accumulated over one radial period and is always larger than 2π due to periastron advance. We can then also define an associated time

$$T_\varphi = \frac{2\pi}{\omega_\varphi} \tag{2.14}$$

that represents the amount of time it takes for the orbit to accumulate 2π of azimuth, averaged over all possible initial r values during a radial cycle.

2.6.2 The parameter q

In an effort to quantify what exactly we mean by the whirl phase of a zoom-whirl orbit, we now define a parameter q related to the ratio of the orbital frequencies. From equations (2.12) and (2.13), we have

$$\frac{\omega_\varphi}{\omega_r} = \frac{\Delta\varphi}{2\pi} \quad . \tag{2.15}$$

Recalling that $\Delta\varphi \geq 2\pi$ relativistically, we can then define

$$\frac{\Delta\varphi}{2\pi} \equiv 1 + q \quad , \tag{2.16}$$

were we separate out the 1 so that q is only a measure of the amount of azimuthal overshoot per radial cycle beyond what one would expect in Newtonian gravity, in which all orbits are ellipses with $\Delta\varphi_{\text{Newton}} \equiv 2\pi$. In general, if an orbit starts at apastron, then we have seen that on its way in to periastron, it can enter a quasi-circular whirling phase. We can further break q down to provide an unambiguous definition of the number of such whirls as

$$q = w + \delta \quad . \tag{2.17}$$

In other words, we can take the integer part w of q as a definition of the integer number of 2π whirls executed by φ beyond the requisite single accumulation of 2π executed Newtonianly. This definition of "whirliness" was proposed in Reference [37] and turns out to be very fruitful, particularly for classifying periodic orbits (as we will see in Section 2.7). Incidentally, the only restriction on the fractional part δ of q is that it is real-valued. δ measures the part of $\Delta\varphi$ that is due to apastron advance.

Figure 2.4 shows a zoom-whirl orbit with $q = 1.07341\ldots$, or written in the form of Equation (2.17) as $q \approx 1+0.07341$. Topologically, this tells us that the orbit whirls once before returning to apastron and that its apastron advances by approximately $2\pi \times 0.07341 \approx 0.461249$ radians per radial cycle.

We can now ask how values of q are distributed over the space of parameters E, L. Levin and Perez-Giz also showed that for any fixed L, the value of q increases monotonically with energy and eccentricity. The lower bound $q_{\min}$ on q for a given L is interestingly *not* zero but rather the q associated with a stable circular orbit[4]. Figure 2.5 shows this monotonic relationship. Notice that $q_{\min} \neq 0$.

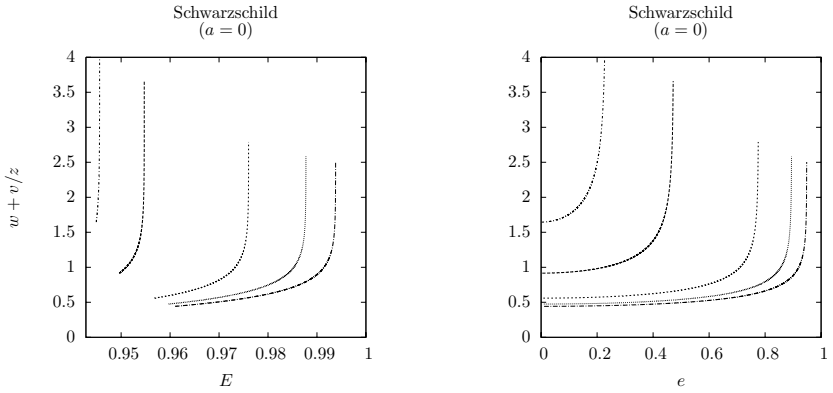

Figure 2.5: Schwarzschild for $L_{isco} < L < L_{ibco}$. In order from left to right, the L values are $3.5, 3.6, 3.8, 3.9, 3.95$. In terms of accumulated angle, $\frac{\Delta\varphi}{2\pi} - 1 = w + \frac{v}{z}$.

One result of that analysis is that $q_{\min} >> 0$ for small enough values of L,

[4]The radial frequency ω_r of a circular orbit is not active, so to speak, and is defined by the frequency of small radial oscillations around such a (stable) circular orbit. The q associated with a circular orbit therefore reflects the q of an orbit that can be interpreted as such a small (infinitesimal eccentricity) oscillation.

so that arbitrarily low eccentricity perturbations to the stable circular orbit will look not like a slowly precessing ellipse but like a low-leaf clover, possibly with many whirls. In other words, motion like Mercury's is excluded in the strong field, even for orbits that are arbitrarily close to circular orbits.

2.7 Periodic orbits

When ω_φ and ω_r are rationally related, the orbit is periodic – it closes on itself and the radial and azimuthal coordinates return to their initial positions[5] simultaneously after a finite amount of time.

2.7.1 The taxonomy of periodic orbits

Equations (2.15) and (2.16) imply that, for a periodic orbit, q is rational. For a rational q, δ in Equation (2.17) must be a rational number less than 1. We express δ for a periodic orbit as $\frac{v}{z}$, where v and z are relatively prime integers. Therefore, for a periodic orbit,

$$q = w + \frac{v}{z} \quad , \tag{2.18}$$

where we have chosen the labels v and z suggestively. We have already determined that w tells us the number of a whirls an orbit undergoes per radial cycle. The integers v and z can similarly be related to the topology of a periodic orbit. z measures the number of leaves or "zooms" in the pattern traced out by the closed orbit. The leaves can be connected to trace out a polygon where the tip of each leaf is a vertex of the polygon. We then label each vertex in the counterclockwise sense (for prograde orbits) by $0, 1, \ldots$ where 0 is the vertex on which the orbit starts. v therefore tells you the first vertex in the pattern the orbit reaches after the 0th vertex.

Therefore, q is a topological property of an orbit and will be independent of choices of coordinates. Figure 2.6 shows two such orbits. Notice that while the two orbits illustrated look topologically similar, they are actually distinct because they fill the leaves in the pattern in a different order. The distinctness of the two orbits is further emphasized in that the two orbits have distinct energies and different geometric properties (e.g. different eccentricities).

[5] We are identifying $\varphi = 0$ and $\varphi = 2\pi$.

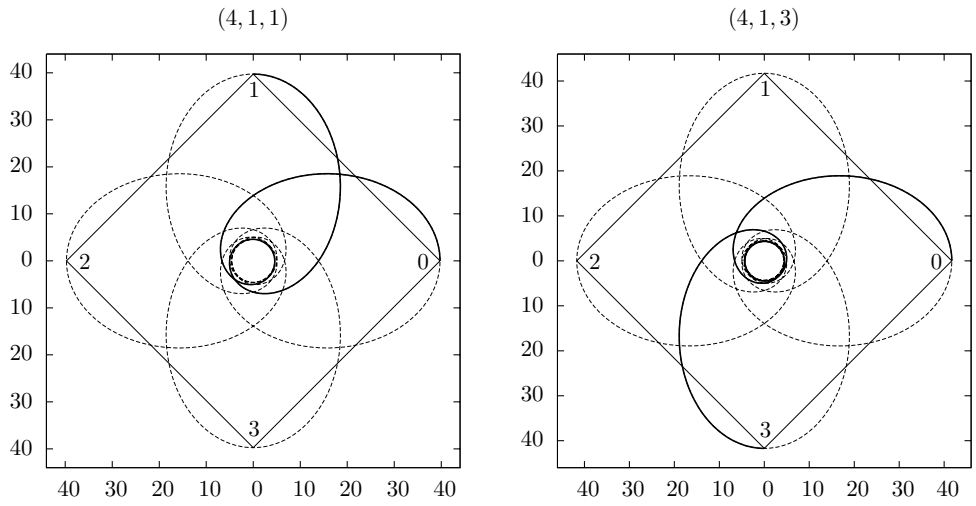

Figure 2.6: 4-leafed orbits with one whirl. Left: Leaves are traced out in sequential order for the $(z = 4, w = 1, v = 1)$ closed orbit. Right: Leaves are traced out of order for the $(z = 4, w = 1, v = 3)$ closed orbit. The orbital parameters are $L = 3.834058$ for both. The energy of the leftmost orbit is $E = 0.979032$ and the energy of the rightmost orbit is $E = 0.979842$.

2.7.2 Periodic tables

Given the existence periodic orbits, we now seek to organize them to map out the space of bound geodesics. An important feature of q that allows us to nicely taxonomize periodic orbits (and, as we will see, all orbits by extension) is that the energy and eccentricity of an orbit increase monotonically with q. The dynamical features of the allowed periodic orbits in the Schwarzschild geometry presented in the V_{eff} described in Figure 2.1 can then be organized into periodic tables for a given L.

Figure 2.7 shows an example of one such table for Schwarzschild orbits. The table is organized such that energy (and therefore q) increase from left to right and top to bottom. Each entry is labeled with a triplet of numbers (z, w, v). Each row has the same values of z and v but increases in w by one in each column.

One nice feature of such a table is that every aperiodic orbit can be interpreted as a slow precession of some low-leaf periodic orbit in the table. This is the strong field generalization of the textbook description of Mercury as a slow precession of an ellipse. While not every orbit is a slow precession of an ellipse, ever orbit is either a low-leaf clover or a slow precession of one.

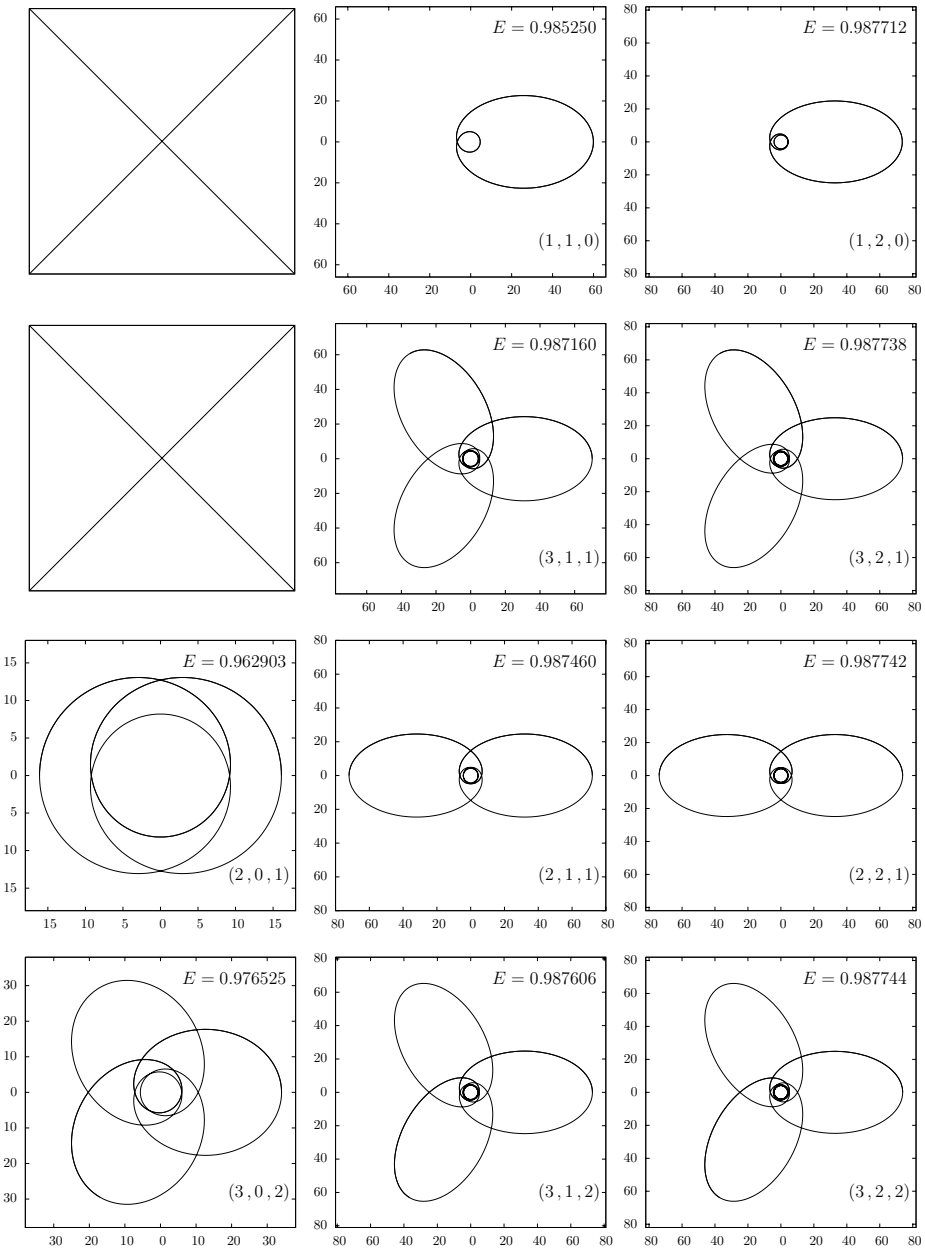

Figure 2.7: All $z = 1, 2, 3$ orbits with $w = 0$ for the first column, $w = 1$ for the middle column, and $w = 2$ for the last column. All orbits have an $L = 3.9$. Orbits increase in energy from top to bottom and left to right. The first radial cycle is emphasized in bold for each orbit. Notice the first and second entry in the first column are blank, indicating the inaccessibility of the $(1, 0, 0)$ and $(3, 0, 1)$ orbits.

2.8 Summary of dynamical results

With this taxonomy, we are able to define zoom-whirl behavior topologically. We find that zoom-whirl orbits are *not* exclusively a high eccentricity phenomenon. Slowly precessing ellipses like the orbit of Mercury are excluded in the strong field. And we are able to generalize the notion of a precessing ellipse to a precessing clover as shown in Figure 2.8.

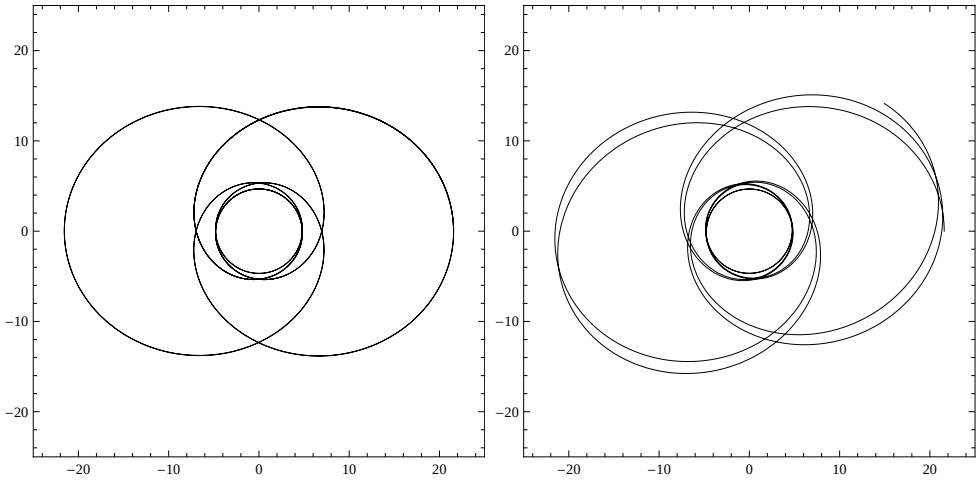

Figure 2.8: Both orbits have $L = 3.718679$. Left: An exactly periodic orbit with $E = 0.966555$ and $q = 1\frac{1}{2}$. Right: A nearby aperiodic orbit with $E = 0.96658$. It looks like a slow precession of the exactly periodic orbit on the left.

The panel on the left of Figure 2.8 is a periodic orbit with a $q = 1\frac{1}{2}$. It is a two-leaf clover as indicated by the z value in the denominator. It whirls once during each radial cycle, as indicated by the w-value, and it fills the next sequential leaf as indicated by the $v = 1$. The orbit on the right has a slightly higher energy and looks like a slow precession of the perfectly periodic orbit on the left. While it does not have rationally related orbital frequencies, it has $q = 1.51521\ldots \approx 1\frac{515}{1000}$. That means it is close to a 1000-leaf clover that skips 515 leaves and whirls once during each zoom (radial cycle).

We can determine the amount by which φ overshoots the 2-leaf clover by $1\frac{515}{1000} = 1\frac{1}{2} + \frac{3}{200}$. That means the precessing two-leaf clover overshoots the angular position of the apastron of the periodic two-leaf clover by $\frac{3}{200}(2\pi) \approx 0.0942$ radians during each radial cycle.

2.9 Kerr equatorial dynamics

Sections 2.1 - 2.8 reviewed the taxonomy of bound geodesics in the Schwarzschild spacetime and culminated in the construction of periodic tables of orbits. In this section, we will show that the analogous structure for bound geodesics exists for equatorial orbits in the Kerr spacetime. To uncover this dynamical structure, we will proceed analogously to how we did in the Schwarzschild case, by first seeking an effective potential description of the geodesic motion and then progressing to the construction of periodic tables.

2.9.1 The geodesic equations

We work in Boyer-Lindquist coordinates and dimensionless units in which ($G = c = 1$) and the central black hole mass M and the test particle mass μ are appropriately absorbed into the coordinates to ensure dimensionality. In these coordinates and units, the Kerr metric is

$$\begin{aligned} ds^2 =& -d\tau^2 \\ =& -\left(1-\frac{2r}{\Sigma}\right)dt^2 - \frac{4ar\sin^2\theta}{\Sigma}dtd\phi + \frac{\Sigma}{\Delta}dr^2 + \Sigma d\theta^2 \\ &+ \sin^2\theta\left(r^2+a^2+\frac{2a^2r\sin^2\theta}{\Sigma}\right)d\phi^2 \quad , \end{aligned} \tag{2.19}$$

where

$$\begin{aligned} \Sigma &\equiv r^2 + a^2\cos^2\theta \\ \Delta &\equiv r^2 - 2r + a^2 \quad . \end{aligned} \tag{2.20}$$

Using the geodesic equations, (2.2), we find the four equations of motion

$$\frac{dt}{d\tau} = \frac{1}{\Sigma}\left\{-a\left(aE\sin^2\theta - L_z\right) + \frac{r^2+a^2}{\Delta}P(r)\right\} \tag{2.21}$$

$$\frac{d\varphi}{d\tau} = \frac{1}{\Sigma}\left\{-\left(aE - \frac{L_z}{\sin^2\theta}\right) + \frac{a}{\Delta}P(r)\right\} \tag{2.22}$$

$$\left(\frac{dr}{d\tau}\right)^2 = \frac{R(r)}{\Sigma^2} \tag{2.23}$$

$$\left(\frac{d\theta}{d\tau}\right)^2 = \frac{\Theta(\theta)}{\Sigma^2} \tag{2.24}$$

where

$$P(r) = E\left(r^2 + a^2\right) - aL_z \tag{2.25}$$

$$R(r) = -\left(1 - E^2\right) r^4 + 2r^3 - \left[a^2\left(1 - E^2\right) + L_z^2\right] r^2 + 2\left(aE - L_z\right)^2 r - Q\Delta \tag{2.26}$$

$$\Theta(\theta) = Q - \cos^2\theta \left\{ a^2\left(1 - E^2\right) + \frac{L_z^2}{\sin^2\theta} \right\} \tag{2.27}$$

and where E, L_z and Q are conserved quantities associated with each geodesic of the Kerr geometry. Just like the Schwarzschild system, Kerr has a time-translation symmetry that leads to a conserved energy (E) and an azimuthal rotation symmetry that leads to a conserved z-component of the angular momentum (L_z). However, Kerr does not have the same polar symmetry of Schwarzschild. Despite the loss of one rotational symmetry, Carter famously found an additional conserved quantity, now called the Carter constant (Q) [52]. Equatorial orbits are characterized by $Q = 0$.

2.9.2 The pseudo-effective potential

As we did in the Schwarzschild system, we would like to map the radial motion an a 1D effective potential. Unfortunately, the Kerr equatorial system does not allow a true effective potential in the quasi-Newtonian sense detailed in Section 2.2 (i.e. that the difference between the effective energy and the effective potential gives the square of the radial velocity with respect to some time parameter). As we show below, however, we can still find a pseudo effective potential that allows us to show that all the features outlined in Table 2.1 persist for equatorial Kerr orbits.

The feature of the radial EOM, equation (2.23), that prohibits a true Newtonian effective potential is that E and L_z are not separable as they were in the Schwarzschild radial EOM (2.7). The lack of separability means that we cannot put all the L_z dependence into V_{eff} and all the E dependence into the $\mathcal{E}_{\text{eff}}$. The best we could do in the conventional sense of a potential would result in a V_{eff} that depends on both E and L_z, so that rather than having a fixed effective potential for a given L_z, we would have a different V_{eff} picture for every E and L_z pair. While mathematically consistent, this is less visually useful than the Schwarzschild effective potential that remains fixed for a given L.

Rather than have a different V_{eff} for every E, L_z pair, we instead define a pseudo-effective potential that will allow us to retrieve all salient orbit information in the way summarized in Table 2.1. We call it a pseudo-effective potential because we will not replicate all aspects of the traditional Newtonian effective potential. Because we are only interested in using the effective potential as a visual tool to see what types of orbits are allowed, our only real interest is in plotting the turning points of eccentric orbits and the radii of circular orbits. Such knowledge would allow us to see immediately whether an orbit is bound, plunging, scattering, etc. So while we will not be able to use our pseudo-effective potential to determine velocity information in the way that a true effective potential can be used, that is irrelevant for our purposes.

Our method for constructing such a function is as follows:

1. Take the RHS of equation (2.23) and set it equal to zero [6].
2. Solve the resulting equation for $E\left(a, r, L_z\right)$.
3. Modeling our pseudo-effective potential after a true effective potential of equation (2.8), set
$$\mathcal{E}_{\text{eff}} = \frac{1}{2}E^2 \quad . \tag{2.28}$$
4. The resulting equation is a pseudo-effective potential equation because it is only the V_{eff} when $\dot{r} = 0$. Unlike (2.8) which is true for all values of $\dot{r}$, we are left with something that is only true for turning points and circular orbits. This turns (2.8) into
$$\mathcal{E}_{\text{eff}} = V_{\text{eff}} \quad . \tag{2.29}$$

So as not to become cumbersome in our language, we will shorthand "pseudo-effective potential" as "effective potential" and label it as V_{eff} in the rest of this document.

Following the prescription laid out in the above list, we can find $E|_{\dot{r}=0}$ for Kerr equatorial orbits to be

$$E = \frac{2aL_z + \sqrt{r\Delta\left(a^2\left(2+r\right) + r\left(L_z^2 + r^2\right)\right)}}{r^3 + a^2\left(2+r\right)} \quad , \tag{2.30}$$

[6] In setting $\dot{r} = 0$, we are restricting our r values to turning points (apastra and periastra) or to r values that are constant (circular orbits).

where L_z is positive for prograde[7] orbits and negative for retrograde[8] orbits. And V_{eff} is

$$V_{\text{eff}} = \frac{1}{2}E^2 \quad . \tag{2.31}$$

Using our Kerr equatorial V_{eff} we can choose an a and an L_z and proceed exactly as we did with the Schwarzschild V_{eff} in Section 2.2. We find that for all a and L_z choices, our V_{eff} curves yield the exact same allowed orbits for the exact same categories described in Table 2.1. In fact, the Kerr equatorial case is just the generalization of the Schwarzschild case. We recover the Schwarzschild case if we set the spin, $a = 0$ in our analysis of the Kerr equatorial case. Figure 2.9 shows the 5 different V_{eff} possibilities for retrograde orbits with a spin of $a = 0.99$ from (2.30) and (2.31).

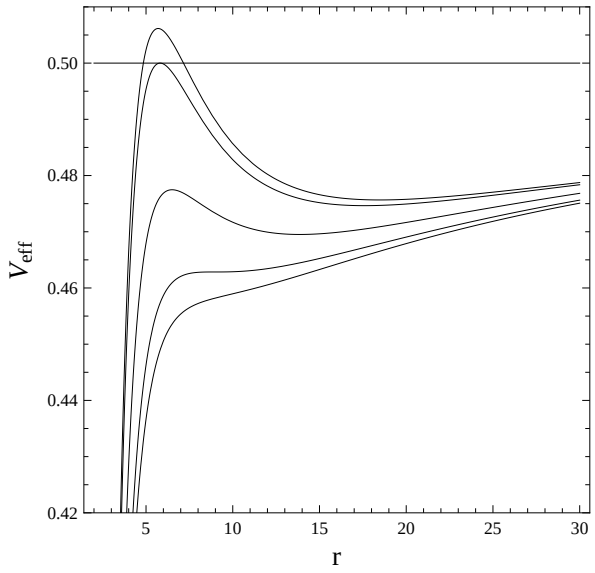

Figure 2.9: A plot of V_{eff} vs r for retrograde orbits with spin $a = 0.99$. The top curve has $L = 4.9 > L_{ibco}$. The second highest curve has $L = L_{ibco} = 4.82135$. The middle curve has $L_{isco} < L = 4.5 < L_{ibco}$. The second lowest curve has $L = L_{isco} = 4.2274$. The lowest curve has $L = 4.1 < L_{isco}$. The straight line is the line $\mathcal{E}_{\text{eff}} = \frac{1}{2}$, the energy divide between bound and unbound orbits.

[7]For equatorial orbits, prograde is defined as an orbit whose L_z and spin, a, are aligned.

[8]For equatorial orbits, retrograde is defined as an orbit whose L_z and spin, a, are antialigned.

2.9.3 Circular, Homoclinic and Zoom-Whirl Orbits

In fact, the entire orbital structure of Kerr equatorial orbits replicates that of the Schwarzschild system as summarized in Table 2.1. Just like the Schwarzschild system, the equatorial Kerr system has constant r circular orbits. To find these circular orbits, we set $\dot{r} = \ddot{r} = 0$ from equation (2.23), and solve for an E_{circ} and $L_{z_{circ}}$. The expressions are

$$E_{circ}(a,r) = \frac{r^{\frac{3}{2}} - 2r^{\frac{1}{2}} \pm a}{r^{\frac{3}{4}}\left(r^{\frac{3}{2}} - 3r^{\frac{1}{2}} \pm 2a\right)^{\frac{1}{2}}} \tag{2.32a}$$

$$L_{z_{circ}}(a,r) = \pm\frac{r^2 \mp 2ar^{\frac{1}{2}} + a^2}{r^{\frac{3}{4}}\left(r^{\frac{3}{2}} - 3r^{\frac{1}{2}} \pm 2a\right)^{\frac{1}{2}}} \tag{2.32b}$$

which are derived in detail in [53]. In (2.32a) and (2.32b), the top sign is used for prograde orbits and the bottom for retrograde orbits.

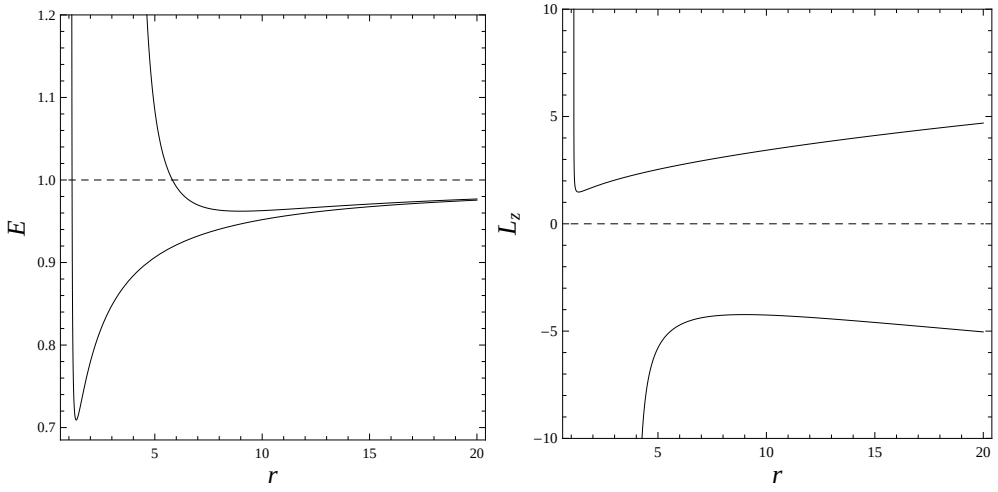

Figure 2.10: Left: The figure shows a plot of L_z vs r for equatorial circular Kerr orbits with $a = 0.995$ and $Q = 0$. Right: Shows a plot of E vs r for circular Kerr equatorial orbits with $a = 0.995$ and $Q = 0$.

In Figure 2.10 we show a plot of E_{circ} and $L_{z_{circ}}$ as a function of r for prograde and retrograde equatorial orbits. We see that while figures 2.2 and 2.10 are quantitatively different, they have the same qualitative features. Namely,

E and $|L_z|$ have a minimum, and the r value of that minimum is the same in the corresponding E and L_z plots. That minimum is the lowest E and L_z value for which there is a circular orbit and that $L_z = L_{z_{isco}}$. For any $L_z > L_{z_{isco}}$ we have two circular orbits, the one with $r > r_{isco}$ is stable and the one with $r > r_{isco}$ is unstable[9]. All stable circular orbits are bound ($E < 1$), but the unstable circular orbits are only bound for $L_z > L_{z_{ibco}}$.

We again have a homoclinic orbit associated with every unstable circular orbit which can be thought of as the infinite whirl limit of orbits with integer values of q. The last panel on the lower left of Figure 2.11 shows a homoclinic orbit. The panels show the progression of the homoclinic orbit as the infinite whirl limit ($q \to \infty$) of periodic orbits with $z = 1$.

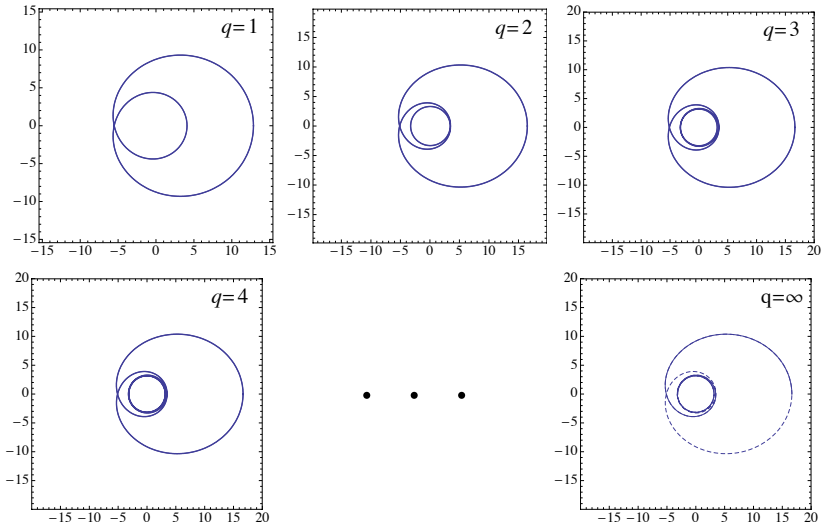

Figure 2.11: The progression of the 1-leaf periodic orbits through $1, 2, 3, 4...\infty$ whirls. The orbits shown are prograde orbits for $a = 0.5$ and $L = 3.158540$, or the average of $L_{\rm isco}$ and $L_{\rm ibco}$. Note that the whirls beyond the second whirl are too closely packed in r to distinguish visually in the plot.

Just as in the Schwarzschild system, the equatorial Kerr motion has a radial and an azimuthal period and frequency which we can define in the identical way we did in Schwarzschild in equations (2.12) and (2.13). Notice, that just as in the Schwarzschild, the equatorial Kerr φ motion depends only on the radial coordinate. Therefore, we define the azimuthal frequency as an azimuthal velocity averaged over the radial period.

[9]The stability of these orbits can be checked by looking at the sign of $\ddot{r}$.

With these orbital frequencies in hand, we again define a q for every orbit exactly as we did in Equation (2.17). The integer part w of q defines the whirliness associated with every orbit. And just as with the Schwarzschild system, we find that bound geodesics in the equatorial Kerr system can exhibit zoom-whirl behavior and that such behavior is not limited to energies near the homoclinic orbit. In fact, as the spin of the central black hole is increased, a given amount of whirliness begins to appears in less eccentric orbits than in the Schwarzschild case.

As in the Schwarzschild case, q increases monotonically with energy and eccentricity. Figure 2.12 shows this relationship. This is crucial for constructing the periodic tables.

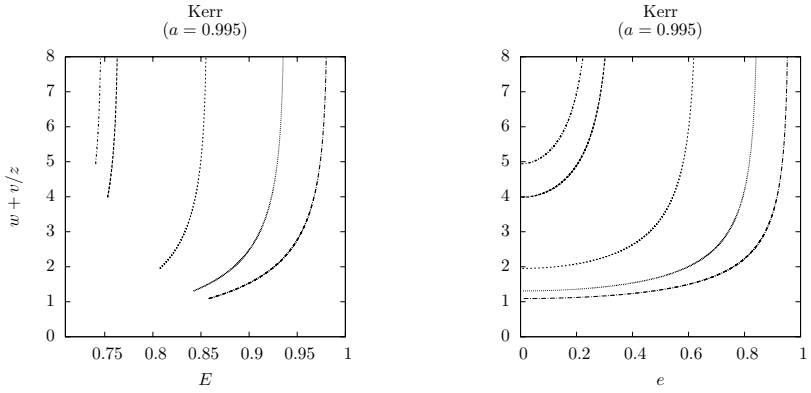

Figure 2.12: Prograde orbits around a spinning black hole with $a = 0.995$. The lines indicate increasing L from left to right through the values $L = 1.57, 1.61, 1.82, 2, 2.1$

2.9.4 Periodic tables

Just as in Section 2.7, periodic orbits have rational q values. We define q for such orbits just as we did in Schwarzschild as $q = w + \frac{v}{z}$, with the topological features of q in the equatorial Kerr system being identical to Schwarzschild.

Given the equatorial Kerr dynamics illuminated by the effective potential picture and summarized in table 2.1 in conjunction with the monotonic relationship between q and the energy and eccentricity of the bound time-like geodesics, we can now construct periodic tables for every fixed a and L_z. Figure 2.13 illustrates one such periodic table.

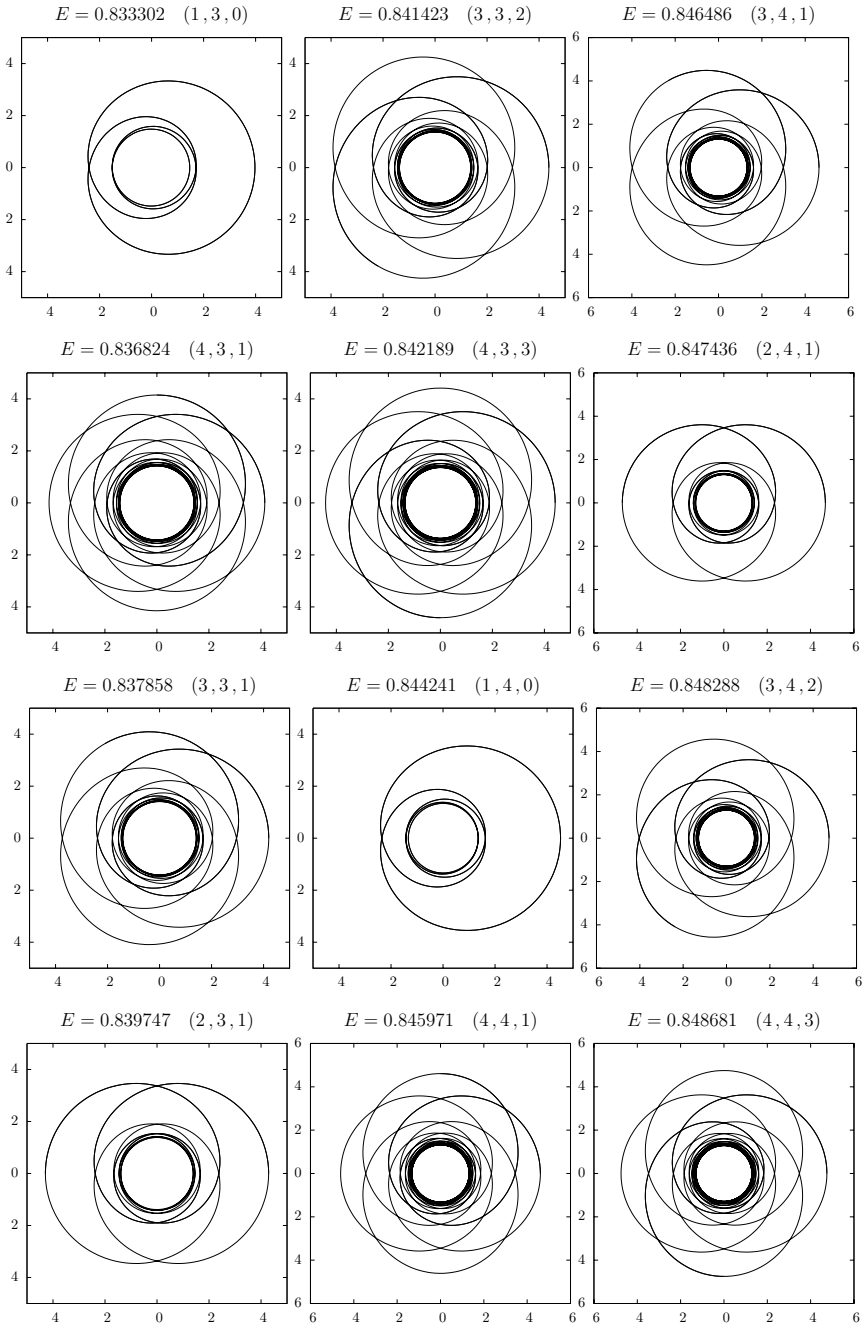

Figure 2.13: A series of $w = 3$ and $w = 4$ orbits for $L = 1.82$ and $a = 0.995$. Orbits increase in energy from top to bottom and left to right. All $z = 1, 2, 3, 4$ orbits are shown.

2.10 Preview of non-planar (3D) orbits

As we have seen in this chapter, we can organize the dynamics in a clear and elegant way when motion is planar. To make a system more physically realistic, we should remove that restriction. This is accomplished by adding spin. In the Kerr case, the spin of the central BH means that motion that does not begin restricted to the equatorial plane (as in this chapter) will evolve in the full 3D space. In comparable mass binaries, the introduction of spin on one or both bodies will likewise destroy the symmetries that guarantee strictly planar motion. The non-planar dynamics of both these systems looks fairly complex and is no longer obviously organizable visually.

We will now proceed to analyze two such nonplanar systems: the PN system with spinning black holes and the generic Kerr system in which we do not limit the motion to be equatorial. In both of these systems, we strive to simplify and understand the dynamics by mimicking the tools used in planar dynamics. It is with that goal in mind that we seek to simplify the seemingly more complicated dynamics of these systems by finding an instantaneous orbital plane that tracks the motion. By analyzing the dynamics within this plane, we will be able to reduce the complicated 3D motion to effective planar motion, and as we will see, we will in fact be able to replicate the dynamical taxonomy of this chapter in both these spinning BH systems.

Chapter 3

Spherical and homoclinic orbits in the PN expansion

3.1 Introduction

In this chapter, we work in the conservative 3PN Hamiltonian approximation plus spin-orbit coupling, considering two spinning black holes in a binary. We focus on special sets of orbits, namely, the spherical orbits. That might seem ironic since we argue in Chapter 1 that gravitational wave science will probe the full range of dynamical possibilities. However, there are several good reasons to devote some time to constant radius orbits.

1. If even one black hole spins, the constant radius orbits are no longer circles (unless spins are exactly aligned or antialigned with the orbital angular momentum) [54; 55]. As a result of spin precession, they fill a band on the surface of a sphere and have thereby been coined spherical orbits (see Fig. 3.1). Long-lived binaries that have shed enough angular momentum to lose their eccentricity but not their spin will exhibit quasi-spherical inspiral and not quasicircular inspiral. To detect waves from realistic binaries, we will need to understand the orbital parameters and precessions of these spherical orbits.

2. We will see in Chapter 4 that even comparable mass black hole pairs could execute zoom-whirl behavior. Thus, BH binaries that enter the LIGO bandwidth with their eccentricity intact will evolve through a sequence of zoom-whirl orbits rather than nearly spherical ones. Still, as

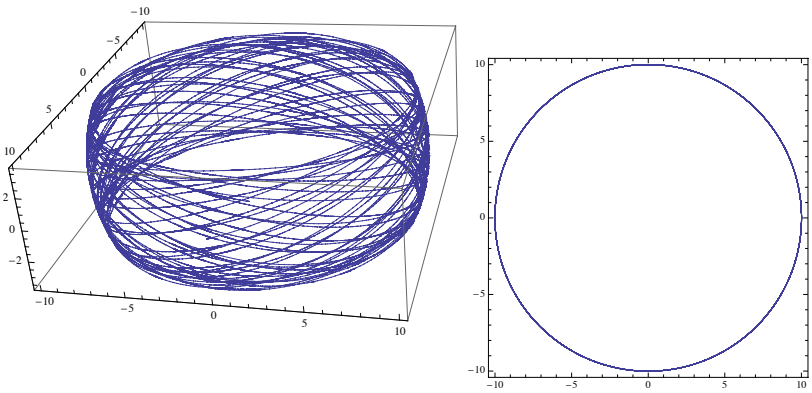

Figure 3.1: A spherical orbit for mass ratio $m_2/m_1 = 1/4$ and spin amplitudes of 3/4. Both spins are initially displaced from the orbital angular momentum by $\pi/4$. Notice the orbit is not closed. Left Panel: The three-dimensional orbit fills out a strip on a sphere. If we waited long enough, the band would be solidly painted, a reflection of the aperiodicity of the orbit. Right Panel: The path as caught by the orbital plane reveals the constant radius.

in Chapter 2, the spherical sets are special since they mark the minimum and maximum energy in the strong-field spectrum of bound orbits for a given angular momentum.[1] The orbital demographic is therefore entirely determined by the spherical orbits [45].

3. Also as in Chapter 2, the energetically bound, unstable spherical orbits mark the divide between inspiral and plunge [56]. More specifically, even comparable-mass black hole spacetimes seem to harbor homoclinic orbits – orbits that approach the unstable spherical orbits in the infinite future or in the infinite past [44; 49; 50; 51]. Such orbits are a classic feature of a nonlinear dynamical system and deserve attention since they mark the transition from inspiral to plunge for *all* pairs. When spin-spin coupling is incorporated in the PN Hamiltonian, the homoclinic set can become the locus of a transition from regular to chaotic behavior.

Among the infinite list of spherical orbits, two are valuable enough to deserve names: the innermost stable spherical orbit (isso) and the innermost bound spherical orbit (ibso). The acronyms are drawn in analogy with the

[1] We *define* the strong-field by the appearance of bound, unstable spherical orbits.

equatorial isco (innermost stable circular orbit) and ibco (innermost bound circular orbit). The isso is the lowest energy spherical orbital, and the ibso is the highest energy, bound spherical orbit.

The isco, well known as the site of the transition from inspiral to plunge for quasicircular inspiral, is actually the zero eccentricity homoclinic orbit [51]. *All other orbits*, besides the quasi-circular one, will transition to plunge through another member of the homoclinic family, hence the importance of the homoclinic set to gravitational wave science [49; 50]. To our knowledge the homoclinic orbits have not yet been identified in the PN Hamiltonian expansion before the present work, although an earlier paper found homoclinic orbits and zoom-whirl behavior in a hybrid PN expansion [44]. Excitingly enough, homoclinic orbits have been observed in fully relativistic, numerical treatments as well [57].

Taken together, this special set – composed of spherical and homoclinic orbits – demarcates dynamical regions and we spend time on their attributes in this chapter. Because of the lack of confidence in the PN expansion at close separations, we do not advocate that these results be taken as quantitatively accurate descriptions of binary black hole dynamics, but rather as qualitatively descriptive.[2] Indeed, we point out peculiar artifacts of the 3PN system as we go along, and the results of this chapter could provide a new terrain on which to test the PN expansion against, for instance, numerical relativity.

Our approach has some overlap with Refs. [54; 55], but is not redundant, and allows us to find homoclinic orbits and stability exponents for use in the periodic orbit taxonomy of chapter 4. We also simplify the initial conditions for spherical orbits in the absence of radiation reaction. For quasispherical orbits with radiation reaction included, see [55].

The outline of this chapter is as follows: In section 3.2 we write out the equations of motion for two spinning bodies in an orbital basis, relying on the results of appendix A. In section 3.3 we determine the orbital parameters of spherical orbits. In section 3.4 we find the homoclinic orbits and emphasize their connection to dynamical instability.

[2]The weakness of the PN approximation famously plagues other attempts to pinpoint the transition from inspiral to plunge through the isso [55].

3.2 3PN Hamiltonian + SO coupling

We will work with a condensed and revealing set of equations of motion in a nonorthogonal orbital coordinate system. For reference, we write out the usual 3PN Hamilton plus spin-orbit coupling for two spinning black holes.

In a Hamiltonian formulation, the equations of motion are derived from

$$\dot{\mathbf{r}} = \frac{\partial H}{\partial \mathbf{p}} \quad , \quad \dot{\mathbf{p}} = -\frac{\partial H}{\partial \mathbf{r}} \quad . \tag{3.1}$$

To begin, take the 3PN Hamiltonian including spin-orbit coupling as it is conventionally written in dimensionless coordinates. If $\mathcal{R}$ is the ADM coordinate vector and $\mathcal{P}$ is the ADM momentum vector, then the dimensionless center-of-mass coordinate vector is $\mathbf{r} = \mathcal{R}/M$ and its canonical momentum is $\mathbf{p} = \mathcal{P}/\mu$ where the total mass is $M = m_1 + m_2$ for a pair with black hole masses m_1 and m_2 and the reduced mass is $\mu = m_1 m_2/M$ with the dimensionless combination $\eta = \mu/M$. All vector quantities will always be in bold so that r is to be understood as the magnitude $r = \sqrt{\mathbf{r} \cdot \mathbf{r}}$. Unit vectors such as $\hat{\mathbf{n}} = \mathbf{r}/r$ will additionally carry a hat as well as being bold. Finally, we have used the dimensionless reduced Hamiltonian $H = \mathcal{H}/\mu$ in Eqs. (3.1), where $\mathcal{H}$ is the physical Hamiltonian, to 3PN order plus spin-orbit terms [58; 59; 60; 61; 62; 62; 63]. H can be expanded as

$$H = H_N + H_{1PN} + H_{2PN} + H_{3PN} + H_{SO} \quad , \tag{3.2}$$

where

$$
\begin{aligned}
H_N &= \frac{\mathbf{p}^2}{2} - \frac{1}{r} \qquad (3.3)\\
H_{1PN} &= \frac{1}{8}\left(3\eta - 1\right)\left(\mathbf{p}^2\right)^2 - \frac{1}{2}\left[\left(3+\eta\right)\mathbf{p}^2 + \eta(\hat{\mathbf{n}}\cdot\mathbf{p})^2\right]\frac{1}{r} + \frac{1}{2r^2}\\
H_{2PN} &= \frac{1}{16}\left(1 - 5\eta + 5\eta^2\right)\left(\mathbf{p}^2\right)^3 + \frac{1}{8}\left[\left(5 - 20\eta - 3\eta^2\right)\left(\mathbf{p}^2\right)^2\right.\\
&\quad \left. -2\eta^2(\hat{\mathbf{n}}\cdot\mathbf{p})^2\mathbf{p}^2 - 3\eta^2(\hat{\mathbf{n}}\cdot\mathbf{p})^4\right]\frac{1}{r}\\
&\quad + \frac{1}{2}\left[\left(5+8\eta\right)\mathbf{p}^2 + 3\eta(\hat{\mathbf{n}}\cdot\mathbf{p})^2\right]\frac{1}{r^2} - \frac{1}{4}\left(1+3\eta\right)\frac{1}{r^3}\\
H_{3PN} &= \frac{1}{128}\left(-5 + 35\eta - 70\eta^2 + 35\eta^3\right)\left(\mathbf{p}^2\right)^4\\
&\quad + \frac{1}{16}\left[\left(-7 + 42\eta - 53\eta^2 - 5\eta^3\right)\left(\mathbf{p}^2\right)^3\right.\\
&\quad \left. +(2-3\eta)\eta^2(\hat{\mathbf{n}}\cdot\mathbf{p})^2(\mathbf{p}^2)^2 + 3(1-\eta)\eta^2(\hat{\mathbf{n}}\cdot\mathbf{p})^4\mathbf{p}^2 - 5\eta^3(\hat{\mathbf{n}}\cdot\mathbf{p})^6\right]\frac{1}{r}\\
&\quad + \left[\frac{1}{16}(-27 + 136\eta + 109\eta^2)(\mathbf{p}^2)^2 + \frac{1}{16}(17+30\eta)\eta(\hat{\mathbf{n}}\cdot\mathbf{p})^2\mathbf{p}^2\right.\\
&\quad \left. + \frac{1}{12}(5+43\eta)\eta(\hat{\mathbf{n}}\cdot\mathbf{p})^4\right]\frac{1}{r^2}\\
&\quad + \left\{\frac{1}{192}\left[-600 + \left(3\pi^2 - 1340\right)\eta - 552\eta^2\right]\mathbf{p}^2\right.\\
&\quad \left. - \frac{1}{64}\left(340 + 3\pi^2 + 112\eta\right)\eta(\hat{\mathbf{n}}\cdot\mathbf{p})^2\right\}\frac{1}{r^3}\\
&\quad + \frac{1}{96}\left[12 + \left(872 - 63\pi^2\right)\eta\right]\frac{1}{r^4} \quad ,\\
H_{SO} &= \frac{\mathbf{L}\cdot\mathbf{S_{eff}}}{r^3} \quad . \qquad (3.4)
\end{aligned}
$$

For two spinning black holes $\mathbf{S_{eff}}$ is[3]

$$\mathbf{S_{eff}} = \delta_1\mathbf{S_1} + \delta_2\mathbf{S_2} \qquad (3.5)$$

[3]The definitions for $\mathbf{S_{eff}}$ can vary in the literature up to an overall constant although the reduced H_{SO} must be the same for all prescriptions.

where the dimensionless reduced spins are defined as

$$\mathbf{S_1} = \mathbf{a_1}(m_1^2/\mu M) \quad , \qquad \mathbf{S_2} = \mathbf{a_2}(m_2^2/\mu M) \quad . \tag{3.6}$$

and

$$\delta_1 \equiv \left(2 + \frac{3m_2}{2m_1}\right)\eta \quad , \qquad \delta_2 \equiv \left(2 + \frac{3m_1}{2m_2}\right)\eta \quad . \tag{3.7}$$

The dimensionless spin amplitudes are confined to the range $0 \leq a_{1,2} \leq 1$. The reduced orbital angular momentum $\mathbf{L} = \mathbf{r} \times \mathbf{p}$ and the spins precess according to

$$\begin{aligned} \dot{\mathbf{L}} &= \frac{\mathbf{S_{eff}} \times \mathbf{L}}{r^3} \\ \dot{\mathbf{S}}_\mathbf{1} &= \delta_1 \frac{\mathbf{L} \times \mathbf{S_1}}{r^3} \\ \dot{\mathbf{S}}_\mathbf{2} &= \delta_2 \frac{\mathbf{L} \times \mathbf{S_2}}{r^3} \quad . \end{aligned} \tag{3.8}$$

The spin precessions can be grouped together,

$$\dot{\mathbf{S}}_\mathbf{1} + \dot{\mathbf{S}}_\mathbf{2} = \frac{\mathbf{L} \times \mathbf{S_{eff}}}{r^3} \quad . \tag{3.9}$$

Notice that the precession of the sum of the spins is equal and opposite to the precession of the orbital angular momentum, so that $\mathbf{J} = \mathbf{L} + \mathbf{S_1} + \mathbf{S_2}$ is conserved. The magnitudes L, S_1 and S_2, the inner product $\mathbf{S_{eff}} \cdot \mathbf{L}$, and the energy (the Hamiltonian) are also constant for a given orbit.

In general, neither $\hat{\mathbf{J}} \cdot \hat{\mathbf{L}}$ nor the magnitude $S_{\rm eff}$ is constant. However, there are notable exceptions [64]. Both $\hat{\mathbf{J}} \cdot \hat{\mathbf{L}}$ and the magnitude $S_{\rm eff}$ are constant (1) if one of the black holes is spinless, a case worked out thoroughly in Chapter 4, (2) if the binaries have exactly equal mass [64], or (3) if both spins are aligned or antialigned with the angular momentum. To see that the claim is true in the equal-mass case (2), notice that $\mathbf{S_{eff}} = \delta_1(\mathbf{S_1} + \mathbf{S_2})$ and therefore $\mathbf{J} = \mathbf{L} + \mathbf{S_{eff}}/\delta_1$. Consequently, $\mathbf{J} \cdot \mathbf{L} = L^2 + \mathbf{S_{eff}} \cdot \mathbf{L}/\delta_1$ is conserved since both terms on the right-hand side are conserved. Furthermore, $\dot{\mathbf{S}}_{\rm eff} = \delta_1(\dot{\mathbf{S}}_\mathbf{1} + \dot{\mathbf{S}}_\mathbf{2})$ and it follows from Eq. (3.9) that the change in $\mathbf{S_{eff}}$ is always perpendicular to $\mathbf{S_{eff}}$ so its magnitude remains constant. In case (3), when the spins are aligned or antialigned with the orbital angular momentum, motion is confined to a plane and there is no precession. Therefore $\mathbf{S_{eff}}$ and $\mathbf{L}$ are constants and the rest follows.

The results of this chapter will apply to a general $\mathbf{S_{eff}}$ unless explicitly stated otherwise.

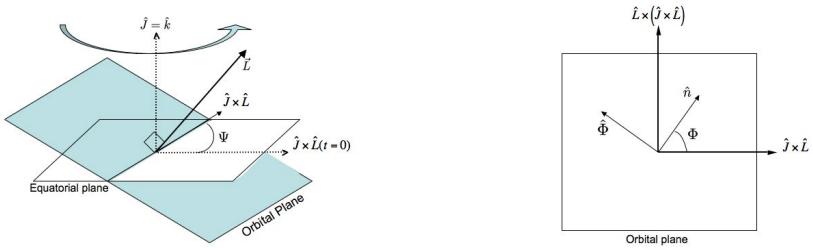

Figure 3.2: Left: The orbital plane precesses around the $\hat{\mathbf{J}} = \hat{\mathbf{k}}$ axis through the angle Ψ. Right: The orbital plane can be spanned by the vectors $(\hat{\mathbf{n}}, \hat{\mathbf{\Phi}})$.

3.2.1 Equations of motion in the orbital plane

In a nonorthogonal orbital basis, the equations of motion assume a simple form that allows us to analyze the dynamics of the black hole pairs. The plane perpendicular to the precessing orbital angular momentum is spanned by the vectors $(\hat{\mathbf{n}}, \hat{\mathbf{\Phi}})$ where $\hat{\mathbf{n}} = \mathbf{r}/r$ and

$$\hat{\mathbf{\Phi}} = \hat{\mathbf{L}} \times \hat{\mathbf{n}} \quad . \tag{3.10}$$

Notice $\hat{\mathbf{n}} \cdot \hat{\mathbf{\Phi}} = 0$, so these basis vectors are orthogonal. The entire orbital plane then precesses around the constant total angular momentum $\mathbf{J} = \mathbf{L} + \mathbf{S_1} + \mathbf{S_2}$ in the direction $\hat{\mathbf{\Psi}}$ defined through

$$\hat{\mathbf{\Psi}} = \hat{\mathbf{J}} \times \frac{(\hat{\mathbf{J}} \times \hat{\mathbf{L}})}{\left|\hat{\mathbf{J}} \times \hat{\mathbf{L}}\right|} \quad . \tag{3.11}$$

Notice that $\hat{\mathbf{\Psi}}$ is not orthogonal to the orbital plane and therefore our orbital basis $(\hat{\mathbf{n}}, \hat{\mathbf{\Phi}}, \hat{\mathbf{\Psi}})$ is not orthogonal.

The construction, familiar from classical celestial mechanics [65; 66; 67; 68], is illustrated in Fig. 3.2. Incidentally, this basis is explicitly constructed for $\mathbf{J} \times \mathbf{L} \neq 0$. When the spin and orbital angular momentum are aligned or antialigned, or the spin is zero, then $\mathbf{J} \times \mathbf{L} = 0$, motion is confined to a plane, and we should use the usual equatorial planar basis.

From Eq. (3.1), we can find equations of motion in coordinates (r, Φ, Ψ) and their canonical momenta (P_r, P_Φ, P_Ψ). As in appendix A, it is convenient

to first isolate the equations of motion in the orbital plane for the variables (r, Φ) and their canonical momenta (P_r, P_Φ):

$$\begin{aligned} \dot{r} &= AP_r + B \\ \dot{P}_r &= A\frac{P_\Phi^2}{r^3} + CP_r + D + 3P_\Phi \frac{\mathbf{S_{eff}} \cdot \hat{\mathbf{L}}}{r^4} \\ \dot{\Phi} &= A\frac{P_\Phi}{r^2} + \frac{\mathbf{S_{eff}} \cdot \hat{\mathbf{L}}}{r^3} - \dot{\Psi}(\hat{\mathbf{J}} \cdot \hat{\mathbf{L}}) \\ \dot{P}_\Phi &= 0 \end{aligned} \tag{3.12}$$

where A, B, C, D are functions of (r, P_r) to be defined momentarily. The momentum $P_\Phi = L$ conjugate to Φ is conserved. In any other basis, although L is constant, it is not a momentum conjugate to any coordinate. Instead, L should be interpreted in terms of the linearly independent coordinates and momenta appropriate for that basis. The added beauty of this non-orthogonal approach is that L *is* a canonical momentum, namely P_Φ – this is not so in the usual spherical coordinate basis where L is neither a coordinate nor a momentum and the Hamiltonian angular equations of motion are less transparent.

The four Eqs. (3.12) describe motion within the orbital plane. The orbital plane itself precesses around the constant $\hat{\mathbf{J}}$ with variable rate $\dot{\Psi}$, derived in appendix A.2 to be

$$\dot{\Psi} = \left(\frac{\hat{\mathbf{J}} \times \left(\mathbf{S_{eff}} \times \hat{\mathbf{L}} \right)}{\left| \hat{\mathbf{J}} \times \hat{\mathbf{L}} \right| r^3} \right) \cdot \hat{\mathbf{\Psi}} \,, \quad \dot{P}_\Psi = \left(\frac{\mathbf{S_{eff}} \times \hat{\mathbf{L}}}{r3} \right) \cdot \hat{\mathbf{J}} \quad , \tag{3.13}$$

and $P_\Psi = \mathbf{L} \cdot \hat{\mathbf{J}} = L_z$ is not a constant.

Again, using the manipulations of appendix A, particularly Eq. (A.27) and the identities $\hat{\mathbf{J}} \cdot \hat{\mathbf{L}} = \cos\theta_L = P_\Psi / P_\Phi$, $|\hat{\mathbf{J}} \times \hat{\mathbf{L}}| = \sin\theta_L$, we can write the final term in the $\dot{\Phi}$ equation of (3.12) as

$$\dot{\Psi}(\hat{\mathbf{J}} \cdot \hat{\mathbf{L}}) = \left(\frac{\left(\mathbf{S_{eff}} \cdot \hat{\mathbf{J}} \right) - \left(\mathbf{S_{eff}} \cdot \hat{\mathbf{L}} \right) P_\Psi / P_\Phi}{\left(1 - (P_\Psi / P_\Phi)^2\right) r^3} \right) \frac{P_\Psi}{P_\Phi} \quad . \tag{3.14}$$

Writing it in this form exploits the dependences on the coordinates, conjugate momenta, and the constant $\mathbf{S_{eff}} \cdot \hat{\mathbf{L}}$. The one term that clearly remains dependent on angles is the term $\mathbf{S_{eff}} \cdot \mathbf{J}$. Therefore, when both black holes spin, the angular equations will depend on the angular precession of the orbital plane.

We will see in chapter 4 a dramatic simplification in the case of one effective spin. As follows from the earlier discussion of the constants of motion, $\mathbf{S_{eff}} \cdot \hat{\mathbf{J}}$ would be constant if either of the spins vanished and this would remove the angular dependence in the above equations. A pair of spinning black holes of equal mass is also reducible to a system with effectively one spin (see appendix A.3). We continue to consider the general case of two misaligned spins for arbitrary mass ratios.

For completeness, we explicitly write out the functions A, B, C, D:

$$\begin{aligned}
A = 1 &+ \frac{1}{2}\left(3\eta - 1\right)\mathbf{p}^2 - \left(3+\eta\right)\frac{1}{r} \\
&+ \frac{3}{8}\left(1 - 5\eta + 5\eta^2\right)\left(\mathbf{p}^2\right)^2 + \frac{1}{4}\left[2\left(5 - 20\eta - 3\eta^2\right)\mathbf{p}^2 - 2\eta^2\left(\hat{\mathbf{n}}\cdot\mathbf{p}\right)^2\right]\frac{1}{r} \\
&+ \left(5 + 8\eta\right)\frac{1}{r^2} + \frac{1}{16}\left(-5 + 35\eta - 70\eta^2 + 35\eta^3\right)\left(\mathbf{p}^2\right)^3 \\
&+ \frac{1}{8}\Big[3\left(-7 + 42\eta - 53\eta^2 - 5\eta^3\right)\left(\mathbf{p}^2\right)^2 + 2\left(2 - 3\eta\right)\eta^2\left(\hat{\mathbf{n}}\cdot\mathbf{p}\right)^2\mathbf{p}^2 \\
&+ 3\left(1-\eta\right)\eta^2\left(\hat{\mathbf{n}}\cdot\mathbf{p}\right)^4\Big]\frac{1}{r} \\
&+ \left[\frac{1}{4}\left(-27 + 136\eta + 109\eta^2\right)\mathbf{p}^2 + \frac{1}{8}\left(17 + 30\eta\right)\eta\left(\hat{\mathbf{n}}\cdot\mathbf{p}\right)^2\right]\frac{1}{r^2} \\
&+ 2\left[-\frac{25}{8} + \left(\frac{1}{64}\pi^2 - \frac{335}{48}\right)\eta - \frac{23}{8}\eta^2\right]\frac{1}{r^3}
\end{aligned} \tag{3.15}$$

$$
\begin{aligned}
B = & -\eta\left(\hat{\mathbf{n}}\cdot\mathbf{p}\right)\frac{1}{r}+\frac{1}{8}\left[-4\eta^2\left(\hat{\mathbf{n}}\cdot\mathbf{p}\right)\mathbf{p}^2-12\eta^2\left(\hat{\mathbf{n}}\cdot\mathbf{p}\right)^3\right]\frac{1}{r}+3\eta\left(\hat{\mathbf{n}}\cdot\mathbf{p}\right)\frac{1}{r^2}\\
& +\frac{1}{16}\Big[2\left(2-3\eta\right)\eta^2\left(\hat{\mathbf{n}}\cdot\mathbf{p}\right)\left(\mathbf{p}^2\right)^2+12\left(1-\eta\right)\eta^2\left(\hat{\mathbf{n}}\cdot\mathbf{p}\right)^3\mathbf{p}^2\\
& -30\eta^3\left(\hat{\mathbf{n}}\cdot\mathbf{p}\right)^5\Big]\frac{1}{r}+\left[\frac{1}{8}\left(17+30\eta\right)\eta\left(\hat{\mathbf{n}}\cdot\mathbf{p}\right)\mathbf{p}^2+\frac{1}{3}\left(5+43\eta\right)\eta\left(\hat{\mathbf{n}}\cdot\mathbf{p}\right)^3\right]\frac{1}{r^2}\\
& +2\left(-\frac{85}{16}-\frac{3}{64}\pi^2-\frac{7}{4}\eta\right)\eta\left(\hat{\mathbf{n}}\cdot\mathbf{p}\right)\frac{1}{r^3} \qquad (3.16)
\end{aligned}
$$

$$
C = -\frac{B}{r} \qquad (3.17)
$$

$$
\begin{aligned}
D = & -(\hat{\mathbf{n}}\cdot\mathbf{p})C-\frac{1}{r^2}-\frac{1}{2}\left(\left(3+\eta\right)\mathbf{p}^2+\eta\left(\hat{\mathbf{n}}\cdot\mathbf{p}\right)^2\right)\frac{1}{r^2}+\frac{1}{r^3}\\
& +\frac{1}{8}\left[\left(5-20\eta-3\eta^2\right)\left(\mathbf{p}^2\right)^2-2\eta^2\left(\hat{\mathbf{n}}\cdot\mathbf{p}\right)^2\mathbf{p}^2-3\eta^2\left(\hat{\mathbf{n}}\cdot\mathbf{p}\right)^4\right]\frac{1}{r^2}\\
& +\left[\left(5+8\eta\right)\left(\mathbf{p}^2\right)+3\eta\left(\hat{\mathbf{n}}\cdot\mathbf{p}\right)^2\right]\frac{1}{r^3}-\frac{3}{4}\left(1+3\eta\right)\frac{1}{r^4}\\
& +\frac{1}{16}\Big[\left(-7+42\eta-53\eta^2-5\eta^3\right)\left(\mathbf{p}\right)^3+\left(2-3\eta\right)\eta^2\left(\hat{\mathbf{n}}\cdot\mathbf{p}\right)^2\left(\mathbf{p}^2\right)^2\\
& +3\left(1-\eta\right)\eta^2\left(\hat{\mathbf{n}}\cdot\mathbf{p}\right)^4\mathbf{p}^2-5\eta^3\left(\hat{\mathbf{n}}\cdot\mathbf{p}\right)^6\Big]\frac{1}{r^2}\\
& +2\left[\frac{1}{16}\left(-27+136\eta+109\eta^2\right)\left(\mathbf{p}^2\right)^2+\frac{1}{16}\left(17+30\eta\right)\eta\left(\hat{\mathbf{n}}\cdot\mathbf{p}\right)^2\mathbf{p}^2\right.\\
& \left.+\frac{1}{12}\left(5+43\eta\right)\eta\left(\hat{\mathbf{n}}\cdot\mathbf{p}\right)^4\right]\frac{1}{r^3}+3\left\{\left[-\frac{25}{8}+\left(\frac{1}{64}\pi^2-\frac{335}{48}\right)\eta-\frac{23}{8}\eta^2\right]\mathbf{p}^2\right.\\
& \left.+\left(-\frac{85}{16}-\frac{3}{64}\pi^2-\frac{7}{4}\eta\right)\eta\left(\hat{\mathbf{n}}\cdot\mathbf{p}\right)^2\right\}\frac{1}{r^4}+4\left[\frac{1}{8}+\left(\frac{109}{12}-\frac{21}{32}\pi^2\right)\eta\right]\frac{1}{r^5} \quad , \qquad (3.18)
\end{aligned}
$$

where $\hat{\mathbf{n}}\cdot\mathbf{p}=P_r$ and $\mathbf{p}^2=P_r^2+L^2/r^2$. The quantities A,B,C,D are obtained by taking various partial derivatives of the Hamiltonian. We save the full derivation of these derivatives for chapter 4 where the same four quantities appear in the special case of only one body spinning. Notice that A,B,C,D, which come from the nonspinning part of the Hamiltonian [45], depend only on (r,P_r) and constants.

Useful results can be drawn from a simple observation. The radial equations in (3.12) have no angular dependence. The energy, angular momentum, and radius of spherical orbits can be derived from the radial equations alone. Therefore we can find spherical orbits simply, despite the precession of the

orbital plane.

The fact that the two equations in (r, P_r) form a self-contained system is a restatement of the fact that the Hamiltonian itself can be viewed in a one-dimensional effective approach as a function of (r, P_r) and constants. It is important to be cautious, however, when investigating the angular motion. The Hamiltonian depends only on (r, P_r) and constants in time, yet those constants in time have to be carefully varied as functions of the angular coordinates and their conjugate momenta in a given basis to correctly derive the remaining equations of motion. This accounts for the labor in appendix A needed to derive the (Φ, P_Φ) and (Ψ, P_Ψ) equations of motion.

Still, the simple dependences of the Hamiltonian allow us to analyze the spherical orbits as one-dimensional radial motion in a simple effective potential. The location of the spherical orbits is implicit in chapter 4 to frame the distribution of all other orbits. For completeness we determine the range of spherical orbits with an eye on that chapter.

3.3 Spherical orbits

3.3.1 Effective potential for spinning black holes

Ideally, in an effective-potential formulation, the radial equation could be cast in the form:

$$\frac{1}{2}\dot{r}^2 + \text{effective potential} = \text{constant} \tag{3.19}$$

where the effective-potential depends only on r and constants of the motion. Now, the Hamiltonian of Eqs. (3.2)-(3.4) does not admit a simple effective-potential formulation since it is a complicated function of $\mathbf{p}^2$. We have already argued that $H(r, \mathbf{p}, \mathbf{S_{eff}})$ can be written as an effective function of (r, P_r) and constants, yet it remains a polynomial function of P_r. However, if we only consider

$$V_{\text{eff}} = H(P_r = 0) \quad , \tag{3.20}$$

then we have a good representation of a pseudo effective-potential *at the turning points*. We cannot misuse the V_{eff} by trying to interpret motion away from the turning points, but it gives a perfectly valid description of the behavior at aphelia and periastra as well as on spherical orbits. Hereafter we will abbreviate the term "pseudo effective-potential" by "effective potential".

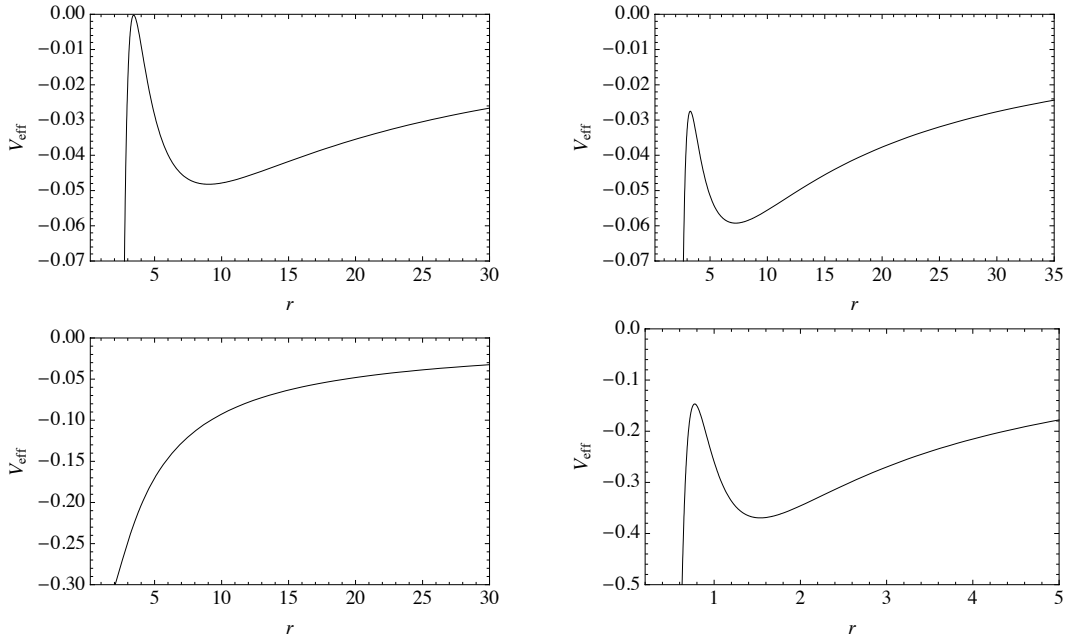

Figure 3.3: An effective potential for two spinning black holes $a_1 = a_2 = 3/4$ of mass ratio $m_2/m_1 = 1/4$ for different values of the angular momentum. The angle between each spin and $\hat{\mathbf{L}}$ is $\pi/4$. Notice the change in scale between panels. Upper left: The appearance of the ibso is marked by the effective potential touching the line $H = 0$. Upper right: As the angular momentum decreases, the potential will have both stable and unstable spherical orbits. Lower left: As the angular momentum is further decreased there occurs a critical value at which the unstable and stable spherical orbits merge at a saddle point, the isso. Lower right: The last panel shows a difference from the Schwarzschild or Kerr stories. At angular momenta and radii below the occurrence of the isso, there occur new sets of stable and unstable spherical orbits. These occur at radii far below which the approximation can be trusted, yet we point out their presence for completeness.

From the Hamiltonian of Eqs. (3.4), the effective potential,

$$V_{\rm eff}(r, L, \mathbf{S_{eff}} \cdot \hat{\mathbf{L}}, \eta) \qquad , \tag{3.21}$$

is a function of orbital parameters $(r, L, \mathbf{S_{eff}} \cdot \hat{\mathbf{L}})$ and the mass ratio. Again, since L and $\mathbf{S_{eff}} \cdot \hat{\mathbf{L}}$ are constants of the motion, for a given $(L, \mathbf{S_{eff}} \cdot \hat{\mathbf{L}})$ and a

given mass ratio, the potential is a function of r only.

Fig. 3.3 shows several snapshots taken of the effective potential for a pair of spinning black holes as the magnitude of L decreases for a given $\mathbf{S_{eff}} \cdot \hat{\mathbf{L}}$ value. (For a detailed exposition on interpreting effective potentials for black hole orbits see Refs. [34; 49; 50].) The spherical orbits are simply the extrema of the potential.[4] An example of such an orbit was shown in Fig. 3.1. Although this orbit is not generally periodic, it does close in the orbital plane as shown in the right panel of Fig. 3.1.

The top left panel of Fig. 3.3 marks the value of L for which a marginally bound, unstable spherical orbit appears. An orbit is marginally bound if its energy $H = 0$, and it is spherical and unstable if it is a maximum of the effective potential. The conditions are summarized as

$$\begin{aligned} V_{\rm eff}(P_r = 0) &= 0 \\ \frac{\partial V_{\rm eff}}{\partial r} &= 0 \\ \frac{\partial^2 V_{\rm eff}}{\partial r^2} &< 0 \qquad \text{(ibso)}, \end{aligned} \tag{3.22}$$

although the first two are sufficient. We call the marginally bound unstable spherical orbit "ibso" in analogy with the innermost unstable circular orbit (ibco) of equatorial orbits.

For angular momenta below $L_{\rm ibso}$, there will be both a stable and unstable, energetically bound spherical orbit, as in the top right snapshot of Fig. 3.3, until the angular momentum gets so low that we reach the lower left panel. Here, the unstable and stable spherical orbits have merged in a saddle point, coined an innermost stable spherical orbit (isso):

$$\begin{aligned} \frac{\partial V_{\rm eff}}{\partial r} &= 0 \\ \frac{\partial^2 V_{\rm eff}}{\partial r^2} &= 0 \qquad \text{(isso)}. \end{aligned} \tag{3.23}$$

The story plotted out by all but the last panel of Fig. 3.3 for $L_{\rm isso} < L < L_{\rm ibso}$ follows the fully relativistic Schwarzschild and Kerr stories as expected

[4] Orbits with the same angular momentum as a stable spherical orbit but different energy will oscillate between two turning points, both of which can be read off the effective-potential diagram. Again, due to spin precession, for misaligned spins these eccentric orbits lift out of a plane. Their spectra is shown in chapter 4 for a spin/spinless black hole pair.

[49; 50]. However, something peculiar then happens in the PN approximation at very low values of the angular momentum. New stable and unstable spherical orbits can appear as shown in the bottom right panel of Fig. 3.3. Or, for some other ranges of parameters, the ibso disappears or the isso disappears or both disappear. Sometimes these problems occur, as in the figure, for radii far below the confidence of the PN approximation. We point out these troublesome features in the spirit of full disclosure. More than this, the details provide a quantitative testing ground for the approximation.

Despite these oddities at low r where the PN approximation would make no claims of quantitative validity anyway, the qualitative features of spherical orbits, homoclinic orbits, and zoom-whirl behavior should survive improved approximations and full numerical treatments [17]. We will locate the E and L of spherical orbits in the next subsection.

3.3.2 Orbital parameters for spherical orbits

For a given black hole pair, that is, a given mass ratio and $\mathbf{S_{eff}}\cdot\hat{\mathbf{L}}$, all orbits are uniquely specified by their (E, L). Using the effective potential, we can easily generate the E and L for spherical orbits and thereby generate initial data for them. Initial conditions for spherical orbits were also found in [54; 55]. Damour [54] noticed that when only spin-orbit terms are included that the Hamiltonian could be expressed as a radial function. One could arrive at this conclusion, as we have in the previous section.[5] The constant radius orbits occur at the extrema of $H(r, P_r)$, in the same spirit as an effective potential method.

From the vantage point of the effective potential, spherical orbits satisfy the condition

$$\frac{\partial V_{\rm eff}}{\partial r} = 0 \tag{3.24}$$

treating L and $\mathbf{S_{eff}}\cdot\hat{\mathbf{L}}$ as constants. We could also take the vantage point of the equations of motion. Since, $P_r = 0$ forces $B = 0$, the condition $\dot{r} = AP_r + B = 0$ can be thought of as synonymous with the condition that $P_r = 0$.

[5] However, in another basis such as the usual basis for spherical coordinates used in [55], projection of the vector equations of motion will give equations of motion in component from that continue to depend on angles even when only one black hole spins, unlike the orbital basis of appendix A.3.

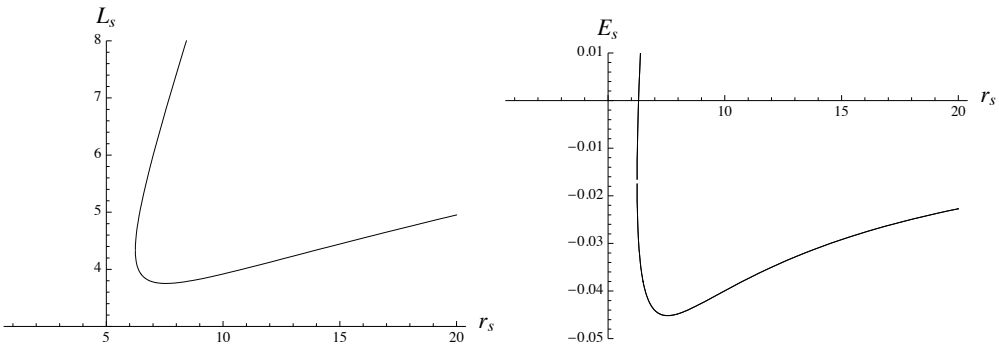

Figure 3.4: $(m_2/m_1 = 10^{-6}, S_{\rm eff} = 0)$. Left: Angular momentum vs r_s. Right: Energy vs r_s.

The constant radius condition is thus the requirement that

$$\dot{P}_r\Big|_{P_r=0} = 0 \tag{3.25}$$

in Eqs. (3.12) and Eq. (3.25) is equivalent to Eq. (3.24).

The roots of the 8th-order equation in L, Eq. (3.25), give the angular momenta of the spherical orbits as a function of spherical radius, $L_s(r_s)$, where we use a subscript s to denote a quantity evaluated at a spherical orbit. (When there is no spin, the condition reduces to a quartic in L^2 with only two of the four roots being real.) Piecing together the real roots we find L_s's such as the one in Fig. 3.4. Although the upper branch grows very quickly in L_s, these values rapidly become physically unreachable since it would require angular velocities greater than the speed of light to be that high up on the upper branch. One can think of $(L_s/r_s) < 1$ as a crude marker of physically allowed values. To find the energy of spherical orbits, $E_s(r_s)$, we simply plug $L_s(r_s)$ into the Hamiltonian when $P_r = 0$. The energy plot is also shown in Fig. 3.4.

There are several things to notice about the L_s and E_s plots, for which we chose values to illustrate the PN approximation to Schwarzschild $(m_2/m_1 = 10^{-6}, S_{\rm eff} = 0)$.[6] The large values of r_s correspond to stable spherical orbits. (Since spin is zero, these constant radius orbits are actually circular equatorial orbits, but we will keep the language more general.) When L_s hits a minimum, we have found the isso – for no $L < L_{\rm isso}$ are there spherical orbits. To the left of that minimum are the unstable spherical orbits. A true peculiarity of the

[6]Since the radial equation depends only on the combination $\mathbf{S_{eff}} \cdot \hat{\mathbf{L}}$, Fig. 3.4 should be equally valid for a nonzero effective spin that is orthogonal $\mathbf{L}$.

figure is the fact that the radii of the unstable spherical orbits begin to move out to larger r. This is simply a flaw in the PN approximation and does not occur in the Schwarzschild system. In the fully relativistic system the unstable spherical orbits always move to smaller radii than the isso, hence the ibso is really innermost, earning its name. Here, the ibso is not actually innermost – due to the poor quality of the approximation – although it remains the highest energy bound spherical orbit when it exists. The ibso cannot be read off of Fig. 3.4, although it can be found simply as the coincident of the roots of Eqs. (3.22).

Figs. 3.4 is for a nonspinning extreme-mass-ratio binary and is therefore valid as an approximation to test particle motion around a Schwarzschild black hole. The details of this figure will be useful for a future test of the PN expansion. Here we note that $L_{\rm ibso} \approx 4.69$, which is about 17% higher than the Schwarzschild value of 4, while $L_{\rm isso} \approx 3.75$, which is about 8% higher than the Schwarzschild value of $\sqrt{12}$. The energy of the ibso is designed to be zero so is not informative but the energy of the isso is $E_{\rm isso} \approx -0.0452$, which is about 21% less negative, that is, less energetically bound, than the Schwarzschild case $(2\sqrt{2}/3) - 1$. Because of the approximate nature of the expansion, it is not necessary to take these comparisons to heart, but they indicate how the spherical orbits and the periodic spectra could facilitate a test of the PN expansion. For a comparison of the isso in different PN approaches including the resummed Kerr-like effective-one-body approach, see [55; 61].

3.3.3 Dependence of binding energies on mass ratios and spin

For completeness, we can see how the ibso and the isso vary as the mass ratio and spins of the black holes are varied. Since the ibso and isso frame the distribution of orbits, they define the ranges of E and L values for all other orbits in the strong-field. The energy at the isso also gives an estimate of the energy emitted on quasicircular inspiral up to the transition to plunge. A larger binding energy at the isso could also mean a larger signal at final coalescence, so these variations attest to various levels of detectability. We will discuss the binding energy of the isso in this section. In the next section we will consider the transition to plunge for eccentric orbits.

A black hole pair is specified by its mass ratio, m_2/m_1, and its spins through the particular combination $\mathbf{S}_{\rm eff}\cdot\hat{\mathbf{L}}$. The Hamiltonian, and the radial equations,

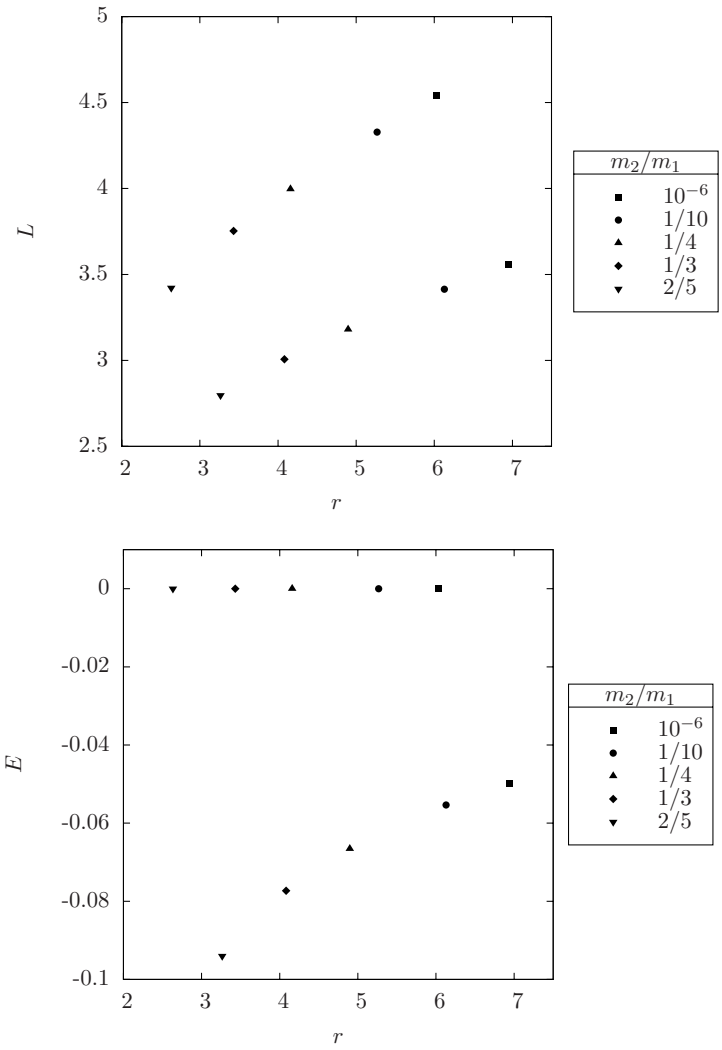

Figure 3.5: All black hole pairs represented have $\mathbf{S_{eff}} \cdot \hat{\mathbf{L}} = 0.35355$. Upper: Angular momentum vs r for the ibso and isso for different mass ratios. The upper point is always the ibso for a given symbol, while the lower point with the same symbol is always the isso. The key lists the different (m_2/m_1). Lower: Energy vs r.

depend only on these two combinations. We will therefore consider the variations in the isso and ibso for black hole pairs distinguished only by their $(m_2/m_1, \mathbf{S_{eff}} \cdot \hat{\mathbf{L}})$ values. It is important to realize that there is a great deal

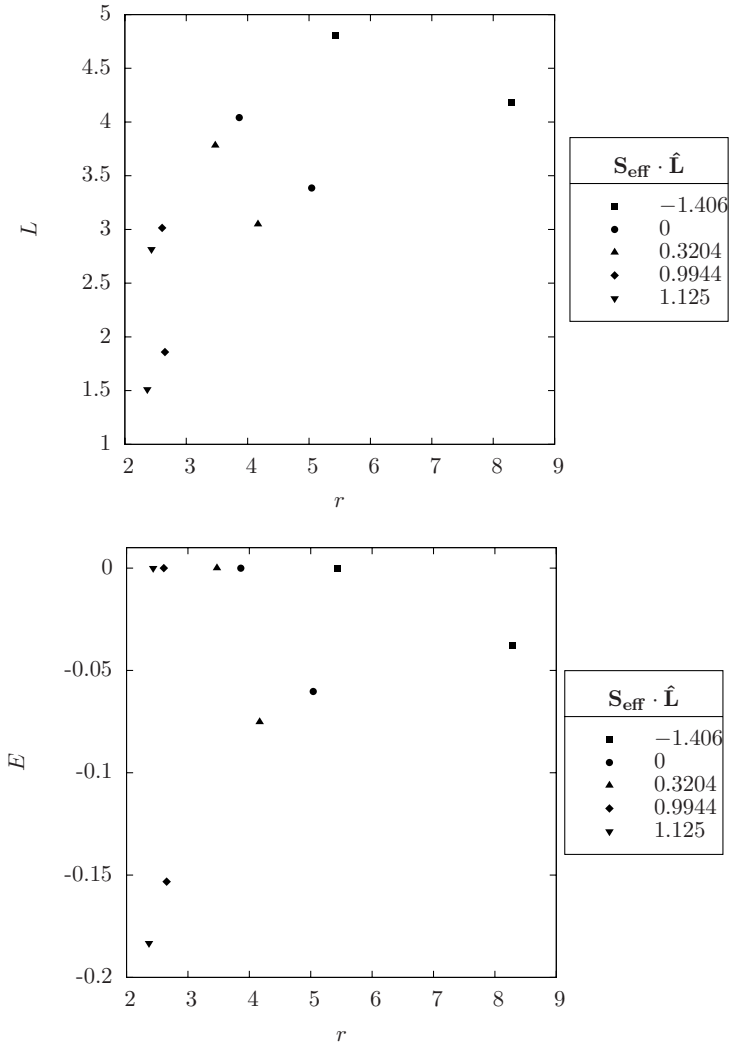

Figure 3.6: Upper: Angular momentum vs r for the ibso and isso for fixed mass ratio $m_1/m_1 = 1/3$ but varying $\mathbf{S_{eff}} \cdot \hat{\mathbf{L}}$. The upper point is always the ibso for a given symbol, while the lower point with the same symbol is always the isso. The key lists $\mathbf{S_{eff}} \cdot \hat{\mathbf{L}}$. Lower: Energy vs r.

of degeneracy among pairs. The ibso and isso values (their energy, angular momenta, and radial values) are identical for two physically distinct black hole pairs. For instance, a black hole with mass ratio $m_2/m_1 = 1/3$ and $\mathbf{S_{eff}} \cdot \hat{\mathbf{L}} = 0.35355$ could be a black hole with initial values $a_1 = 1/4$, $a_2 = 0$,

and the spin of the heavier black hole aligned with the initial orbital angular momentum. However, this is not the only combination of spin amplitudes and angles that will give the combination $\mathbf{S_{eff}} \cdot \hat{\mathbf{L}} = 0.35355$. While different black hole pairs can give degenerate isso and ibso values, they will be physically distinguishable through their angular motion.

In Fig. 3.5 the L of the ibso and isso is plotted in the upper panel and the E of the isso and of the ibso are plotted in the lower panel. Qualitative conclusions can be drawn from these figures. We notice that as the mass ratio is increased towards 1, the radius of both the isso and ibso decrease, although the isso moves in faster. Therefore the isso is pushed to larger binding energies as the mass ratio is increased towards 1. Because the Hamiltonian is a high-order polynomial in r, there can be more than one marginally bound orbit and more than one saddle point for a given $(m_2/m_1, \mathbf{S_{eff}} \cdot \hat{\mathbf{L}})$ pair, as demonstrated in the lowest panel of Fig. 3.3. The second occurrence of a marginally bound orbit and/or saddle point appears in the vicinity of $r \sim 1$ where the approximation is uninterpretable. (There may even be third occurrences.) It is unclear if there is any physical content to these other stable and unstable spherical orbits. Fig. 3.5 plots only the ibso/isso pair for r values > 2.

For the value of $\mathbf{S_{eff}} \cdot \hat{\mathbf{L}} \sim 0.35355$ used in the figure, either the ibso or the isso disappears (or both disappear) as m_2 approaches m_1. There may still be very small radii ($r \sim 1$) ibso's and/or isso's, but the sensible ones disappear. This peculiarity is probably an artifact of the approximation, a point we return to momentarily.

Fig. 3.6 fixes the mass ratio at $m_2/m_1 = 1/3$ and varies $\mathbf{S_{eff}} \cdot \hat{\mathbf{L}}$. Increasing $\mathbf{S_{eff}} \cdot \hat{\mathbf{L}}$ has the same effect of pushing the isso to smaller separations and therefore to larger binding energies, although again the isso moves in faster – discounting any marginally bound spherical orbit or saddle points that occur in the vicinity of $r \sim 1$. (In fact, as Fig. 3.6 shows, at some point the isso actually occurs at a smaller radius than the ibso.) So, all other factors being equal, spins antialigned with the orbital angular momentum push the isso out to larger radii and smaller binding energies, while aligned spins pull the isso into smaller radii and larger binding energies. For the mass ratio of this figure, the ibso or the isso actually vanishes (or both vanish) as $\mathbf{S_{eff}} \cdot \hat{\mathbf{L}}$ is increased much beyond the values shown.

These trends are consistent with those for spherical orbits discussed in Ref. [55]. To directly compare with Ref. [55], we plot (dimensionful) energy versus orbital frequency. In this article, the authors restrict their study to equal-mass binaries with spins aligned or antialigned with the orbital angular momentum.

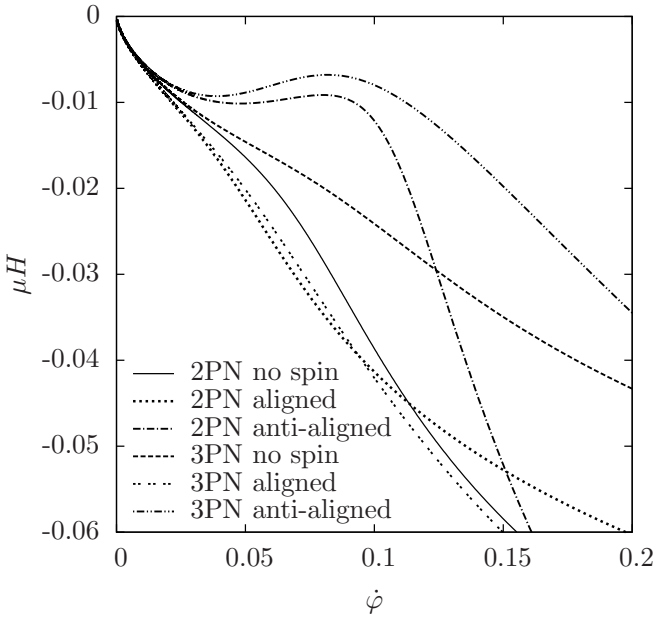

Figure 3.7: The energy of the spherical orbits as a function of the orbital frequency for equal-mass pairs. For cases with spin, the amplitude is maximal. To compare with [55], we have used the dimensionful energy μH. This figure matches exactly Fig. 1 of Ref. [55].

Under this restriction $\mathbf{J} \times \mathbf{L} = 0$, and we are automatically confined to the equatorial plane. The orbital frequency is then $\dot{\varphi} = \dot{\Phi} + \dot{\Psi}$, as we will see in chapter 4. Plotting energy versus orbital frequency $\dot{\varphi}$ in Fig. 3.7, we reproduce the results of Fig. 1 of Ref. [55], confirming consistency of our results with theirs.

The authors of Ref. [55] also remark on the absence of an isso (called a last stable spherical orbit (lsso) in their lexicon). Because of this failing of the PN expansion, they advocate instead the use of the seemingly more reliable effective-one-body (EOB) approach [54; 69; 70]. It would be interesting to extend to the EOB method the investigation of the zoom-whirl orbits of chapter 4 and the homoclinic limit of the zoom-whirls that we turn to in the next section. We leave that to a future work and continue to use the 3PN Hamiltonian as an example of our general method.

The disappearance of the ibso accompanies the disappearance of all unstable spherical orbits. Once this happens, there can be no isso since the isso

is really the point of merger of the unstable and stable spherical orbits.[7] As is already known, in the absence of spin there are no bound unstable circular orbits at 2PN [65; 69; 71; 72; 73]. At 3PN there are no bound unstable circular orbits for mass ratios bigger than about $m_2/m_1 \sim 1/2$. (See also [61; 74].) The absence of a bound unstable circular orbit is clearly a shortcoming of the approximation since we know that the Schwarzschild spacetime possess an unstable circular orbit as a reflection of its high nonlinearity. Furthermore, the unstable circular orbits are present in fully relativistic treatments as the equal-mass numerical investigation of Ref. [17] shows. Therefore, the ibso and isso should emerge for $m_2 \to m_1$ at higher orders. Incidentally, their disappearance at 3PN order implies the expansion is very likely approximating the dynamics as more stable than it really is and therefore less vulnerable to chaos than it really is for these comparable-mass binaries.

We have already warned the reader that the trends are qualitative indicators. We do not invest too much in the numbers due to pressures on the PN expansion at such large values of $(m_1 + m_2)/r$. After all, the PN expansion is an expansion in small $(m_1 + m_2)/r$ and will naturally begin to falter for small r.

We have focused on the binding energy of the isso primarily to fit into the wider conversation that has focused on quasicircular inspiral. However, the eccentric binaries formed by tidal capture in dense regions will not transition from inspiral to plunge through the isso. Rather they will transition through the eccentric separatrix between bound and plunging orbits. We investigate that separatrix briefly in the final section.

3.4 Homoclinic orbits – the separatrix between bound and plunging orbits

It is worthwhile to mention another important kind of orbit that occurs in our dynamical system, the homoclinic orbit [44; 51]. Homoclinic orbits are intriguing for several reasons, not least of which is that they mark the orbits through which the transition from inspiral to plunge should occur. In fact, the isso itself, the transition point for quasicircular orbits, is a zero eccentricity homoclinic orbit [49; 50; 51]. We make the connection between the energeti-

[7] This is not the only reason the isso disappears. Sometimes the isso disappears because the potential simply never flattens out.

cally bound, unstable spherical orbits and the homoclinic orbit explicit in this final section.

Formally, homoclinic orbits are defined as trajectories that asymptote to the same hyperbolic invariant set in the infinite future as in the infinite past. In these black hole settings, the role of the hyperbolic invariant set is played by the energetically bound, unstable spherical orbits. Although in the lexicon of black hole physics these orbits have been coined "unstable", they are, strictly speaking hyperbolic, which is to say they possess both a stable eigendirection and an unstable eigendirection under linear perturbations. And, the eigendirections lie along the homoclinic orbit in the local neighborhood of the unstable circle they approach. Although we will not demonstrate that alignment here, the point was emphasized in detail in Refs. [49; 50] for Kerr equatorial dynamics.

The stability exponents can be found by linearizing in small perturbations around Eqs. (3.12). This was done for equatorial Kerr orbits in Ref. [50]. Although we will not write out the explicit procedure here, we mention that the spherical orbits have radial eigenvalues that come in plus/minus pairs, as they must in a Hamiltonian system. The radial eigenvalues are real for the unstable spherical orbits and imaginary for the stable spherical orbits. The isso occurs at the merger of the eigenvalues at zero. A direct computation of the stability exponents around circular orbits confirms that the stable spherical orbits and the unstable spherical orbits are distributed around the isso as Fig. 3.4 shows.

Through the phase space analysis we have shown that the energetically bound, unstable circular orbits are actually hyperbolic – they have a positive stability exponent as well as a negative stability exponent. We could compute the eigenvectors and show they lie along the homoclinic orbit in the local neighborhood of the unstable circle as was done for Kerr in Ref. [50]. However, for our purposes it is sufficient and illuminating to consider a physical space picture.

We can identify the separatrix – i.e. the homoclinic orbit – in an effective-potential picture. In particular, consider a binary with mass ratio $m_2/m_1 = 1/4$ for which the heavier black hole spins with amplitude $a_1 = 1/2$ offset from $\hat{\mathbf{L}}$ by $\pi/4$ and the lighter black hole is nonspinning. (Again, any equivalent combination of $\mathbf{S_{eff}}\cdot\hat{\mathbf{L}}$ is described by this same figure.) The unstable spherical orbit r_u at the maximum of $V_{\rm eff}$ in Fig. 3.8 is drawn in physical space in Fig. 3.9. Although the orbit is a closed circle in the orbital plane, it fills out a band on a sphere in three dimensions. Because of numerical instability near

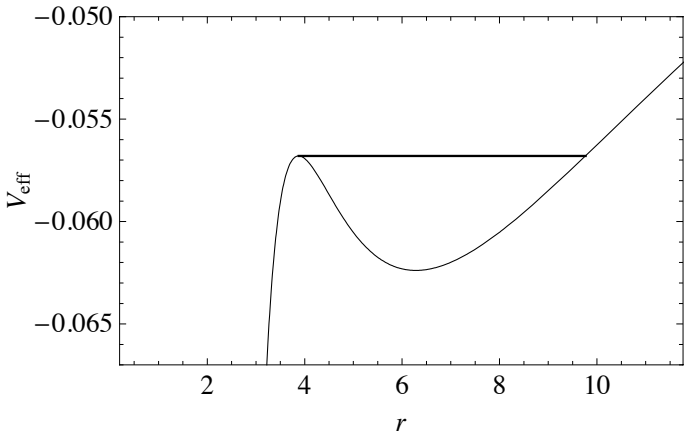

Figure 3.8: An effective-potential for $m_2/m_1 = 1/4$, with the spin of the heavier black hole displaced from $\hat{\mathbf{L}}$ by $\pi/4$ and amplitude $a_1 = 1/2$ while the lighter black hole has no spin. The straight line is the energy of the unstable spherical orbit. It is also the energy at another, larger turning point $r_a \sim 10$, which identifies the apastron of the homoclinic orbit.

this orbit, we only show a few windings.

The energy of this orbit, $E_s(r_u)$, is indicated by a straight line across the potential of Fig. 3.8. Note that this energy touches the potential at the unstable radius r_u and at some larger radius, roughly $r \sim 10$. This larger radius is the apastron of an orbit. If the two black holes are released at an initial separation in center-of-mass coordinates equal to this apastron but with no radial velocity, their orbit will roll down the potential (although the shape changes when $P_r \neq 0$) and then climb back up the other side asymptotically approaching the spherical orbit at the top of the hill. By definition, this is a homoclinic orbit (Fig. 3.10). To our knowledge, it is the first of its kind to be found out of the equatorial plane [37; 49; 50].

The orbit winds around the center of mass an infinite number of times as it asymptotically approaches the unstable spherical orbit. Although not strictly periodic – the homoclinic orbit never returns to apastron – it will be significant for the periodic tables [37; 45] as a maximum energy orbit for a given L in the strong-field regime [49; 50].

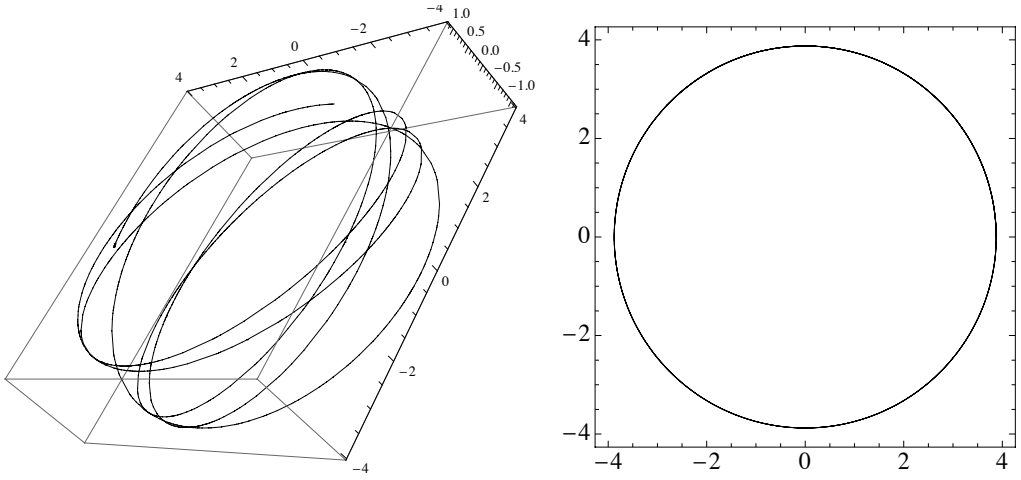

Figure 3.9: The unstable spherical orbit that is the maximum of $V_{\rm eff}$ for Fig. 3.8. Unlike the effective potential, the details of the full orbit do depend on the specific combination $\mathbf{S_{eff}} \cdot \hat{\mathbf{L}}$. Left: As viewed in three dimensions. Right: As viewed in the orbital plane.

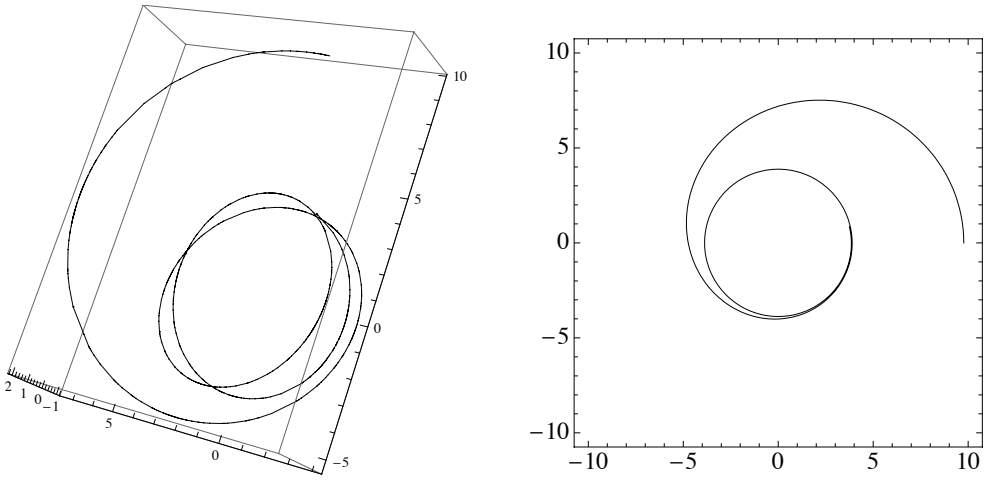

Figure 3.10: The homoclinic orbit for Fig. 3.8 approaching the unstable spherical orbit. Left: As viewed in 3d. Right: As viewed in the orbital plane. Because of numerical instability near the highly unstable constant radius orbit, we only show a few windings.

3.5 Summary

This chapter provides the energetic frame in which the periodic tables of Chapter 4 will be set. Although in support of chapter 4's goals, the analysis of spherical orbits could be relevant to additional tests of the PN expansion for spinning black hole pairs and could have a place in the discussion of initial values for numerical relativity. Additionally, we find the nonequatorial homoclinic orbits that whirl an infinite number of times as they asymptote to the unstable spherical orbit. The homoclinic separatrix is important in defining the transition to plunge for all orbits, including eccentric and precessing orbits. It would be interesting to extend this study to the EOB method [54; 69; 70] in a future work.

Chapter 4

Periodic tables in the PN expansion

4.1 Introduction

At first glance, the generic orbits of a black hole pair resist coherent description. Dynamically, black hole pairs involve non-linear relativistic effects leading to an extreme form of perihelion precession, coined zoom-whirl behavior, as well as spin precession that in turn drives orbits out of a plane. The three-dimensional precessions fill out a tangled path that shapes the gravitational waves both LIGO [5] and LISA [12] were designed to observe [75; 76; 77; 78; 79; 80; 81]. Despite appearances, we show the path can be untangled and a coherent description of fully three-dimensional precessing orbits proves entirely possible for one spinning black hole and one nonspinning black hole – neglecting radiation reaction.

The complicated three-dimensional motion can be beautifully decomposed into two-dimensional motion in an orbital plane with a precession of the orbital plane superposed [75]. Through this modular decomposition, we are able to define a complete taxonomy of all three-dimensional orbits in terms of orbits that are closed in the orbital plane. Further, we find the spectrum of orbits for a given black hole system. Importantly, the spectrum in the strong-field regime shows zoom-whirl behavior during which an orbit sweeps out to apastron and back in a zoom followed by a multiplicity of nearly circular whirls around the center of mass. It must be emphasized that our results prove zoom-whirl behavior is ubiquitous even for comparable-mass binaries. Importantly, zoom-

whirl motion has already been observed in numerical relativity [57].

From the outset, we acknowledge that the PN approximation is pushed to its breaking point in the strong-field regime where zoom-whirl behavior is most prevalent. However, the method we advocate – locating a periodic skeleton in an orbital basis – can be applied to any description of black hole binaries, including the effective one-body (EOB) approach [54] and extreme mass ratio inspirals (EMRIs) modeled by the Kerr spacetime [37]. Additionally, the closed-orbit taxonomy offers a new terrain for the comparison of the PN expansion to fully relativistic treatments [82; 83; 84]. Although quantitative results will change in improved approximations, the qualitative features should be robust, as the detection of zoom-whirl behavior in fully relativistic numerical experiments implies [57].

When radiation reaction is included [85; 86; 87], the black hole pair will transit through a sequence of geodesics. In other words, the pair will move through a sequence of periodic tables as energy and angular momentum are shed to gravitational waves. This chapter is devoted solely to decoding the underlying conservative dynamics in this system.

4.1.1 Preview

To provide the reader with a road map through intermediate results accumulated on our way to the periodic taxonomy, we preview some highlights here.

Our method can be broken into two main steps:

1. Simplified Equations of Motion. Since the perihelion precesses and the orbital plane precesses, the motion around a spinning black hole depends on angles as well as on the radius. In usual spherical coordinates, the equations of motion are quite complicated. By working in a nonorthogonal orbital basis, we show explicitly that the equations of motion are independent of (nonorthogonal) angular variables.

Physically, we exploit the observation[1] that the orbit lies in the plane spanned by the coordinate $\mathbf{r}$ and its canonical momentum $\mathbf{p}$; that is, the orbital plane is perpendicular to the orbital angular momentum, $\mathbf{L} = \mathbf{r} \times \mathbf{p}$. The plane itself then precesses around the constant total angular momentum, $\mathbf{J}$. The importance of the orbital plane was clear in some of the earliest papers

[1] The orbital plane is also emphasized in applications of PN dynamics to pulsar timing [65; 66; 67; 68].

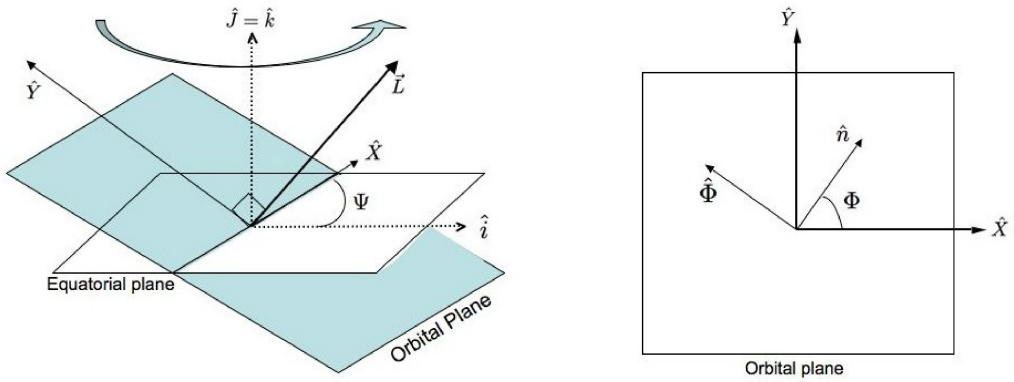

Figure 4.1: Left: The orbital plane precesses around the $\hat{\mathbf{J}} = \hat{\mathbf{k}}$ axis through the angle Ψ. Right: The orbital plane can be spanned by the vectors $(\hat{\mathbf{X}}, \hat{\mathbf{Y}})$ or the vectors $(\hat{\mathbf{n}}, \hat{\mathbf{\Phi}})$.

on spin precession [75], although that early work generally imposed a quasi-circular restriction on the orbits.

We decompose all motion into precession of the perihelion within the orbital plane with a precession of the entire plane superimposed, with no restrictions or approximations. While in this chapter we only have one body spinning, the orbital plane construction here goes beyond that of Chapter 3 to facilitate description of eccentric motion in that plane. A preview of the explicit construction is shown in Fig. 4.1. A fully precessing orbit is shown in the left diagram of Fig.4.2 while in the right diagram the orbital plane traps a simpler view.

The simplified Hamilton's equations immediately inform us that all eccentric orbits have constant aphelia and perihelia.[2] When the aphelia and perihelia are one and the same, we have non-equatorial constant radius orbits, also known as spherical orbits (as previously found in [54; 55]). The spherical orbits are not necessarily periodic; they fill out a band on the surface of a sphere. They are nonetheless significant in our campaign to fully dissect the dynamics and are treated in section 3.3.

[2]The constancy of periastron and apastron for every orbit might must have been implicitly understood in Refs. [54; 88].

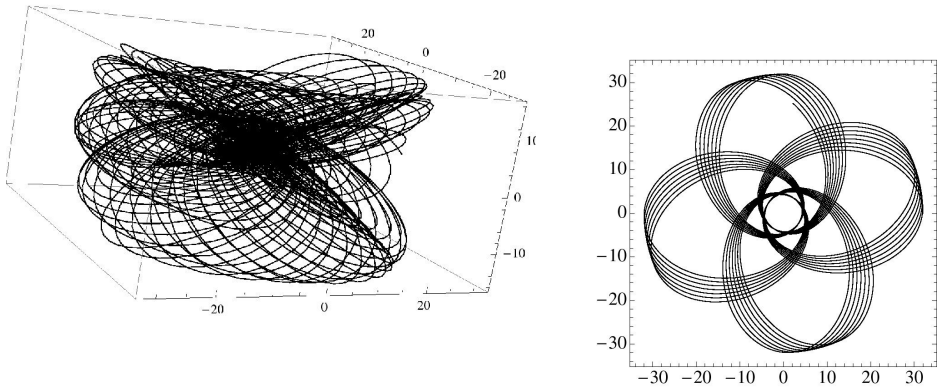

Figure 4.2: Left: Fully three-dimensional orbit. Right: The trajectory as captured in the orbital plane.

The simplified Hamilton's equations show that zoom-whirl patterns will be symmetric from one radial cycle to another when viewed in the orbital plane, as can be seen on the right of Fig. 4.2. A related subtle feature is that the three coordinate velocities in the orbital basis depend only on radius and are therefore periodic as an orbit executes a radial cycle from apastron to apastron. Taken together these symmetries in the orbital plane are intriguing for gravitational wave analysis. The waveforms must be decomposable into the orbital basis and therefore Fourier decomposable into the three fundamental frequencies. It remains to be seen how advantageous this might be for gravitational wave astronomy.

2. Taxonomy of Fully 3D Orbits. We offer a method to completely taxonomize the dynamics with the restriction that only one of the black holes spins. Our approach includes *all* fully three-dimensional orbits described by the third-order Post-Newtonian (3PN) Hamiltonian plus spin-orbit couplings.

Our taxonomy extends the periodic tables for Kerr equatorial orbits [37] to fully non-equatorial orbits of comparable mass black hole binaries. Ref. [37] introduced a taxonomy for equatorial Kerr motion with the following salient features. Each entry in the Kerr periodic tables of Ref. [37] is a perfectly closed equatorial orbit identified by a rational number

$$q = w + \frac{v}{z} \tag{4.1}$$

where w counts the number of whirls, z counts the number of leaves, and v

indicates the order in which the leaves are traced out. Since the rationals are dense on the number line, the periodics are dense in phase space. Consequently, *any* generic equatorial orbit can be *arbitrarily* well-approximated by a nearby periodic orbit. In this way, any generic orbit is approximately equivalent to a high-leaf orbit (high z). Additionally, any generic orbit can be approximated as a precession around a low-leaf orbit, a technique that might ultimately benefit signal extraction.

Our ambition in this chapter is both to extend the taxonomy to comparable mass binaries and to resolve the non-equatorial motion of spinning binaries. Truly periodic three-dimensional motion follows when the trajectory closes in the orbital plane *and* the precession of the entire plane closes simultaneously. Fully closed motion requires two rationals, each representing a ratio of fundamental frequencies. And although in principle there must exist orbits that are fully periodic in the three-dimensional motion – as Poincaré argued [89] – our taxonomy of bound orbits needs only the weaker condition of periodicity in the orbital plane. Not every orbit that is closed in the orbital plane will be closed in the full three-dimensional space. In other words, for the less restrictive condition of orbital plane periodicity we only need one rational ratio of frequencies. As will be explained in detail in section 4.3, the aperiodic orbit of Fig. 4.2 can be approximated as a precession around a 4-leaf clover in the orbital plane.

Although the PN approximation is poor in the strong-field, the qualitative results should survive a full relativistic treatment. Spin-spin couplings will impose additional modulations on the orbital plane picture but since spin-spin couplings are higher order in the PN expansion, the expectation has been that their effect can be treated as a perturbation [55].

We emphasize that for real spinning astrophysical black holes, the orbits we resolve in this paper are not an exotic subset of orbits, but rather are descriptive of *all* bound orbits – *all* non-circular orbits are captured in the spectrum of rationals. There is a long-standing argument that black hole binaries will circularize by the time they enter the bandwidth of the gravitational wave observatories. However this is not possible for spinning black holes. Circular orbits *do not exist* for misaligned spins. Although spherical orbits do exist, we saw in chapter 3 that they are destroyed by the spin-spin effects. What's more, black hole pairs formed in dense clusters are not expected to circularize by the time of merger and are expected to be plentiful sources for advanced LIGO [40]. While we restrict ourselves to one spinning black hole and one nonspinning in sections 4.2, 4.3 and 4.4, the scenario is both astrophysically

possible in its own right and theoretically important to lay the foundation for the two spinning case with spin-spin included which we discussed in chapter 3.

We express Hamilton's equations in a nonorthogonal orbital basis in section 4.2. We discuss the closed-orbit taxonomy in section 4.3. In section 4.4, we show periodic tables for two different black hole binaries, a comparable-mass binary and a nonspinning extreme-mass-ratio pair. In the conclusions, section 4.5, we discuss the modulations predicted from spin-spin couplings and those imposed by spinning both black holes. Appendix B details the projection of Hamilton's equations onto our orbital basis.

4.2 Hamilton's equations of motion in the orbital basis

The culmination of this section will be the compact form of the equations of motion (Eqs. (3.12)) in a nonorthonormal orbital basis. Getting there will require a few short subsections. We begin with the 3PN Hamiltonian including spin-orbit couplings.

4.2.1 The 3PN Hamiltonian + spin-orbit couplings

Although the 3PN Hamiltonian is nearly a page long, the Hamiltonian formulation of black hole pairs has certain advantages over the Kerr fully relativistic description of test particle motion around a single black hole. Most notable in this context, the ADM-Hamiltonian effectively describes center-of-mass motion in flat space. This will allow us to manipulate spatial vectors at will and locate the orbital plane.(This work suggested a means to generalize to the fully relativistic Kerr system which we detail in chapter 5.)

The 3PN Hamiltonian we write below is the same as that used in Chapter 3, except that the spin-orbit term will be written in a form more appropriate to the case of only one spinning body. We reproduce the entire Hamiltonian and some of the equations of motion redundantly here for ease of reference.

As in Chapter 3, the dimensionless reduced Hamiltonian $H = \mathcal{H}/\mu$, where $\mathcal{H}$ is the physical Hamiltonian, can be written to 3PN order as

$$H = H_{PN} + H_{SO} \quad , \tag{4.2}$$

where

$$H_{PN} = H_N + H_{1PN} + H_{2PN} + H_{3PN} \tag{4.3}$$

$$\begin{aligned}
H_N &= \frac{\mathbf{p}^2}{2} - \frac{1}{r} \\
H_{1PN} &= \frac{1}{8}(3\eta - 1)\left(\mathbf{p}^2\right)^2 - \frac{1}{2}\left[(3+\eta)\,\mathbf{p}^2 + \eta(\hat{\mathbf{n}}\cdot\mathbf{p})^2\right]\frac{1}{r} + \frac{1}{2r^2} \\
H_{2PN} &= \frac{1}{16}\left(1 - 5\eta + 5\eta^2\right)\left(\mathbf{p}^2\right)^3 + \frac{1}{8}\Big[\left(5 - 20\eta - 3\eta^2\right)\left(\mathbf{p}^2\right)^2 \\
&\quad -2\eta^2(\hat{\mathbf{n}}\cdot\mathbf{p})^2\mathbf{p}^2 - 3\eta^2(\hat{\mathbf{n}}\cdot\mathbf{p})^4\Big]\frac{1}{r} \\
&\quad + \frac{1}{2}\left[(5+8\eta)\,\mathbf{p}^2 + 3\eta(\hat{\mathbf{n}}\cdot\mathbf{p})^2\right]\frac{1}{r^2} - \frac{1}{4}(1+3\eta)\,\frac{1}{r^3}
\end{aligned}$$

$$\begin{aligned}
H_{3PN} &= \frac{1}{128}\left(-5 + 35\eta - 70\eta^2 + 35\eta^3\right)\left(\mathbf{p}^2\right)^4 \\
&\quad + \frac{1}{16}\Big[\left(-7 + 42\eta - 53\eta^2 - 5\eta^3\right)\left(\mathbf{p}^2\right)^3 \\
&\quad +(2-3\eta)\eta^2(\hat{\mathbf{n}}\cdot\mathbf{p})^2(\mathbf{p}^2)^2 + 3(1-\eta)\eta^2(\hat{\mathbf{n}}\cdot\mathbf{p})^4\mathbf{p}^2 - 5\eta^3(\hat{\mathbf{n}}\cdot\mathbf{p})^6\Big]\frac{1}{r} \\
&\quad + \Bigg[\frac{1}{16}(-27 + 136\eta + 109\eta^2)(\mathbf{p}^2)^2 + \frac{1}{16}(17+30\eta)\eta(\hat{\mathbf{n}}\cdot\mathbf{p})^2\mathbf{p}^2 \\
&\quad + \frac{1}{12}(5+43\eta)\eta(\hat{\mathbf{n}}\cdot\mathbf{p})^4\Bigg]\frac{1}{r^2} \\
&\quad + \Bigg\{\frac{1}{192}\left[-600 + \left(3\pi^2 - 1340\right)\eta - 552\eta^2\right]\mathbf{p}^2 \\
&\quad - \frac{1}{64}\left(340 + 3\pi^2 + 112\eta\right)\eta(\hat{\mathbf{n}}\cdot\mathbf{p})^2\Bigg\}\frac{1}{r^3} \\
&\quad + \frac{1}{96}\left[12 + \left(872 - 63\pi^2\right)\eta\right]\frac{1}{r^4} \quad .
\end{aligned} \tag{4.4}$$

The reduced spin-orbit Hamiltonian is

$$H_{SO} = \delta_1 \frac{\mathbf{L}\cdot\mathbf{S}}{r^3} \tag{4.5}$$

where in this chapter, we restrict our analysis to only one spinning body with reduced spin

$$\mathbf{S} = \mathbf{a}(m_1^2/\mu M) \quad , \tag{4.6}$$

mass m_1, and

$$\delta_1 \equiv \left(2 + \frac{3m_2}{2m_1}\right)\eta \quad . \tag{4.7}$$

Physical values of the dimensionless spin amplitude range over $0 \leq a \leq 1$. We omit spin-spin coupling terms. The reduced orbital angular momentum is

$$\mathbf{L} = \mathbf{r} \times \mathbf{p} \quad . \tag{4.8}$$

Notice that with units included, the physical orbital angular momentum is $\mathbf{L}\mu M$.

The equations of motion are given by

$$\dot{\mathbf{r}} = \frac{\partial H}{\partial \mathbf{p}} \quad , \quad \dot{\mathbf{p}} = -\frac{\partial H}{\partial \mathbf{r}} \tag{4.9}$$

and the evolution equation for the spins and the angular momentum can be found from the Poisson brackets:

$$\begin{aligned} \dot{\mathbf{S}} &= \{\mathbf{S}, H\} = \frac{\partial H}{\partial \mathbf{S}} \times \mathbf{S} \\ \dot{\mathbf{L}} &= \{\mathbf{L}, H\} = \frac{\partial H}{\partial \mathbf{L}} \times \mathbf{L} \end{aligned} \tag{4.10}$$

which comes to

$$\begin{aligned} \dot{\mathbf{S}} &= \delta_1 \frac{\mathbf{L} \times \mathbf{S}}{r^3} \\ \dot{\mathbf{L}} &= \delta_1 \frac{\mathbf{S} \times \mathbf{L}}{r^3} \quad . \end{aligned} \tag{4.11}$$

4.2.2 Conserved quantities

It is well-known that this system has many useful conserved quantities.[3] The Hamiltonian is conserved by construction. The conservation of total angular

[3] Although it is by now well-confirmed that there is chaos when the black holes spin [42; 43; 88; 90; 91; 92; 93; 94], we are dealing with a restricted situation of only one body spinning in the Hamiltonian formulation and our orbits are not chaotic to this order in the approximation [64]. This is not in conflict with earlier work on chaos in the Lagrangian approximation [95]. As we will see, at higher order including spin-spin couplings, a pair of spinning black holes loses constants of the motion opening a window for chaotic motion.

momentum follows from Eqs. (4.11)

$$\mathbf{J} = \mathbf{L} + \mathbf{S} \quad . \tag{4.12}$$

Also conserved are the magnitude of S and L, as can be confirmed by taking the dot-products with Eqs. (4.11):

$$\begin{aligned} \mathbf{S}\cdot\dot{\mathbf{S}} &= \frac{1}{2}\frac{d}{dt}(S^2) \propto \mathbf{L}\cdot(\mathbf{S}\times\mathbf{L}) = 0 \\ \mathbf{L}\cdot\dot{\mathbf{L}} &= \frac{1}{2}\frac{d}{dt}(L^2) \propto \mathbf{S}\cdot(\mathbf{L}\times\mathbf{S}) = 0 \end{aligned} \tag{4.13}$$

Finally, the component of $\mathbf{L}$ in the $\mathbf{J}$ direction must be conserved as can be seen from

$$\begin{aligned} \dot{\mathbf{L}} &= \delta_1 \frac{\mathbf{S}\times\mathbf{L}}{r^3} \\ &= \delta_1 \frac{\mathbf{J}\times\mathbf{L}}{r^3} \end{aligned} \tag{4.14}$$

from which it follows that the change in $\mathbf{L}$ is always perpendicular to $\mathbf{J}$.

4.2.3 The equations of motion

We want to express the equations of motion derived from Eq. (4.9) in the following form:

$$\begin{aligned} \dot{\mathbf{r}} &= A\mathbf{p} + B\hat{\mathbf{n}} + \text{spin pieces} \\ \dot{\mathbf{p}} &= C\mathbf{p} + D\hat{\mathbf{n}} + \text{spin pieces} \quad . \end{aligned} \tag{4.15}$$

This form helps consolidate the equations of motion before we project from the vector equations to component equations in the next section (section 4.2.4). We need to identify the functions A, B, C, D in terms of derivatives of the Hamiltonian, which can be thought of as a function of $(r, \mathbf{p}, (\hat{\mathbf{n}}\cdot\mathbf{p}))$. Considering the non-spinning piece, H_{PN} first, we break up the partial derivatives on the right hand side of Hamilton's equations in the following way,

$$\left.\frac{\partial H_{PN}}{\partial \mathbf{p}}\right|_{\mathbf{r}} = \left.\frac{\partial H_{PN}}{\partial \mathbf{p}^2}\right|_{r,(\hat{\mathbf{n}}\cdot\mathbf{p})} \frac{\partial \mathbf{p}^2}{\partial \mathbf{p}} + \left.\frac{\partial H_{PN}}{\partial(\hat{\mathbf{n}}\cdot\mathbf{p})}\right|_{r,\mathbf{p}} \frac{\partial(\hat{\mathbf{n}}\cdot\mathbf{p})}{\partial \mathbf{p}}$$

and

$$-\left.\frac{\partial H_{PN}}{\partial \mathbf{r}}\right|_{\mathbf{p}} = -\left.\frac{\partial H_{PN}}{\partial(\hat{\mathbf{n}}\cdot\mathbf{p})}\right|_{r,\mathbf{p}} \frac{\partial(\hat{\mathbf{n}}\cdot\mathbf{p})}{\partial \hat{\mathbf{n}}}\frac{\partial \hat{\mathbf{n}}}{\partial \mathbf{r}} - \left.\frac{\partial H_{PN}}{\partial r}\right|_{\mathbf{p},(\hat{\mathbf{n}}\cdot\mathbf{p})} \frac{\partial r}{\partial \mathbf{r}},$$

where we are careful to indicate the quantities held fixed in each term. Using

$$\frac{\partial(\hat{\mathbf{n}}\cdot\mathbf{p})}{\partial\hat{\mathbf{n}}}\frac{\partial\hat{\mathbf{n}}}{\partial\mathbf{r}} = \frac{\mathbf{p}}{r} - \frac{(\hat{\mathbf{n}}\cdot\mathbf{p})}{r}\hat{\mathbf{n}} \tag{4.16}$$

we define

$$\begin{aligned}
A &\equiv 2\left.\frac{\partial H_{PN}}{\partial\mathbf{p}^2}\right|_{r,(\hat{\mathbf{n}}\cdot\mathbf{p})} && (4.17)\\
B &\equiv \left.\frac{\partial H_{PN}}{\partial(\hat{\mathbf{n}}\cdot\mathbf{p})}\right|_{r,\mathbf{p}} \\
C &\equiv -\frac{1}{r}\left.\frac{\partial H_{PN}}{\partial(\hat{\mathbf{n}}\cdot\mathbf{p})}\right|_{r,\mathbf{p}} = -\frac{B}{r} \\
D &\equiv -\left.\frac{\partial H_{PN}}{\partial r}\right|_{\mathbf{p},(\hat{\mathbf{n}}\cdot\mathbf{p})} + \left.\frac{\partial H_{PN}}{\partial(\hat{\mathbf{n}}\cdot\mathbf{p})}\right|_{r,\mathbf{p}}\frac{(\hat{\mathbf{n}}\cdot\mathbf{p})}{r} \\
&= -\left.\frac{\partial H_{PN}}{\partial r}\right|_{\mathbf{p},(\hat{\mathbf{n}}\cdot\mathbf{p})} - (\hat{\mathbf{n}}\cdot\mathbf{p})C \quad . && (4.18)
\end{aligned}$$

The variations of the spinning piece of the Hamiltonian are simply

$$\begin{aligned}
\frac{\partial H_{SO}}{\partial\mathbf{p}} &= \delta_1\frac{\mathbf{S}\times\mathbf{r}}{r^3} \\
-\frac{\partial H_{SO}}{\partial\mathbf{r}} &= -\delta_1\frac{\mathbf{p}\times\mathbf{S}}{r^3} + 3\delta_1\frac{\mathbf{L}\cdot\mathbf{S}}{r^4}\hat{\mathbf{n}} \quad . && (4.19)
\end{aligned}$$

With these definitions, and making use of $-\mathbf{p}\times\mathbf{S} = \mathbf{S}\times\mathbf{p}$, we can write the vector equations of motion compactly as

$$\begin{aligned}
\dot{\mathbf{r}} &= A\mathbf{p} + B\hat{\mathbf{n}} + \delta_1\frac{\mathbf{S}\times\mathbf{r}}{r^3} \\
\dot{\mathbf{p}} &= C\mathbf{p} + D\hat{\mathbf{n}} + \delta_1\frac{\mathbf{S}\times\mathbf{p}}{r^3} + 3\delta_1\frac{\mathbf{L}\cdot\mathbf{S}}{r^4}\hat{\mathbf{n}} \quad . && (4.20)
\end{aligned}$$

To go from these vector equations to component form requires we choose a basis. In the next section we will build the orbital basis of Fig. 4.1, and cast Eqs. (4.20) in component form.

4.2.4 The orbital basis

We will build a *nonorthogonal*, unit normalized basis $(\hat{\mathbf{n}}, \hat{\mathbf{\Phi}}, \hat{\mathbf{\Psi}})$ in this section. This orbital basis leads to profound clarity of expression.

There are two special planes to consider. There is the orbital plane, which is the plane perpendicular to $\mathbf{L}$, and there is the equatorial plane, which is the plane perpendicular to $\mathbf{J}$ (see Fig. 4.1). We will find an orthonormal basis that spans the orbital plane and then add the motion of the plane itself, which will be in a direction that is not orthogonal to the orbital plane. The technique of moving into an orbital plane and projecting equations of motion onto this basis is familiar from celestial mechanics and has seen application in the PN approximation to binary pulsars [65; 66; 67; 68]. We depart from the usual approach by adopting a nonorthogonal basis.

The vectors $\hat{\mathbf{n}}$ and $\mathbf{p}$ lie in the orbital plane by the definition $\mathbf{L} = r\hat{\mathbf{n}} \times \mathbf{p}$. We can also span the orbital plane by orthonormal vectors $(\hat{\mathbf{n}}, \hat{\mathbf{\Phi}})$ where

$$\hat{\mathbf{\Phi}} = \hat{\mathbf{L}} \times \hat{\mathbf{n}} \quad . \tag{4.21}$$

We will work in terms of $(\hat{\mathbf{n}}, \hat{\mathbf{\Phi}})$ when considering motion in the orbital plane.

To separate out the precession of the orbital plane from the three-dimensional motion, another basis will be useful for intermediate steps. The $(\hat{\mathbf{X}}, \hat{\mathbf{Y}})$ basis spans the orbital plane but rotates with the precession of $\mathbf{L}$:

$$\begin{aligned} \hat{\mathbf{X}} &= \frac{\hat{\mathbf{J}} \times \hat{\mathbf{L}}}{\sin\theta_L} \\ \hat{\mathbf{Y}} &= \hat{\mathbf{L}} \times \hat{\mathbf{X}} \quad , \end{aligned} \tag{4.22}$$

where $\theta_L = \arccos(\hat{\mathbf{L}} \cdot \hat{\mathbf{J}})$ is constant. The $\hat{\mathbf{X}}$ axis is orthogonal to both $\hat{\mathbf{J}}$ and $\hat{\mathbf{L}}$ by construction and so lies on the intersection of the orbital plane and the equatorial plane. The entire orbital plane maintains a fixed angle $\theta_Y = \pi/2 - \theta_L$ with $\mathbf{J}$ as it precesses with the precession of $\mathbf{L}$. The motion of the orbital plane can be understood as the motion of $\hat{\mathbf{X}}$ in the equatorial plane through an angle Ψ where

$$\hat{\mathbf{\Psi}} = \hat{\mathbf{J}} \times \hat{\mathbf{X}} \quad . \tag{4.23}$$

Let $\hat{\mathbf{J}} = \hat{\mathbf{k}}$ and let the unit vectors $\hat{\mathbf{i}}$ and $\hat{\mathbf{j}}$ span the equatorial plane. The speed of Ψ motion can then be determined:

$$\dot{\cos}\,\Psi = \dot{\hat{\mathbf{X}}} \cdot \hat{\mathbf{i}} = \frac{(\hat{\mathbf{J}} \times \dot{\mathbf{L}}) \cdot \hat{\mathbf{i}}}{L \sin\theta_L} = \Omega_L \hat{\mathbf{\Psi}} \cdot \hat{\mathbf{i}} = -\Omega_L \sin\Psi, \tag{4.24}$$

where we have explicitly used the constancy of the magnitude L. From this we conclude

$$\Omega_L = \dot{\Psi} = \delta_1 \frac{J}{r^3} \quad . \tag{4.25}$$

does not depend on any angles.

To find our simplified equations of motion we work in the nonorthogonal, unit normalized basis $(\hat{\mathbf{n}}, \hat{\mathbf{\Phi}}, \hat{\mathbf{\Psi}})$ in the next section.

Final equations of motion in the orbital plane

The four equations of motion in the orbital plane are obtained by projecting Hamilton's equations onto the basis vectors $(\hat{\mathbf{n}}, \hat{\mathbf{\Phi}})$. We do this explicitly in appendix B, where the projections onto the orbital basis vectors generate the four equations,

$$\begin{aligned}
\dot{\mathbf{r}} \cdot \hat{\mathbf{n}} &= \frac{\partial H}{\partial \mathbf{p}} \cdot \hat{\mathbf{n}} \\
\dot{\mathbf{r}} \cdot \hat{\mathbf{\Phi}} &= \frac{\partial H}{\partial \mathbf{p}} \cdot \hat{\mathbf{\Phi}} \\
\dot{\mathbf{p}} \cdot \hat{\mathbf{n}} &= -\frac{\partial H}{\partial \mathbf{r}} \cdot \hat{\mathbf{n}} \\
\dot{\mathbf{p}} \cdot \hat{\mathbf{\Phi}} &= -\frac{\partial H}{\partial \mathbf{r}} \cdot \hat{\mathbf{\Phi}} \quad .
\end{aligned} \tag{4.26}$$

Compiling the equations of appendix B concisely gives the remarkably simple equations of motion in the orbital plane coordinates (r, Φ) and and their canonical momenta (P_r, P_Φ),

$$\begin{aligned}
\dot{r} &= AP_r + B \\
\dot{P}_r &= A\frac{L^2}{r^3} - \frac{B}{r}P_r + D + 3\delta_1 \frac{\mathbf{S}\cdot\mathbf{L}}{r^4} \\
\dot{\Phi} &= A\frac{L}{r^2} - \frac{L}{J}\Omega_L \\
\dot{P}_\Phi &= 0 \quad ,
\end{aligned} \tag{4.27}$$

where $P_\Phi = L$. The orbital plane precesses at a rate that depends only on r, as calculated in the previous section (§4.2.4):

$$\dot{\Psi} = \Omega_L = \delta_1 \frac{J}{r^3} \quad , \quad \dot{P}_\Psi = 0 \tag{4.28}$$

with $\delta_1 \equiv \left(2+\frac{3m_2}{2m_1}\right)\eta$ and $P_\Psi = L_z$. For completeness, we can track the precessions of the spin and the angular momentum:

$$\begin{aligned}\dot{\mathbf{S}} &= \Omega_L \hat{\mathbf{J}} \times \mathbf{S} \\ \dot{\mathbf{L}} &= \Omega_L \hat{\mathbf{J}} \times \mathbf{L} \quad .\end{aligned} \tag{4.29}$$

As noted earlier, $\mathbf{S}\cdot\mathbf{L}$ =constant. Notice, this basis is explicitly constructed for $\mathbf{S}\times\mathbf{L} \neq 0$. When the spin and orbital angular momentum are aligned, anti-aligned, or spin is zero, then motion is confined to a plane and we should use the usual equatorial planar basis. This is done explicitly in section 4.4.1.

The functions A, B, C, D of Eqs. (4.18) depend only on r, P_r and constants. This can be seen by noting that A, B, C, D are functions of $(r, (\hat{\mathbf{n}}\cdot\mathbf{p}), \mathbf{p}^2)$. Now, $\mathbf{p}$ can be written in terms of a piece in the radial direction and a piece perpendicular to the radial direction:

$$\begin{aligned}\mathbf{p} &= (\mathbf{p}\cdot\hat{\mathbf{n}})\hat{\mathbf{n}} + (\hat{\mathbf{n}}\times\mathbf{p})\times\hat{\mathbf{n}} \\ &= P_r\hat{\mathbf{n}} + \frac{\mathbf{L}}{r}\times\hat{\mathbf{n}}\end{aligned} \tag{4.30}$$

so that

$$\mathbf{p}^2 = P_r^2 + \frac{L^2}{r^2} \tag{4.31}$$

and L equals a constant. The term $\mathbf{p}^2$ can therefore be expressed as a function of (r, P_r) only. Meanwhile, $(\hat{\mathbf{n}}\cdot\mathbf{p}) = P_r$ and so any function of $(r, (\hat{\mathbf{n}}\cdot\mathbf{p}), \mathbf{p}^2)$ is equally well a function only of (r, P_r) and constants.

Consequently, the above equations of motion are, amazingly enough, independent[4] of the angles (Φ, Ψ). The purely radial dependence of the equations of motion immediately informs us of four crucial facts (valid to this order in the PN approximation):

1. *There are constant radius orbits.* That such orbits should exist was already indicated in Ref. [54; 55]. Their properties were flushed out in significantly more detail in Chapter 3, where they drop out particularly simply in the orbital basis. In the equatorial plane these are of course the usual circular

[4]The simplicity of the orbital equations of motion can of course be recast in terms of symmetries. Rotations about $\hat{\mathbf{L}}$ through the angle Φ, $R_{\hat{\mathbf{L}}}(\Phi)$, and rotations about $\hat{\mathbf{J}}$ through the angle Ψ, $R_{\hat{\mathbf{J}}}(\Psi)$, leave the dynamics invariant. The coordinates Φ and Ψ are cyclic and $\dot{P}_\Phi = \dot{P}_\Psi = 0$. The symmetries correspond to conserved L and L_z with $P_\Phi = L$ and $P_\Psi = L_z$.

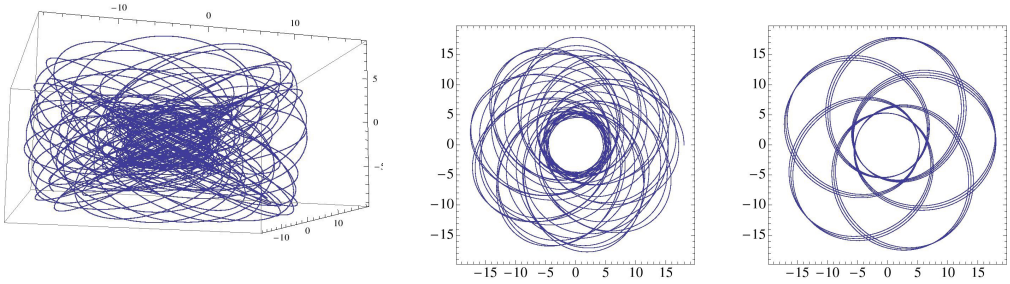

Figure 4.3: A generic orbit in the strong field. The initial conditions are $m_2/m_1 = \frac{1}{4}$, $L = 3.5$, $\theta_{LS} = \frac{\pi}{3}$, $a = 0.9$, and $r_i = 18$. Left: The full three-dimensional orbit. Middle: A projection of the full orbit onto the equatorial plane. Looking closely, the angle swept out from leaf to leaf is not the same under this projection. Right: The orbit as caught by the orbital plane. The angle swept out in the orbital plane from leaf to leaf is always the same. Further, the constancy of the apastron is clear.

orbits. Out of the equatorial plane they have been called spherical orbits in the literature since the orbits trace out an annulus on the surface of a sphere. We will continue in this spirit and call them spherical orbits, or, more exactly, constant radius orbits. To see that they exist, notice that the spherical orbits correspond to solutions of $\dot{r} = \dot{P}_r = 0$ and these roots – according to Eqs. (4.27) – can only depend on constants $(m_1/m_2, S, L, \theta_{LS})$, not on angles. In fact, we have a pseudo effective-potential description as we explain in the next section.

2. *All eccentric orbits have constant apastra and perihelia.* Similar to the reasoning above, the solutions to the condition $P_r = 0$ are the turning points[5] and thus are the apastron and perihelion of any orbit. These values can depend only on constants.

3. *The orbital angle and precessional angle swept out between successive apastra are constant.* The angles swept out as an orbit moves from one apas-

[5]When $P_r = 0$, $B = 0$ and so $\dot{r} = AP_r + B = 0$. Therefore we take the $\dot{r} = 0$ condition to be synonymous with $P_r = 0$.

tron to another are simply given by

$$\Delta\Phi = 2\int_{r_a}^{r_p} \frac{\dot{\Phi}}{\dot{r}} dr$$
$$\Delta\Psi = 2\int_{r_a}^{r_p} \frac{\dot{\Psi}}{\dot{r}} dr \tag{4.32}$$

and depend only on constants.

4. *All three coordinates velocities are periodic in* r. The three coordinate velocities in the orbital basis

$$\dot{r}\ , \quad \dot{\Phi}\ , \quad \text{and} \quad \dot{\Psi}\ , \tag{4.33}$$

depend only on the variable r (or $P_r(r)$) and thereby inherit r's periodicity. They can be averaged over one radial cycle to define three fundamental frequencies

$$\omega_r = \frac{2\pi}{T_r}\ , \quad \omega_\Phi\ , \quad \text{and} \quad \omega_\Psi \tag{4.34}$$

where T_r is the radial period from apastron to apastron (Explicit forms for ω_Φ and ω_Ψ are given a bit later in Eqs. (4.35) and (4.40)).[6]

The powerful simplicity of the description in the orbital basis is visually manifest in Fig. 4.3. The leftmost diagram shows a fully three-dimensional generic orbit. The rightmost diagram is the same snapshot captured in the orbital plane. Notice how the orbital plane reveals the constancy of the three-dimensional apastron and perihelion as claimed in point (2) above. Also notice that the spacing between leaves is always symmetric in the orbital plane. Said another way, the angle swept out in the orbital plane between apastra is always the same, as claimed in point (3). Neither of these features is apparent from the fully three-dimensional snapshot or from the projection onto the *equatorial* plane shown in the middle panel. Another generic orbit is shown in Fig. 4.4.

The four facts above have two significant implications:

• A gravitational waveform can be Fourier decomposed in the three fundamental frequencies of Eq. (4.33).

• There should be a spectrum of orbits that are closed in the orbital plane, and that spectrum must have a correspondence with the rationals. We can

[6]Points (1) and (2) are also true for Kerr non-equatorial orbits, although (3) and (4) are not.

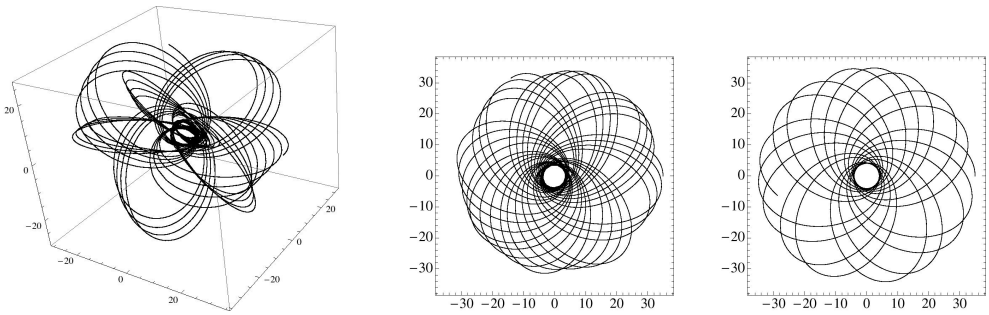

Figure 4.4: The initial conditions are $m_2/m_1 = \frac{1}{4}$, $L = 3.5$, $\theta_{LS} = \frac{\pi}{3}$, $a = 0.9$ and $E = -0.023548373360051289666$. Left: The full orbit. Middle: A projection on the equatorial plane. Right: The orbit as it appears in the orbital plane

therefore generalize the Kerr taxonomy of Ref. [37] to nonequatorial orbits of comparable-mass black hole binaries.

We complete the dynamical picture by moving on to the periodic taxonomy for black hole binaries.

4.3 Closed orbit taxonomy

Any dynamical study benefits from locating the closed orbits – orbits that return to their initial values after some finite period. Poincaré was the first to realize that periodic orbits structure the entire dynamics [89]. Although a set of measure zero, the periodic orbits are dense in phase space. Consequently, any orbit can be approximated as near some periodic orbit. In that sense, the periodic set forms the skeleton of the dynamics. What is more, they are all one needs to know since, to arbitrary precision, even an aperiodic generic orbit is arbitrarily close to some periodic orbit, though possibly one with very high period.

The periodic set corresponds to a spectrum of rational numbers. That spectrum of rationals shows that the zoom-whirl behavior known for extreme-mass-ratio binaries is prevalent in the strong-field regime of comparable binaries as well. Zoom-whirl behavior is therefore not exotic but rather the norm for the strong-field. The spectrum of rationals renders the zoom-whirl behavior of any orbit quantifiable and unambiguous.

Consider the coordinate velocities of Eq. (4.33). Taking the time average

of the Φ-frequency over one radial cycle gives the fundamental frequency

$$\omega_\Phi = \frac{2}{T_r}\int_{r_a}^{r_p}\frac{\dot{\Phi}}{\dot{r}}dr = \frac{\Delta\Phi}{T_r} = \omega_r\frac{\Delta\Phi}{2\pi} \quad , \tag{4.35}$$

so that

$$\frac{\omega_\Phi}{\omega_r} = \frac{\Delta\Phi}{2\pi}\,. \tag{4.36}$$

An orbit that is closed in the orbital plane has rationally related frequencies

$$\frac{\omega_\Phi}{\omega_r} = 1 + q_\Phi \quad . \tag{4.37}$$

From Eq. (4.36), we can interpret the rational in terms of the angle swept out from leaf to leaf in the orbital plane,

$$\frac{\Delta\Phi}{2\pi} = 1 + q_\Phi = 1 + w_\Phi + \frac{v_\Phi}{z_\Phi} \quad , \tag{4.38}$$

where we have written the rational in terms of a triplet of integers, as can always be done [37]. In the equatorial case we know that $\Delta\Phi > 2\pi$ for all eccentric orbits; all relativistic orbits overshoot as the famous precession of the perihelion of Mercury attests. For that reason we have separated out a 1 from the definition of q_Φ in Eq. (4.38).[7]

By analogy with the equatorial Kerr case of Ref. [37], z_Φ counts the number of leaves (or zooms), v_Φ specifies the order in which the leaves are traced out, and w_Φ counts the number of additional full 2π whirls taken between apastron and apastron. To clarify the role of v_Φ, label the leaves sequentially 0 through $z-1$ starting with the initial apastra. Then v_Φ equals the number of the leaf that the orbit jumps to after the starting apastron. The meaning of the rational is best illustrated with an example. An orbit with $q_\Phi = 1/3$ is shown in Fig. 4.5. This is a 3-leaf orbit ($z_\Phi = 3$) that moves to the first leaf in the pattern ($v_\Phi = 1$). Since $w_\Phi = 0$, there are no additional whirls from leaf to leaf. In Fig. 4.6, we show a $q_\Phi = 2/3$ orbit. That is, a 3-leaf orbit ($z_\Phi = 3$)

[7] There is an interesting anomaly that has to be mentioned. As it happens, in this 3PN approximation, it is possible for periodics in the orbital plane to *undershoot* 2π; that is, from one apastron to another $\Delta\Phi < 2\pi$ ($q_\Phi < 0$). This never happens with Kerr orbits and may just be a peculiarity in the approximation. Also notice that while some orbits may undershoot in the orbital plane, Φ is not the whole story (see the footnote in section 4.4.1) and some of the apparent regression is more than compensated for by Ψ.

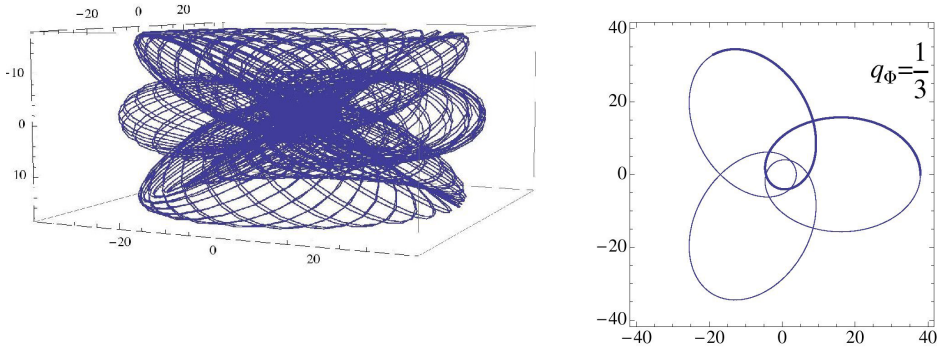

Figure 4.5: A $q_\Phi = 1/3$ orbit. The initial conditions are $m_2/m_1 = \frac{1}{4}$, $L = 3.5$, $\theta_{LS} = \frac{\pi}{3}$, $a = 0.9$, and $E = -0.0220582156$. Left: Fully three-dimensional orbit. Right: The trajectory is a 3-leaf periodic in the orbital plane. The first radial cycle is in bold.

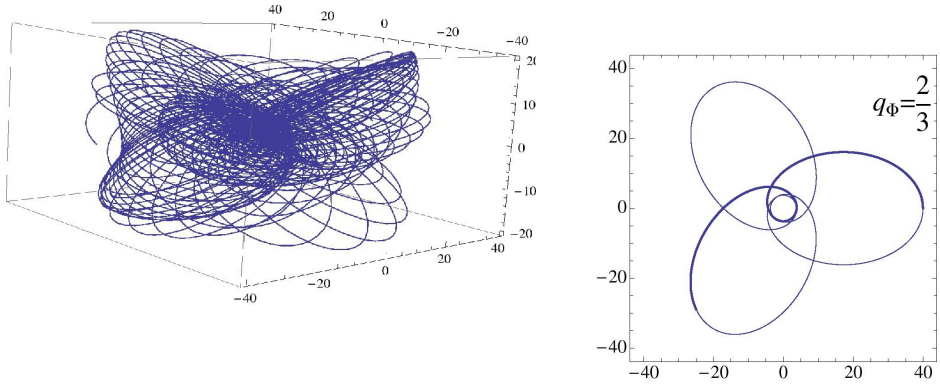

Figure 4.6: A $q_\Phi = 2/3$ orbit. The initial conditions are $m_2/m_1 = \frac{1}{4}$, $L = 3.5$, $\theta_{LS} = \frac{\pi}{3}$, $a = 0.9$, and $E = -0.0211669686$. Left: Fully three-dimensional orbit. Right: The trajectory is a 3-leaf periodic in the orbital plane that skips a leaf each radial cycle. The first radial cycle is in bold.

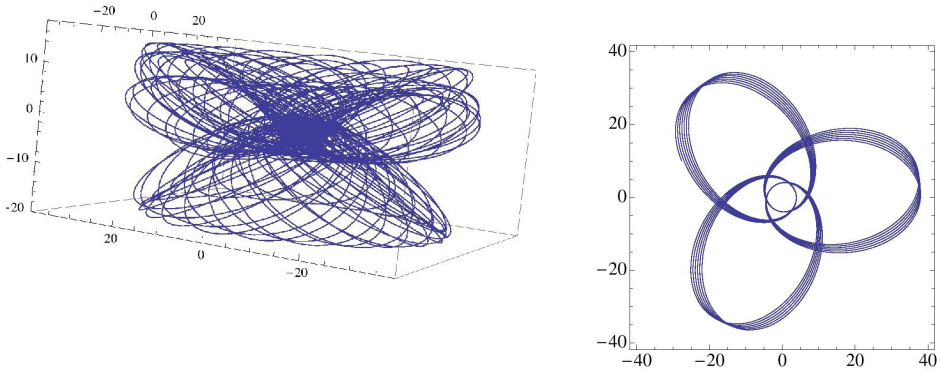

Figure 4.7: An orbit for which $q_\Phi = \frac{67}{200}$. The initial conditions are $m_2/m_1 = \frac{1}{4}$, $L = 3.5$, $\theta_{LS} = \frac{\pi}{3}$, $a = 0.9$, and $E = -0.0220323426$ Left: The full three-dimensional orbit. Right: The orbit in the orbital plane is a precession of the exact $q_\Phi = 1/3$ orbit.

that moves to the second leaf in the pattern ($v_\Phi = 2$). Since $w_\Phi = 0$ there are no additional whirls from leaf to leaf. For a z_Φ-leaf orbit, the range of v_Φ for orbits that overshoot, that is precess, is

$$\begin{aligned} 1 \leq v_\Phi \leq z_\Phi - 1\,, &\qquad \text{if } z_\Phi > 1 \\ v_\Phi = 0\,, &\qquad \text{if } z_\Phi = 1 \quad . \end{aligned} \tag{4.39}$$

To avoid degeneracy, we require that z_Φ and v_Φ be relatively prime, or in other words, that $q_\Phi = 2/4$ is the same as $q_\Phi = 1/2$.

The periodic orbits in the orbital plane are a set of measure zero in the space of orbits, just as the rationals are a set of measure zero in the set of the real numbers. However, just as the rationals are dense on $\mathbb{R}$, the periodics are dense in the space of orbits, and so any generic orbit can be arbitrarily well approximated by an orbit that is closed in the orbital plane.

For instance, the orbit of Fig. 4.7 is very near the 3-leaf orbit and can be interpreted as a precessing 3-leaf orbit. Or we could do better by approximating this orbit as a $q_\Phi = 67/200$, that is, an orbit with 200 leaves that skips to the 67th successive leaf in the pattern with each radial cycle.

By the same token, the randomly selected orbit of Fig. 4.3 is very nearly a $q_\Phi = 1/5$, that is, a 5-leaf clover, and that of Fig. 4.4 is very nearly a $q_\Phi = 7/25$

– an orbit with 25 leaves that skips to the 7th successive leaf in the pattern with each radial cycle.

It is important to notice that, although the orbit of Fig. 4.5 closes in the orbital plane after 3 radial cycles, it does not close in the full three-dimensional space since the orbital plane has not returned to its original location after only 3 radial cycles. A fully closed orbit also has to close in Ψ. Taking the time average of the rate of change $\dot{\Psi}$ over one radial cycle gives the fundamental frequency

$$\omega_\Psi = \frac{2}{T_r}\int_{r_a}^{r_p}\frac{\dot{\Psi}}{\dot{r}}dr = \frac{\Delta\Psi}{T_r} = \omega_r\frac{\Delta\Psi}{2\pi} \quad , \tag{4.40}$$

so that

$$\frac{\omega_\Psi}{\omega_r} = \frac{\Delta\Psi}{2\pi}\,. \tag{4.41}$$

The average precessional frequency may not be rationally related to the radial frequency for a rational q_Φ:

$$\frac{\omega_\Psi}{\omega_r} = \sigma_\Psi \quad , \tag{4.42}$$

where by σ_Ψ we mean any real number, not just a rational. This time we do not separate out a 1 from the definition of the number. So, σ_Ψ represents the fraction of 2π swept out as the plane precesses. The orbit of Fig. 4.5 has a $\sigma_\Psi \approx 0.346...$, where we have only listed the first 3 significant figures. Although numerical imprecision of the computer truncates this at a finite number of digits, and therefore effectively approximates σ_Ψ by a rational, it is in principle an irrational. After 3 radial cycles, the orbit has closed in the orbital plane but not in three dimensions. The entire orbital plane has overshot its initial location by $3\sigma_\Psi - 1 \sim 0.038....$ Therefore, even the 3-leaf clover in the orbital plane of Fig. 4.5 will fill out the surface of the three-dimensional picture.

In fact, from the equations of motion, Eqs. (4.27) and (4.28), we know that

$$1 + q_\Phi = -\frac{L}{J}\sigma_\Psi + f(E,L) \quad , \tag{4.43}$$

where $f(E,L)$ is a function of E, L through the dependence of the apastra and periastra's dependence on E, L. This curve for $(m_2/m_1 = 1/4, a = 0.9, \theta_{LS} = \pi/3, L = 3.5)$ is shown on the top of Fig. 4.8. Eq. (4.43) is interesting for two reasons. It means that σ_Ψ is not generally a rational number when q_Φ is rational. What is even more interesting is that this does not seem to matter.

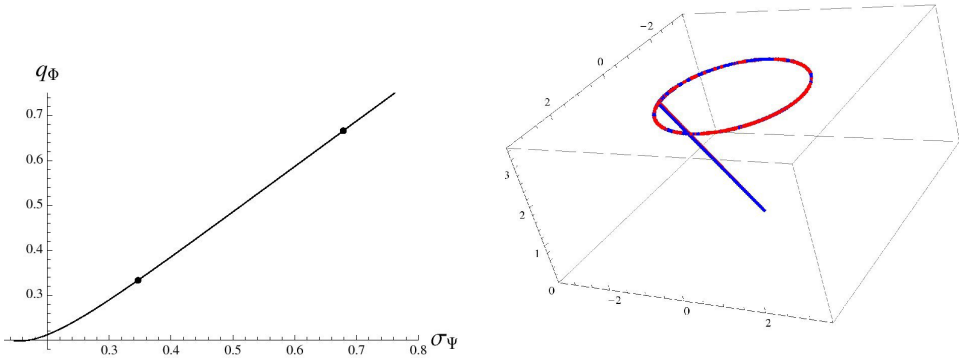

Figure 4.8: $(m_2/m_1 = 1/4, a = 0.9, \theta_{LS} = \pi/3, L = 3.5)$. Left: q_Φ versus σ_Ψ. The dots mark $(q_\Phi = 1/3, \sigma_\Psi \approx 0.346...)$ and $(q_\Phi = 2/3, \sigma_\Psi \approx 0.679...)$. Right: The circle traced out by the tip of the vector $\mathbf{L}$ for the orbit of Fig. 4.5. The straight line represents the $\mathbf{L}$ vector when 3 radial cycles have elapsed and the $q_\Phi = 1/3$ orbit has closed in the orbital plane. The same plot for the precessing 3-leaf clover of Fig. 4.7 is superposed although the two are so close that they cannot be distinguished in the graph. The fact that they cannot be distinguished confirms that the two orbits are genuinely near each other in 3d as well as in the orbital plane.

Because q_Φ effectively fixes the value of σ_Ψ for a given L through relation (4.43), if a generic orbit is well approximated by a periodic in the orbital plane, the precession of its orbital plane is also nearby in the phase space sense.[8]

This point is emphasized in the right panel of Fig. 4.8, which shows the circle traced out by the precession of the $\mathbf{L}$ vector for the 3-leaf clover in the orbital plane of Fig. 4.5. The straight line from the origin to the ring indicates the direction of $\mathbf{L}$ after 3 radial cycles have elapsed and the 3-leaf clover has executed one complete period in the orbital plane. The σ_Ψ of this orbit is $\approx 0.346...$ so that in 3 radial cycles the orbital plane has just overshot its initial location. By comparison, the nearby orbit of Fig. 4.7 has a $\sigma_\Psi \approx 0.348...$ and its orbital plane similarly has just barely overshot its initial location. The orbit of Fig. 4.7 precesses around the 3-leaf clover of Fig. 4.5, and its entire orbital plane precesses around $\mathbf{J}$, sticking close to the precession of the 3-leaf clover's

[8] Of course, we can always approximate any irrational, including σ_Ψ by a rational. But then we are describing approximately periodic orbits as opposed to orbits that are formally exactly periodic, and there does not appear to be any advantage in taking this tack. Hereafter, we will consider σ_Ψ to be generally irrational for any rational q_Φ.

orbital plane. In fact, the precessions of $\mathbf{L}$ are superposed in the right diagram of Fig. 4.8 and the difference between them is imperceptible at the resolution shown. The fact that the precession of $\mathbf{L}$ for these two orbits is effectively indistinguishable confirms that the two orbits are not only near each other in the orbital plane, but they are genuinely near each other in 3D as well.

Formally, the above argument ensures that any orbit can be approximated as arbitrarily near an orbit that is periodic in the orbital plane with the same L. In other words, the orbital periodic spectrum for a given L is dense. If we remove the restriction of comparing orbits of the same L, it follows that the set of orbits periodic in the orbital plane is dense in the entire space. The argument can be sketched as follows. According to Poincaré, the set of orbits that is fully periodic in 3D is dense in the phase space. This set is a subset of the orbital plane periodic set. Therefore, if the subset is dense, the set itself must be dense.

In short, we can understand the entire three-dimensional orbital dynamics through orbits that are closed in the orbital plane and that one rational, not two, is needed for a taxonomy. These conclusions are of course only valid up to 3PN with spin-orbit coupling. In the summary we will discuss the modulation expected by going to higher order in the approximation. In the meantime, we move on to the periodic tables for comparable-mass binaries.

4.4 Periodic tables

Since *every* orbit can be approximated as one that is periodic in the orbital plane – just as *every* irrational can be approximated by a rational – we can build a table of orbits for black hole binaries with a given mass ratio, spin, and angle between the spin and the orbital angular momentum $(m_2/m_1, S, L, \theta_{LS})$. Such a periodic table works in analogy to the chemical periodic table (see figures 4.10 and 4.12 below). Every entry represents a closed orbit labeled by a rational. The energy and the rationals both increase monotonically from top to bottom and then from left to right. Unlike the chemical periodic table, the black hole periodic tables are infinite since the rationals are infinite, and we show only a handful of entries.

When we discuss specific tables, we will always take all entries in a given table to have the same $(m_2/m_1, S, L, \theta_{LS})$. The entries vary only in energy (and therefore in q_Φ). Periodic tables can be constructed for any values of these parameters. However, some ranges give fuller tables in the sense that

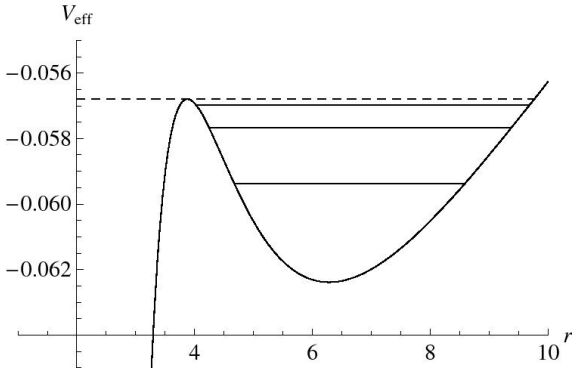

Figure 4.9: $(m_2/m_1 = 1/4, a = 0.5, \theta_{LS} = \pi/4)$. The pseudo effective-potential as a function of r shows a maximum at the unstable spherical orbit and a minimum at the stable spherical orbit. The homoclinic orbit is indicated with a dashed line. The other lines correspond to, in ascending order, $q_\Phi = \frac{2}{5}, \frac{1}{2}, \frac{2}{3}$. The higher q_Φ orbits quickly stack together near the homoclinic orbit.

certain ranges permit more whirliness. Understanding the ranges of whirliness requires careful consideration of properties of the spherical orbits. Several results concerning non-equatorial spherical orbits were presented in Chapter 3. Here we summarize the pertinent results for constructing periodic tables with use of a pseudo effective-potential picture.

A sensible condition for an effective potential formulation is that the Hamiltonian depend only on r and constants. Generally, the Hamiltonian of Eqs. (4.2)-(4.4) does not admit a simple effective potential formulation since it is a complicated function of $\mathbf{p}^2$. We have already argued that $H(r, \mathbf{p}, \mathbf{S})$ can be written as a radial Hamiltonian $H(r, P_r)$, yet it remains a complicated function or P_r. However, if we only consider

$$V_{\rm eff} = H(P_r = 0) \quad , \tag{4.44}$$

then we have a good representation of the effective potential *at the turning points*. We cannot misuse the $V_{\rm eff}$ by trying to interpret motion away from the turning points, but it gives a perfectly valid description of the behavior at aphelia and periastra as well as on spherical orbits. Hereafter we will abbreviate the term "pseudo effective-potential" by "effective potential". An effective potential for comparable mass binaries is shown in Fig. 4.9.

Evident is the lowest energy orbit at the stable spherical orbit. The highest energy nonplunging orbit is the unstable spherical orbit. We are interested

in energetically bound orbits here, i.e. orbits with $E \leq 0$. If the unstable spherical orbit has energy $E < 0$, then the spectrum of periodic orbits densely fills the energy range between the stable and unstable spherical orbit. If instead the unstable spherical orbit has energy $E > 0$, then the the spectrum of periodic orbits densely fills the energy range between the stable spherical orbit and the marginally bound orbit at $E = 0$. The energy levels of a few periodic orbits are indicated by solid lines in Fig. 4.9.

Since q_Φ is monotonic with energy, the entries in the periodic table are bounded:

$$q_{\rm min} \leq q_\Phi \leq q_{\rm max} \quad . \tag{4.45}$$

The value of $q_{\rm min}$ is the q_Φ of the stable spherical orbit and $q_{\rm max}$ is set by the q_Φ of the maximum energy bound orbit.

The value of $q_{\rm max}$ depends on the largest energy orbit allowed for that L. When an unstable spherical orbit exists there is always an orbit with the same E and L at a large radius. The maximum of $V_{\rm eff}$ in Fig. 4.9 marks the unstable spherical orbit. Drawing a line of constant energy across the effective potential locates the apastron of the orbit with the same E and L as the unstable spherical trajectory. When released from apastron, this orbit whirls an infinite number of times as it approaches the unstable spherical orbit and is formally a homoclinic orbit; that is, it approaches the same invariant set in the infinite future and the infinite past. Although not strictly periodic – the homoclinic orbit never returns to apastron – it can be considered the infinite winding limit of the 1-leaf periodic orbits [37]. As such, it is the $w_\Phi = \infty$ limit and we assign homoclinic orbits a $q_\Phi = \infty$. Consequently, if the range of parameters has a bound unstable spherical orbit, then it has a ($q_\Phi = \infty$) homoclinic orbit and the associated periodic tables will exhibit much whirliness.

Since, for a given L, the stable spherical orbits bound the allowed energy range from below, they also bound the value of q_Φ from below. One might presume that $q_{\rm min} = 0$ but, importantly, this is not the case. To see this notice that a spherical orbit obviously does not have a radial cycle. The $q_{\rm min}$ set by the stable spherical orbit can instead be thought of as the value of q_Φ for a nearby eccentric orbit in the limit that the eccentricity vanishes:

$$q_{\rm min} \to \lim_{e\to 0} \frac{\omega_\Phi}{\omega_r} - 1 \quad . \tag{4.46}$$

This allows us to derive the $q_{\rm min}$ from a stability analysis since the limit of zero eccentricity is effectively the limit of constant radius, which implies $\dot{\Phi}\Big|_{r_s}$

is constant and that $\omega_r = i\lambda_r$ is given by a small perturbation around the stable spherical orbit. We then have, just as we found in Ref. [37] that[9]

$$q_{\rm min}(r_s) = \frac{\dot{\Phi}\Big|_{r_s}}{|\lambda_r|} - 1 \quad . \tag{4.47}$$

We choose for the sake of illustration, to consider tables capable of probing high whirliness. For this reason we stay within the range set by the innermost stable spherical orbit (isso) and the innermost bound spherical orbit (ibso), $L_{\rm isso} < L < L_{\rm ibso}$. Of course, the drawback is that we are pushing the PN expansion to the breaking point. Although these inner strong-field orbits probe beyond the confidence of the 3PN approximation, the general method of constructing periodic tables in a full relativistic treatment is robust, as proven by the Kerr demonstration of Ref. [37].

Periodic tables in the orbital plane

The purpose of the post-Newtonian expansion is of course to approximate the behavior of comparable-mass binaries. A periodic table for a binary with $m_2/m_1 = 1/4$ is shown in Fig. 4.10. The heavier black hole has a spin amplitude of $a = 1/2$ and the angle is $\hat{\mathbf{L}} \cdot \hat{\mathbf{S}} = \cos(\pi/4)$. The orbits do not lie in a plane and are fully three-dimensional, like those of Figs. 4.3 and 4.4. Each entry is an orbit that is periodic in the orbital plane, although not necessarily fully periodic. The energy and the rational of each entry increase from top to bottom and from left to right.

Notice that the first two entries are blank before the appearance of the 2-leaf clover in entry 3. These are blank because, for this $(m_2/m_1, a, S, L, \theta_{LS})$, the $q_\Phi = 0$ and $q_\Phi = 1/3$ orbits simply do not exist since $q_{\rm min}$ is just above $1/3$ (and $q_{\rm max} = \infty$). We saw this before in the Kerr system [37]. The implication is important. *All* eccentric orbits – for this range of parameters – show zoom-whirl behavior. None of them look like the slight precession of the perihelion of Mercury.

[9] Although most orbits precess in the orbital plane, Eq. (4.47) actually allows for regression when $\frac{\dot{\Phi}|_{r_s}}{|\lambda_r|} < 1$. When the orbital plane and the equatorial plane align $(\mathbf{S} \times \mathbf{L}) = 0$, regression seems intuitively obvious. It only means that Φ is not the whole story of the motion of $\hat{\mathbf{n}}$ and we must also add in Ψ to see that the actual orbit precesses in the equatorial plane, as we will do explicitly by moving to the equatorial basis in section 4.4.1. We did, however, also see regression out of the equatorial plane, and it is difficult to say whether it is a flaw in the PN approximation or if it will survive a full relativistic treatment.

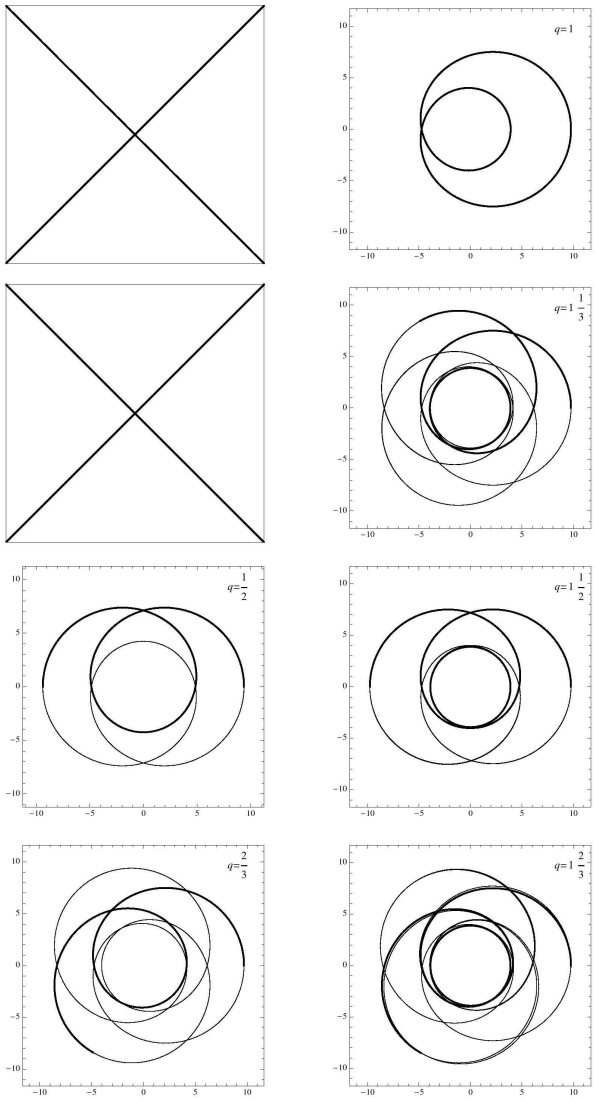

Figure 4.10: A nonequatorial periodic table for which the heavier black hole spins with amplitude $a = \frac{1}{2}$, the mass ratio is $m_2/m_1 = \frac{1}{4}$, $L = 3.2$ and $\theta_{LS} = \frac{\pi}{4}$. All valid entries up to $z_\Phi = 3$ are shown. The final entry begins to show a departure from true periodicity as a result of numerical error. The high numerical precision required to keep the simulated orbit near a perfectly periodic one is a reflection of the tight stacking of high q_Φ orbits near the top of the potential in Fig. 4.9.

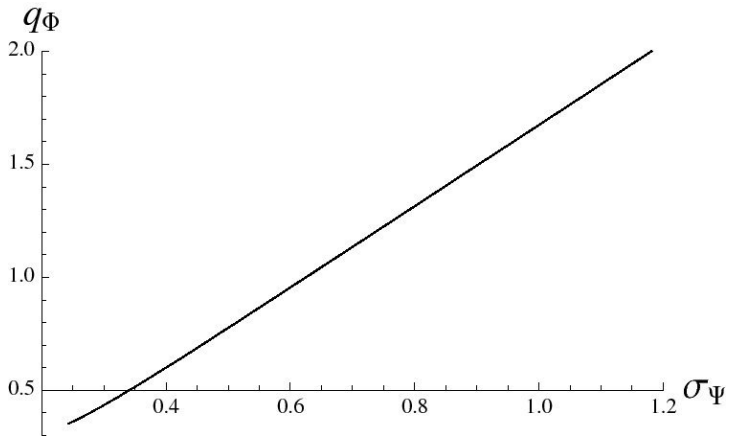

Figure 4.11: q_Φ versus σ_Ψ for the table in Fig. 4.10.

Every orbit in this system can be arbitrarily well approximated by an entry in the table, because the precessional motion of the entire plane is also effectively fixed by the rational q_Φ as the plot of Fig. 4.11 shows. If σ_Ψ could be chosen independently of q_Φ for a given L, our conclusion would not follow. However, q_Φ versus σ_Ψ lies on a one-dimensional curve. Once q_Φ is known, σ_Ψ can be read off. Physically this means that an orbit that is very near a $q_\Phi = 1/2$ will precess around the 2-leaf clover in the orbital plane and that the precession of the entire orbital plane will be very close to the precession of the true 2-leaf clover's orbital plane.

4.4.1 Periodic tables in the equatorial plane

Some binary parameters will automatically restrict motion to the *equatorial* plane and these require special discussion. For instance, if neither black hole spins then the system is spherically symmetric and all orbits are confined to a plane: the orbital plane *is* the equatorial plane. Similarly, if one of the black holes spins but the spin is aligned with the angular momentum or antialigned, then the motion will again be restricted to the equatorial plane. We summarize these three cases as $\mathbf{S} \times \mathbf{L} = 0$ scenarios.

When $\mathbf{S} \times \mathbf{L} = 0$, our orbital basis $(\hat{\mathbf{n}}, \hat{\mathbf{\Phi}}, \hat{\mathbf{\Psi}})$ is not defined and must be replaced with the usual planar basis $(\hat{\mathbf{n}}, \hat{\varphi})$, where φ is the usual angle

measured[10] between $\hat{\mathbf{n}}$ and $\hat{\mathbf{l}}$. The equation of motion for φ is simply

$$\dot{\varphi} = \dot{\Phi} + \dot{\Psi} \quad . \tag{4.48}$$

The q we must use for the equatorial plane of the nonspinning system is then

$$\frac{\omega_\varphi}{\omega_r} = 1 + q \quad . \tag{4.49}$$

Each entry is specified by this one rational which represents the ratio of the time averaged orbital angular frequency in the equatorial plane to the radial frequency. The rational can be read off the topology of the orbit as $q = w + v/z$; that is, the number of whirls, the number of leaves and the order in which the leaves are laid out fix q.

The table of Fig. 4.12 reflects a nonspinning black hole system with an extreme mass ratio of $m_2/m_1 = 10^{-6}$. The first 3 entries are blank since $q_{\rm min}$ is just below 1/2. Although we only show entries up to $z_\Phi = 4$ for $w_\Phi \leq 2$, for these parameters $q_{\rm max} = \infty$. We point out the intriguing possibility that periodic tables could be used to further test the accuracy of the post-Newtonian expansion [82].

4.5 Summary

To recap, for comparable-mass binaries with one spinning black hole and one nonspinning black hole as approximated by the conservative 3PN Hamiltonian plus spin-orbit coupling, our main results are:

1. Simplified Equations of Motion in an Orbital Basis

From these equations we find

- constant aphelia and perihelia for nonequatorial eccentric orbits, and
- three fundamental frequencies that depend only on radius.

2. Taxonomy of Fully Three-Dimensional Orbits

From this we find that

- there exists a spectrum of closed orbits in the orbital plane corresponding to a subset of the rationals;
- one rational, not two is required for an orbital plane taxonomy of constant

[10] If we were only slightly out of the equatorial plane, we would see regression in the orbital plane because much of the motion is taken through Ψ. Intuitively then, those instance of regression that are just barely out of the equatorial plane are not that surprising.

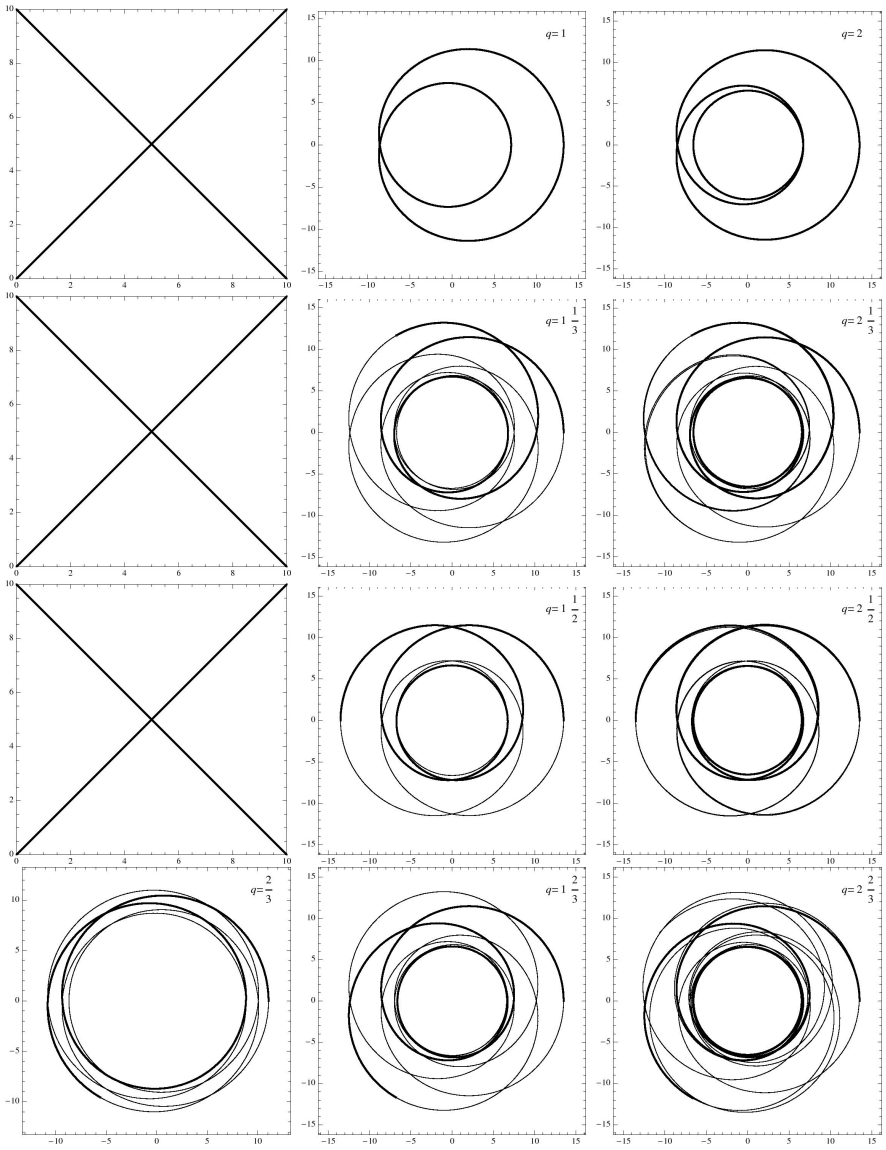

Figure 4.12: A periodic table for orbits in a nonspinning system $a = 0$, extreme-mass-ratio system, $\frac{m_2}{m_1} = 10^{-6}$. The angular momentum is $L = 3.9$. Since $a = 0$ all orbits lie in the equatorial plane. Periodic tables such as this one could be used to expand on comparisons with the full relativistic system. All valid entries up to $z_\Phi = 4$ are shown. As before, the final entry begins to show a departure from true periodicity as a result of numerical error.

angular momentum slices;

• *all* orbits can be approximated as near an orbit that is perfectly closed in the orbital plane; and

• zoom-whirl behavior is ubiquitous in comparable-mass binary dynamics and entirely quantifiable through the spectrum of rationals.

These points apply to the conservative dynamics. But, of course, black hole dynamics is not conservative. Energy and angular momentum are lost to gravitational waves. An actual orbit will roll through a sequence of periodic tables under the dissipative losses. An orbit can then be described by a $\dot{q}_\Phi$. The utility of the tables will depend of the rate at which the orbit moves through the sequence of underlying geodesics. If the losses are very rapid, there will not be an opportunity for the distinct orbits described in this paper to leave an imprint in the gravitational waves. If the losses are more gradual, then the waveforms will reflect the zoom-whirl features of these orbits. Since the parameter space for initial values is so large, a lengthy and detailed analysis of dissipation is required and currently under investigation.

Chapter 5

Periodic orbits in the generic Kerr spacetime

5.1 Introduction

In 1968, Carter famously showed that there were four constants of motion[35; 52] for the orbits around Kerr black holes, one for each canonical momentum, so that the orbits are integrable. Despite this fact, Kerr geodesics have long evaded a simple geometric classification. While any geodesic orbit can be computed easily, a concise general account of how changes to the constants of motion would alter its shape has been unavailable.

The goal of this chapter is to generalize the equatorial taxonomy summarized in Chapter 2 to fully generic $3D$ Kerr motion. This generalization is by no means straightforward. As in the equatorial Kerr case, we lose the ability to describe the orbital motion using the simple Newtonian-like effective potential technique. And as in the equatorial case, we will instead formulate a pseudo-effective potential for Kerr motion in order to make progress. The difference will be that the pseudo-effective potential for nonequatorial Kerr orbits is harder to come by. The difficulty stems from introducing a third spatial degree of freedom when dealing with the Kerr non-equatorial system. The details of the difficulties that arise when introducing the third degree of freedom are subtle and explained in detail in Section 5.3.

To that end, this chapter is divided into two major parts. The first part, Sections 5.2 and 5.3, will offer the necessary background on generic Kerr motion and show how we can correctly generalize the standard Schwarzschild

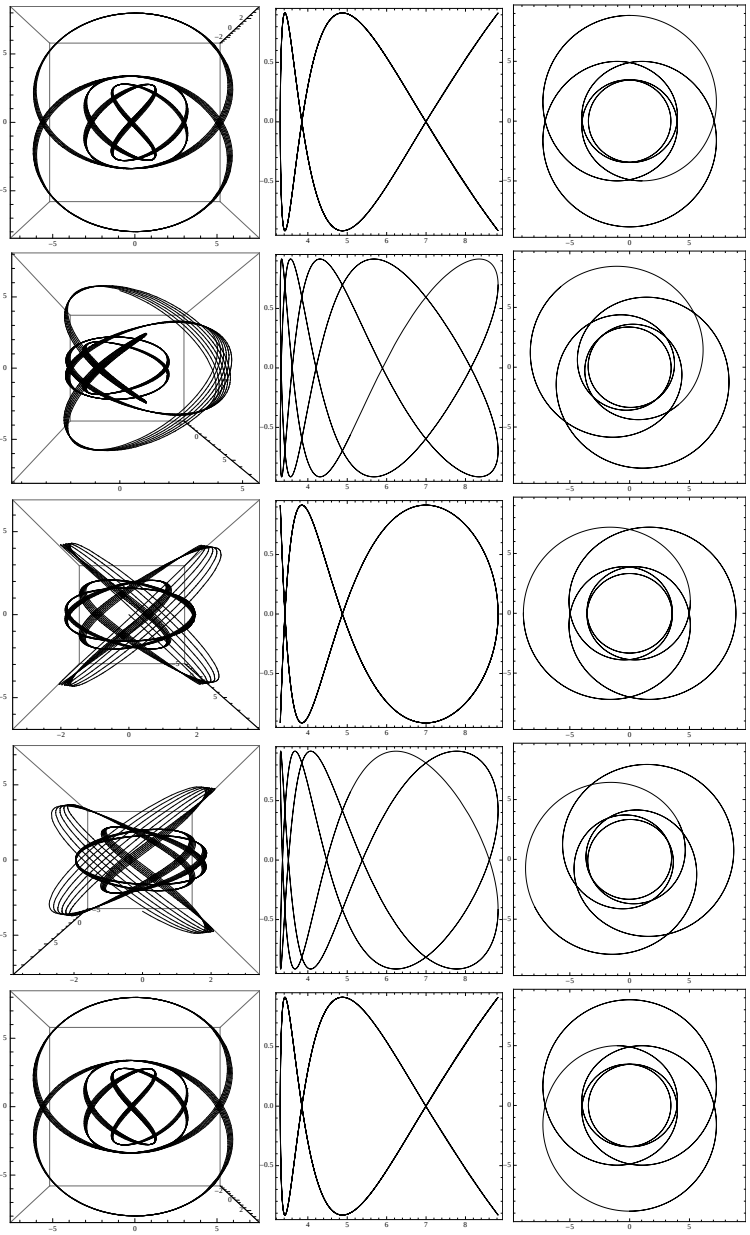

Figure 5.1: r-θ periodic orbits ($q_{r\theta} = 1\frac{1}{2}$) with $L = 3$, $E = 0.932516$, $\cos\iota = 0.4$ and $a = 0.99$, but with different $r - \theta$ phasing. Column 1 shows the full 3D orbit. Column 2 is the projection of the orbit into the r-$\cos\theta$ plane. Column 3 is the projection into the orbital plane. All rows have $r_0 = r_a = 8.82713$ and $\varphi_0 = 0$. The initial θ values are as follows: Row 1 $\theta_0 = \theta_{\rm min} = 0.414139$; Row 2 $\theta_0 = 0.8$; Row 3 $\theta_0 = \frac{\pi}{2}$; Row 4 $\theta_0 = 2$; Row 5 $\theta_0 = \theta_{\rm max} = 2.72745$.

effective potential technique to fully general Kerr non-equatorial motion. We will do this in such a way that all salient properties from the Schwarzschild V_{eff} picture manifest themselves immediately. This will involve making an unorthodox, but simple, hybrid choice of orbital parameters.

The second part of this chapter, Sections 5.4 through 5.9, will then use the techniques developed in Chapter 2 to lay out the spherical, homoclinic, and periodic orbits as a generalization of the material from [37] presented in Chapter 2. Building the periodic tables is a demonstration not simply that such periodic orbits exist but that their topological features vary in a clear systematic way as orbital parameters vary. Once this organization is realized, we will discuss possible astrophysical utility of such a scheme.

As a preview, we show a series of periodic orbits in $3D$ on the leftmost column of Fig. 5.1, in the $r-\theta$ plane in the middle column, and projected in an effective orbital plane in the final column. These orbits are closed in $r-\theta$ and also in the orbital plane, but are not fully closed in $3D$. The following sections will be devoted to realizing this argument. Similar reasoning led to the taxonomy of generic $3D$ orbits in a post-Newtonian expansion of two black holes presented in Chapters 3 and 4.

Note that we could identify orbits that are fully periodic in 3D and argue that all generic orbits are approximated at arbitrary precision by that set of measure zero [37]. However, it is sufficient to consider the less restrictive, larger set of orbits that are periodic only in $r-\theta$, as these will be shown to be perfectly periodic when projected into an instantaneous orbital plane, as Fig. 5.1 illustrates.

5.2 The basics

5.2.1 The geodesic equations with E, L_z and Q

We begin with the Kerr metric restated from Chapter 2 in Boyer-Lindquist coordinates and geometrized units ($G = c = 1$) and the conventional choice of

$M = \mu = 1$:

$$\begin{aligned} ds^2 &= -\,d\tau^2 \\ &= -\left(1 - \frac{2r}{\Sigma}\right) dt^2 - \frac{4ar\sin^2\theta}{\Sigma} dt d\varphi + \frac{\Sigma}{\Delta} dr^2 + \Sigma d\theta^2 \\ &\quad + \sin^2\theta \left(r^2 + a^2 + \frac{2a^2 r \sin^2\theta}{\Sigma}\right) d\varphi^2 \quad , \end{aligned} \tag{5.1}$$

where

$$\begin{aligned} \Sigma &\equiv r^2 + a^2\cos^2\theta \\ \Delta &\equiv r^2 - 2r + a^2 \quad . \end{aligned} \tag{5.2}$$

Carter reduced the equations to first integrals of motion [35; 52], exploiting the four constants of motion E, L_z, Q and μ. Unlike in Chapter 2, where we expressed the EOM with respect to proper time τ, here we express them with respect to Mino time [96] λ, which is related to the particle's proper time τ by $d\lambda = \frac{d\tau}{\Sigma}$. Those EOM are

$$\dot{r} = \pm\sqrt{R} \tag{5.3a}$$

$$\dot{\theta} = \pm\sqrt{\Theta} \tag{5.3b}$$

$$\dot{\varphi} = \frac{a}{\Delta}\left(2rE - aL_z\right) + \frac{L_z}{\sin^2\theta} \quad , \tag{5.3c}$$

$$\dot{t} = \frac{(r^2 + a^2)^2 E - 2arL_z}{\Delta} - a^2 E \sin^2\theta \quad . \tag{5.3d}$$

We will often refer to Equations (5.3) as the Carter equations. An overdot denotes differentiation with respect λ, and the quantities $R(r)$ and $\Theta(\theta)$ are given by

$$\Theta(\theta) = Q - \cos^2\theta \left\{ a^2(1 - E^2) + \frac{L_z^2}{\sin^2\theta} \right\} \tag{5.4}$$

$$\begin{aligned} R(r) &= -(1 - E^2) r^4 + 2r^3 - \left[a^2(1 - E^2) + L_z^2\right] r^2 \\ &= +\,2(aE - L_z)^2 r - Q\Delta \end{aligned} \quad . \tag{5.5}$$

5.2.2 The conserved quantities E, L and ι

While the four conserved quantities are conventionally chosen to be μ, E, L_z and Q, because each of those quantities are constants of the motion, any

combination of them is also a constant of the motion. Therefore, there are an infinite number of choices of four independent quantities we could make for our conserved quantities. Because of the organizational insight we can gain from a different combination of constants, we have chosen to use μ, E, effective angular momentum (L) and effective inclination angle (ι), where L and ι are defined as

$$\begin{aligned} L^2 &= L_z^2 + Q \\ \cos\iota &= \frac{L_z}{L} \quad . \end{aligned} \tag{5.6}$$

This construction of conserved quantities was first used by [97; 98] and used occasionally in other references [99; 100; 101; 102]. For now we assert this choice of constants and in Section 5.5 we justify why it is necessary for the construction developed in this chapter.

Recasting Equations (5.3), (5.4) and (5.5) in terms of ι and L instead of Q and L_z yields

$$\dot{r} = \pm\sqrt{R} \tag{5.7a}$$

$$\dot{\theta} = \pm\sqrt{\Theta} \tag{5.7b}$$

$$\dot{\varphi} = \frac{a}{\Delta}\left(2rE - aL\cos\iota\right) + \frac{L\cos\iota}{\sin^2\theta} \quad , \tag{5.7c}$$

$$\dot{t} = \frac{(r^2+a^2)^2 E - 2arL\cos\iota}{\Delta} - a^2 E\sin^2\theta \quad . \tag{5.7d}$$

where

$$\Theta(\theta) = L^2\left(1-\cos^2\iota\right) - \cos^2\theta\left\{a^2(1-E^2) + \frac{L^2\cos^2\iota}{\sin^2\theta}\right\} \tag{5.8}$$

$$\begin{aligned} R(r) = {} & \left(E^2-1\right)r^4 + 2r^3 + \left(a^2\left\{E^2-1\right\} - L^2\right)r^2 \\ & + 2r\left(a^2E^2 - 2aEL\cos\iota + L^2\right) + a^2L^2\left(\cos^2\iota - 1\right) \quad . \end{aligned} \tag{5.9}$$

$R(r)$ and $\Theta(\theta)$ are the polar and radial quasi-potentials, respectively [103] and they reveal some well-known geometric information about bound non-plunging orbits (orbits that neither escape to infinity nor cross the horizon of the central black hole). First, they reveal the radial turning points, which occur at roots of $R(r)$. For a given E, L and ι, the quartic polynomial has four roots. The outermost two are periastron and apastron, between which the radial position of a bound orbit oscillates. A similar analysis of the roots

of $\Theta(\theta)$ reveals that every bound orbit oscillates between a fixed $\theta_{\rm min}$ and $\theta_{\rm max}$ symmetrically distributed about the equatorial plane[1], i.e. $\theta_{\rm min} = \pi - \theta_{\rm max}$ [49; 99; 103]. The upshot is that every $3D$ orbit will generally lie in a toroidal wedge around the equatorial plane bounded r_p and r_a in radial coordinate and between $\theta_{\rm max}$ and $\pi - \theta_{\rm max}$ in polar angle [100].

To see these properties of the motion explicitly, we now construct a pseudo-effective potential picture based on the analysis of Chapter 2.

5.3 $V_{\rm eff}$ for generic Kerr orbits

Section 2.9 details the method of finding a pseudo-effective potential for the equatorial Kerr system. We now generalize that approach to find the generic Kerr $V_{\rm eff}$.

Before we solve for $V_{\rm eff}$ we need to address a feature of the general Kerr system that was not present in the equatorial Kerr system. Equatorially, we had a two-orbital-parameter (E, L) [2] family of orbits, whereas in the generic Kerr system we have a three-orbital-parameter (E, L, ι) family of orbits. The equatorial Kerr system is completely specified by two fixed ι-values. To capture the same dynamical features in the general Kerr system, we will therefore seek to construct an effective potential for each fixed ι.

To clarify, our approach for mapping the radial motion of the general Kerr system to a $V_{\rm eff}$ is laid out as follows:

1. We set $\dot{r} = 0$ in equation (5.7) and solve for E which is equivalent to setting $R(r) = 0$ in equation (5.9)[3].

2. The resulting E expression will be a function of two parameters L and ι. For each fixed ι we will see that the orbital dynamics work out in exactly the same way they did in Schwarzschild and Kerr equatorial of chapter 2.

[1] For equatorial orbits, $\theta_{\rm min} = \theta_{\rm max} \equiv \pi/2$.

[2] In the Kerr equatorial case, all prograde orbits have an $\iota = 0$, $\cos\iota = 1$ and all retrograde orbits have an $\iota = \pi$, $\cos\iota = -1$. The Kerr equatorial system can be derived from the Kerr $3D$ system with two specific ι values. This is different then using Q as one of the constants of the motion because the Q parameter does not distinguish between prograde and retrograde orbits. All equatorial orbits have $Q = 0$.

[3] This is the genesis of the referring to $R(r)$ as a quasi-potential.

3. In the spirit of the Schwarzschild V_{eff}, we set the general Kerr $V_{\text{eff}} = \frac{1}{2}E^2$. Unlike in the Schwarzschild system, the general Kerr V_{eff} is only a valid representation of the radial velocity at an orbit's turning points and for constant r orbits.

Following our above prescription, we find the expression for E when $\dot{r} = 0$ to be

$$E = \frac{2aLr\cos\iota}{r\left(r^3 + a^2\left(2+r\right)\right)} + \frac{\sqrt{r\left(a^2 + \left(-2+r\right)r\right)\left(r^3\left(L^2+r^2\right) + a^2\left(2+r\right)\left(L^2 - L^2\cos^2\iota + r^2\right)\right)}}{r\left(r^3 + a^2\left(2+r\right)\right)} \quad , \tag{5.10}$$

and

$$V_{\text{eff}} = \frac{1}{2}E^2 \quad . \tag{5.11}$$

We point out how to recover both the Schwarzschild and equatorial Kerr V_{eff} expressions of Chapter 2 from our general Kerr V_{eff} in equation (5.10) and (5.11). When we first looked at the equatorial Kerr system in Section 2.9 we were using the conventional constants of the motion, E, L_z and Q. In this notation, all equatorial orbits have $Q = 0$ and L_z can be positive or negative. This resulted in two different effective potential systems for a given Q, one for prograde and one for retrograde.

Switching to the E, L and ι constants produces one effective potential curve for each ι rather then the two such curves produced for a given Q. Equatorially, prograde orbits correspond to $\iota = 0$ and retrograde orbits to $\iota = \pi$. Setting $\iota = 0$ in (5.10) correctly yields the prograde equatorial Kerr V_{eff} in (2.30) and setting $\iota = \pi$ in (5.10) correctly returns the retrograde equatorial Kerr V_{eff} in (2.30). Similarly, setting $a = 0$ in (5.10) yields the correct Schwarzschild V_{eff} in (2.9).

Now armed with a V_{eff} for the generic Kerr system, we set out to catalog the orbital dynamics for arbitrary inclinations. In Figure 5.2, we show V_{eff} for a variety of L-values for two fixed values of ι. There are five different L values plotted one corresponding to each regime in Table 2.1. It turns out, that for any given ι, you reproduce the qualitative features of allowed orbits described by Table 2.1. Qualitatively, the radial dynamics for every given ι exactly mimic the orbital dynamics of both the Schwarzschild system.

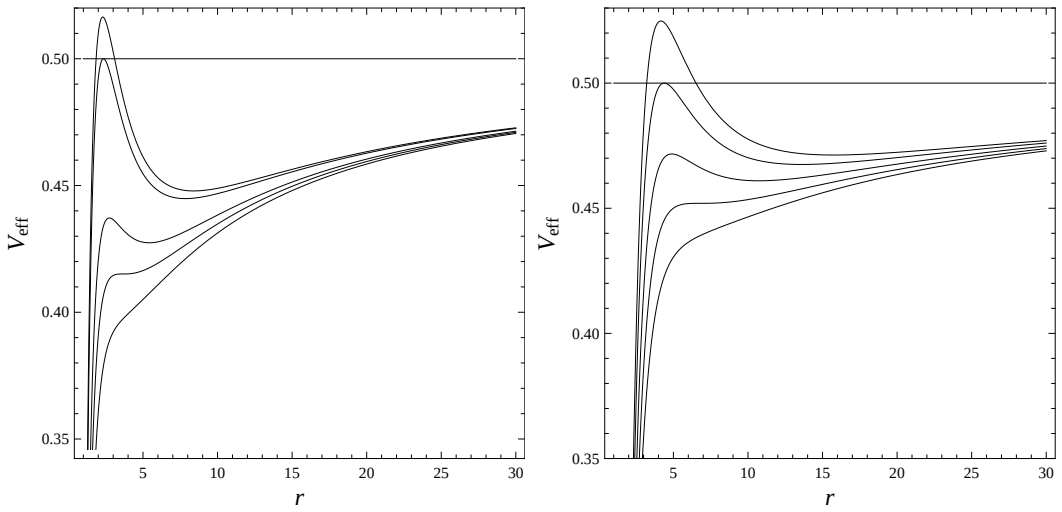

Figure 5.2: Left: All V_{eff} curves have $a = 0.99$ and $\cos\iota = 0.4$. The highest curve has an $L = 3.4 > L_{ibso}$. The second highest curve has $L = L_{ibso} = 3.32432$. The middle curve has $L_{isso} < L = 3 < L_{ibso}$. The second lowest curve has an $L = L_{isso} = 2.85501$. The lowest curve has $L = 2.7 < L_{isso}$. The horizontal line at $V_{\text{eff}} = \frac{1}{2}$ shows the energy of the marginally bound orbits. Right: Shows five V_{eff} curves all with $a = 0.99$ and $\cos\iota = -0.4$. The highest curve has an $L = 4.5 > L_{ibsso}$. The second highest has $L = L_{ibso} = 4.283298$. The middle curve has $L_{isso} < L = 4 < L_{ibso}$. The second lowest curve has an $L = L_{isso} = 3.74594$. And the lowest has $L = 3.5 < L_{isso}$. The horizontal line at $V_{\text{eff}} = \frac{1}{2}$ shows the energy of the marginally bound orbits.

We point out that we could also define a polar effective potential exactly analogously to the radial one. We find that just as the radial motion of bound nonplunging nonscattering orbits clearly executes oscillations between an apastron and periastron, the polar motion oscillates between a minimum and maximum angle.

5.4 Spherical orbits

Armed with a generic Kerr V_{eff} we now seek to analyze the constant r orbits which will provide a complementary method of exploring much of the orbital dynamics illustrated with the V_{eff}.

In the cases of Schwarzschild and equatorial Kerr motion, orbits of constant

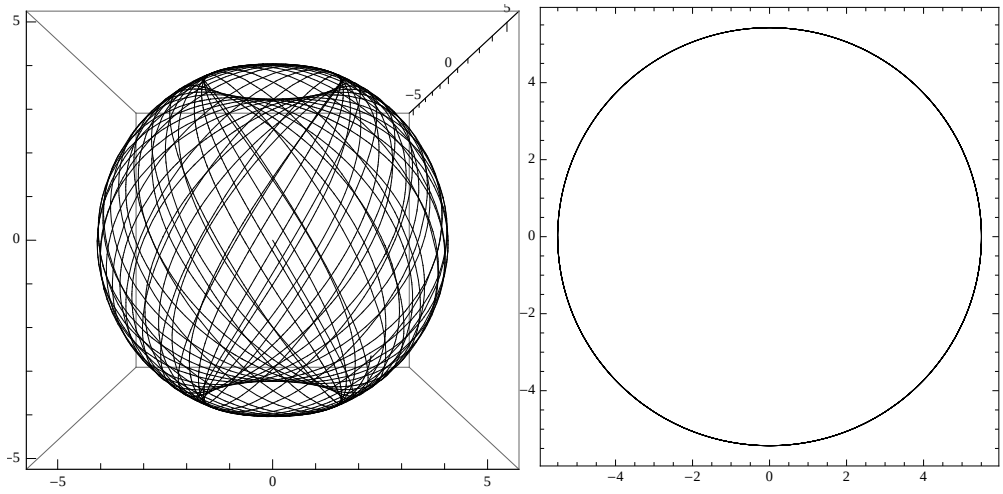

Figure 5.3: Spherical orbit with orbital parameters $a = 0.99$, $E = 0.924561$, $L = 3$ and $\cos\iota = 0.15873$. Left: The orbit in $3D$. Right: The orbit projected into the orbital plane.

r — circular orbits — serve to organize the ranges of orbital parameters over which bound, nonplunging motion exists. Constant r orbits in the general Kerr geometry play a similar organizational role but need not lie in a plane. Thus, they are not necessarily circular orbits but rather spherical. Figure 5.3 shows such a spherical orbit in the full 3D in the left panel and projected into the orbital plane in the right panel.

Spherical orbits were first treated in [103] and later analyzed in the context of radiation reaction in [99; 101] (in the latter references, these constant r orbits are referred to as "circular, nonequatorial orbits", but we use the original shorter moniker "spherical" from Ref. [103]). Like circular orbits, spherical orbits have $\dot{r} = \ddot{r} = 0$; unlike their circular counterparts, spherical orbits do not have $\dot{\theta} = 0$.

As in the equatorial Kerr case, our starting point is the radial quasi-potential $R(r)$. Returning to our expression for $R(r)$ from equation 5.9 and its derivatives in terms of E, ι and L given by

$$R'(r) = 4\left(E^2-1\right)r^3 + 6r^2 + 2\left(a^2\left\{E^2-1\right\} - L^2\right)r + 2\left(a^2E^2 - 2aEL\cos\iota + L^2\right) \tag{5.12a}$$

$$R''(r) = 12\left(E^2-1\right)r^2 + 12r + 2\left(a^2\left\{E^2-1\right\} - L^2\right) \quad , \tag{5.12b}$$

where a $'$ denotes differentiation with respect to r, the condition $\dot{r} = 0$ implies

$R(r) = 0$ from equation (5.7). Solving for $\ddot{r}$ from equation (5.7) we find that

$$\begin{aligned} \ddot{r} &= \frac{1}{2}\frac{\dot{R}}{\sqrt{R}} \\ &= \frac{1}{2}\frac{\dot{r}R'}{\sqrt{R}} \\ &= \frac{1}{2}R' \quad , \end{aligned} \tag{5.13}$$

where $R'(r) = \frac{dR}{dr}$. We can see immediately from equation (5.13) that $\ddot{r} = 0$ implies $R'(r) = 0$. Similarly, $\dddot{r} = 0$ implies that $R''(r) = 0$.

To find expressions for all E_s and L_s for a fixed a and ι, we set $R(r) = R'(r) = 0$ and solve for $E_s(r, a, \iota)$ and $L_s(r, a, \iota)$. Solving the two coupled quadratic equations yields four solutions for each of E_s and L_s. We determine the physically admissible solutions by imposing that L_s always be positive, i.e. an effective angular momentum *magnitude*. Additionally, because each fixed ι should replicate the orbital structure of the Schwarzschild geometry, both the L_s and E_s solutions should asymptote at low r-values to the innermost time-like spherical orbit. There should also be a minimum L_s and E_s value corresponding to the innermost bound spherical orbit (ibso). And the r at which the minima occur on the L_s and E_s graphs should be the same. Finally, at large r, our L_s plot should reproduce the Newtonian limit, $L \propto \sqrt{r}$ and E_s should asymptote to 1.

Combining the above conditions, we find

$$
\begin{aligned}
E_s\left(r,a,\iota\right) = & \Bigg[\left(-3+r\right)\left(-2+r\right)^2 r^7 + a^8 \sin^4\iota\left(1+r\right) \\
& - 2ar\cos\iota\Delta\left(-a^2\sin^2\iota + r^2\right)\sqrt{r\left(-a^4\sin^2\iota + 2a^2\sin^2\iota\Delta + r^4\right)} \\
& - a^4 r^2 \sin^2\iota\Big[a^2\left\{4 - 4\left(-1+r\right)r + \cos^2\iota\left(1+r\right)\left(-5+4r\right)\right\} \\
& + 2\left(-1+r\right)r\left\{2 - 3\left(-2+r\right)r + \cos^2\iota\left(-4 + r\left(-1+2r\right)\right)\right\}\Big] \\
& + a^2 r^5\Big[4\left(-2+r\right)\left\{1 + \left(-3+r\right)r\right\} \\
& + \cos^2\iota\Big\{8 + r\left(-23 + \left(17-4r\right)r\right)\Big\}\Big]\Bigg]^{\frac{1}{2}} \\
& \Big/\Bigg[\left(-a^4\sin^2\iota - 2a^2r^2\sin^2\iota - r^4\right)\times \\
& \quad\Big\{-\left(-3+r\right)^2 r^4 - a^4\sin^2\iota\left(1+r\right)^2 \\
& \quad + 2a^2r^2\left(-\left(-3+r\right)\left(1+r\right) + \cos^2\iota\left(-3+r^2\right)\right)\Big\}\Bigg]^{\frac{1}{2}}
\end{aligned}
\tag{5.14}
$$

$$
\begin{aligned}
L_s\left(r,a,\iota\right) = & \left\{\frac{-\Delta\sqrt{r\left(-a^4\sin^2\iota + 2a^2\sin^2\iota\Delta + r^4\right)}}{-a^4\sin^2\iota - \left(-2+r\right)^2 r^2 + a^2 r\left(4 - 2r + \cos^2\iota\left(-3+2r\right)\right)}\right. \\
& \left. + \frac{ar\cos\iota\left(a^2 + r\left(-4+3r\right)\right)}{-a^4\sin^2\iota - \left(-2+r\right)^2 r^2 + a^2 r\left(4 - 2r + \cos^2\iota\left(-3+2r\right)\right)}\right\} \\
& \times E_s\left(r,a,\iota\right) \quad .
\end{aligned}
\tag{5.15}
$$

We recover the functions E_c and L_c given in equation (2.32) for equatorial Kerr circular orbits by setting $\iota = 0$ for prograde and $\iota = \pi$ for retrograde in equations (5.14) and (5.15). From there, we recover the well-known Schwarzschild functions E_c and L_c in equation (2.11) by setting $a = 0$ in (5.14) and (5.15) (note that, by spherical symmetry, those values must be and are independent of ι).

Figure 5.4 shows both L_s and E_s as functions of r with parameters $\cos\iota = 0.4$ and $a = 0.99$. The following qualitative features are representative of all ι and a values and mimic the features of Schwarzschild. Both E_s and L_s have minima that occur at the same r. The minimum L_s, L_{isso}, corresponds to the

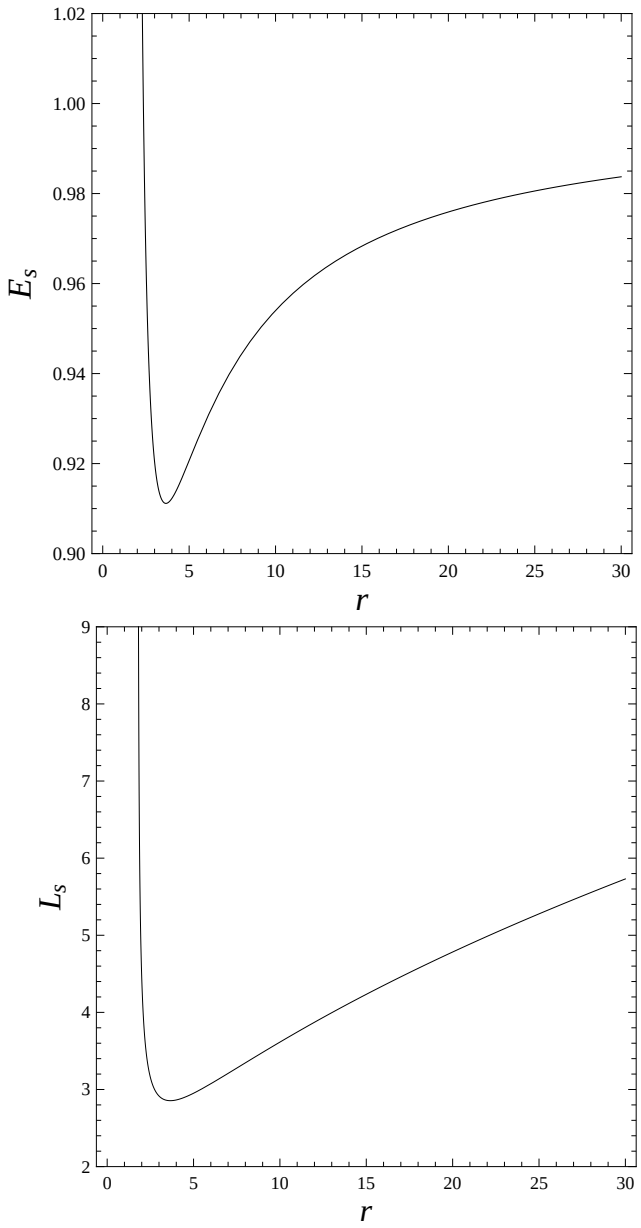

Figure 5.4: Top: The figure shows a plot of L_s vs r for spherical Kerr orbits with $a = 0.99$ and $\cos\iota = 0.4$. Bottom: Shows a plot of E_s vs r for spherical Kerr orbits with the $a = 0.99$ and $\cos\iota = 0.4$.

least L_s for which there exists a spherical orbit. The V_{eff} plot corresponding to $L = L_{\text{isso}}$ has a saddle point where the stable and unstable spherical orbits merge. For all $L > L_{\text{isso}}$ there are two spherical orbits, whose r-values exactly correspond to the local minimum and maximum of the effective potential plots of that L, ι and a. The maximum is the unstable spherical orbit and the minimum is the stable spherical orbit. There is a critical value $L_s = L_{\text{ibso}}$ at which the unstable spherical orbit has $E_s = 1$, and for all $L_s > L_{\text{ibso}}$, the unstable spherical orbit is unbound with $E_s > 1$. For a fixed ι and a, all the qualitative properties of the generic Kerr orbits replicate the Schwarzschild system.

The innermost bound spherical orbit, ibso, is defined as the spherical orbit with critical energy $E_{\text{ibso}} = 1$. To find the L_{ibso} and r_{ibso}, we set (5.9) and (5.12a) to zero with $E = 1$. The innermost stable spherical orbit, isso, is the minimum of the L_s plot and is subject to the further constraint $R''(r) = 0$. We therefore find the isso for a given ι and a by setting (5.9) and all two of equation (5.12) to zero simultaneously and solving for L_{isso}, r_{isso} and E_{isso}.

5.5 Conserved quantities revisited

Now that we have an effective potential formulation of the general Kerr system in terms of the conserved quantities E, L and ι that mimics the Schwarzschild system, we provide an explanation for our choice of conserved quantities framed in that effective potential picture.

Our goal was to realize a generic Kerr orbit structure that generalized the Schwarzschild and equatorial Kerr orbit structures presented in [37]. To bring that goal to fruition, we look for a set of conserved quantities such that we could hold one fixed and reproduce all the qualitative features of Schwarzschild dynamics (isso, ibso, etc.).

Using the conventional Q, L_z and E, the equatorial Kerr system is defined by $Q = 0$. There are two sets of L_z and E solutions for circular orbits, one prograde and one retrograde. Figure 2.10 shows the two solutions for $a = 0.995$ and $Q = 0$. We can see that the solutions never intersect and each solution has all the qualitative features present in the standard organization of Schwarzschild orbits.

However, when Q becomes large enough, regardless of the spin, we see a loss of adherence to these features. Specifically, there is no longer an isso, and the two sets of solutions for L_z and E for a fixed Q mix. While this

phenomenon is not seen until Q gets large, it is present for all spin values. The discontinuity in the L_z and E spherical graphs, as well as the loss of the isso is seen for the full range of a values.

The upshot is that there are values of Q that do not allow us to reproduce the familiar qualitative organization of Schwarzschild dynamics if we choose to look at orbits of constant Q as an ensemble. In contrast, we find that with (E, L, ι), for every fixed ι, the qualitative dynamical picture mimics the familiar Schwarzschild one beautifully. In this picture, each ι corresponds to a fixed orbital inclination so that equatorial orbits correspond to one of two ι values: $\iota = 0$ for prograde, and $\iota = \pi$ for retrograde. Furthermore, whereas each fixed Q admits two associated E and L_z solutions each for spherical orbits, each ι produces only one curve each for L_s and E_s.

Figure 5.5 shows a set of E and L_z plots for spherical orbits with $Q = 12.5$. We can see the loss of the isso and the mixing of the two separate solutions. The curves are no longer even single-valued at a given r. Moreover, the $E_s(r)$ curve can have more than 2 orbits with a given E, as opposed to only the stable and unstable constant r orbits we are used to in the Schwarzschild effective potential picture. We have picked four points on the fixed Q plots, each with a unique set of orbital parameters, E, L_z and Q. For each of those points, we have determined the corresponding E, L and ι and plotted the $E_s(r)$ and $L_s(r)$ curves for each of those ι values. Notice that there is no such breakdown when we look at curves of fixed ι rather than fixed Q. Instead, the latter curves faithfully reproduce the expected qualitative features of the corresponding Schwarzschild or equatorial Kerr curves.

Figure 5.6 shows that this breakdown occurs for all spins. Figure 5.7 shows the progression of the E and L for spherical orbits as inclination is increased from $\iota = 0$, prograde equatorial, to $\iota = \pi$, retrograde equatorial. Notice, as ι is increased there is no loss of *isso* and there are no discontinuities for the r values at which spherical orbits are allowed. Every fixed ι reproduces an orbital structure that is identical to the equatorial one. This conserved quantities choice therefore allows us to taxonomize the orbital space in the exact way we do for equatorial orbits.

5.6 Homoclinic and zoom-whirl orbits

Now that we have determined that each fixed ι qualitatively mimics the radial dynamics of the Schwarzschild system we explore the bound orbits to see

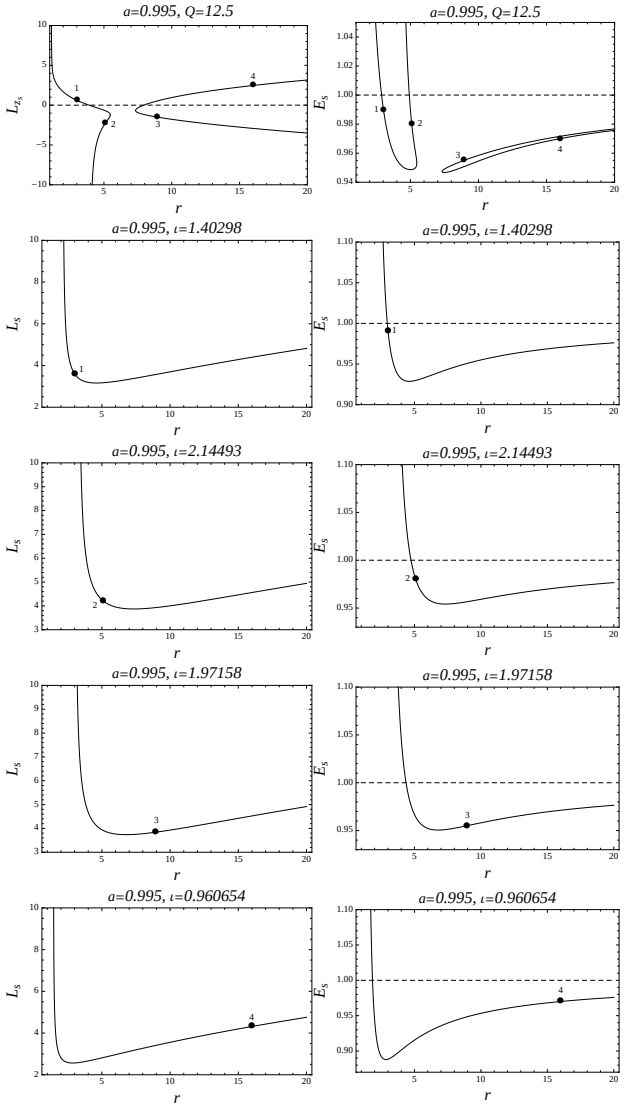

Figure 5.5: Top: Curves of L_{z_s} vs. r and E_s vs. r for spherical orbits all with fixed $Q = 12.5$. Below: Curves of $L_s(r)$ and $E_s(r)$ for spherical orbits with four different fixed ι values. Their parameter values are: (1) $E = 0.99$, $L_z = 0.598971$, $r = 3.01492$, $L = 3.58591$, $\iota = 1.40298$; (2) $E = 0.98$, $L_z = -2.28682$, $r = 5.09346$, $L = 4.21065$, $\iota = 2.14493$; (3) $E = 0.955$, $L_z = -1.49806$, $r = 8.92632$, $L = 3.83981$, $\iota = 1.97158$; (4) $E = 0.97$, $L_z = 2.47180$, $r = 15.9948$, $L = 4.31391$, $\iota = 0.960654$.

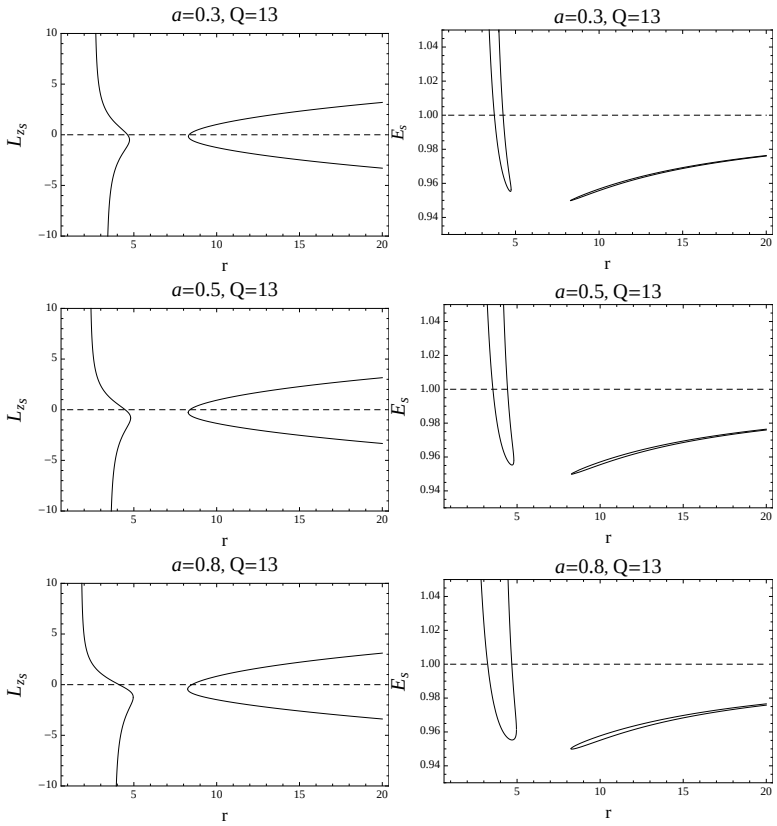

Figure 5.6: The above plots show the breakdown of the $Q = 0$ equatorial Kerr picture as Q increases. The left column shows L_z for spherical orbits and the right column show E for spherical orbits. $Q = 13$ in each plot, but the value of a increases. Top: $a = 0.3$. Middle: $a = 0.5$. Top: $a = 0.8$.

whether their features can be described analogously to how we describe those of Schwarzschild orbits.

As is the case in the Schwarzschild system, every unstable spherical orbit in the generic Kerr system is associated with a homoclinic orbit that marks the transition to plunge. Figure 5.8 shows one such orbit. Also as in the Schwarzschild system, homoclinic orbits can be thought of as the infinite whirl limit of the zoom-whirl class of orbits. Figure 5.9 shows a zoom-whirl orbit from 3 perspectives.

We will classify whirliness analogously to how we do in Chapter 2. We begin with defining the orbital frequencies. Every bound Kerr orbit has an

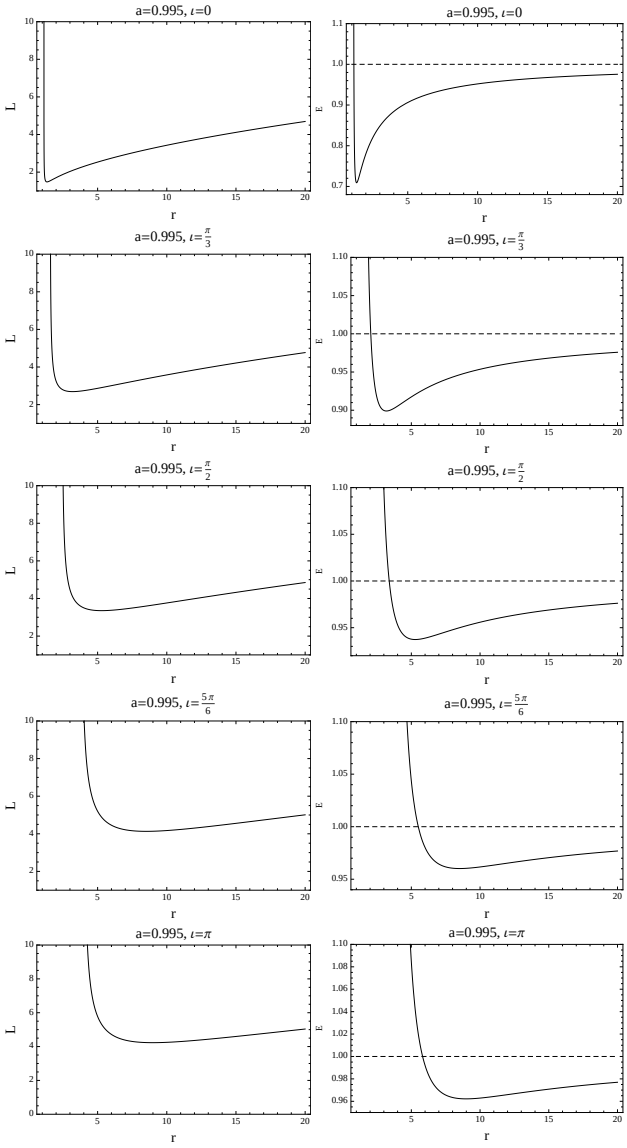

Figure 5.7: The above plots show the progression of the E and L plots for spherical orbits for a fixed $a = 0.995$ and a varying inclination, ι. Top: $\iota = 0$. Second: $\iota = \frac{\pi}{3}$. Third: $\iota = \frac{\pi}{2}$. Fourth: $\iota = \frac{5\pi}{6}$. Bottom: $\iota = \pi$.

associated triplet of fundamental frequencies $(\omega_r, \omega_\theta, \omega_\varphi)$, which can be defined for any choice of time coordinate [104]. The simplicity afforded by the choice of Mino time and exploited heavily in [96; 105] is that, since the radial and

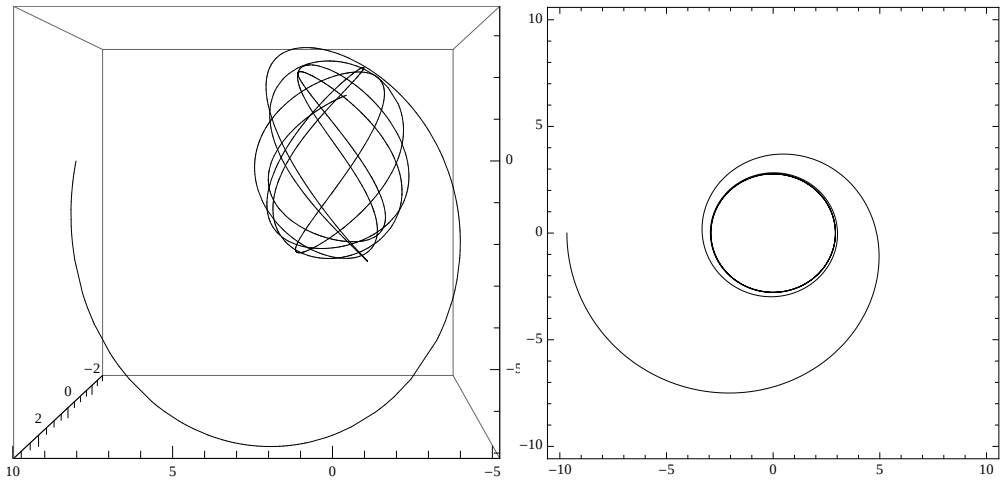

Figure 5.8: A homoclinic orbit associated with the unstable spherical orbit with $a = 0.99$ and orbital parameters $E = 0.935084$, $L = 3$ and $\cos\iota = 0.4$ Left: Shows the homoclinic orbit in 3D. Right: Shows the projection of the homoclinic orbit into the orbital plane.

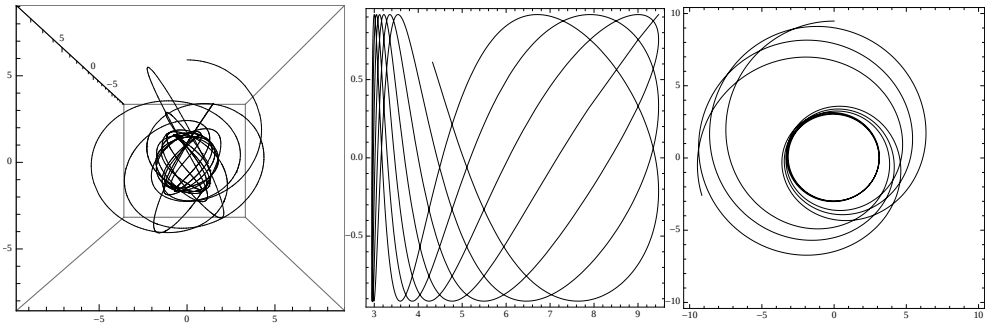

Figure 5.9: A zoom-whirl orbit, $q_{r\theta} = 2.09572\ldots$, with orbital parameters $a = 0.99$, $E = 0.9346$, $L = 3$ and $\cos\iota = 0.4$. Left: Shows the orbit in 3D. Middle: Shows the orbit projected into the $r - \theta$ axis. Right: Shows the orbit projected into the orbital plane.

polar motions decouple in Mino time, each of $r(\lambda)$ and $\theta(\lambda)$ is independently periodic. As a result, the Mino-time frequencies can be defined and computed directly from equations (5.3a) and (5.3b).

We will only be concerned with the radial and polar frequencies here. To obtain them, we first define the radial and polar Mino periods via

$$\Lambda_r = 2\int_{r_p}^{r_a} \frac{d\lambda}{dr} dr = 2\int_{r_p}^{r_a} \frac{dr}{\sqrt{R(r)}} \tag{5.16a}$$

$$\Lambda_\theta = 4\int_{\theta_{\min}}^{\pi/2} \frac{d\lambda}{d\theta} d\theta = 4\int_{\theta_{\min}}^{\pi/2} \frac{d\theta}{\sqrt{\Theta(\theta)}} \quad . \tag{5.16b}$$

The corresponding Mino-time frequencies are then

$$\omega_r \equiv \frac{2\pi}{\Lambda_r} \tag{5.17a}$$

$$\omega_\theta \equiv \frac{2\pi}{\Lambda_\theta} \quad . \tag{5.17b}$$

Note that we use Mino time purely for ease and convenience and that the frequency *ratios* which figure prominently in our analysis are independent of the choice of time variable.

We define $q_{r\theta}$ from the ratio of polar and radial frequencies as

$$q_{r\theta} \equiv \frac{\omega_\theta}{\omega_r} - 1 \quad . \tag{5.18}$$

In exact analogy to Schwarzschild, a generic orbit's $q_{r\theta}$ can be expressed as

$$q_{r\theta} = w + \delta \quad , \tag{5.19}$$

where w is the number of whirls and δ corresponds to the amount the apastron precesses in the orbital plane.

5.7 $r-\theta$ periodic orbits

We want to consider $3D$ orbits that are closed in $r-\theta$. That closure will result when the polar and radial frequencies are rationally related, or in language more directly useful for our orbital plane description of the motion, when the quantity $q_{r\theta}$ is rational. For $r-\theta$ periodic orbits, because $q_{r\theta}$ must be rational,

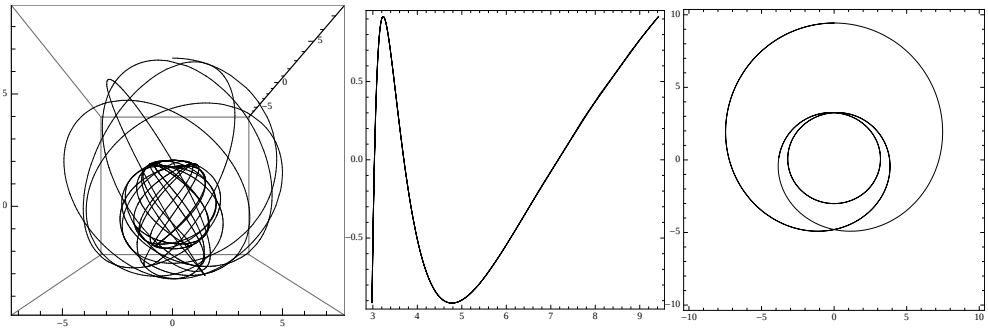

Figure 5.10: A periodic orbit with orbital parameters $a = 0.99$, $E = 0.934454$, $L = 3$ and $\cos\iota = 0.4$. Left: Shows the orbit in 3D. Middle: Shows the orbit projected into the $r-\theta$ axis. Right: Shows the orbit projected into the orbital plane.

the quantity δ in Equation (5.19) must be rational. We therefore express $q_{r\theta}$ for periodic orbits as the familiar

$$q_{r\theta} = w + \frac{v}{z} \quad , \tag{5.20}$$

where w, v and z measure the topological features of the $r-\theta$ periodic orbit projected into the orbital plane. Figure 5.10 shows an $r-\theta$ periodic orbit with a $q_{r\theta} = 2$ from 3 perspectives, 3D, $r-\theta$ projection and orbital plane.

To be useful, a classification based on orbits with rational $q_{r\theta}$ has to have two properties: the rational $q_{r\theta}$ must tell us about the topology of the orbit, and it must relate that topology to more physical conserved quantities. In the subsequent sections, we show that this is indeed the case.

5.8 The energy spectrum

In the spirit of the equatorial classification of [37], we now describe how $q_{r\theta}$ varies with energy. The result, for a given L, ι, is that $q_{r\theta}$ increases monotonically with energy. The lowest energy bound orbit is the stable spherical orbit, and, importantly, this orbit has the lowest value of $q_{r\theta}$ for that combination of L, ι. As detailed in Ref. [37] and reviewed in Chapter 2, the constant radius orbits do not have rational value zero, as can be proven by taking the zero eccentricity limit, $e \to 0$.

Since $q_{r\theta}$ is monotonic, its upper bound $q_{r\theta}^{\max}$ is the value of $q_{r\theta}$ for the maximum energy bound non-plunging orbit for a given L. Whether $q_{r\theta}^{\max}$ is

finite or infinite depends on whether L is greater than or less than $L_{\rm ibso}$. If $L > L_{\rm ibso}$, the unstable spherical orbit is unbound and has energy $E > 1$. $q_{r\theta}^{\rm max}$ is therefore the $q_{r\theta}$ value of the $E = 1$ orbit, and despite the fact that the $E = 1$ orbit just reaches $r = \infty$ after infinite time, its $q_{r\theta}$ is nonetheless finite. As we reduce L, $q_{r\theta}^{\rm max}$ increases monotonically, and eventually $q_{r\theta}^{\rm max} \to \infty$ once $L = L_{\rm ibso}$. For all $L < L_{\rm ibso}$, $q_{r\theta}^{\rm max}$ remains infinite [49; 50]. This happens because the maximum energy bound non-plunging orbit is now the homoclinic orbit (or separatrix orbit), which formally has an infinite number of whirls during its lone infinite-period radial cycle. A detailed analysis of the homoclinic orbit can be found in [49; 50].

Figure 5.11 is a plot of the $q_{r\theta}$ versus energy for a given a, ι and 3 sets of L values. It is representative of the general trend we see for any combination[4] of a, L, ι. As the energy increases, so does $q_{r\theta}$. As L decreases towards $L_{\rm isso}$, the minimum value of $q_{r\theta}$ increases. This trend was seen equatorially in Ref. [37].

In figure 5.11 we see that the $q_{r\theta}$ also increases with eccentricity, e. Again this is a general trend so that $q_{r\theta}$ is monotonic with eccentricity. The larger $q_{r\theta}$, again for a fixed (a, L, ι), the more eccentric the orbit.

We have shown that $q_{r\theta}$ corresponds to an energy spectrum for $3D$ orbits. What we want now is to show this also corresponds to a measure of zoom-whirliness and so is also a topological indicator. As we will see, quite incredibly, this $q_{r\theta}$ measures the amount by which the angle *in the orbital plane* overshoots 2π, that is, precesses, in one radial period. In other words, when $q_{r\theta}$ is rational, it is a direct measure of the topology of the orbit in the orbital plane and increases monotonically with energy, thereby defining a spectrum of zoom-whirl orbits in the orbital plane.

5.9 Periodic tables and the orbital plane

We preface this section with the caveat that the orbital plane construction below naively employs flat space vector algebra and vector calculus constructions (e.g. cross products of 3-vectors) without fully taking into account the curvature of the background Kerr spacetime. Prima facie, it is not obvious that the formalism should accurately capture geometric or topological features of 3D orbits. Nevertheless, we have the amazing result that the $r - \theta$ periodic orbits correspond to a spectrum of zoom-whirl orbits in this effective orbital

[4] The case of $\iota = 0, \pi$ needs to be handled as in Ref. [37] because that is motion that takes place entirely in the equatorial plane.

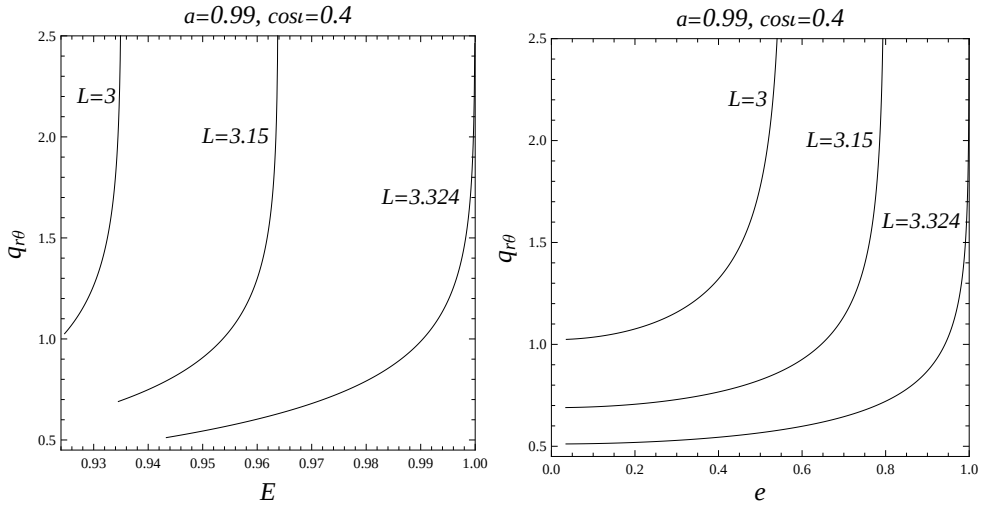

Figure 5.11: Top: The plot shows the monotonic relationship between $q_{r\theta}$ and energy for all bound orbits with a given a, L and $\cos\iota$. We show three different L values all with $a = 0.99$ and $\cos\iota = 0.4$. The graphs cut off on the left at the energy value for the stable spherical orbit with that a, ι and L. Bottom: The plot shows, for the above parameter values, the monotonic relationship between $q_{r\theta}$ and orbital eccentricity $e \equiv \frac{r_a - r_p}{r_a + r_p}$. The lower eccentricity bound is $e = 0$, also corresponding to the stable spherical orbits.

plane, beautifully mirroring the equatorial result of Ref. [37]. For now, we simply state our results, which are compelling, and report that a more precise analysis of the connection between the orbital plane construction and a relativistically precise projection of the motion is left for future work. A very precise implementation for the PN-expansion of two black holes is given in Chapters 3 and 4.

5.9.1 The orbital plane

We consider the projection of $r - \theta$ periodic orbits in an instantaneous orbital plane that we define naively as the plane in the tangent space spanned by $\vec{R}$ and $\vec{P}$, defined below, with a corresponding angular momentum $\vec{\mathcal{L}} = \vec{R} \times \vec{P}$. At every instant, the orbital plane is the plane perpendicular to the angular momentum vector.

It is useful to define

$$\rho = (r^2 + a^2)^{1/2} \tag{5.21}$$

and convert from ellipsoidal to Cartesian coordinates

$$\begin{aligned} x &= \rho \sin\theta \cos\varphi \\ y &= \rho \sin\theta \sin\varphi \\ z &= r \cos\theta \quad . \end{aligned} \tag{5.22}$$

Then,

$$\vec{\mathcal{L}} = \vec{R} \times \vec{P} \tag{5.23}$$

where

$$\begin{aligned} \vec{R} &= (x, y, z) \\ \vec{P} &= (P_x, P_y, P_z) \end{aligned}$$

for which

$$P^i = \frac{\partial x^i}{\partial q^j} g^{kj} P_k \tag{5.24}$$

where $i = x, y, z$ and $k, j = r, \theta, \varphi$. For convenience we take the $M \to 0$ limit [36],

$$\begin{aligned} ds^2 &= -dt^2 + \frac{(r^2 + a^2\cos^2\theta)}{(r^2 + a^2)} dr^2 \\ &\quad + (r^2 + a^2\cos^2\theta) d\theta^2 + (r^2 + a^2)\sin^2\theta d\varphi^2 \end{aligned} \tag{5.25}$$

so that

$$\begin{aligned} P_x &= \frac{r\rho}{\Sigma} \sin\theta\cos\varphi P_r + \frac{\rho}{\Sigma}\cos\theta\cos\varphi P_\theta - \frac{\sin\varphi}{\rho\sin\theta} P_\varphi \\ P_y &= \frac{r\rho}{\Sigma} \sin\theta\sin\varphi P_r + \frac{\rho}{\Sigma}\cos\theta\sin\varphi P_\theta + \frac{\cos\varphi}{\rho\sin\theta} P_\varphi \\ P_z &= \frac{\rho^2}{\Sigma}\cos\theta P_r - \frac{r}{\Sigma}\sin\theta P_\theta \quad . \end{aligned} \tag{5.26}$$

To find the orbital plane, we write

$$\begin{aligned} \vec{\mathcal{L}} &= \mathcal{L}_z \hat{k} + \mathcal{L}_\perp \hat{\perp} \\ \mathcal{L}_\perp \hat{\perp} &= \mathcal{L}_x \hat{i} + \mathcal{L}_y \hat{j} \end{aligned} \tag{5.27}$$

so that we can define

$$\begin{aligned}\hat{X} =& \hat{k} \times \hat{\perp} \\ \hat{Y} =& \hat{\mathcal{L}} \times \hat{X} \quad .\end{aligned} \tag{5.28}$$

The orbital plane is spanned by $\hat{X}, \hat{Y}$. (For a more detailed exposition on the orbital plane variables, see Ref. [45; 46].) This informally defined orbital plane is sufficient, as we will see, since it effectively soaks out any φ motion.

5.9.2 Periodic tables

Fig. 5.12 shows a table of orbits in the effective orbital plane. Our periodic table assembles orbits with rational $q_{r\theta}$ as an energy spectrum, with energy increasing from top to bottom and then from left to right. The topology of zoom-whirl orbits in the effective orbital plane is encoded in $q_{r\theta}$ through

$$q_{r\theta} = w + \frac{v}{z} \quad , \tag{5.29}$$

where w is the number of nearly circular whirls and v indicates the order in which the z zooms, or leaves, are traced out. So the $q_{r\theta} = 1 + 2/3$ orbit is a $(z = 3)$-leaf clover, that executes $w = 1$ whirls during each each radial cycle before it moves to the $v = 2$ leaf in the pattern.

This result is quite remarkable: $q_{r\theta}$ is a measure of the number of times the orbit returns to $\theta_{\rm min}$ per radial cycle, yet it gives topological information about the degree of precession in a very different angular variable, namely the angle swept out in the orbital plane. Had we instead projected the orbit onto the $r - \theta$ plane, the periodic orbits would look like Lissajous figures as in Fig. 5.13. The geometric information in Fig. 5.12 is severely obscured when the trajectories are plotted as Lissajous figures.

Fig. 5.1 shows trajectories with the same orbital parameters but different $r - \theta$ phasing. All orbits have the same E, L, ι and therefore the same $(r_a, r_p, \theta_{\rm max})$. However, r_a coincides with different initial values of θ in the range $\pi - \theta_{\rm max} < \theta_o < \theta_{\rm max}$ for each picture. Under shifts in $r - \theta$ phase, the $3D$ orbits are all rather different (illustrated in the first column) as are their corresponding Lissajous figures (illustrated in the second column). Notice, in stark contrast, that varying the initial phasing of r-vs.-θ merely corresponds to an overall rotation of the *very same* zoom-whirl orbit in the orbital plane (illustrated in the final column).

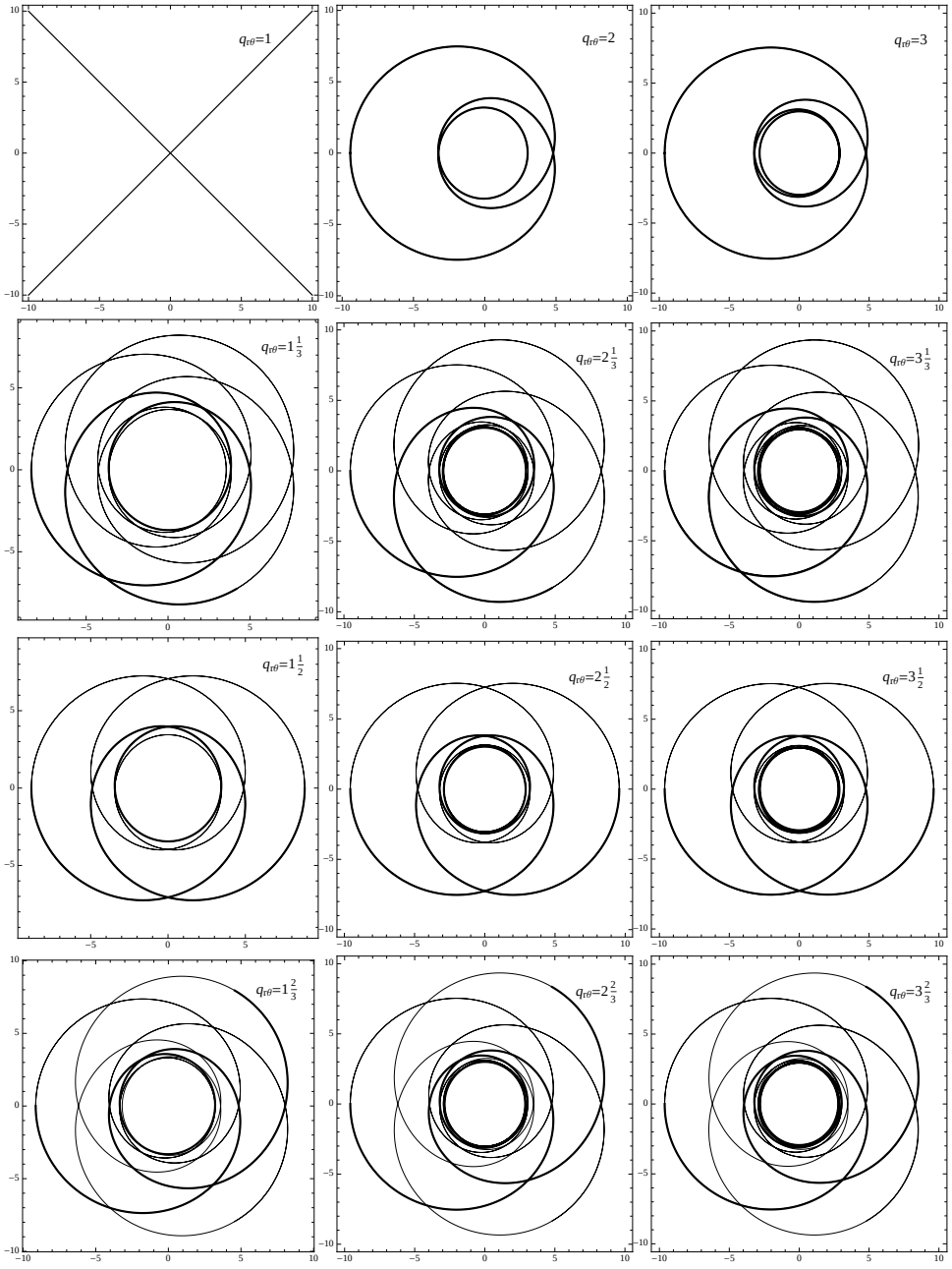

Figure 5.12: A periodic table for which the orbits have been projected into the orbital plane. All orbits were started at $r_0 = r_a$ and $\theta_0 = \theta_{\max}$. The orbital parameters are: $a = 0.99$, $L = 3$, $\cos\iota = 0.4$. The energy increases from top to bottom and left to right.

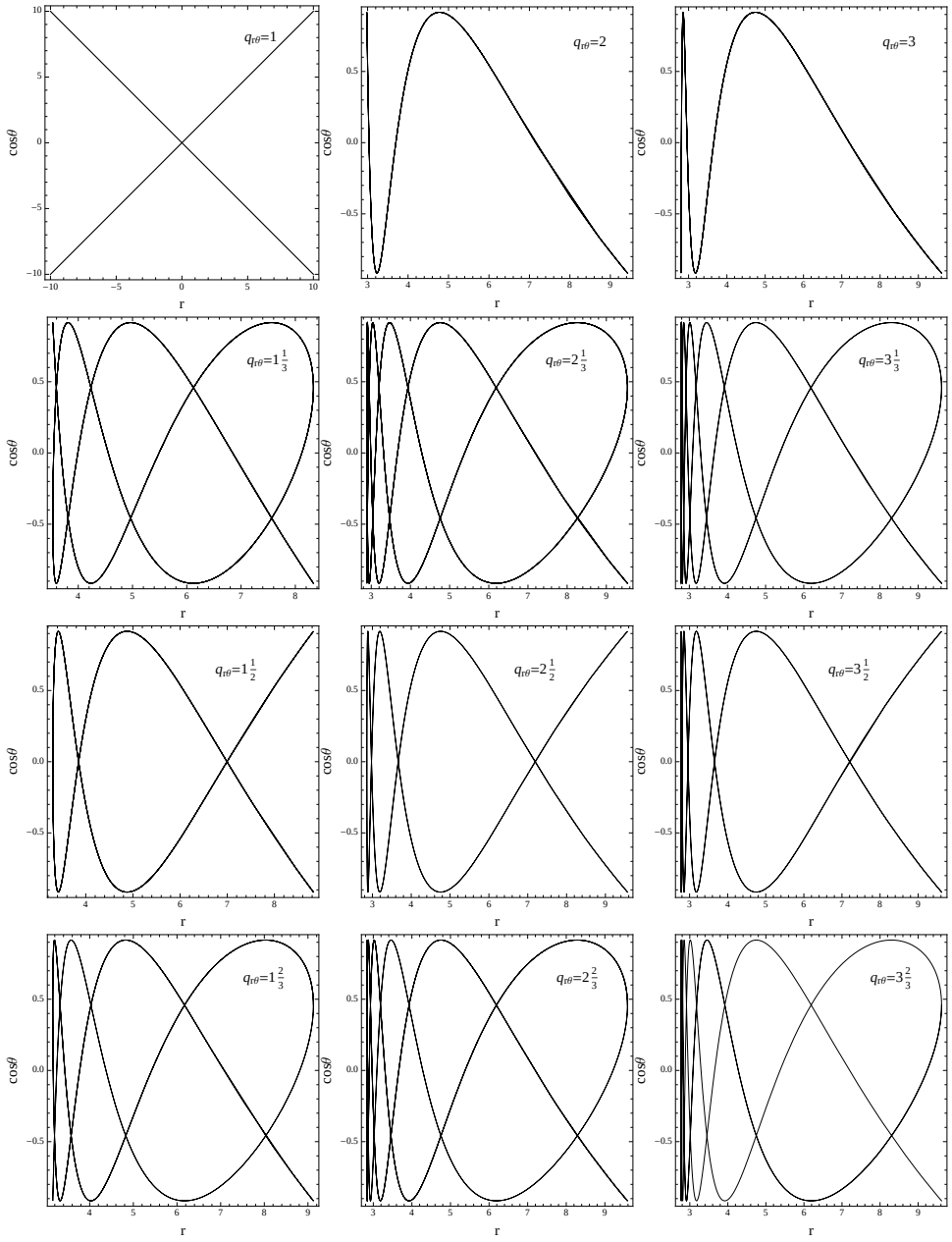

Figure 5.13: A periodic table for which the orbits have been projected into the r-$\cos\theta$ plane. All orbits were started at $r_0 = r_a$ and $\theta_0 = \theta_{\max}$. The orbital parameters are: $a = 0.99$, $L = 3$, $\cos\iota = 0.4$. The energy increases from top to bottom and left to right.

5.10 Summary of Kerr nonequatorial dynamics

Our results are neatly summarized in Figures 5.12 and 5.1. Fig. 5.12 illustrates that orbits periodic in $r-\theta$ assemble into a spectrum of multi-leaf clovers when projected in a loosely defined orbital plane. The topology of the orbit is encoded in a rational number $q_{r\theta} = \frac{\omega_\theta}{\omega_r} - 1$, from which one can immediately read off the number of leaves (or zooms), the ordering of the leaves, and the number of whirls. For a given L, ι, the rational number $q_{r\theta}$ monotonically increases with energy and with eccentricity. So, a simple 3-leaf clover ($q_{r\theta} = 1/3$) has less energy and is less eccentric than a 2-leaf ($q_{r\theta} = 1/2$) of the same L, ι. Significantly, the rational number $q_{r\theta}$ is bounded below so that there are no $q_{r\theta} \to 0$ orbits in the strong-field regime. *There are therefore no tightly precessing elliptical orbits* in the strong-field regime. All eccentric orbits will have a countable number of leaves.

Moreover, as Fig. 5.1 illustrates, a change in $r-\theta$ phase corresponds to a simple rotation of the orbit in the effective orbital plane. An orbit that hits apastron at $\theta_{\rm max}$ will be rotated by $\pi/2$ in the orbital plane relative to an orbit with identical (E, L, ι) that hits apastron at $\theta = \pi/2$.

Any aperiodic orbit will be arbitrarily well-approximated by a nearby periodic orbit. What's more, aperiodic orbits will look like precessions of low-leaf clovers. Just as Mercury is a precession of the ellipse, an orbit with $q_{r\theta} = 1/2+\epsilon$ is the precession of a 2-leaf clover that accumulates an extra $2\pi\epsilon$ of azimuth during each radial cycle. Our results therefore provide a complete taxonomy for generic Kerr orbits.

Chapter 6

Computational applications of periodic orbits

6.1 Introduction

Stellar mass compact objects inspiraling into supermassive black holes will be important astrophysical sources of gravitational waves (GWs) for future space-based detectors. Accurate GW templates for such extreme mass-ratio inspirals (EMRIs) require detailed knowledge of the motion of the source, so there has been a community effort to calculate EMRI trajectories. If we neglect the gravitational self-force of the small object, its orbit is a Kerr geodesic that, up to parameters specifying the initial position, is characterized by three constant orbital parameters: an energy E, an azimuthal angular momentum L_z, and the Carter constant Q. Determining the inspiral is tantamount to calculating how the self-force causes both the positional parameters and the orbital parameters to evolve in time.

Despite ongoing efforts, direct evaluation of the self-force in the Kerr case is still not possible. Accordingly, there have been parallel efforts to approximate its effects. The focus of this chapter is the adiabatic approximation, which captures the slow secular evolution of E, L_z, Q by solving a system of ordinary

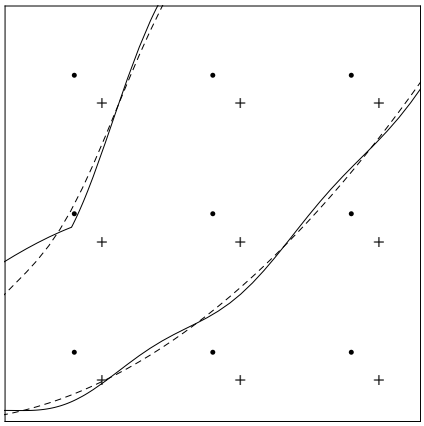

Figure 6.1: Above is a heuristic depiction of two possible numerical grids that could be used to generate adiabatic approximations (dashed curves) to true inspirals (solid curves) in the orbital parameter space. The dots represent a set of resonant grid points and the plus signs a set of non-resonant grid points. The resulting adiabatic curves are the same in either case but significantly less costly to produce with the resonant grid. A true inspiral may evolve in a way that is not well-approximated adiabatically as it approaches a low-order resonance, as on the left. That divergence, if it occurs, happens regardless of whether the resonant point is used as part of the numerical grid.

differential equations (ODEs) of the form

$$\frac{dE}{dt} = \mathcal{F}_E\left(E, L_z, Q\right) \tag{6.1a}$$

$$\frac{dL_z}{dt} = \mathcal{F}_{L_z}\left(E, L_z, Q\right) \tag{6.1b}$$

$$\frac{dQ}{dt} = \mathcal{F}_Q\left(E, L_z, Q\right) \quad . \tag{6.1c}$$

For now, it suffices to know that the righthand sides (RHSs) of equations (6.1) are so costly to evaluate that these equations will have to be integrated using a numerical grid. More specifically, the EL_zQ velocity field will be pre-computed only on a dense mesh of points in EL_zQ-space. Real-time integration of (6.1) will then rely on derivative values interpolated off of that grid.

In this chapter, we advocate building such grids using only points corresponding to resonant geodesics, for which the frequencies of the radial and polar motions are rationally related. As we will see, intermediate calculations

that comprise the bulk of the computational expense can be recycled among several Fourier modes on resonant grid points but must be recomputed for every mode in the non-resonant case. We estimate that, compared to using non-resonant grid points, our prescription could reduce the computational cost of an EMRI grid by an order of magnitude or more. The resonant-grid prescription will also facilitate faster computation of GW snapshots from geodesic sources.

We represent our proposal schematically in Figure 6.1. First, the RHSs of equations (6.1) are evaluated directly on a grid of either resonant points (dots) or non-resonant points (plus signs). At any other point, the RHS values can be interpolated from the values at the grid points. The adiabatic equations (6.1) are continuous and smooth, so regardless of which grid is used, integrating them produces the same adiabatic solutions (dashed curves). The only difference is that the resulting adiabatic curves cost significantly less to generate with the resonant grid.

Ref. [106] and more recently, Ref. [107] have noted that such adiabatic approximations may fail to capture important features of the true inspiral (solid curves) near low-order[1] resonances. Heuristically speaking, those authors argue that while an adiabatic solution may remain fairly faithful to an inspiral that steers clear of resonant points (lower right of the figure), those approximations may fare much worse for an inspiral that transits near a resonant point (middle left of the figure). To pre-empt possible confusion, we remark that there is no inconsistency between this observation and our proposal. The decision to include any particular EL_zQ point, resonant or not, in the numerical grid is unrelated to whether the resulting adiabatic curves will faithfully reflect EMRI motion near that same point. The ironic coincidence is that the points where the adiabatic approximation is most likely to fare poorly[2] are also the optimal grid points for generating adiabatic curves.

The rest of this chapter is organized as follows. In Section 6.2, we review some relevant features of resonant Kerr orbits in both physical space and phase space. In Section 6.3, we summarize how one arrives at the adiabatic equations of motion and clarify why an averaging prescription required to derive those equations must be a torus average rather than a time average, an issue that has raised some debate in the literature [106; 108; 109; 110; 111; 112].

[1] A resonance is low-order if the numerator and denominator of the rational frequency ratio are both small integers.

[2] To balance the argument, Ref. [106] also offers plausible reasons why the adiabatic approximation may still be valid near resonances.

Partly to help make the averaging argument and partly because we will focus on frequency-domain approaches to solving the adiabatic equations, Section 6.3 also provides some necessary mathematical background on Fourier analysis in both the non-resonant and resonant cases. With a clear view of the adiabatic program now in hand, Section 6.4 presents the main result of the chapter, namely a concrete prescription for computational savings that frequency-domain EMRI codes can leverage by using resonances. Finally, Section 6.5 speculates about how a more unorthodox use of resonances could offer additional efficiencies provided it can be practically implemented.

6.2 Resonant Kerr orbits

The paramount role of resonant orbits was the central theme of chapters 2-5. (We use the terms "resonant", "closed", and "periodic" interchangeably.) A spectrum of closed orbits, which manifests as a spectrum of multi-leaf clovers, entirely structures black hole dynamics. Although completely closed orbits must return to their initial values[3] of (r, θ, φ) simultaneously, only the r-θ periodicity detailed in Chapter 5 is relevant to this chapter. The rational number associated with the r-θ frequencies determines the multi-leaf clover geometry. What's more, that rational obediently stacks in energy monotonically: lower rationals correspond to lower energies than do higher rationals. Such orbits constitute a measure zero set but are nonetheless dense in the phase space. Every non-resonant orbit is arbitrarily close to some resonant orbit.

We first consider resonant orbits in *physical space* and then again in *phase space*. Since we will be concerned with functions that do not depend explicitly on either the azimuthal angle or on coordinate time, it will suffice for us to restrict attention to geodesic motion in two coordinates (r, θ) in physical space and to the projection of the motion into a $4D$ submanifold of the phase space spanned by (r, θ) and their conjugate momenta.

6.2.1 Resonant orbits in physical space

We begin by briefly reviewing the aspects of Chapter 5 that are relevant to this chapter.

The black hole is completely characterized by its mass M and spin a. The geodesic of the lighter companion is characterized by four dimensionless

[3] φ need only return to its initial position mod 2π.

constants μ, E, L_z, Q. In Boyer-Lindquist coordinates and dimensionless units, which is equivalent to setting $M = \mu = 1$, the radial and polar Kerr equations of motion can be written as

$$\dot{r} = \pm\sqrt{R(r)} \tag{6.2}$$
$$\dot{\theta} = \pm\sqrt{\Theta(\theta)} \quad , \tag{6.3}$$

where

$$\begin{aligned} R(r) \equiv & -\left(1-E^2\right) r^4 + 2r^3 \\ & -\left[a^2\left(1-E^2\right) + L_z^2\right] r^2 + 2\left(aE - L_z\right)^2 r - Q\Delta \end{aligned} \tag{6.4}$$

$$\Theta(\theta) \equiv Q - \cos^2(\theta)\left\{a^2\left(1-E^2\right) + \frac{L_z^2}{\sin^2\theta}\right\} \tag{6.5}$$

and

$$\Delta \equiv r^2 - 2r + a^2 \quad . \tag{6.6}$$

An overdot denotes differentiation with respect to Mino time [96], λ, related to proper time τ by

$$\frac{d\tau}{d\lambda} = \Sigma \equiv r^2 + a^2\cos^2\theta \quad . \tag{6.7}$$

The advantage of using Mino time is that the r and θ equations of motion decouple and that each is a function only of one coordinate. To make connections with observations, we will often care about how certain quantities evolve with respect to coordinate time t. However, coordinate time turns out to be mathematically cumbersome, so throughout this chapter, we perform all intermediate calculations related to such quantities by first changing variables to Mino time.

Solving equations (6.4) and (6.5) for the radial and polar turning points, we find that the radial coordinate varies between a periastron r_p and an apastron r_a and that the polar coordinate similarly varies between some minimum value θ_{min} and maximum value $\theta_{max} = \pi - \theta_{min}$. All turning points depend only on the constants E, L_z, Q. We introduce the simplifying notation

$$\vec{\mathcal{E}} \equiv (E, L_z, Q) \tag{6.8}$$

for those 3 orbital parameters and reserve the symbol $\mathcal{E}$ to refer to any one of E, L_z, Q individually.

The radial and polar coordinates are each periodic with respective Mino periods

$$\Lambda_r = 2\int_{r_p}^{r_a} \frac{dr}{\sqrt{R(r)}} \tag{6.9a}$$

$$\Lambda_\theta = 4\int_{\theta_{min}}^{\pi/2} \frac{d\theta}{\sqrt{\Theta(\theta)}} \tag{6.9b}$$

and corresponding frequencies

$$\Omega_r = \frac{2\pi}{\Lambda_r} \tag{6.10a}$$

$$\Omega_\theta = \frac{2\pi}{\Lambda_\theta} \quad . \tag{6.10b}$$

The radial and polar velocities are also periodic with the same corresponding periods and frequencies. If the frequency ratio

$$1 + q_{r\theta} \equiv \frac{\Omega_\theta}{\Omega_r} \tag{6.11}$$

is a rational number, an r-θ projection of the resulting orbit closes after a finite time.

Note from equations (6.4), (6.5) and (6.9) that the frequencies and $q_{r\theta}$ depend only on the constants $\vec{\mathcal{E}}$. $q_{r\theta}$ is also a topological invariant and thus coordinate independent. A $q_{r\theta}$ for which the relatively prime numerator and denominator are both low-valued integers will be referred to as "low-order". We arbitrarily call low-order resonant orbits those for which the numerator and denominator of $q_{r\theta}$ are each less than 10.

Projections of periodic orbits into the r-θ plane produce Lissajous figures. The top panel of Figure 6.2 shows the Lissajous figure of a periodic orbit with a low-order $q_{r\theta}$, while the bottom panel shows the analogous projection of a neighboring orbit with an irrational $q_{r\theta}$.

The figures produced by projecting into the r-θ plane are less topologically insightful than the figures in an orbital plane, loosely defined in the Kerr system as the plane perpendicular to the orbital angular momentum [47]. In the orbital plane, the rational $q_{r\theta}$ has powerful topological information and can be interpreted as $q_{r\theta} = w + v/z$, where the integer w represents the number of nearly circular whirls near periastron, the integer z is the number of elliptical

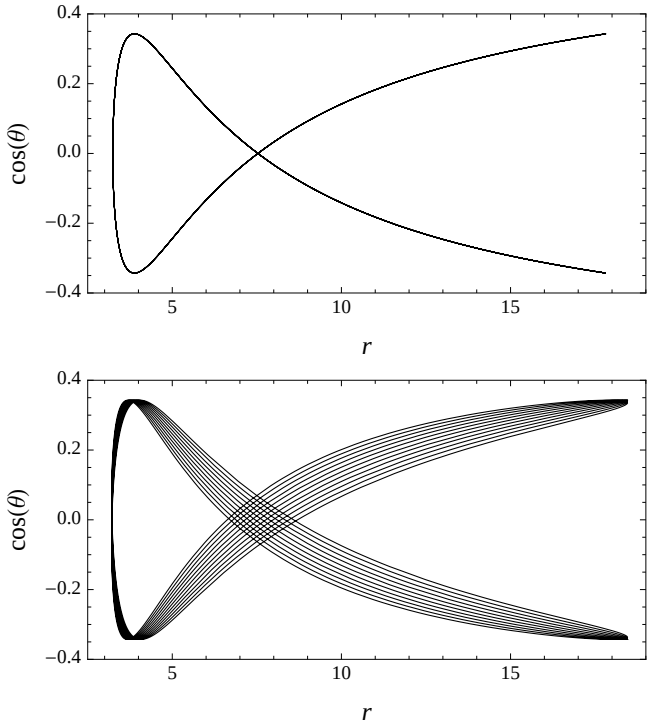

Figure 6.2: Top: A low-order periodic orbit with $q_{r\theta} = \frac{1}{2}$, $a = 0.9$, $E = 0.954788$, $L_z = 2.65115$ and $Q = 0.944969$, projected on the r-θ plane (we plot r-$\cos\theta$ to make the figure more viewable) with initial conditions $r_0 = r_a = 17.8148$ and $\theta_0 = \theta_{min} = 1.22079$. Bottom: A non-resonant orbit with $q_{r\theta} \approx \frac{125{,}857}{250{,}000}$, $a = 0.9$, $E = 0.956$, $L_z = 2.65115$ and $Q = 0.944969$, with initial conditions $r_0 = r_a = 18.4568$ and $\theta_0 = \theta_{min} = 1.22076$.

leaves in the multi-leaf clover pattern, and the integer v is the order in which the leaves are hit [37; 47]. To illustrate, the same two orbits of Figure 6.2 are plotted in the orbital plane in Figure 6.3. The orbit in the top panel of Figure 6.3 has $q_{r\theta} = 1/2$ and therefore corresponds to a 2-leaf clover, as is now evident. The bottom panel non-resonant orbit is close to a resonant orbit with $q_{r\theta} \approx \frac{125{,}857}{250{,}000}$ which would correspond to a $250,000$-leaf clover that skips $125,857$ leaves in the pattern each time. Notice that $\frac{125{,}857}{250{,}000} = \frac{1}{2} + \frac{857}{250{,}000}$ so that the orbit is really a tight precession of the 2-leaf clover through an angle of $\left(\frac{857}{250{,}000}\right) 2\pi \approx 0.02154$ radians per radial cycle.

While they do fix the turning points, the constants $\vec{\mathcal{E}}$ do not uniquely fix

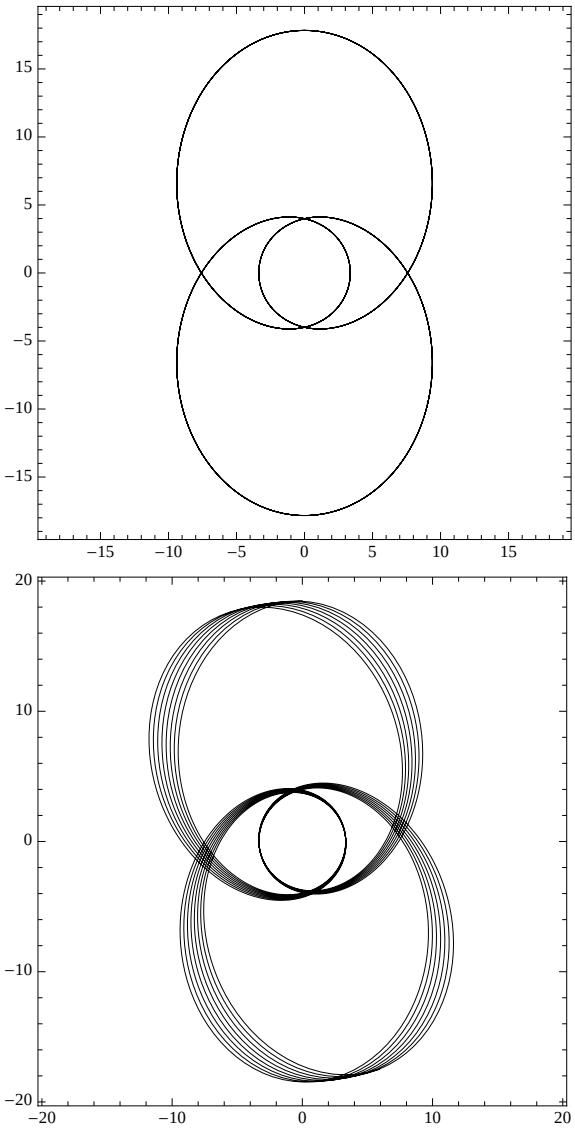

Figure 6.3: Top: The same orbits from Figure 6.2, projected into the orbital plane.

the orbit [113]. An orbit that hits apastron at θ_{min} is not identical to the orbit that hits apastron at a different value of θ, as shown in Fig. 6.4. Since $q_{r\theta}$ depends only on constants, a $q_{r\theta} = 1/2$ orbit is always a 2-leaf clover in the orbital plane [47]. However, orbits with different r-θ initial conditions (r_0, θ_0)

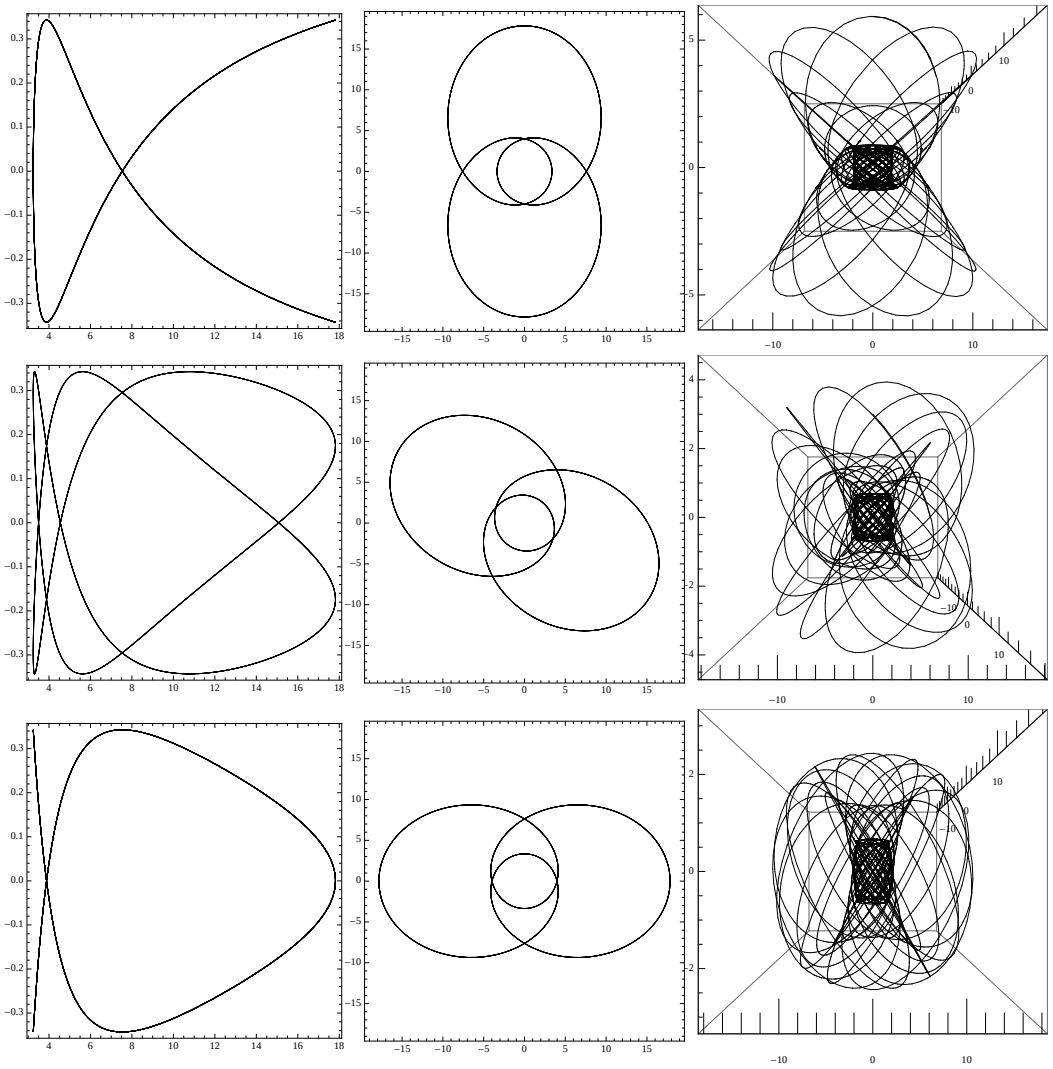

Figure 6.4: The above figures are all $q_{r\theta} = \frac{1}{2}$ orbits with $a = 0.9$ and orbital parameters $L_z = 2.65115$, $Q = 0.944969$ and $E = 0.954788$. The three figures in each row have the same initial coordinates. The column on the left shows an r-$\cos\theta$ projection of the orbit, the middle column is a projection in the orbital plane, and the right column is the $3D$ orbit. All three rows have $r_0 = r_a = 17.8148$. The first row has $\theta_0 = \theta_{min} = 1.22079$ and is the same orbit shown in the top panel of Figs. 6.2 and 6.3, the middle row has $\theta_0 = 1.39579$, and the bottom row has $\theta_0 = \frac{\pi}{2}$.

are rotated relative to each other in the orbital plane.

As Fig. 6.4 shows, the resulting orbits are genuinely distinct in 3D. Presumably, they could have distinct gravitational wave emissions. Interestingly, though, perihelion precession happens on a faster time scale than plane precession. It is therefore reasonable to suspect that all orbits with the same $q_{r\theta}$ generate similar waveforms and that the different plane precessions induce modest differences in the modulations of the amplitude [114]. We remain agnostic on the relative importance of r-θ initial values on the waveform generated and instead focus on efficient calculation of adiabatic inspirals.

6.2.2 Resonant orbits in phase space – phase space tori

In the 4D space spanned by $(r, p_r, \theta, p_\theta)$, all orbits (resonant or non-resonant) lie on 2D tori that can be constructed as the Cartesian product of two closed curves. We obtain one of those closed curves if we project an orbit into the r-p_r plane. The area of the curve is the familiar action J_r used in action-angle coordinates. Analogously, the projection of the same orbit into the θ-p_θ plane yields another closed curve with area J_θ. We now consider that pair of curves as a locus of points on a 2D surface with the topology of the 2-torus $\mathbb{S}^1 \times \mathbb{S}^1 \equiv \mathbb{T}^2$. Every set of orbital parameters $\vec{\mathcal{E}}$ defines one such torus that we denote $\mathbb{T}^2_{\vec{\mathcal{E}}}$.

The use of Mino time as an evolution parameter furnishes one (but certainly not the only) coordinate system for $\mathbb{T}^2_{\vec{\mathcal{E}}}$, according to the following construction. As already mentioned, the motions $r(\lambda)$ and $\theta(\lambda)$ are each individually periodic in Mino time, with periods Λ_r and Λ_θ (and frequencies Ω_r and Ω_θ), respectively. Scaling the evolution parameter λ on each of the r-p_r and θ-p_θ curves by Ω_r and Ω_θ, respectively, leads to a natural definition of angle variables $\chi_r \equiv \Omega_r \lambda$ and $\chi_\theta \equiv \Omega_\theta \lambda$. We choose a specific trajectory $(r(\lambda), p_r(\lambda), \theta(\lambda), p_\theta(\lambda))$ in order to assign χ_r and χ_θ values, respectively, along the r-p_r and θ-p_θ curves, but the trajectory is only a device that we discard once the torus coordinate system is in place. The points at 0 and 2π in each of χ_r, χ_θ are identified, so the torus can be represented as a 2π-by-2π square with opposite sides identified as in Fig. 6.5. We will make a simplifying choice that $(r_a, \theta_{\min})$ corresponds to the origin[4] of the torus. Then, a reflection in the line $\chi_r = \pi$ corresponds

[4]Many references, including [96; 100; 106; 108], instead tacitly choose the point $(r = r_p, p_r = 0, \theta = \theta_{\min}, p_\theta = 0)$ as the origin of the torus coordinates. We say "tacitly" because they refer to the individual orbit with those initial conditions as a fiducial geodesic to use in their analyses. Another interpretation of that choice is that they are working not with

to keeping r fixed and reversing the sign of p_r, and analogously for reflections in $\chi_\theta = \pi$. Note that each quadrant of the toroidal square therefore contains the same (r, θ) pairs but with all possible sign combinations for the momenta $(++, +-, -+, --)$.

Note that each χ_r corresponds to an ordered pair[5] (r, p_r) and each χ_θ corresponds to an ordered pair (θ, p_θ). We discuss alternative coordinate systems for $\mathbb{T}^2_{\vec{\mathcal{E}}}$ in Appendix C and elsewhere in this article but will use only the (χ_r, χ_θ) coordinates for calculations.

On the compact (χ_r, χ_θ) square defined above, geodesic trajectories are lines of slope $\Omega_\theta/\Omega_r = 1 + q_{r\theta}$. With respect to Mino time, those orbits are given parametrically by

$$\chi_r(\lambda) = \Omega_r \lambda + \chi_{r_0} \tag{6.12a}$$
$$\chi_\theta(\lambda) = \Omega_\theta \lambda + \chi_{\theta_0} \quad . \tag{6.12b}$$

Two different initial positions $\vec{\chi}_0$ and $\vec{\chi}'_o$ produce distinct orbits unless there exist real numbers x and y that simultaneously satisfy

$$\frac{y - \chi_{\theta_0}}{x - \chi_{r_0}} = \frac{\Omega_\theta}{\Omega_r} \quad , \tag{6.13}$$

and

$$\begin{aligned} \chi'_{r_0} &= x \bmod 2\pi \\ \chi'_{\theta_0} &= y \bmod 2\pi \quad . \end{aligned} \tag{6.14}$$

If these conditions are met, then the two different initial positions produce time-translated versions of the same orbit.

When Ω_θ/Ω_r is irrational, we will call both the torus and any orbits on that torus **non-resonant**. Orbits on non-resonant tori never close and instead sample the entire torus ergodically: an orbit starting from any initial condition will pass arbitrarily close to every point in the torus after some finite (but

one geodesic but with one *torus* and that they have instead chosen a fiducial origin for a χ_r-χ_θ coordinate system on that torus.

[5] Some references describe the mapping of functions of the form $F(r, \theta)$ to corresponding functions $F(\chi_r, \chi_\theta)$. In fact, no function that enters an adiabatic EMRI calculation depends on r and θ alone. The notation $F(r, \theta)$ in those references is used because, once restricted to a torus, the value of each coordinate determines its conjugate momentum up to a sign. Still, the values of those signs affect the value of the function. We believe a notation such as $F(r, p_r, \theta, p_\theta)$ for these pre-torus phase space functions is more appropriate.

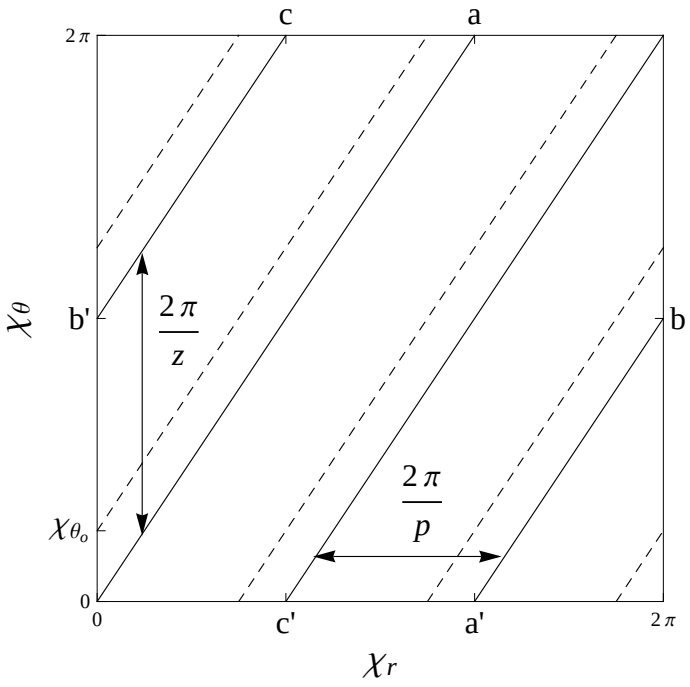

Figure 6.5: The above picture shows a resonant torus mapped to a square with the path of two resonant orbits traced out. The solid line shows the path of a resonant orbit with $\chi_{r_0} = \chi_{\theta_0} = 0$ and the orbit traced out by the dotted line has $\chi_{r_0} = 0$ and $\chi_{\theta_0} = 0.7894$. The resonant torus and both resonant orbits have $\frac{\Omega_\theta}{\Omega_r} = 1 + q_{r\theta} = \frac{p}{z} = \frac{3}{2}$.

possibly very long) time. Therefore, non-resonant orbits with different $\vec{\chi}_0 \equiv (\chi_{r_0}, \chi_{\theta_0})$ are arbitrarily close to time translations of every other non-resonant orbit with the same $\vec{\chi}_0$. We will alternately refer to such orbits as aperiodic or biperiodic.

When the frequency ratio Ω_θ/Ω_r is a rational number $\frac{p}{z}$, we will call both the underlying torus and orbits on that torus **resonant**. Orbits that live on resonant tori inherit the rational frequency ratio and thus always trace out closed curves. Since no single resonant orbit ergodically fills the torus, even after infinite time, two resonant orbits with the same $\vec{\mathcal{E}}$ but different $(\chi_{r_0}, \chi_{\theta_0})$ are not necessarily time translations of each other. *The set of all resonant orbits with the same* $\vec{\mathcal{E}}$ does fill the entire torus. Because they return to their initial conditions after a finite time, we will alternately refer to these orbits as periodic or singly periodic.

Figure 6.5 shows two resonant orbits on the resonant torus defined by $E = 0.954788$, $L_z = 2.65115$, $Q = 0.944969$. Each is thus a $q_{r\theta} = \frac{1}{2}$ orbit, or 2-leaf clover in the orbital plane. These are the same two orbits illustrated in physical space in the top two rows of Figure 6.4. The two orbits are distinguished by their initial position $\vec{\chi}_0$ on the torus. The solid line orbit, which starts at $\chi_{r_0} = 0$, $\chi_{\theta_0} = 0$, corresponds to the physical space orbit with initial conditions $r_0 = r_a = 17.81477$ and $\theta_0 = \theta_{\rm min} = 1.220793$. The dotted line orbit with initial conditions $\chi_{r_0} = 0$ and $\chi_{\theta_0} = 0.7854$ has physical space initial conditions of $r_0 = r_a = 17.81477$ and $\theta_0 = 1.39579$. Notice that any two adjacent line segments belonging to a single orbit are separated in χ_r by $\frac{2\pi}{p}$ and in χ_θ by $\frac{2\pi}{z}$ but are not traced out sequentially for general $\frac{p}{z}$.

In the same way that the rational numbers have zero measure on the line, the set of resonant tori has zero measure in the 4D phase space. To date, most of the literature on the adiabatic EMRI problem has ignored resonant geodesics precisely for this reason. Nevertheless, as we will see, the judicious exploitation of this measure zero set leads to significant computational efficiencies in adiabatic EMRI calculations.

6.3 Averaging in the adiabatic approximation

Given the background on geodesic dynamics, we now turn to the adiabatic approximation of EMRIs, an approximation that has seen substantial debate in the literature. As we elucidate below, most of that debate conflates the question of what kind of averaging procedure to use in the equations of motion (6.1) with other related but logically independent questions about the adiabatic approximation. In this section, we clarify why phase space averaging (as opposed to time averaging) is the correct averaging procedure. We also establish the results we will need in Section 6.4 to exploit resonant orbits for computational savings.

6.3.1 The adiabatic equations of motion

Let $\vec{X}$ denote the Boyer-Lindquist coordinates of the inspiraling object along with its canonical radial and polar momenta. In the absence of radiation

reaction, the equations of motion are

$$\frac{d\vec{X}}{dt} = \vec{G}(\vec{X}, \vec{\mathcal{E}}) \tag{6.15a}$$

$$\frac{d\vec{\mathcal{E}}}{dt} = 0 \quad , \tag{6.15b}$$

where the RHSs $\vec{G}$ of the positional equations are some form of the equations for geodesic motion, e.g. Hamilton's equations for free-particle Kerr motion. Radiation reaction adds to the RHSs new functions

$$\frac{d\vec{X}}{dt} = \vec{G}(\vec{X}, \vec{\mathcal{E}}) + \vec{F}(\vec{X}, \vec{\mathcal{E}}) \tag{6.16a}$$

$$\frac{d\vec{\mathcal{E}}}{dt} = 0 + \vec{f}(\vec{X}, \vec{\mathcal{E}}) \tag{6.16b}$$

that are determined by the full gravitational self-force on the particle. Those unknown functions can be expanded in a perturbation series in powers of a natural small parameter: the system's mass ratio $\varepsilon \equiv \mu/M \ll 1$. Furthermore, at each order in ε, the functions above decompose into a sum of dissipative and conservative pieces:

$$\begin{aligned} \vec{F} &= \varepsilon \left[\vec{F}^{(1)}_{\text{diss}} + \vec{F}^{(1)}_{\text{cons}} \right] \\ &\quad + \varepsilon^2 \left[\vec{F}^{(2)}_{\text{diss}} + \vec{F}^{(2)}_{\text{cons}} \right] + \mathcal{O}\left(\varepsilon^3\right) \end{aligned} \tag{6.17a}$$

$$\vec{f} = \varepsilon \left[\vec{f}^{(1)}_{\text{diss}} + \vec{f}^{(1)}_{\text{cons}} \right] + \varepsilon^2 \left[\vec{f}^{(2)}_{\text{diss}} + \vec{f}^{(2)}_{\text{cons}} \right] + \mathcal{O}\left(\varepsilon^3\right) \quad . \tag{6.17b}$$

See [112] and references therein for a fuller account.

We expect a natural separation of timescales in this system. The "fast" positional variables $\vec{X}$ will change substantially on a short timescale equal to an orbital period $T_{\text{orb}} \sim M$, while the "slow" orbital parameters $\vec{\mathcal{E}}$ only change substantially on the much longer timescale $T_{\text{rad}} \sim M/\varepsilon$. Due to the coupling of the $\vec{X}$ and $\vec{\mathcal{E}}$ equations, both $\vec{X}(t)$ and $\vec{\mathcal{E}}(t)$ should exhibit oscillations around a secularly trending central value, but the oscillations in $\vec{\mathcal{E}}$ should be $\mathcal{O}(\varepsilon)$. In such a system, a first-order averaging procedure seeks an approximate and hopefully more tractable set of equations for the slow variables from which the dependence on the fast variables (and thus the source of the small oscillations) is removed [115; 116; 117].

Averaging must therefore decouple the $\vec{\mathcal{E}}$ equations from the $\vec{X}$ equations in (6.16) in order to isolate the secular trend in the former.[6] One can even adopt the point of view that the desideratum of a preliminary averaging procedure is to decouple the equations for the slow and the fast variables from each other as much as possible. We represent those averaged, decoupled equations for the orbital parameters (equivalent to equation (6.1)) as

$$\begin{aligned} \frac{d\vec{\mathcal{E}}_{\text{secular}}}{dt} &= \left\langle \frac{d\vec{\mathcal{E}}}{dt} \right\rangle \\ &= \left\langle \vec{f}\left(\vec{X}, \vec{\mathcal{E}}\right) \right\rangle \\ &= \vec{\mathcal{F}}\left(\vec{\mathcal{E}}\right) \quad . \end{aligned} \tag{6.18}$$

Throughout this chapter, we will represent averages of all sorts with angle brackets $\langle\rangle$ and use subscripts on the brackets to denote the type of average implied. Note that in (6.18), we have used $\langle\cdots\rangle$ to denote an average without yet specifying which variables that average is to be taken over.

6.3.2 Flux balance and its relationship to averaging

Although we now have the general form of the adiabatic equations, we cannot write them explicitly because we still do not know how to evaluate the self-force. Mino showed [96; 106] that, under the assumption of non-resonance, the infinite time-averaged values[7] of the functions $\mathcal{F}_E$ and $\mathcal{F}_{L_z}$ equal the sum of the infinite time-averaged fluxes of the corresponding orbital parameters at radial infinity and the central black hole horizon in GWs emitted by the system[8]. While there is no conserved Q-current to associate with a GW Q-flux, Mino likewise showed that there are analogous infinite time-averaged quantities at infinity and the horizon that sum to the infinite time-averaged value of $\mathcal{F}_Q$. Though not strictly physically accurate, we will henceforth refer to those quantities as fluxes of Q for ease. Subsequent work [108; 118; 119] has led to explicit formulae for these Q-fluxes.

[6] Note that the converse is not possible, since the fast variables are coupled to the slow ones at zeroth order, where the slow variables appear as constant parameters.

[7] The quantities of physical interest are averages over coordinate time t.

[8] Mino's proof suggests that this equivalence is only true for non-resonant geodesics and possibly a small subset of resonant geodesics.

Fortunately, we do know how to calculate the aforementioned time-averaged fluxes at infinity and the horizon via the computationally mature Teukolsky formalism. Various Teukolsky-based (TB) codes can compute the required fluxes from equatorial orbits [120], spherical orbits[9] (constant r) [99], and now generic orbits of arbitrary inclination and eccentricity [100; 118; 121].

These developments have led to the following two-stage implementation of the adiabatic approximation. The first stage, usually called the radiative approximation[10], keeps only the lowest-order contributions from the dissipative self-force (since the conservative contributions will average to zero). The second stage, called the flux-balance method, uses the time-averaged *nonlocal* fluxes (computable) as proxies for the averaged *local* contributions of the dissipative self-force (not currently computable). The RHSs of equation (6.18) end up with nonlocal fluxes inside the brackets and an interpretation of those brackets as infinite time-averages.

There is a problem, however, with this prescription, which intertwines two logically distinct facets of the adiabatic approximation to EMRIs:

1. Is it mathematically appropriate to interpret the angle brackets in equation (6.18) as a time-average, or is some other sort of average required?

2. Given the answer to 1, can we evaluate the RHS of (6.18), either directly or by finding a numerically equivalent proxy?

After all, the fact that we *can* compute a time-averaged proxy does not imply that we *should* be time averaging in the first place.

The form of equation (6.18) suggests two ways to average the RHS in order to remove the dependence on the positional variables: for fixed $\vec{\mathcal{E}}$, we can either phase space average over the torus, or we can evaluate the RHS along a specific orbit on that torus and then average over time. In Section 6.3.5, we offer a definitive argument in favor of torus averaging instead of time averaging.

[9] Many authors refer to orbits of constant radial coordinate r as "circular" even when they are nonequatorial. We prefer the term "spherical" for such orbits (as used in [103]) and reserve the term circular for constant r equatorial orbits.

[10] There is some dispute about whether the neglected secular effects of the averaged conservative piece of the self-force manifest themselves at the same order in the small expansion parameter μ/M as the dissipative pieces [109; 110; 111; 112]. That dispute does not concern us here. Whatever its limitations, the radiative approximation, is here to stay for at least the foreseeable future, if for no other reason than that it is the only relativistically correct approximation to the inspiral motion accessible to numerical calculation in the status quo.

To arrive at that conclusion, we must first distinguish between torus functions and time functions. Torus functions assign a value to every point on a phase space torus, while time functions assign a value to points along an individual orbit that are labeled by the value of an evolution parameter (i.e. a time variable). Our conclusions about adiabatic averaging will be based on differences in how Fourier analysis is done on these two domains — a 2-dimensional compact position space for the torus-functions and a 1-dimensional noncompact time axis for the time-functions. Moreover, numerically accurate flux calculations require frequency-domain TB codes that separately compute fluxes from individual Fourier modes, and the aforementioned different domains also impact the details of the modewise flux calculation.

Before delving into those details, we must mention an important point. Average values, whether in the torus or time sense, are coordinate dependent, and in certain applications it matters which coordinates the average is taken over. The angle brackets in equation (6.18), for instance, will turn out to denote a torus average not over $\vec{\chi}$ but over a different set of torus coordinates $\vec{\gamma} \equiv (\gamma_r, \gamma_\theta)$ described in Appendix C. However, torus averages with respect to $\vec{\chi}$ are much easier to compute than those over $\vec{\gamma}$, in much the same way as Mino time averages are easier to compute than are coordinate time averages. Luckily, for every torus function $U(\vec{\gamma})$ and every time function $u(t)$, we can always construct different functions $V(\vec{\chi})$ and $v(\lambda)$ such that

$$\langle U \rangle_{\vec{\gamma}} = \langle V \rangle_{\vec{\chi}} \tag{6.19}$$

$$\langle u \rangle_t = \langle v \rangle_\lambda \quad . \tag{6.20}$$

The relationship between U and V (or between u and v) is highlighted in Appendix C.1. Sections 6.3.3 and 6.3.4 present the necessary Fourier analysis details.

We will always avail ourselves of the simplification in equation (6.19). Accordingly, throughout the rest of the chapter, we focus exclusively on torus averages over $\vec{\chi}$ and time averages over Mino time λ with the understanding that they may merely be computation-friendly proxies for averages of different but related functions over different torus or time coordinates.

6.3.3 Torus averaging and Fourier analysis of torus-functions

We will call a **torus function** $f(\vec{\chi};\vec{\mathcal{E}})$ any rule that assigns a complex number to every point on a phase space torus. Note that $\vec{\mathcal{E}}$ specifies both the torus function and the phase-space torus that serves as its domain. Usually, we will be discussing properties of torus functions evaluated at some definite value of $\vec{\mathcal{E}}$. We thus omit the explicit dependence on the orbital parameters $\vec{\mathcal{E}}$ for brevity, except where it might lead to confusion.

We assume that every such torus-function is continuous and differentiable in all its arguments (including $\vec{\mathcal{E}}$). We also require it to be single-valued on the torus, which implies 2π periodicity in each of the angle variables:

$$f(\chi_r,\chi_\theta) = f(\chi_r+2\pi,\chi_\theta) = f(\chi_r,\chi_\theta+2\pi) \quad . \tag{6.21}$$

Like any function that is independently periodic in two independent variables, a torus-function has a double Fourier series representation

$$f(\vec{\chi}) = \sum_{k,n} A_{kn} e^{-in\chi_r} e^{-ik\chi_\theta} \tag{6.22}$$

with the A_{kn}'s given as usual by

$$A_{kn} = \frac{1}{(2\pi)^2}\int_0^{2\pi} d\chi_r \int_0^{2\pi} d\chi_\theta\, f(\chi_r,\chi_\theta) e^{+in\chi_r} e^{+ik\chi_\theta} \quad . \tag{6.23}$$

In order to distinguish them from another set of double-indexed quantities we introduce later, we will refer to the A_{kn}'s as **spatial Fourier coefficients** or **torus Fourier coefficients**.

We now define, in the usual way, the following useful quantities. The **torus average of** f is

$$\begin{aligned} \langle f(\vec{\chi})\rangle_{\vec{\chi}} &\equiv \frac{1}{(2\pi)^2}\int_0^{2\pi} d\chi_r \int_0^{2\pi} d\chi_\theta\, f(\chi_r,\chi_\theta) \\ &= A_{00} \quad . \end{aligned} \tag{6.24}$$

The **torus averaged Fourier power of** f is

$$\mathcal{P}_{\vec{\chi}} \equiv \frac{1}{(2\pi)^2}\int_0^{2\pi} d\chi_r \int_0^{2\pi} d\chi_\theta |f(\chi_r,\chi_\theta)|^2 \quad . \tag{6.25}$$

By Parseval's theorem, the torus-averaged power must also equal

$$\mathcal{P}_{\vec{\chi}} = \sum_{k,n} |A_{kn}|^2 \quad . \tag{6.26}$$

The **2D power spectrum of** f is the contribution to the torus-averaged Fourier power from each pair of spatial frequencies or wavenumbers $(\kappa_r, \kappa_\theta)$. Note that because the period in each of the χ_r and χ_θ directions is 2π, the corresponding fundamental spatial frequencies are $\kappa_r = \kappa_\theta = 1$, so we see power only at integer lattice points (k, n) in the 2D wavenumber space.

All statements above are standard results from the Fourier analysis of functions on a compact 2D spatial domain. They apply equally well on resonant and non-resonant tori.

6.3.4 Time averaging and Fourier analysis of time-functions

We can evaluate any torus function along a curve (6.12) on its associated torus that corresponds to an orbit. Since each orbit is specified by its initial position $\vec{\chi}_0$ on the torus, each torus function naturally induces a 2-parameter family of time functions, one for each $(\chi_{r_0}, \chi_{\theta_0})$ pair. Time functions, then, are grouped into 5-parameter families – 3 parameters $\vec{\mathcal{E}}$ to specify a torus, and 2 parameters $\vec{\chi}_0$ to specify an orbit on that torus.

We denote one member of such a family as $f\left(\vec{\chi}(\lambda); \vec{\chi}_0; \vec{\mathcal{E}}\right)$. We will sometimes omit the explicit $\vec{\chi}_0$ and $\vec{\mathcal{E}}$-dependence of a time function and simply write $f(\lambda)$, again except where clarity would suffer. Throughout this chapter, we adopt the notational convention that a time function and the torus function from which it is derived are denoted by the same symbol (f, in the examples so far).

For time functions, non-resonant and resonant tori must be treated separately.

Non-resonant tori

When Ω_θ/Ω_r is irrational, every k, n pair leads to a distinct frequency

$$\Omega_{kn} \equiv n\Omega_r + k\Omega_\theta \,, \qquad k, n \in \mathbb{Z} \quad . \tag{6.27}$$

Such a biperiodic time-function is not periodic: it is bounded on $(-\infty, \infty)$, but there is no finite time interval over which the function exactly repeats itself. Still, every biperiodic function has a unique discrete Fourier representation [122]

$$f(\lambda; \vec{\chi}_0) = \sum_{k,n} A_{kn;\lambda} e^{-i(n\Omega_r + k\Omega_\theta)\lambda} \quad . \tag{6.28}$$

Note that the harmonics are *not* equally spaced in frequency. The temporal Fourier coefficients $A_{nk;\lambda}$ (which we have named suggestively) are given by the limit

$$A_{kn;\lambda} = \lim_{\Lambda\to\infty} \frac{1}{\Lambda} \int_{b-\Lambda/2}^{b+\Lambda/2} d\lambda\, f(\lambda; \vec{\chi}_0) e^{i(n\Omega_r + k\Omega_\theta)\lambda} \quad , \tag{6.29}$$

which exists and is independent of b [122] (henceforth, we set $b = 0$ for convenience). Equivalently, we could say that the Fourier transform of $f(\lambda; \vec{\chi}_0)$ consists of a series

$$\widetilde{f}(\Omega) = \sum_{k,n} A_{kn;\lambda}\, \delta\left(\Omega - (n\Omega_r + k\Omega_\theta)\right) \tag{6.30}$$

of delta-function impulses unequally spaced in frequency.

Paralleling the Fourier discussion of torus functions, we now define the time-averaged value, time-averaged Fourier power, and the 1D power spectrum of a time function associated with a non-resonant orbit. Biperiodic functions offer no single period over which to time-average in a natural way. Given the existence[11] of expressions like (6.29), averaging over all time seems like a sensible choice. The theory of almost-periodic functions states that such an infinite time-average indeed exists [123], so we define

$$\langle f(\lambda; \vec{\chi}_0)\rangle_\lambda = \lim_{\Lambda\to\infty} \frac{1}{\Lambda} \int_{-\infty}^{\infty} d\lambda\, f(\lambda; \vec{\chi}_0) \quad . \tag{6.31}$$

[11] Technically, the logical presentation of Fourier coefficients and time-averages for biperiodic (or more general multiperiodic) functions goes in the reverse order. First, the existence of the infinite time-average in (6.29) is established for a biperiodic function $f(\lambda)$. The existence of the Fourier coefficients in (6.29) then follows from the existence of the average value and the fact that $f(\lambda)e^{i(n\Omega_r + k\Omega_\theta)\lambda}$ is also biperiodic. We have chosen this order to parallel the presentations in Sections 6.3.3 and 6.3.4.

We will refer to $\langle f \rangle_\lambda$ simply as *the* time-average of f rather than as the infinite time-average value, as it is sometimes called. Comparing equations (6.29) and (6.31), the time-average equals

$$\langle f(\lambda; \vec{\chi}_0) \rangle_\lambda \equiv A_{00;\lambda} \quad . \tag{6.32}$$

We define the time-averaged Fourier power of $f(\lambda)$ as a special case of (6.31) by

$$\mathcal{P}_\lambda \equiv \lim_{\Lambda \to \infty} \frac{1}{\Lambda} \int_{-\frac{\Lambda}{2}}^{\frac{\Lambda}{2}} d\lambda |f(\lambda; \vec{\chi}_0)|^2 \quad . \tag{6.33}$$

Parseval's theorem also applies to biperiodic time-functions [123], so

$$\mathcal{P}_\lambda = \sum_{k,n} |A_{kn;\lambda}|^2 \quad . \tag{6.34}$$

That fact allows us to define a 1D power spectrum for $f(\lambda)$ as the contribution to the time-averaged power from each temporal frequency Ω. The graph of $|A_{kn;\lambda}|^2$ over the 1D Ω-space would show power only at the discrete and unequally spaced set of frequencies (6.27).

The question now is how to evaluate these time averages in practice. Though equation (6.29) defines the $A_{kn;\lambda}$'s, such integrals over infinite intervals divided by infinite quantities do not lend themselves to simple evaluation, either analytically or numerically[12].

To compute the temporal Fourier coefficients of $f(\lambda; \vec{\chi}_0)$, we must instead proceed circuitously. Consider the spatial Fourier representation (6.22) of the torus-function $f(\vec{\chi})$ evaluated along the orbit (6.12), which yields

$$f(\lambda; \chi_{r_0}, \chi_{\theta_0}) = \sum_{k,n} A_{kn} e^{-in\chi_{r_0} + k\chi_{\theta_0}} e^{-i(n\Omega_r + k\Omega_\theta)\lambda} \quad . \tag{6.35}$$

[12]To evaluate equation (6.29) numerically, larger and larger values of Λ would be required before converging to some accuracy. This is computationally impractical because such a process will in general converge extremely slowly. Thus, as the size of the integration interval grows, so will the required number of evaluations of the integrand, a particularly problematic development if the integrand is expensive to calculate. Moreover, the prefactor of $1/\Lambda$ can eventually become so small that there is loss of significance in the final answer, thus compromising accuracy.

By uniqueness[13] of the Fourier representation of $f(\lambda;\vec{\chi}_0)$, and comparing equations (6.28) and (6.35), we conclude that the temporal Fourier coefficients of $f(\lambda;\vec{\chi}_0)$ and the spatial Fourier coefficients of $f(\vec{\chi})$ are related[14] by

$$A_{kn;\lambda} \equiv A_{kn} e^{-in\chi_{r_0}+k\chi_{\theta_0}} \quad . \tag{6.36}$$

We note that each temporal coefficient differs from the corresponding spatial coefficient in (6.23) only by a complex phase determined by the initial conditions $\vec{\chi}_0$ of the orbit. Consequently, their magnitudes are identical, regardless of the initial position of the orbit:

$$|A_{kn};\lambda| = |A_{kn}| \ , \quad \forall\vec{\chi}_0 \in \mathbb{T}^2_{EL_zQ} \quad . \tag{6.37}$$

This fact is consistent with the ergodic property of these orbits. Every orbit eventually comes arbitrarily close to every point on the torus, so shifting initial conditions leads to a new orbit that is arbitrarily close to a time translation of the original orbit. And, of course, time translations only affect the complex phase of temporal Fourier coefficients.

If we know the torus function $f(\vec{\chi})$, its spatial Fourier coefficients A_{kn} can be computed by any number of efficient numerical routines, without any of the difficulties that beset computation of the $A_{kn;\lambda}$'s via direct evaluation of the definition (6.28). This fact, combined with equation (6.36), leads to the only practical recipe for computing the $A_{kn;\lambda}$'s of the orbit with initial position $\vec{\chi}_0$, namely to compute instead the A_{kn}'s and then use equation (6.36). Ref. [105] introduced just such a technique in the specific context of functions of Kerr geodesics.

All the other quantities mentioned in this section are likewise determined from their torus function counterparts. From equations (6.32) and (6.36), $A_{00;\lambda} = A_{00}$. We thus conclude that on a non-resonant torus, the time average of $f(\lambda)$ equals the torus average of its associated torus-function $f(\vec{\chi})$. Moreover, since this is true for every time function on that torus, the time average

[13] The set of complex exponential functions $e^{-i\Omega\lambda}$ for all Ω are a basis for absolutely integrable functions on the space $\lambda \in (-\infty,\infty)$. $f(\lambda;\vec{\chi}_0)$ inherits absolute integrability from the associated torus function $f(\vec{\chi})$, which has a spatial double Fourier series representation and thus is absolutely integrable by assumption. Equation (6.28) is therefore a projection onto the complex exponential basis, and projections onto basis sets are unique.

[14] We denoted the knth temporal Fourier coefficient by $A_{kn;\lambda}$ in anticipation of its close relationship to the knth spatial Fourier coefficient A_{kn} of the associated torus function and added the λ subscript to remind us of when we are dealing with spatial vs. temporal Fourier coefficients.

of such a function is independent of the initial condition $\vec{\chi}_0$:

$$\langle f(\lambda;\vec{\chi}_0)\rangle_\lambda = \langle f(\vec{\chi})\rangle_{\vec{\chi}} \ , \quad \forall \vec{\chi}_0 \in \mathbb{T}^2_{EL_zQ} \quad . \tag{6.38}$$

Likewise, equations (6.37) and (6.26) imply that, on a non-resonant torus, the time-averaged Fourier power of $f(\lambda;\vec{\chi}_0)$ equals the torus-averaged Fourier power of $f(\vec{\chi})$ for every $\vec{\chi}_0$:

$$\mathcal{P}_\lambda \equiv \mathcal{P}_{\vec{\chi}} \quad \forall \vec{\chi}_0 \in \mathbb{T}^2_{EL_zQ} \quad . \tag{6.39}$$

Equations (6.26), (6.37) and (6.39) together imply equation (6.34)[15]. By extension, the 1D power spectrum of $f(\lambda)$ can be derived from the 2D power spectrum of $f(\vec{\chi})$ by mapping wavenumber pairs to frequencies using eq. (6.27).

All of the above relationships between torus-function quantities and those of any biperiodic time function induced via (6.35) are well-established and well-known in the literature on almost-periodic functions [122; 123] and on integrable Hamiltonian systems [115]. Many of these facts, however, are used but not so clearly delineated in this way in the literature relating to EMRI calculations. We have gone through the trouble of including them here not only for completeness and clarity but also to emphasize that we can only execute the above recipes if we know the corresponding torus function $f(\vec{\chi})$.

This leads us to a crucial observation. If all we know is $f(\lambda)$, either as some closed-form expression in terms of λ or as a numerical time-series, there is no practical scheme for computing its temporal Fourier coefficients $A_{kn;\lambda}$, even though those coefficients are perfectly well-defined. In addition to the initial conditions $\vec{\chi}_0$ associated with $f(\lambda)$, we *must* also know the torus-function $f(\vec{\chi})$ (or at least its spatial Fourier coefficients A_{kn}) in order to compute the $A_{kn;\lambda}$'s. We summarize the implications of this fact for flux balancing in section 6.3.5.

All of the equivalences noted between torus-function quantities and their time-function counterparts followed from the assumption of non-resonance. On resonant tori, all of these equivalences break down, as we now show.

Resonant tori

Unlike time functions evaluated along non-resonant orbits, time functions on resonant orbits are singly periodic, with (possibly very long) period Λ_P and corresponding fundamental frequency $\Omega_P = 2\pi/\Lambda_P$. The single periodicity of

[15] This proves Parseval's theorem for biperiodic functions.

time functions of resonant orbits means that all frequency-domain quantities have straightforward and familiar definitions.

Any time function evaluated on a resonant orbit has a Fourier series representation

$$f\left(\lambda;\vec{\chi}_0\right) = \sum_j C_{j;\lambda} e^{-ij\Omega_P\lambda} \tag{6.40}$$

whose coefficients[16] are single-index objects

$$C_{j;\lambda} = \frac{1}{\Lambda_P}\int_{-\Lambda_P/2}^{\Lambda_P/2} d\lambda\, f\left(\lambda;\vec{\chi}_0\right) e^{+ij\Omega_P\lambda} \quad . \tag{6.41}$$

Like the $A_{kn;\lambda}$'s, each $C_{j;\lambda}$ varies with the initial condition $\vec{\chi}_0$. Unlike the $A_{kn;\lambda}$'s, the Fourier transform of $f(\lambda;\vec{\chi}_0)$ is a sequence

$$\widetilde{f}(\Omega) = \sum_j C_{j;\lambda}\,\delta\left(\Omega - j\Omega_P\right) \tag{6.42}$$

of equally spaced delta-function impulses in frequency space.

In the resonant case, we define the time average of $f(\lambda)$ straightforwardly as

$$\left\langle f(\lambda;\vec{\chi}_0)\right\rangle_\lambda \equiv \frac{1}{\Lambda_P}\int_{-\frac{\Lambda_P}{2}}^{\frac{\Lambda_P}{2}} d\lambda\, f(\lambda;\vec{\chi}_0) = C_{0;\lambda} \quad . \tag{6.43}$$

Likewise, we define the time-averaged power as

$$\mathcal{P}_\lambda(\vec{\chi}_0) \equiv \frac{1}{\Lambda_P}\int_{-\frac{\Lambda_P}{2}}^{\frac{\Lambda_P}{2}} d\lambda\, \left|f(\lambda;\vec{\chi}_0)\right|^2 \quad . \tag{6.44}$$

By Parseval's theorem, the time-averaged power is also given by

$$\mathcal{P}_\lambda(\vec{\chi}_0) = \sum_j \left|C_{j;\lambda}\right|^2 \quad . \tag{6.45}$$

To flush out how the $C_{j;\lambda}$'s relate to the spatial A_{kn}'s and to the initial condition $\vec{\chi}_0$, we begin, as in the non-resonant case, by inducing a time function

[16] Periodicity of $f(\lambda)$ implies that the integral in equation (6.41) has the same value taken over any interval of length Λ_P. We choose the symmetric interval $[-\Lambda_P/2, \Lambda_P/2]$ solely for aesthetic reasons.

(6.35) from a torus function. In the resonant case, the frequency ratio Ω_θ/Ω_r is a rational number p/z, where p and z are relatively prime and $p > z$. (In terms of integers in the definition $q_{r\theta} = w + \frac{v}{z}$, $p = (w+1)z+v$.) The individual r and θ frequencies and periods are therefore related to the fundamental frequency and total period of the periodic orbit by

$$\Omega_r = z\Omega_P \tag{6.46a}$$
$$\Omega_\theta = p\Omega_P \tag{6.46b}$$

and

$$\Lambda_r = \frac{\Lambda_P}{z} \tag{6.47a}$$
$$\Lambda_\theta = \frac{\Lambda_P}{p} \quad . \tag{6.47b}$$

As a result, all kn combinations for which

$$nz + kp = j \tag{6.48}$$

lead to identical frequencies

$$n\Omega_r + k\Omega_\theta = nz\Omega_P + kp\Omega_P = j\Omega_P \tag{6.49}$$

in the arguments of the exponential functions on the RHS of equation (6.35).

The selection rule (6.48) maps every kn pair to some j. By the uniqueness of Fourier representations, we conclude from equations (6.35) and (6.40) that

$$C_{j;\lambda}(\vec{\chi}_0) = \sum_{\substack{k,n: \\ nz+kp=j}} A_{kn} e^{-i(n\chi_{r_0}+k\chi_{\theta_0})} \quad . \tag{6.50}$$

Note that equation (6.50) is really only a summation over a single index since the value of k in any term is determined by the value of n and the (fixed) value of j.

It is tempting to rewrite each term on the RHS of equation (6.50) as $A_{kn;\lambda}$, mimicking the notation for the non-resonant temporal Fourier coefficients. We refrain from doing so because we seek a clear distinction between spatial and temporal Fourier coefficients, and temporal double-index coefficients are not defined in the resonant case [123; 124]. Fourier representations are unique, so the familiar single-index representation (6.40) is the only such projection of

$f(\lambda)$ onto a set of mutually orthogonal basis functions. If we were to write an expression like (6.28) on a resonant orbit, the different harmonics on the RHS would not all be orthogonal, and we would not have a bona fide Fourier expansion in hand until we collapsed all terms corresponding to the same frequency into a single term.

Equation (6.36) implied that, on non-resonant orbits, several quantities one can compute for a time-function $f(\lambda;\vec{\chi}_0)$ turn out to be independent of $\vec{\chi}_0$: the magnitudes of its Fourier coefficients, its time-averaged value, its time-averaged Fourier power, and its power spectrum. In contrast, equation (6.50) implies that, on resonant orbits, each of those quantities *does* depend on the initial condition $\vec{\chi}_0$. Each $C_{j;\lambda}$ is a sum of spatial A_{kn}'s with $\vec{\chi}_0$-dependent phases rather than just one such term (cf. equation (6.36)), so both the magnitudes

$$|C_{j;\lambda}|\,(\vec{\chi}_0) = \left| \sum_{\substack{k,n:\\ nz+kp=j}} A_{kn} e^{-i(n\chi_{r_0}+k\chi_{\theta_0})} \right| \tag{6.51}$$

and time-averaged value

$$\begin{aligned} \langle f(\lambda;\vec{\chi}_0)\rangle_\lambda &= C_{0;\lambda}(\vec{\chi}_0) \\ &= \sum_{\substack{k,n:\\ nz+kp=0}} A_{kn} e^{-i(n\chi_{r_0}+k\chi_{\theta_0})} \\ &= A_{00} + \sum_{\substack{n\neq 0, k\neq 0:\\ nz+kp=0}} A_{kn} e^{-i(n\chi_{r_0}+k\chi_{\theta_0})} \end{aligned} \tag{6.52}$$

retain $\vec{\chi}_0$-dependence. The squared magnitudes

$$\begin{aligned} |C_j\,(\chi_{r_o},\chi_{\theta_o})|^2 &= \sum_{\substack{kn:\\ j=nz+kp}} A_{kn} e^{-i(n\chi_{r_o}+k\chi_{\theta_o})} \sum_{\substack{k'n':\\ j=n'z+k'p}} A^*_{k'n'} e^{i(n'\chi_{r_o}+k'\chi_{\theta_o})} \\ &= \sum_{\substack{k=k', n=n':\\ j=nz+kp}} |A_{kn}|^2 \\ &\quad + \sum_{\substack{k\neq k', n\neq n':\\ j=nz+kp,\\ j=n'z+k'p}} A_{kn} A^*_{k'n'} e^{-i(n-n')\chi_{r_o}} e^{-i(k-k')\chi_{\theta_o}} \quad . \end{aligned} \tag{6.53}$$

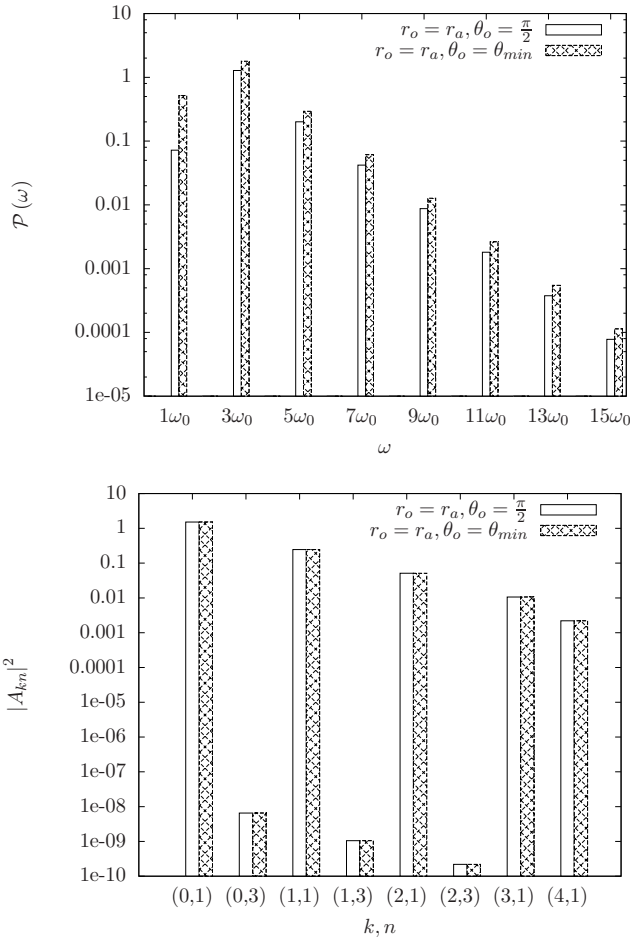

Figure 6.6: Top: The Fourier power spectrum of the function $r\cos\theta$ for a $q_{r\theta} = \frac{1}{2}$ periodic orbit for two different sets of initial coordinates, $\left(r_0 = r_a, \theta_0 = \frac{\pi}{2}\right)$ and $(r_0 = r_a, \theta_0 = \theta_{min})$, but the same sets of orbital parameters, $a = 0.9$, $E = 0.954788$, $L_z = 2.65115$ and $Q = 0.944969$. Bottom: The magnitudes of some spatial Fourier coefficients for the same orbits in the top panel.

also depend on $\vec{\chi}_0$ through cross terms, and the time-averaged power and power spectra inherit this dependence via (6.45). Figure 6.6 illustrates this point for the test function $r\cos\theta$.

Via its $\vec{\chi}_0$-dependence, equation (6.52) defines a torus function in the variables $\chi_{r_0}, \chi_{\theta_0}$. Complex exponentials have a zero average value, so averaging that torus function over all $\chi_{r_0}, \chi_{\theta_0}$ kills every term in the summation on the

RHS of (6.52), leaving only A_{00}. But A_{00} is the torus averaged value of the associated torus function $f(\vec{\chi})$. We conclude that the torus-average over all initial conditions of the time average of a time function equals the torus-average of the underlying torus-function. An identical argument applies if we torus average the squared-magnitudes (6.53) of the coefficients over all $\vec{\chi}_0$ and, by extension, if we likewise torus-average the time-averaged power (6.44).

The upshot is that the parallels between torus functions and time functions obtained in the non-resonant case break down in the resonant case:

$$\langle f(\lambda; \vec{\chi}_0)\rangle_\lambda \neq \langle f(\chi_r, \chi_\theta)\rangle_{\vec{\chi}} \tag{6.54}$$

$$\mathcal{P}_\lambda(\vec{\chi}_0) \neq \mathcal{P}_{\vec{\chi}} \quad . \tag{6.55}$$

However, torus averages over initial conditions and torus averages of time averaged *are* equal for both a function f and its Fourier power:

$$\langle\langle f(\lambda; \vec{\chi}_0)\rangle_\lambda\rangle_{\vec{\chi}} = \langle f(\chi_r, \chi_\theta)\rangle_{\vec{\chi}} \tag{6.56}$$

$$\langle \mathcal{P}_\lambda(\vec{\chi}_0)\rangle_{\vec{\chi}} = \mathcal{P}_{\vec{\chi}} \quad . \tag{6.57}$$

To clarify, equations (6.54) and (6.55) state that the time average of a time function and the torus average of its associated torus-function are not *identically equal* as they are in the non-resonant case. That does not, of course, preclude the possibility that the two could be *circumstantially equal* for some particular choice of initial condition $\vec{\chi}_0$. In fact, for real-valued functions f, the mean-value theorem guarantees that $\langle f(\lambda; \vec{\chi}_0)\rangle_\lambda = \langle f(\vec{\chi})\rangle_{\vec{\chi}}$ for at least one $\vec{\chi}_0^{\text{mvt}} \in \mathbb{T}^2_{\vec{\mathcal{E}}}$. In general, f will be complex-valued, and we have no such guarantee. The time-averaged Fourier power, however, is strictly real, so there is at least one $\vec{\chi}_0^{\text{mvt}}$ such that $\mathcal{P}_\lambda(\vec{\chi}_0^{\text{mvt}}) = \mathcal{P}_{\vec{\chi}}$. We explore some implications of this fact for adiabatic EMRI calculations in Section 6.5.

6.3.5 And the winner is... torus averaging

To summarize, time averaging is equivalent to torus averaging for non-resonant orbits. Furthermore, torus averaging is the only practical recipe for computing Fourier coefficients and so torus averaging is the explicit computation instituted in practice.

However, time averaging is *inequivalent* to torus averaging for resonant orbits. Thus torus averaging wins out for two reasons. First, torus averaging along a resonant torus crucially washes away any $\vec{\chi}_0$ positional dependence,

while time averaging does not. The $\vec{\chi}_0$-dependence violates the spirit of averaging, namely to remove all dependence on the fast variables. Second, and more seriously, though the time-averaged equations are continuous in $\vec{\chi}_0$ for fixed $\vec{\mathcal{E}}$, they are in general discontinuous in $\vec{\mathcal{E}}$ for fixed $\vec{\chi}_0$. The situation will resemble that of Thomae's modified Dirichlet function

$$D_M(x) = \begin{cases} 0 & \text{if } x \text{ is irrational} \\ \frac{1}{z} & \text{if } x = p/z, \text{ with } p \text{ and } z \text{ coprime} \\ 1 & \text{if } x = 0 \end{cases} , \tag{6.58}$$

which is continuous at the irrationals, discontinuous on the rationals, and nowhere differentiable[17] [126]. Pragmatically speaking, even if a set of ODEs with such pathologically discontinuous and non-differentiable equations had a solution, it is unclear how one would numerically integrate them. Furthermore, the continuity furnished by torus-averaged fluxes is absolutely essential for the proper construction of a grid through which adiabatic trajectories are to be interpolated, as discussed in the introduction.

In short, torus-averaged equations are well-behaved, while time-averaged equations lose the continuity and differentiability that guarantee the resulting equations are well-posed and have unique solutions, the very basis of every standard numerical integration scheme.

The arguments made in favor of torus averaging apply to the radiative approximation, based on an average of the dissipative piece of the *local* self-force on the inspiraling particle. But when it comes to flux-balance as a specific implementation of the radiative approximation, this now leaves a logical gap. As acknowledged in [96; 106], the flux-balance arguments that allow the nonlocal fluxes of conserved quantities to be used as proxies for the local dissipative self-force have been derived on a time-averaged basis and under the assumption of non-resonance. Since time and torus averages agree for non-resonant orbits/tori, the time-averaged nonlocal fluxes are still good proxies for the torus-averaged local dissipative self-force in the non-resonant case.

[17] Such a function certainly seems unphysical. It violates the hypotheses of continuity and differentiability in all arguments required by the theorems bounding the error in a solution to time-averaged equations with almost-periodic dependence on time [117]. More pathologically, it violates the hypotheses for the well-posedness of an initial value problem and for the existence of solutions to systems of ODEs [125]. Such a function would not be Riemann integrable, and it is unclear whether a system of such functions would even be Lebesgue integrable.

What has never been made explicit is whether flux-balance is also valid in the resonant case, on either a time averaged or torus-averaged basis. We resolve this issue now: time averaged flux-balancing may not be true on resonant orbits in general, but that will be irrelevant since it will be true on a torus-averaged basis. Mino showed that, under the assumption of non-resonance, the time-averaged fluxes of $\vec{\mathcal{E}}$ at infinity and the horizon furnish proxies for the time averaged RHSs of equations (6.18). But then, by the arguments we have heavily exploited, the corresponding torus-averaged versions must also be equal. And since torus averages are insensitive to the resonance or non-resonance of the underlying torus *and are continuous in* $\vec{\mathcal{E}}$, the flux-balance prescription is valid in a torus-averaged sense for all orbits. If the torus-averaged fluxes were not good proxies for the torus-averaged local equations only at resonances, a discrete set of measure zero, then they could not be continuous in $\vec{\mathcal{E}}$. But we have shown torus averages are everywhere continuous. *De facto*, then, Mino's argument establishes the validity of torus-averaged flux-balancing generally.

It would thus seem that both flux-balancing as a general procedure and its specific implementation in a frequency-domain application of the Teukolsky formalism treat non-resonant and resonant tori equally, as stated in [112]. Flux-balancing is, in fact, thusly impartial, but interestingly, the Teukolsky formalism is not. As we will show below, a TB torus-averaged flux calculation can achieve computational savings of an order of magnitude or more on low-order resonant tori that are simply not available on non-resonant tori. These efficiencies follow from a simple observation about the Fourier integrals a TB code must evaluate and are independent of the specific implementation in code of the Teukolsky formalism. Thus, rather than disfavoring resonances, as has been commonly assumed, the Teukolsky formalism actually shows favoritism for resonances, and properly leveraged, that favoritism can substantially accelerate adiabatic inspiral calculations.

6.4 Computational savings along resonances

We now explain computational efficiencies that exploit resonant tori. Although specific to the Teukolsky formalism, the computational expedience can be understood without all details of that formalism. We simply assert some features and formulae from a TB flux calculation that we require to make our argument. For reference, Appendix D.1 gives a somewhat more detailed overview

of the Teukolsky formalism and offers at least skeletal derivations of the formulae listed below. For a fuller treatment of the Teukolsky formalism, which is beyond the scope of this work, we direct the reader to the references listed in Appendix D.1.

As a reminder, our argument is specific to *frequency-domain* Teukolsky calculations and corresponding codes. In the context of the EMRI problem, such codes compute a combined multipole and Fourier decomposition of the metric perturbations at infinity and the black hole horizon due to a geodesic source.

6.4.1 The fluxes of E, L_z, Q

The fluxes of the conserved quantities $\vec{\mathcal{E}}$ are usually reported as quantities averaged over *coordinate* time t on non-resonant orbits[18]. By the arguments of Section 6.3.4 and Appendix C, this is equivalent to the torus-averages of the fluxes on all tori over the torus coordinates $\vec{\gamma}$. We therefore report those same expressions here as torus-averaged fluxes. For E and L_z, those expressions are [100; 108]

$$\left\langle \frac{dE}{dt} \right\rangle_{\vec{\gamma}}^{H/\infty} = \sum_{lmkn} \frac{\alpha_{lmkn}^{\infty/H}}{4\pi\omega_{mkn}^2} \left| Z_{lmkn}^{\infty/H} \right|^2 \tag{6.59a}$$

$$\left\langle \frac{dL_z}{dt} \right\rangle_{\vec{\gamma}}^{H/\infty} = \sum_{lmkn} \frac{\alpha_{lmkn}^{\infty/H} m}{4\pi\omega_{mkn}^3} \left| Z_{lmkn}^{\infty/H} \right|^2 \quad . \tag{6.59b}$$

Based on Mino's argument in [96], Refs. [119; 127] worked out the corresponding expression for the time-averaged Q flux for non-resonant orbits, which we also report as the torus-averaged flux

$$\begin{aligned} \left\langle \frac{dQ}{dt} \right\rangle_{\vec{\gamma}}^{H/\infty} &= -2 \left\langle a^2 E \cos^2\theta \right\rangle_{\vec{\gamma}} \left\langle \frac{dE}{dt} \right\rangle_{\vec{\gamma}}^{H/\infty} \\ &\quad + 2 \left\langle \cot^2\theta \right\rangle_{\vec{\gamma}} \left\langle \frac{dL_z}{dt} \right\rangle_{\vec{\gamma}}^{H/\infty} \\ &\quad - \sum_{lmkn} \frac{k\omega_\theta}{2\pi\omega_{mkn}^3} \alpha_{lmkn}^{\infty/H} \left| Z_{lmkn}^{\infty/H} \right|^2 \quad . \end{aligned} \tag{6.59c}$$

[18] See Appendix D.2 for the time-averaged fluxes from resonant orbits.

The prefactors in the first two lines of (6.59c) are computed only once for the entire torus. Thus, substituting equations (6.59a) and (6.59b) into the RHS of (6.59c) and combining like terms with those in the summation of the last line, the flux for Q has the same general form as the fluxes of E and L_z have. Our savings arguments will be based on that form, so although we will speak about E and L_z for concreteness, those arguments will apply to Q as well. Appendices D.1 and D.2 summarize the derivations of these expressions.

Before proceeding with those arguments, we clarify the notation in equations (6.59). First, the apparent discrepancy between the ordering of the H/∞ superscripts on the left- and righthand sides of the equations is not a typographical error. On the LHS, the superscript denotes fluxes at the black hole horizon and radial infinity, respectively. The somewhat backward notational choice to have the fluxes at infinity depend on a quantity labeled Z^H_{lmkn} and the horizon fluxes on Z^∞_{lmkn} is, at this point, ingrained in the literature. To maintain a modicum of notational uniformity, we have labeled the weighting factors $\alpha^{H/\infty}$ with the same backward superscript convention. The exact form of those weighting factors will not concern us. What matters for our purposes is that every factor α^H_{lmkn} for the fluxes at infinity is equal to 1 and that every factor α^∞_{lmkn} for the fluxes at the horizon is real and depends on k, n only through ω_{kn}. All the arguments to follow apply equally to fluxes at infinity and at the horizon. We borrow the notation $\star$ from Ref. [100] to denote either of H/∞.

Continuing, the indices l, m are standard multipole indices[19], with $l \geq 2, -l \leq m \leq l$. Our argument will focus on the Fourier analysis of each l, m term individually, so that, unless explicitly stated otherwise, l, m are taken to be fixed everywhere in this section, while k, n each run from $-\infty$ to ∞. The frequencies

$$\omega_{mkn} \equiv m\omega_\varphi + \omega_{kn} = m\omega_\varphi + n\omega_r + k\omega_\theta \tag{6.60}$$

are the combined harmonics ω_{kn} of the r and θ fundamental frequencies (the coordinate time version of equation (6.27)) and the fundamental azimuthal frequency ω_φ. Note that the integer m is both a multipole index and the relative contribution of ω_φ to each frequency ω_{mkn}. Other than attaching itself as a label to frequencies in this way, however, m will not appear as a Fourier index in any sense below.

Finally, Appendix D.2 explains why we have written the fluxes as average

[19]The values $l = 0, 1$ are not relevant in GW calculations, for which the lowest nonvanishing moment is the $l = 2$ quadrupole.

values over the $\vec{\gamma}$ torus coordinates mentioned in Section 6.3.2 and in Appendix C. We note here simply that if we seek adiabatic solutions in the form $\vec{\mathcal{E}}(t)$ (as opposed to $\vec{\mathcal{E}}(\lambda)$), then the angle brackets in (6.18) should also be averages over $\vec{\gamma}$, so that (6.59) have the correct form to be proxies for $\vec{\mathcal{F}}(\vec{\mathcal{E}})$. The representations of the LHSs of the flux equations as averages over $\vec{\gamma}$ is otherwise irrelevant, since in light of (6.19), we will always seek equivalent and easier to compute $\vec{\chi}$-averaged quantities.

6.4.2 $Z^{\star}_{lmkn}$ as Fourier coefficients of a torus function

With these preliminaries out of the way, we are ready to list the features of the RHSs of (6.59) that we will need for our savings arguments both in this section and in Section 6.5. For our principal argument, what matters is that for fixed l, m values, each $Z^{\star}_{lmkn}$ takes the form of a Fourier coefficient of some torus function,

$$Z^{\star}_{lmkn} = \int_0^{2\pi} d\chi_r \int_0^{2\pi} d\chi_\theta \, e^{i(n\chi_r + k\chi_\theta)} f^{\star}_{lm;\omega=\omega_{mkn}}(\chi_r, \chi_\theta) \quad . \quad (6.61)$$

This form of the $Z^{\star}_{lmkn}$'s associated with a geodesic source of arbitrary eccentricity and inclination is detailed in several references (see, for instance, [100; 105; 108; 118; 119; 127]) and summarized in Appendix D.1.

Equation (6.61) parallels the form of equation (6.23) from Section 6.3.3, but there is one critical difference. For fixed l, m, the function $f^{\star}_{lm;\omega}(\chi_r, \chi_\theta)$ further depends on a continuous parameter ω that must be set to ω_{mkn} when evaluating $Z^{\star}_{lmkn}$ for a given multipole mode. Postponing for the moment any details of the function $f^{\star}_{lm;\omega}(\chi_r, \chi_\theta)$ or its derivation, we remark that this dependence on the coordinate time harmonic frequencies of the source as an external parameter persists despite the fact that equation (6.61) is a spatial Fourier integral.

Thus, for fixed l, m, the $Z^{\star}_{lmkn}$ are not the Fourier coefficients of a single function but rather isolated Fourier coefficients of several different functions[20]. On a non-resonant torus, every k, n pair leads to a different value of ω_{mkn}, and every coefficient computed has a distinct function $f^{\star}_{lm;\omega}(\chi_r, \chi_\theta)$ in the integrand. On a resonant torus with associated frequency ratio $\omega_\theta/\omega_r = \Omega_\theta/\Omega_r =$

[20] This is part of the reason why we cannot compute all the $Z^{\star}_{lmkn}$ coefficients for a given l, m at once with, for instance, a 2-dimensional Fast Fourier Transform (FFT).

p/z, all k, n pairs that satisfy the selection rule (6.48) for the same j lead to identical values of Ω_{mkn}, and some coefficients with different values of k, n will share the same integrand function $f^\star_{lm;\omega}(\chi_r, \chi_\theta)$. The practical implications of this asymmetry for a TB flux calculation constitute the basis of our savings argument.

In anticipation of later arguments, we also note that for each fixed value of the pair l, m, the resulting doubly infinite sum over k, n in (6.59) has the appearance of a torus-averaged Fourier power in the sense of Section 6.3.3 with the identification

$$\begin{aligned} |A_{kn}|^2 &= \text{prefactor} \times |Z^\star_{lmkn}|^2 \\ A_{kn} &= \sqrt{\text{prefactor}} \times Z^\star_{lmkn} \quad . \end{aligned} \tag{6.62}$$

The prefactors in front of $|Z^\star_{lmkn}|^2$ turn out to be real-valued and non-negative for all values of the indices, so it is valid to subsume them into some new coefficients A_{kn}.

6.4.3 Recycling computations between Fourier modes

The complex-valued quantities $Z^\star_{lmkn}$ are the backbone of a frequency-domain Teukolsky calculation, and a code that implements such a calculation spends by far the lion's share of its CPU budget on computing them. To explain how resonances can be leveraged to optimize that budget, we must look a bit more closely at the integrand functions $f^\star_{lm;\omega}(\chi_r, \chi_\theta)$.

The main ingredients in $f^\star_{lm;\omega}(\chi_r, \chi_\theta)$ are two separate functions that have the same sort of ω dependence described above: a radial Teukolsky function $R^\star_{lm;\omega}(r)$ and a spin-weighted spheroidal harmonic ${}_{-2}S^{a\omega}_{lm}(\theta)$. We imagine re-expressing the former as a torus function of χ_r alone and the latter as a torus function of χ_θ alone but will continue to write them as functions of r and θ, as they are in the rest of the literature. $f^\star_{lm;\omega}(\chi_r, \chi_\theta)$ consists of a somewhat messy assortment of terms and factors involving these two functions, several of their derivatives, the coordinates and velocities of the particle (both of these are absorbed into the torus coordinates χ_r, χ_θ), and other elementary functions.

Each of $R^\star_{lm;\omega}$ and ${}_{-2}S^{a\omega}_{lm}(\theta)$ satisfies an ODE that depends on l, m and ω in a nontrivial and partly implicit way (see Appendix D.1). No simple closed-form solutions to these equations exist that make the functional dependence of the solutions on those parameters explicit. As a result, for every distinct set of values (l, m, ω), those ODEs must be solved from scratch to obtain the

numerical representations of $R^{\star}_{lm;\omega}$ and ${}_{-2}S^{a\omega}_{lm}$ needed to evaluate the integrand. Particularly in the case of $R^{\star}_{lm;\omega}$, this operation is computationally costly.

Schematically, then, one calculates each $Z^{\star}_{lmkn}$ for fixed l, m via the following steps:

1. Determine the frequency $\omega = \omega_{mkn}$
2. Obtain a representation of ${}_{-2}S^{a\omega}_{lm}$
3. Obtain a representation of $R^{\star}_{lm;\omega}$ for $\star = H, \infty$ (this step requires first determining an eigenvalue of the ${}_{-2}S^{a\omega}_{lm}$ ODE)
4. Evaluate $f^{\star}_{lm;\omega}(\vec{\chi}_i)$ at whatever abscissae $\vec{\chi}_i$ are required by the specific numerical integration algorithm chosen
5. Compute whatever weights w_i the integration algorithm may require for those function values and tabulate the integral (6.61) as $\sum_i w_i f^{\star}_{lm;\omega}(\vec{\chi}_i)$.

On a non-resonant torus, each k, n pair produces a different answer to step 1 and requires the execution from scratch of all the remaining steps as well. On a resonant torus, in contrast, the k, n pairs can be grouped by a common value of j in the selection rule (6.48). Steps 1–3 need only be performed once for an entire j-group. Depending on the integration algorithm selected, steps 4 and 5 may also only need to be performed once or a small number of times per j-group, with a total number of reusable function evaluations set by the $Z^{\star}_{lmkn}$ in the group requiring the greatest number of sample points to attain some target accuracy. We will make the reasonable assumption that steps 1 and 5, even if done several times per j-group, are a small fraction of the total cost of evaluating all the coefficients in that group, and we will take the cost of steps 2-4 as an estimate of the total cost of computing any single coefficient.

Consider now evaluating all the $Z^{\star}_{lmkn}$ on a low-order resonant torus with $\omega_\theta/\omega_r = \Omega_\theta/\Omega_r = p/z = 1 + q_{r\theta}$ and on a neighboring non-resonant torus with nearly identical orbital parameters. By the continuity of the $Z^{\star}_{lmkn}$ with respect to $\vec{\mathcal{E}}$, coefficient values will be nearly identical on those two tori. The integer values of $n_{\max}, k_{\max}$ determined should also be identical or nearly identical on the two tori (we assume for simplicity that they are identical). Let $\mathcal{N}_2$ and $\mathcal{N}_1$ denote, respectively, the number of separate times steps 2–4 above must be executed on the non-resonant torus and resonant torus. To make a more apples to apples comparison, one can instead let $\mathcal{N}_2$ represent the total number

of distinct executions of steps 2–4 on the resonant torus if the resonance of that torus is not acknowledged from the outset. Roughly speaking, generating all the $Z^{\star}_{lmkn}$ with $|n| \leq n_{\max}, |k| \leq k_{\max}$ on the non-resonant torus will require $\mathcal{N}_2/\mathcal{N}_1$ times more computation than it will on the neighboring resonant torus. Symmetries in the underlying equations imply that the value of $Z^{\star}_{l(-m)(-k)(-n)}$ is uniquely determined by the value of $Z^{\star}_{lmnk}$. Thus, in practice, one of the indices n and k can be restricted to run over only nonnegative values, and the value of $\mathcal{N}_2/\mathcal{N}_1$ should take that fact into account.

Figure 6.7 estimates the savings factor $\mathcal{N}_2/\mathcal{N}_1$ for resonant tori with various values of $q_{r\theta}$ and for several representative hypothetical values of $n_{\max}$ and $k_{\max}$ consistent with the reported performance of the TB code for arbitrary eccentricities and inclinations described in Ref. [100][21]. For simplicity, we have taken $n_{\max} = k_{\max}$.

We can see the following trends in the histograms. First, for a given $k_{\max}, n_{\max}$, if we fix the value of p and increase z or vice versa, the savings factor drops. Thus, the savings factor is largest when both p and z are as low as possible. The greatest savings (over an order of magnitude) accrue when $z = 1$. Second, the larger the values of $k_{\max}, n_{\max}$, i.e. the more slowly converging the expressions for the fluxes, the greater the savings factor for a given p/z. Generally speaking, the most slowly converging fluxes are for orbits with moderate to high eccentricities [100; 118], which typically have higher associated values of $q_{r\theta}$ since they are closer to the separatrix between plunging and non-plunging motion [47]. Thus, for instance, a rough approximation of the true savings factor in the top two panels of Figure 6.7 would be given by a roughly horizontal or slightly downward sloping line connecting the histogram bar with the lowest $q_{r\theta}$ at the lowest $n_{\max}$ with the highest $q_{r\theta}$ at the highest $n_{\max}$. A good rough predictor for the expected savings would thus be the z value of a torus, yielding a savings factor of ~ 30 for $z = 1$ and ~ 7 for $z = 6$. The lowest savings factor on that graph of ~ 3 (corresponding to the not-so-low-order resonance with $p/z = 25/6$) is nothing to sneeze at, and more typically the savings factor from acknowledging resonance would appear to be around an order of magnitude on average.

While a detailed audit of comparative cost would have to be done on a

[21] We estimate $n_{\max}$ and $k_{\max}$ based on the code in [100] rather than the similar code in [121] only because the truncation rules used in [100] are more amenable to direct cost comparison with our proposal. Both codes seem to need to compute a total number of modes of similar order of magnitude to achieve high flux accuracy, and both are apt to profit from our proposal.

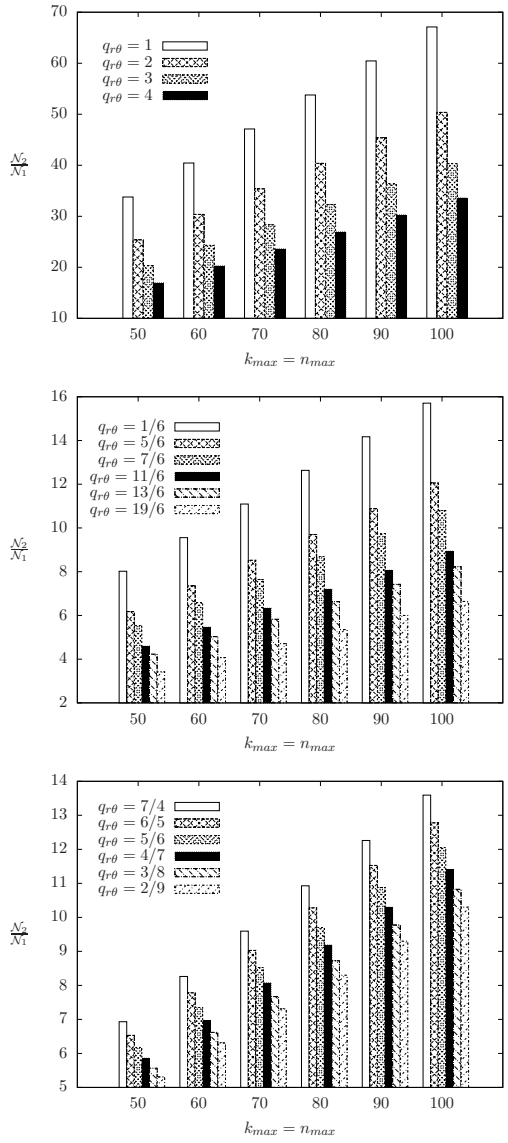

Figure 6.7: The three histograms show the average number of $Z^{\star}_{lmnk}$ coefficients that pertain to a single frequency on a resonant torus, a number that corresponds to the savings factor $\mathcal{N}_2/\mathcal{N}_1$. We show the savings factor for a variety of $q_{r\theta}$ geodesics and a variety of $n_{\max}$ and $k_{\max}$. Top: $q_{r\theta} =$ Integers. Middle: $q_{r\theta}$ is a variety of values all with the same denominator, $z = 6$. Bottom: $q_{r\theta}$ is a variety of non-integer values all with $p = 11$ but different z.

code-specific basis, the potential payoff of these observations makes a case for testing our proposal in existing codes.

6.4.4 Numerical EMRI grids

Even if we stipulate that fluxes can be computed more efficiently on low-order resonant tori than on non-resonant tori, is this fact necessarily useful? After all, points in $\vec{\mathcal{E}}$-space corresponding to resonant tori, let alone low-order ones, are already a measure zero set, so to construct the inspiral curve $\vec{\mathcal{E}}(t)$, wouldn't the RHSs of the adiabatic ODEs have to be evaluated in general (and, formally, infinitely more often) on non-resonant tori than on resonant ones? Interestingly, while the answer to that question is "yes", the actual calculation of TB fluxes itself need only ever be done on resonant tori, and at least predominantly (and possibly exclusively) on low-order ones, at least for the foreseeable future.

The reason has to do with the *absolute* computational cost of those fluxes, even on resonant tori. Simply inserting a TB frequency-domain flux routine into the RHS of, say, a standard Runge-Kutta ODE solver to generate inspiral curves in real-time is untenable, even with a large number of processors at one's disposal to parallelize the TB calculation. Instead, solution of the adiabatic ODEs will proceed as follows. For each value of the black hole parameters, one would build a numerical grid of flux values on some dense mesh of points in $\vec{\mathcal{E}}$-space and then interpolate off of that grid to obtain the fluxes for arbitrary values of $\vec{\mathcal{E}}$. Once handed such a grid, those interpolated flux values would go into a standard ODE solver which could presumably generate inspiral curves very efficiently. The main expense to consider, then, is the construction of the grid.

Our proposal is that such a grid should be built using exclusively resonant grid points. More specifically, we propose a hierarchical population of such a grid, beginning with the low-order resonant points and then increasing the order of the resonance (or just increasing z, if our loose conjecture about horizontal lines in the top panels of Figure 6.7 proves to be correct) until some requisite grid density is obtained to minimize interpolation error. Those grid density requirements may force the evaluation of fluxes on some higher-order resonances, but no resonant grid point (whether low- or high-order) will ever be more expensive to populate with Fourier flux data than a nearby non-resonant grid point will be. The worst-case scenario near certain locations in the space would be to break even by using a resonant versus a non-resonant grid point.

Our hierarchical approach would seem to at least lower if not minimize the total computational cost of such a grid.

We remark on two features of our proposal. First, the savings factor discussed depends only on the decision to use resonant tori for TB calculations and no other implementation-specific features of that calculation. Thus, those savings will multiply any additional savings that may stem from other algorithmic improvements in any such implementation or from the availability of more or faster processors to perform the TB calculations.

Second, its efficacy has nothing to do with interesting physical effects that may occur in the neighborhood of resonant orbital parameter values during a real inspiral [107]. The flux-balance method, and in fact the adiabatic approximation in general, may fail to capture these effects. Any such failure is immaterial to our argument, which rests not on *physical* properties of resonant tori but rather *mathematical* ones they have in specific relation to frequency-domain TB calculations. In other words, despite the fact that the adiabatic approximation might be least faithful to reality in and around resonances, leveraging resonances is nonetheless the most efficient means of attaining an adiabatic approximation for those regimes where it is likely to be faithful.

6.4.5 Gravitational waveform snapshots

As already argued, we are free to interpret the coefficients $Z^{\star}_{lmkn}$ either as spatial Fourier coefficients of a torus function of $\vec{\chi}$ or of a different torus function of $\vec{\gamma}$. As shown in Appendix D.1, the t-function versions of the $Z^{\star}_{lmkn}$ coefficients are used to build the Weyl scalar ψ_4 at radial infinity, from which the two polarizations of the waveform h are constructed. These waveform "snapshots" from geodesic sources [100] are useful for exploring how a known orbital motion impacts GW signals, and though they will quickly go out of phase with a true inspiral signal, they are still likely to play a pivotal role in hierarchical searches for GWs from EMRIs.

More specifically, with the $\vec{\gamma}$-coefficients $Z^{\star}_{lmkn}$ in hand, h can be reconstructed from the associated t-coefficients. By analogy to equation (6.36), we get

$$Z^{\star}_{lmkn;t} \equiv Z^{\star}_{lmkn} e^{-i(n\gamma_{r_0}+k\gamma_{\theta_0})} \quad , \tag{6.63}$$

in the non-resonant case, and by analogy to equation (6.50) get

$$Z^{\star}_{lmj;t}(\vec{\gamma}_0) = \sum_{\substack{k,n:\\ nz+kp=j}} Z^{\star}_{lmkn} e^{-i(n\gamma_{r_0}+k\gamma_{\theta_0})} \tag{6.64}$$

in the resonant case if we know the initial conditions. Since the waveforms (or, rather, their Fourier representations) depend on the $Z^{\star}_{lmkn}$ coefficients, then like the fluxes, they will also probably need to be interpolated from a grid that stores the $Z^{\star}_{lmkn}$ values themselves instead of or in addition to the fluxes. The same arguments made above for the fluxes thus cross-apply to waveform snapshots.

6.5 Speculations on further savings

In this section, we sketch a speculative but tantalizing possibility for further efficiencies in adiabatic EMRI grid construction beyond those discussed in Section 6.4. The idea centers around calculating time-averaged rather than torus-averaged fluxes on resonant tori. At first glance, that suggestion seems to fly in the face of earlier arguments that the RHSs of the adiabatic equations should be torus-averaged fluxes and that torus averages and time averages are not identical on resonant tori. The apparent incongruity disappears, however, in light of two facts:

1. On any resonant torus, the mean value theorem guarantees that torus-averaged fluxes equal time-averaged fluxes on certain special orbits.

2. For low-order resonances, those time-averaged fluxes are more accurate and cheaper to compute.

The additional savings are beyond the cost benefit of incorporating the proposal of Section 6.4.

We substantiate these claims below in turn. We caution the reader that, in contrast to the savings of Section 6.4, those discussed in this section may prove more elusive in practice because determining the special orbits mentioned in step 1 above could prove so difficult as not to be net-beneficial. We discuss such limitations and suggest fruitful avenues of numerical investigation to help further reduce the cost of generating adiabatic inspirals.

6.5.1 Using time-averages to compute torus-averages

The time-averaged fluxes from a single resonant orbit do not appear elsewhere in the literature. As we explain in Appendix D.2, the arguments of Section 6.3.4 imply that those fluxes are (note, these are single-index objects in j)

$$\left\langle \frac{dE}{dt} \right\rangle_t^\star = \sum_{lmj} \frac{\alpha^\star_{lmj}}{4\pi\omega^2_{mj}} \left| Z^\star_{lmj;\lambda} \right|^2 \tag{6.65}$$

$$\left\langle \frac{dL_z}{dt} \right\rangle_t^\star = \sum_{lmj} \frac{\alpha^\star_{lmj} m}{4\pi\omega^3_{mj}} \left| Z^\star_{lmj;\lambda} \right|^2 \quad . \tag{6.66}$$

It remains to be shown whether the following would translate to $\left\langle \frac{dQ}{dt} \right\rangle_t$. We restrict attention in this section to E and L_z fluxes for the sake of exposition.

As before, we assume fixed l, m in everything below. In the fluxes, the frequencies

$$\omega_{mj} \equiv m\omega_\varphi + j\omega_P \quad , \tag{6.67}$$

the real-valued weight factors $\alpha^\star_{lmj}$, and the temporal Fourier coefficients

$$Z^\star_{lmj;\lambda} = \frac{1}{\Lambda_P} \int_0^{\Lambda_P} d\lambda \, e^{ij\Omega_P \lambda} f^\star_{lmj;\lambda} \left(\vec{\chi}(\lambda; \vec{\chi}_0) \right) \tag{6.68}$$

all become single-index quantities by the arguments of Section 6.3.4. We recall from equation (6.62) that the torus-averaged fluxes have the form of a torus-averaged power of some unspecified torus-function. Likewise, for fixed values of l, m, the time-averaged fluxes (6.65) and (6.66) have the appearance of a time-averaged Fourier power in the sense of Section 6.3.4 with the identification

$$\begin{aligned} |C_{j;\lambda}|^2 &= \text{prefactor} \ \times \left| Z^\star_{lmj;\lambda} \right|^2 \\ C_{j;\lambda} &= \sqrt{\text{prefactor}} \times Z^\star_{lmj;\lambda} \quad . \end{aligned} \tag{6.69}$$

Each time-averaged flux, like any time-averaged Fourier power, is real-valued. Therefore, by equations (6.69) and (6.57) and the mean-value argument made at the end of Section 6.3.4, there exist initial positions $\vec{\chi}^{\text{mvt},\star}_{0;E}$, $\vec{\chi}^{\text{mvt},\star}_{0;L_z}$ on the torus such that

$$\left\langle \frac{dE}{dt} \right\rangle_t^\star \left(\vec{\chi}^{\text{mvt},\star}_{0;E} \right) = \left\langle \frac{dE}{dt} \right\rangle_{\vec{\gamma}}^\star \tag{6.70}$$

$$\left\langle \frac{dL_z}{dt} \right\rangle_t^\star \left(\vec{\chi}^{\text{mvt},\star}_{0;L_z} \right) = \left\langle \frac{dL_z}{dt} \right\rangle_{\vec{\gamma}}^\star \quad . \tag{6.71}$$

Actually, there must be at least two continuous 1-parameter families of special initial values $\vec{\chi}_{0;E}^{\text{mvt},\star}$ (one for each of $\star = H, \infty$) and two such families for $\vec{\chi}_{0;L_z}^{\text{mvt},\star}$: any two initial conditions that lie on the same orbit simply time-translate that orbit, and time-translation does not change time-averaged function values or time-averaged powers.

None of the values $\vec{\chi}_{0;E}^{\text{mvt},\star}$ and $\vec{\chi}_{0;L_z}^{\text{mvt},\star}$ need agree. Thus, if we sought to determine the torus-averaged fluxes indirectly by instead evaluating time-averaged fluxes, we might need to evaluate each coefficient $Z_{lmj;\lambda}^{\star}$ as many as four[22] times, once for each of the initial conditions $\vec{\chi}_{0;E}^{\text{mvt},\star}$ and $\vec{\chi}_{0;L_z}^{\text{mvt},\star}$.

We can, however, also apply the mean-value argument individually to each real-valued $\left|Z_{lmj;\lambda}^{\star}\right|^2$. In this case, we would obtain a sequence of special initial conditions $\vec{\chi}_{0;j}^{\text{mvt},\star}$ that cause each $\left|Z_{lmj;\lambda}^{\star}\right|^2$ to attain its torus-averaged value over all possible initial conditions. The different $\vec{\chi}_{0;j}^{\text{mvt},\star}$ would not necessarily agree for different values of j. Since the prefactors in (6.69) are independent of initial position, each $\vec{\chi}_{0;j}^{\text{mvt},\star}$ would simultaneously set the jth term in the power spectrum of every flux to its torus-averaged value. Evaluating the time-averaged fluxes for any of the individual initial conditions $\vec{\chi}_{0;j}^{\text{mvt},\star}$ would not produce a torus-averaged flux. However, since the average of a sum of terms must equal the sum of the individual averages of those terms, the sum of the resulting $|C_{j;\lambda}|^2$ (each evaluated at a possibly different $\vec{\chi}_{0;j}^{\text{mvt},\star}$) would yield the torus-averaged value of all fluxes simultaneously. Recalling that each integrand in (6.68) is different anyway, there is no further waste in evaluating each one using a different initial condition $\vec{\chi}_{0;j}^{\text{mvt},\star}$.

It is important to note that we have simply made an existence argument for $\vec{\chi}_{0;E}^{\text{mvt},\star}$, $\vec{\chi}_{0;L_z}^{\text{mvt},\star}$ and every $\vec{\chi}_{0;j}^{\text{mvt},\star}$. What those values actually are would vary from problem to problem, and finding them for the Teukolsky problem may not be practical. The integrands in (6.68) are not especially analytically transparent, so it may be that they can only be determined by evaluating those integrands for several initial conditions $\vec{\chi}_0$, which would defeat the purpose of invoking the mean-value theorem in the first place. Still, we believe the potential added savings from knowing the $\vec{\chi}_{0;j}^{\text{mvt},\star}$ merits exploring whether the Teukolsky calculation harbors some structure or symmetries that would allow those initial conditions to be determined with little or no added expense. We turn to those additional potential savings now.

[22] Or, rather, six times, since each $\vec{\chi}_{0;Q}^{\text{mvt},\star}$ would likely also be different from $\vec{\chi}_{0;E}^{\text{mvt},\star}$ and $\vec{\chi}_{0;L_z}^{\text{mvt},\star}$.

6.5.2 Relative cost of time-averaged vs. torus-averaged functions on low-order resonant tori

Assume that we have in hand the $\vec{\chi}_{0;j}^{\mathrm{mvt},\star}$ for each j and agree to evaluate the coefficients $Z^{\star}_{lmj;\lambda}$ using those special initial conditions. The added efficiency is twofold: each $C_{j;\lambda}$ should potentially be less expensive to compute than any given A_{kn} (by reducing a double integral to a single integral), and fewer such $C_{j;\lambda}$'s than A_{kn}'s will have to be computed in order to achieve a given target accuracy in the torus-averaged fluxes (by reducing a double sum to a single sum). In fact, the more efficient calculation might even increase the resulting flux accuracy. We justify those claims in turn below.

Cost of a coefficient

For ease of illustration, we will estimate the relative computational costs of a single $C_{j;\lambda}$ and of any single A_{kn} for which k, n satisfy the selection rule (6.48). To make the comparison more stark, we remap the integral (6.68) to the interval $[0, 2\pi]$ via a linear change of variable

$$\chi_P \equiv \Omega_P \lambda \tag{6.72}$$

to obtain

$$Z^{\star}_{lmj;\lambda} = \frac{1}{2\pi} \int_0^{2\pi} d\chi_P \, e^{ij\chi_P} f^{\star}_{lmj;\lambda} \left(\vec{\chi}(\chi_P; \vec{\chi}_0) \right) \quad . \tag{6.73}$$

The relative cost of the single integral (6.73) and its double-index counterpart (6.61) will depend on the specific numerical integration algorithms used to evaluate them and are difficult to estimate. However, we can sketch a crude argument that the single integral should be more cost efficient by considering the Fast Fourier transform (FFT) as the algorithm.

Consider first the $1D$ integral (6.73), which we can interpret as the jth Fourier coefficient of a periodic function on $[0, 2\pi]$. For a periodic function, an FFT will return all the Fourier coefficients from C_{-N_1} through C_{N_1} by sampling the integrand at $2N_1 + 1$ equally spaced abscissae[23]. So to capture C_j, we would need $2|j| + 1$ evaluations of the integrand. However, the highest index coefficients computed via an FFT are heavily afflicted by aliasing error,

[23] To make the formulae that follow more intelligible, we are separately counting the value at 2π, even though it is the same as the value at 0

while the lowest index coefficients computed are relatively free of such error. To minimize aliasing effects, we imagine increasing the number of sample points (and thus of coefficients computed) by some integer safety factor[24] $\mathcal{S}$ so that C_j will be one of lowest index coefficients returned by the FFT and thus fairly free of aliasing error. The total number of integrand evaluations under this scheme for computing C_j would thus be $\mathcal{S}(2|j|+1)$.

Now imagine evaluating the double integral (6.61) using a $2D$ FFT, which we (even more crudely) envision simply as nested $1D$ FFTs. Assuming the same safety factor $\mathcal{S}$ throughout, we would need $\mathcal{S}(2|n|+1)\,\mathcal{S}(2|k|+1) = \mathcal{S}^2(2|n|+1)(2|k|+1)$ function evaluations. Re-expressing j in terms of n and k via the selection rule and using the number of integrand evaluations as a metric of numerical expense, the ratio of the cost of A_{kn} to the cost of C_j would be

$$\frac{\text{cost of } A_{kn}}{\text{cost of } C_j} = \mathcal{S}\frac{(2|n|+1)(2|k|+1)}{2|nz+kp|+1} \quad . \tag{6.74}$$

Generally speaking, for small values of both p and z, the denominator in the cost ratio is smaller than the numerator since n and k more often than not have opposite signs for a given j. It is conceivable that a single A_{kn} could turn out less costly to evaluate than C_j, but the likelihood of that would become higher as both p and z became large, for which case a resonant torus would be barely distinguishable from a non-resonant torus in terms of all the aspects discussed in this chapter.

The argument above artificially increases the true cost of evaluating both integrals and is not intended even to be fully convincing, let alone a proof. Rather, it is a heuristic illustration of a rule of thumb in numerical integration that, with similarly behaved integrands, $1D$ integrals are less costly to compute than $2D$ integrals.

Number of coefficients

In contrast to the relative cost of computing a coefficient, we can say more definitively that the total number of single-index coefficients needed to achieve some specified accuracy in the torus-averaged fluxes will be less than the number of double-index coefficients needed to obtain the same accuracy.

Suppose achieving a certain flux accuracy for a given l, m pair requires computing all A_{kn} with indices up to $n_{\max}$ and $k_{\max}$. Denote the total number

[24] Ref. [128] recommends a factor of at least 4 for most applications.

of torus coefficients computed by $\mathcal{N}_{\vec{\chi}}$. The $Z^\star$ coefficients satisfy $|Z^\star_{lm\omega}|^2 = \left|Z^\star_{l(-m)(-\omega)}\right|^2$ [129], so one of n and k need only run over non-negative values to obtain all the coefficients with $|n| \leq n_{\max}, |k| \leq k_{\max}$. The total number of coefficients actually computed is therefore (having k run only non-negative)

$$\mathcal{N}_{\vec{\chi}} \;=\; (2n_{\max}+1)\,(k_{\max}+1) - n_{\max} \quad . \tag{6.75}$$

For comparison, we determine the number $\mathcal{N}_\lambda$ of C_j coefficients (evaluated at $\vec{\chi}^{\,\mathrm{mvt},\star}_{0;j}$) that we would have to calculate so that, in light of the arguments of subsection 6.5.1, every $|A_{kn}|^2$ above would automatically be included in the sum of all $|C_j|^2$. As we showed in subsection 6.5.1, the maximum j index that needs to be included in the single-index series that will thusly catch every k, n pair is

$$j_{\max} \;=\; zn_{\max} + pk_{\max} \quad . \tag{6.76}$$

The symmetry of $Z^\star$ implies that j need not run both positive and negative, and the number of C_j's we would need to calculate to ensure at least the same level of flux convergence as that attained with the A_{kn} coefficients is

$$\mathcal{N}_\lambda \;=\; zn_{\max} + pk_{\max} + 1 \quad . \tag{6.77}$$

Comparing equations (6.75) and (6.77), we see that we need a factor of

$$\begin{aligned} \mathcal{N}_{\mathrm{savings}} \;&=\; \frac{\mathcal{N}_{\vec{\chi}}}{\mathcal{N}_\lambda} \\ &=\; \frac{(2k_{\max}+1)\,(n_{\max}+1) - k_{\max}}{zn_{\max} + pk_{\max} + 1} \end{aligned} \tag{6.78}$$

fewer coefficients. The reduction in the number of coefficients therefore depends on the order of the periodic orbit as well as on $n_{\max}$ and $k_{\max}$. The lower the values of p and z, the greater the reduction factor.

Figure 6.7 showed the average number of kn modes on a resonant torus per distinct frequency. It also gives a general sense of how $\mathcal{N}_{\mathrm{savings}}$ varies with $k_{\max}$ and $n_{\max}$. The agreement between the two is not exact because, when computing all j coefficients up to the maximum $j_{\max}$, some additional frequencies will be included that do not correspond to any of the included kn frequencies with $|k| \leq k_{\max}, |n| \leq n_{\max}$. Therefore, Figure 6.7 overestimates $\mathcal{N}_{\mathrm{savings}}$ but only slightly and gives a better estimate for the larger values of

$k_{\max}, n_{\max}$. For example, for $q_{r\theta} = \frac{1}{6}$, equation (6.78) gives $\mathcal{N}_{\text{savings}} \approx 7.84$ for $n_{\max} = k_{\max} = 50$ and $\mathcal{N}_{\text{savings}} \approx 12.45$ for $n_{\max} = k_{\max} = 80$, both of which agree with the values in the histogram of Figure 6.7 within a few percent. On the basis of Figure 6.7, we can therefore conclude that focusing on temporal rather than spatial Fourier coefficients and invoking the above mean-value arguments could reduce by a factor of an order of magnitude or so the total number of $Z^\star$ coefficients required to obtain accurate torus-averaged fluxes.

Chapter 7

Conclusions

Even in the absence of radiation reaction, there are important conclusions to draw from the conservative dynamics of binary black hole systems. For Schwarzschild and Kerr equatorial test particle orbits, Chapter 2 summarizes the results of reference [37], which describes how the topological properties of periodic orbits, i.e. the measure zero set of orbits that close after a finite time, vary with respect to orbital parameters. On this basis, it also introduced, for all bound orbits in these systems, a taxonomy in which every aperiodic orbit can be viewed as a slow precession of the multi-leaf clover pattern traced out by some "nearby" member of the periodic set. The taxonomy generalizes in a natural way to include descriptions of say, Mercury's orbit as a precessing Keplerian ellipse. Dynamically, the taxonomy also furnished an invariant and unambiguous definition of so called "zoom-whirl" behavior and showed among other things that simple Mercury-type precessing ellipses are forbidden in the very strong field regime, even for arbitrarily small perturbations of circular orbits.

In this work we have found that, somewhat surprisingly, these same conclusions apply in the strong-field regime of our comparable-mass spinning black hole binaries as well as the full Kerr system, even out of the equatorial plane. Our periodic tables in the orbital plane show zoom-whirl behavior as the norm in the strong-field regime and not as the exception. We have also shown one practical application of our taxonomy for the extreme-mass-ratio GW community. Computation of adiabatic inspirals with a numerical grid composed of resonant orbits could be an order of magnitude more efficient than the same computation performed with a non-resonant grid. If our speculations are verified and the double sums mentioned in Chapter 6 can be collapsed to single

sums (and double integrals to single integrals), there may be substantial additional savings since fewer and simpler coefficients will be required. To date, no accurate adiabatic EMRIs have been computed. Such a dramatic boost in speed would bring EMRIs more within computational reach.

The further importance of the orbital dynamics lies in its direct imprint in the gravitational waveform [44; 100]. The waveform will necessarily reflect the features above. For instance, an equatorial circular orbit (neglecting radiation reaction) is described by essentially one frequency. By contrast, *all other orbits* in the strong-field regime generate highly modulated waveforms naturally described by harmonics of the 3 orbital frequencies, which in turn directly correspond to the natural frequencies of a nearby periodic orbit.

Naturally, we should ask about the astrophysical likeliness of detecting any such orbits with either ground-based or space-based gravitational wave observatories. Although estimates vary [130], stellar mass black hole pairs are currently the favored source for advanced ground-based detectors and extreme-mass-ratio black hole pairs are considered the favored source for space-based observatories. It is challenging to definitively assess the spins and eccentricities of black hole/black hole binaries given the absence of observational constraints [131]. Still, one can guess that long-lived stellar binaries that might collapse to a pair of bound black holes would circularized by the time the pair enters the strong-field due to angular momentum lost in the form of gravitational radiation.[1] By contrast, for shorter-lived black hole binaries formed in globular clusters, the astrophysical likeliness of eccentric orbits sliding in the LIGO bandwidth is assessed to be $\gtrsim 30\%$ for eccentricities > 0.1 in Ref. [40].

All such binaries would necessarily transit near the periodic set on inspiral. Even if the inspiral happens too quickly to witness multiple executions near a low-leaf clover, the orbit can still be sewn together as a skip from a piece of one periodic orbit to a piece of another. Finally, while the spins and eccentricities of extreme and intermediate black hole binaries detectable by space-based detectors are difficult to predict, we should expect them to spend a more generous allotment of windings on eccentric orbits in the strong-field.

In this work, we restricted ourselves to spin-orbit coupling in the post-Newtonian system and a non-spinning test particle in the Kerr system. We found that the spherical orbits constrain the range of allowed bound orbits in the following sense. In both systems, for a given set of orbital parameters, the

[1] However, when spin-spin coupling is included, there are no circular or even spherical orbits.

stable spherical orbit is the lowest energy geodesic and the unstable spherical orbit[2] is the highest energy orbit in the strong-field [3].

As we showed in both the PN expansion and the generic Kerr system, between these two spherical orbits lies an infinite set of orbits that are closed in the orbital plane. The periodic set corresponds to a subset of the rationals, with the rational identifying a given orbit increasing monotonically between the stable spherical orbit and the unstable spherical orbit. The homoclinic orbit is the infinite whirl limit of the periodic set and would be the final entry in a periodic table of orbits corresponding to the infinite limit of the rationals. This pattern of a periodic set framed by constant radius orbits and limiting to a homoclinic orbit is consistent with the picture that has emerged for equatorial Kerr black hole orbits [37; 49; 50] and summarized in Chapter 2 of this thesis.

The consistency of the picture for arbitrary mass ratio black holes with the Kerr case is precisely what is surprising, or at least intriguing. The geodesics in a Kerr spacetime are known to be integrable [52]. There are enough constants of the motion to restrict trajectories to regular tori and prohibit chaotic mixing. As Poincaré intuited, the structure of the periodic orbits encodes the entire dynamics, and the regularity of the system is in fact reflected in the regularity of the periodic spectrum. The simplicity of the spherical orbits and the periodic set they frame suggests that even when both black holes spin and are of comparable mass, there is no chaos – at least not in physically plausible regimes –if only spin-orbit coupling is included.[4]

Put another way, homoclinic orbits are also a sign of nonlinearity. They mark the intersection of the stable and unstable manifolds of a hyperbolic invariant set. They are the precursor to chaos in the sense that under perturbation, the homoclinic orbit breaks up into a homoclinic tangle and will be the locus of a fractal set of orbits [50; 132]. The fractal set is sometimes referred to as a strange repeller and is the analog for conservative systems of strange attractors in dissipative systems [42; 133; 134; 135].

Systems with a regular set of periodic orbits that culminate in a homoclinic limit are not chaotic. However, the spinning pairs are vulnerable to chaos

[2] We actually consider the emergence of an ibso to define the strong-field. For the equal-mass cases that resist the development of an ibso, it is as if the approximation is not effective enough to enter the strong field.

[3] Barring the failures of the approximation at these close separations.

[4] It is possible that for $\mathbf{S_{eff}} \cdot \hat{\mathbf{L}}$ much larger than would be physically allowed for a black hole. After all, with the inclusion of spin-orbit coupling, one of the constants of motion, P_Ψ, has been lost, opening the door for chaos.

as evidenced by their very possession of a homoclinic orbit. Indeed, chaos has by now been well confirmed in the form of a fractal set when spin-spin coupling is included [42; 43; 64; 90; 91; 95]. As suspected in Ref. [88], our work suggests that the emergence of chaos must be directly tractable to the spin-spin coupling.

Before closing, we have to mention effects we have neglected in this work, namely the explicit addition of spin-spin coupling to the post-Newtonian orbital basis picture and the addition of spin to a test particle companion around a Kerr black hole (in which spin-spin coupling is already naturally incorporated into the description as accelerated motion in a Kerr background). In the PN case, such spin-spin corrections introduce additional precessions of the spins of the BHs, and this destroys the constancy of the angle between $\mathbf{S} \cdot \mathbf{L}$. The spin-spin coupling generally introduces explicit angular dependence in the equations of motion and causes additional wobbling of the precessional motion. Although often interpreted as a small perturbation to the system here, the impact of spin-spin coupling can be particularly destructive [88] and deserves further inspection. Similarly, the addition of a spinning test particle in the Kerr system may cause a loss of conserved quantities and therefore may make that system susceptible to chaos.

We conjecture that, when spin-spin coupling is turned on, the transition to chaos could be witnessed through the destruction of the correspondence of the periodic set with the rationals. The additional precessional effects of spin-spin coupling, we suggest, must destroy the homoclinic orbit, replace it with a homoclinic tangle – a fractal set of orbits – and induce chaotic scattering among geodesics in the vicinity.

Bibliography

[1] A. Einstein, *On the electrodynamics of moving bodies*, Annalen Phys. **17**, 891 (1905). 1

[2] A. Einstein, *On the General Theory of Relativity*, Sitzungsber. Preuss. Akad. Wiss. Berlin (Math. Phys.) **1915**, 778 (1915). 1

[3] A. Einstein, *The Field Equations of Gravitation*, Sitzungsber. Preuss. Akad. Wiss. Berlin (Math. Phys.) **1915**, 844 (1915). 1

[4] URL http://www.geo600.org/. 2

[5] URL http://www.ligo.caltech.edu. 2, 61

[6] URL http://tamago.mtk.nao.ac.jp/. 2

[7] URL http://www.ego-gw.it/public/about/welcome.aspx. 2

[8] R. O'Shaughnessy, V. Kalogera, and K. Belczynski, *Binary compact object coalescence rates: The role of elliptical galaxies*, Astrophys. J. **716**, 615 (2010) [0908.3635]. 2

[9] S. Banerjee, *Stellar mass black holes in star clusters: gravitational wave emission and detection rates*, PoS **TEXAS2010**, 058 (2010) [1102.4614]. 2

[10] K. Belczynski, T. Bulik, M. Dominik, and A. Prestwich, *The coalescence rates of double black holes* (2011) [1106.0397]. 2

[11] K. Belczynski, V. Kalogera, F. A. Rasio, R. E. Taam, and T. Bulik, *On the rarity of double black hole binaries: Consequences for gravitational-wave detection*, Astrophys. J. **662**, 504 (2007) [astro-ph/0612032]. 2

[12] URL http://sci.esa.int/lisa. 3, 61

[13] K. J. Rhook and J. S. B. Wyithe, *Realistic Event Rates for Detection of Supermassive Black Hole Coalescence by LISA*, Mon. Not. Roy. Astron. Soc. **361**, 1145 (2005) [astro-ph/0503210]. 3

[14] J. R. Gair et al., *Event rate estimates for LISA extreme mass ratio capture sources*, Class. Quant. Grav. **21**, S1595 (2004) [gr-qc/0405137]. 3

[15] L. J. Rubbo, K. Holley-Bockelmann, and L. S. Finn, *Event rate for extreme mass ratio burst signals in the LISA band*, AIP Conf. Proc. **873**, 284 (2006) [astro-ph/0602445]. 3

[16] E. Berti, *LISA observations of massive black hole mergers: event rates and issues in waveform modelling*, Class. Quant. Grav. **23**, S785 (2006) [astro-ph/0602470]. 3

[17] F. Pretorius, *Simulation of binary black hole spacetimes with a harmonic evolution scheme*, Class. Quant. Grav. **23**, S529 (2006) [gr-qc/0602115]. 3, 49, 56

[18] F. Herrmann, I. Hinder, D. Shoemaker, P. Laguna, and R. A. Matzner, *Gravitational recoil from spinning binary black hole mergers*, gr-qc/0701143 (2007). 3

[19] M. Campanelli, C. O. Lousto, Y. Zlochower, B. Krishnan, and D. Merritt, *Spin Flips and Precession in Black-Hole-Binary Mergers*, Phys. Rev. D **75**, 064030 (2007) [gr-qc/0612076]. 3

[20] M. Campanelli, C. O. Lousto, P. Marronetti, and Y. Zlochower, *Accurate evolutions of orbiting black-hole binaries without excision*, Phys. Rev. Lett. **96**, 111101 (2006) [gr-qc/0511048]. 3

[21] J. G. Baker, J. Centrella, D.-I. Choi, M. Koppitz, and J. van Meter, *Gravitational wave extraction from an inspiraling configuration of merging black holes*, Phys. Rev. Lett. **96**, 111102 (2006) [gr-qc/0511103]. 3

[22] P. Marronetti et al., *Binary black holes on a budget: Simulations using workstations*, Class. Quant. Grav. **24**, S43 (2007) [gr-qc/0701123]. 3

[23] M. A. Scheel et al., *Solving Einstein's equations with dual coordinate frames*, Phys. Rev. D **74**, 104006 (2006) [gr-qc/0607056]. 3

[24] L. Blanchet, *Gravitational radiation from post-Newtonian sources and inspiralling compact binaries*, Living Rev. Rel. **9**, 4 (2006). 4, 5

[25] T. Damour, P. Jaranowski, and G. Schaefer, *Equivalence between the ADM-Hamiltonian and the harmonic- coordinates approaches to the third post-Newtonian dynamics of compact binaries*, Phys. Rev. **D63**, 044021 (2001) [gr-qc/0010040]. 4

[26] V. C. de Andrade, L. Blanchet, and G. Faye, *Third post-Newtonian dynamics of compact binaries: Noetherian conserved quantities and equivalence between the harmonic coordinate and ADM-Hamiltonian formalisms*, Class. Quant. Grav. **18**, 753 (2001) [gr-qc/0011063]. 4

[27] L. Blanchet and G. Faye, *Equations of motion of point-particle binaries at the third post-Newtonian order*, Phys. Lett. **A271**, 58 (2000) [gr-qc/0004009]. 4

[28] L. Blanchet and G. Faye, *General relativistic dynamics of compact binaries at the third post-Newtonian order*, Phys. Rev. **D63**, 062005 (2001) [gr-qc/0007051]. 4

[29] R. L. Arnowitt, S. Deser, and C. W. Misner, *The dynamics of general relativity* (1962) [gr-qc/0405109]. 4

[30] T. Damour, P. Jaranowski, and G. Schaefer, *Dynamical invariants for general relativistic two-body systems at the third post-Newtonian approximation*, Phys. Rev. **D62**, 044024 (2000) [gr-qc/9912092]. 4

[31] P. Jaranowski and G. Schaefer, *The binary black-hole problem at the third post-Newtonian approximation in the orbital motion: Static part*, Phys. Rev. **D60**, 124003 (1999) [gr-qc/9906092]. 4

[32] S. A. Teukolsky, *Rotating Black Holes: Separable Wave Equation for Gravitational and Electromagnetic Perturbations*, Phys. Rev. Lett. **29 16**, 1114 (1972). 5, 200, 201, 203

[33] S. A. Teukolsky, *Perturbations of a Rotating Black Hole. I. Fundamental Equations for Gravitaional, Electromagnetic, and Neutrino-Field Perturbations*, Ap. J. **185**, 635 (1973). 5, 200, 202, 203

[34] R. Wald, *General Relativity* (1984). 6, 10, 48

[35] C. W. Misner, K. S. Thorne, and J. A. Wheeler, *Gravitation*, first ed. (W. H. Freeman, 1973). 6, 10, 91, 94

[36] S. Carroll, *Spacetime and Geometry: An Introduction to General Relativity* (Benjamin Cummings, 2003). 6, 10, 113

[37] J. Levin and G. Perez-Giz, *A Periodic Table for Black Hole Orbits*, Phys. Rev. D **77**, 103005 (2008) [0802.0459]. 7, 8, 10, 19, 22, 58, 62, 64, 76, 77, 84, 85, 93, 103, 110, 111, 112, 124, 164, 166

[38] B. Aschenbach, *Measurement of Mass and Spin of Black Holes with QPOs* (2007) [0710.3454]. 7

[39] S. F. Portegeis-Zwart and S. L. W. McMillan, *Black Hole Mergers in the Universe*, ApJ **528**, L17URL {http://www.citebase.org/abstract?id=oai:arXiv.org:astro-ph/9910061},year={2001}. 7

[40] L. Wen, *On the Eccentricity Distribution of Coalescing Black Hole Binaries Driven by the Kozai Mechanism in Globular Clusters*, Ap. J. **598**, 419 (2003)URL http://www.citebase.org/abstract?id=oai:arXiv.org:astro-ph/0211492. 8, 65, 165

[41] R. M. O'Leary, B. Kocsis, and A. Loeb, *Gravitational waves from scattering of stellar-mass black holes in galactic nuclei* (2008) [0807.2638]. 8

[42] J. Levin, *Gravity Waves, Chaos, and Spinning Compact Binaries*, Phys. Rev. Lett. **84**, 3515 (2000)URL http://www.citebase.org/abstract?id=oai:arXiv.org:gr-qc/9910040. 8, 68, 166, 167

[43] J. Levin, *The fate of chaotic binaries*, Phys. Rev. D **67**, 044013 (2003)URL http://www.citebase.org/abstract?id=oai:arXiv.org:gr-qc/0010100. 8, 68, 167

[44] J. Levin, R. O'Reilly, and E. Copeland, *Gravity waves from homoclinic orbits of compact binaries*, Phys. Rev. D **62**, 024023 (2000) [gr-qc/9909051]. 8, 37, 38, 56, 165

[45] J. Levin and R. Grossman, *Dynamics of Black Hole Pairs I: Periodic Tables*, Phys. Rev. **D79**, 043016 (2009) [0809.3838]. 9, 37, 45, 58, 114

[46] R. Grossman and J. Levin, *Dynamics of Black Hole Pairs II: Spherical Orbits and the Homoclinic Limit of Zoom-Whirliness*, Phys. Rev. **D79**, 043017 (2009) [0811.3798]. 9, 114

[47] R. Grossman, J. Levin, and G. Perez-Giz, *The harmonic structure of generic Kerr orbits* (2011) [1105.5811]. 9, 123, 124, 125, 153

[48] R. Grossman, J. Levin, and G. Perez-Giz, *Faster computation of adiabatic EMRIs using resonances* (2011) [1108.1819]. 9

[49] J. Levin and G. Perez-Giz, *Homoclinic Orbits around Spinning Black Holes I: Exact Solution for the Kerr Separatrix*, Phys. Rev. **D79**, 124013 (2009) [0811.3814]. 17, 37, 38, 48, 49, 56, 57, 58, 96, 111, 166

[50] G. Perez-Giz and J. Levin, *Homoclinic Orbits around Spinning Black Holes II: The Phase Space Portrait*, Phys. Rev. **D79**, 124014 (2009) [0811.3815]. 17, 37, 38, 48, 49, 56, 57, 58, 111, 166

[51] Bombelli and Calzetta, *Chaos around a black hole*, Class and Quant. Grav. **9 12**, 2573 (1992). 17, 37, 38, 56

[52] B. Carter, *Global Structure of the Kerr Family of Gravitational Fields*, Phys. Rev. **174 5**, 1559 (1968). 28, 91, 94, 166

[53] J. M. Bardeen, W. H. Press, and S. A. Teukolsky, *Rotating black holes: locvally nonrotating frames, energy extraction, and scalar synchrotron radiation*, Ap. J. **178**, 347 (1972). 31

[54] T. Damour, *Coalescence of Two Spinning Black Holes: An Effective One-Body Approach*, Phys. Rev. D **64**, 124013 (2001)URL http://www.citebase.org/abstract?id=oai:arXiv.org:gr-qc/0103018. 36, 38, 49, 55, 60, 62, 63, 73

[55] A. Buonanno, Y. Chen, and T. Damour, *Transition from inspiral to plunge in precessing binaries of spinning black holes*, Phys. Rev. D **74**, 104005 (2006). viii, 36, 38, 49, 51, 54, 55, 63, 65, 73

[56] U. Sperhake et al., *Eccentric binary black-hole mergers: The transition from inspiral to plunge in general relativity*, Phys. Rev. **D78**, 064069 (2008) [0710.3823]. 37

[57] F. Pretorius and D. Khurana, *Black hole mergers and unstable circular orbits*, Class. Quant. Grav. **24**, S83 (2007) [gr-qc/0702084]. 38, 62

[58] G. Schaefer, *THE GRAVITATIONAL QUADRUPOLE RADIATION REACTION FORCE AND THE CANONICAL FORMALISM OF ADM*, Annals Phys. **161**, 81 (1985). 39

[59] T. Damour and G. Schaefer, *HIGHER ORDER RELATIVISTIC PERIASTRON ADVANCES AND BINARY PULSARS*, Nuovo Cim. **B101**, 127 (1988). 39

[60] P. Jaranowski and G. Schaefer, *3rd post-Newtonian higher order Hamilton dynamics for two- body point-mass systems*, Phys. Rev. **D57**, 7274 (1998) [gr-qc/9712075]. 39

[61] T. Damour, P. Jaranowski, and G. Schaefer, *On the determination of the last stable orbit for circular general relativistic binaries at the third post-Newtonian approximation*, Phys. Rev. D **62**, 084011 (2000)URL http://www.citebase.org/abstract?id=oai:arXiv.org:gr-qc/0005034. 39, 51, 56

[62] T. Damour, P. Jaranowski, and G. Schafer, *Dimensional regularization of the gravitational interaction of point masses*, Phys. Lett. B **513**, 147 (2001)URL http://www.citebase.org/abstract?id=oai:arXiv.org:gr-qc/0105038. 39

[63] T. Damour and N. Deruelle, *Generalized lagrangian of two point masses in the post-post-Newtonian approximation of general-relativity*, C. R. Acad. Sci. Paris **293**, 537 (1981). 39

[64] A. Gopakumar and C. Königsdörffer, *The deterministic nature of conservative post-Newtonian accurate dynamics of compact binaries with leading order spin-orbit interaction*, Phys. Rev. D **72**, 121501 (2005)URL http://www.citebase.org/abstract?id=oai:arXiv.org:gr-qc/0511009. 41, 68, 167

[65] G. Schäfer and N. Wex, Phys. Lett. A **174**, 196 (1993). 42, 56, 62, 71

[66] N. Wex and S. Kopeikin, *Frame dragging and other precessional effects in black hole-pulsar binaries*, astro-ph/9811052 (1998). 42, 62, 71

[67] B. Gong, *The precession of orbital plane and the significant variabilities of binary pulsars*, astro-ph/0401152 (2004). 42, 62, 71

[68] C. Königsdoerffer and A. Gopakumar, *Post-Newtonian accurate parametric solution to the dynamics of spinning compact binaries in eccentric orbits: The leading order spin-orbit interaction*, Phys. Rev. D **71**, 024039 (2005)URL http://www.citebase.org/abstract?id=oai:arXiv.org:gr-qc/0501011. 42, 62, 71

[69] A. Buonanno and T. Damour, *Effective one-body approach to general relativistic two-body dynamics*, Phys. Rev. D **59**, 084006 (1999)URL http://www.citebase.org/abstract?id=oai:arXiv.org:gr-qc/9811091. 55, 56, 60

[70] A. Buonanno, Y. Pan, J. G. Baker, J. Centrella, B. J. Kelly, S. T. McWilliams, and J. R. van Meter, *Toward faithful templates for non-spinning binary black holes using the effective-one-body approach* (2007)URL http://www.citebase.org/abstract?id=oai:arXiv.org:0706.3732. 55, 60

[71] L. E. Kidder, C. M. Will, and A. G. Wiseman, *Spin effects in the inspiral of coalescing compact binaries*, Phys. Rev. D **47**, 4183 (1993)URL http://www.citebase.org/abstract?id=oai:arXiv.org:gr-qc/9211025. 56

[72] N. Wex and G. Schäfer, Class. and Quantum Grav. **10**, 2729 (1993). 56

[73] T. Damour, B. R. Iyer, and B. S. Sathyaprakash, *Improved filters for gravitational waves from inspiralling compact binaries*, Phys. Rev. **D57**, 885 (1998) [gr-qc/9708034]. 56

[74] L. Blanchet, *Innermost circular orbit of binary black holes at the third post-Newtonian approximation*, Phys. Rev. **D65**, 124009 (2002) [gr-qc/0112056]. 56

[75] T. A. Apostolatos, C. Cutler, G. J. Sussman, and K. S. Thorne, *Spin induced orbital precession and its modulation of the gravitational wave forms from merging binaries*, Phys. Rev. D **49**, 6274 (1994). 61, 63

[76] L. E. Kidder, *Coalescing binary systems of compact objects to post-Newtonian 5/2 order. 5. Spin effects*, Phys. Rev. D **52**, 821 (1995) [gr-qc/9506022]. 61

[77] P. Grandclement, V. Kalogera, and A. Vecchio, *Searching for gravitational waves from the inspiral of precessing binary systems. I: Reduction of detection efficiency*, Phys. Rev. D **67**, 042003 (2003) [gr-qc/0207062]. 61

[78] G. Faye, L. Blanchet, and A. Buonanno, *Higher-order spin effects in the dynamics of compact binaries. I: Equations of motion*, Phys. Rev. D **74**, 104033 (2006) [gr-qc/0605139]. 61

[79] L. Blanchet, A. Buonanno, and G. Faye, *Higher-order spin effects in the dynamics of compact binaries. II: Radiation field*, Phys. Rev. D **74**, 104034 (2006) [gr-qc/0605140]. 61

[80] A. Vecchio, *LISA observations of rapidly spinning massive black hole binary systems*, Phys. Rev. D **70**, 042001 (2004) [astro-ph/0304051]. 61

[81] R. N. Lang and S. A. Hughes, *Measuring coalescing massive binary black holes with gravitational waves: The impact of spin-induced precession*, Phys. Rev. D **74**, 122001 (2006) [gr-qc/0608062]. 61

[82] M. Campanelli, C. O. Lousto, H. Nakano, and Y. Zlochower, *Comparison of Numerical and Post-Newtonian Waveforms for Generic Precessing Black-Hole Binaries*, gr-qc/08080713 (2008). 62, 88

[83] I. Hinder, F. Herrmann, P. Laguna, and D. Shoemaker, *Comparisons of eccentric binary black hole simulations with post-Newtonian models*, gr-qc/08061037 (2008). 62

[84] M. Boyle et al., *High-accuracy numerical simulation of black-hole binaries: Computation of the gravitational-wave energy flux and comparisons with post-Newtonian approximants*, gr-qc/08044184 (2008) [0804.4184]. 62

[85] H. Wang and C. M. Will, *Post-Newtonian gravitational radiation and equations of motion via direct integration of the relaxed Einstein equations. IV: Radiation reaction for binary systems with spin-spin coupling*, Phys. Rev. **D75**, 064017 (2007) [gr-qc/0701047]. 62

[86] M. E. Pati and C. M. Will, *Post-Newtonian gravitational radiation and equations of motion via direct integration of the relaxed Einstein equations. II: Two-body equations of motion to second post-Newtonian order,*

and radiation-reaction to 3.5 post- Newton, Phys. Rev. **D65**, 104008 (2002) [gr-qc/0201001]. 62

[87] C. M. Will, *Post-Newtonian gravitational radiation and equations of motion via direct integration of the relaxed Einstein equations. III. Radiation reaction for binary systems with spinning bodies*, Phys. Rev. **D71**, 084027 (2005) [gr-qc/0502039]. 62

[88] M. D. Hartl and A. Buonanno, *Dynamics of precessing binary black holes using the post-Newtonian approximation*, Phys. Rev. D **71**, 024027 (2005). 63, 68, 167

[89] H. Poincaré, *Méthodes Nouvelles de la Mécanique Céleste* (Gauthier Villars, Paris, 1892). 65, 76

[90] X. Wu and Y. Xie, *Revisit on "Ruling out chaos in compact binary systems"*, Phys. Rev. D **76 12**, 124004 (pages 6) (2007)URL http://link.aps.org/abstract/PRD/v76/e124004. 68, 167

[91] X. Wu and Y. Xie, *Resurvey of order and chaos in spinning compact binaries*, Phys. Rev. D **77 10**, 103012 (pages 13) (2008)URL http://link.aps.org/abstract/PRD/v77/e103012. 68, 167

[92] S. Suzuki and K. ichi Maeda, *Chaos in Schwarzschild Spacetime : The Motion of a Spinning Particle*, Phys. Rev. D **55**, 4848 (1997)URL http://www.citebase.org/abstract?id=oai:arXiv.org:gr-qc/9604020. 68

[93] N. J. Cornish and J. Levin, *Comment on "Ruling out chaos in compact binary systems"*, Phys. Rev. Lett. **89**, 179001 (2002)URL http://www.citebase.org/abstract?id=oai:arXiv.org:gr-qc/0207020. 68

[94] N. J. Cornish and J. Levin, *Lyapunov timescales and black hole binaries*, Class. Quant. Grav. **20**, 1649 (2003)URL http://www.citebase.org/abstract?id=oai:arXiv.org:gr-qc/0304056. 68

[95] J. Levin, *Chaos and Order in Models of Black Hole Pairs*, Phys. Rev. D **74**, 124027 (2006)URL http://www.citebase.org/abstract?id=oai:arXiv.org:gr-qc/0612003. 68, 167

[96] Y. Mino, *Perturbative approach to an orbital evolution around a supermassive black hole*, Phys.Rev. **D67**, 084027 (2003) [gr-qc/0302075]. 94, 107, 122, 127, 132, 146, 148

[97] F. D. Ryan, *Effect of gravitational radiation reaction on circular orbits around a spinning black hole*, Phys. Rev. **D52**, 3159 (1995) [gr-qc/9506023]. 95

[98] F. D. Ryan, *Effect of gravitational radiation reaction on nonequatorial orbits around a Kerr black hole*, Phys. Rev. **D53**, 3064 (1996) [gr-qc/9511062]. 95

[99] S. A. Hughes, *The evolution of circular, non-equatorial orbits of Kerr black holes due to gravitational-wave emission*, erratum-ibbid.d **63**, 049902 (2001)URL http://www.citebase.org/abstract?id=oai:arXiv.org:gr-qc/9910091. 95, 96, 99, 133, 200, 202, 209

[100] S. Drasco and S. Hughes, *Gravitational wave snapshots of generic extreme mass ratio inspirals*, Phys. Rev. D **73**, 024027 (2006) [gr-qc/0509101]. 95, 96, 127, 133, 148, 149, 150, 153, 156, 165, 200, 202, 203, 205, 209

[101] S. A. Hughes, *Evolution of circular, non-equatorial orbits of Kerr black holes due to gravitational-wave emission: II. Inspiral trajectories and gravitational waveforms*, Phys. Rev. D **64**, 064004 (2001)URL http://www.citebase.org/abstract?id=oai:arXiv.org:gr-qc/0104041. 95, 99

[102] K. Glampedakis, S. A. Hughes, and D. Kennefick, *Approximating the inspiral of test bodies into Kerr black holes*, Phys. Rev. D **66**, 064005 (2002)URL http://www.citebase.org/abstract?id=oai:arXiv.org:gr-qc/0205033. 95

[103] D. C. Wilkins, *Bound Geodesics in the Kerr Metric*, Phys. Rev. **D5**, 814 (1972). 95, 96, 99, 133

[104] W. Schmidt, *Celestial mechanics in Kerr spacetime*, Class. Quant. Grav. **19**, 2743 (2002)URL http://www.citebase.org/abstract?id=oai:arXiv.org:gr-qc/0202090. 107

[105] S. Drasco and S. A. Hughes, *Rotating black hole orbit functionals in the frequency domain*, Phys. Rev. D **69 4**, 044015 (2004) [arXiv:astro-ph/0308479]. 107, 139, 150, 196, 197, 198, 203, 206

[106] Y. Mino, *Self-force in the radiation reaction formula*, Prog. Theor. Phys. **113**, 733 (2005) [gr-qc/0506003]. 120, 127, 132, 146

[107] E. E. Flanagan and T. Hinderer, *Transient resonances in the inspirals of point particles into black holes* (2010) [1009.4923]. 120, 156

[108] E. F. S Drasco and S. A. Hughes, *Computing inspirals in Kerr in the adiabatic regime: I. The scalar case*, Class. Quant. Grav. **22**, 801 (2005) [arXiv:gr-qc/0505075]. 120, 127, 132, 148, 150, 202, 209

[109] A. Pound, E. Poisson, and B. G. Nickel, *Limitations of the adiabatic approximation to the gravitational self-force*, Phys. Rev. **D72**, 124001 (2005) [gr-qc/0509122]. 120, 133

[110] A. Pound and E. Poisson, *Multi-scale analysis of the electromagnetic self-force in a weak gravitational field*, Phys. Rev. **D77**, 044012 (2008) [0708.3037]. 120, 133

[111] A. Pound and E. Poisson, *Osculating orbits in Schwarzschild spacetime, with an application to extreme mass-ratio inspirals*, Phys. Rev. **D77**, 044013 (2008) [0708.3033]. 120, 133

[112] T. Hinderer and E. E. Flanagan, *Two timescale analysis of extreme mass ratio inspirals in Kerr. I. Orbital Motion*, Phys. Rev. **D78**, 064028 (2008) [0805.3337]. 120, 131, 133, 147

[113] J. Levin, *Energy Level Diagrams for Black Hole Orbits*, Class. Quant. Grav. **26**, 235010 (2009) [0907.5195]. 125

[114] J. Levin, S. T. McWilliams, and H. Contreras, *Inspiral of Generic Black Hole Binaries: Spin, Precession, and Eccentricity*, ArXiv e-prints (2010) [1009.2533]. 127

[115] V. I. Arnold, V. V. Kozlov, and A. I. Neishtadt, *Mathematical Aspects of Classical and Celestial Mechanics*, third ed. (Springer, 2002). 131, 140, 198

[116] J. Kevorkian and J. D. Cole, *Multiple Scale and Singular Perturbation Methods* (Springer, 1996). 131

[117] F. Verhulst, *Methods and applications of singular perturbations*, vol. 50 of *Texts in Applied Mathematics* (Springer, New York, 2005), ISBN 978-0387-22966-9; 0-387-22966-3, boundary layers and multiple timescale dynamicsURL http://dx.doi.org/10.1007/0-387-28313-7. 131, 146

[118] K. Ganz, W. Hikida, H. Nakano, N. Sago, and T. Tanaka, *Adiabatic Evolution of Three 'Constants' of Motion for Greatly Inclined Orbits in Kerr Spacetime*, Prog. Theor. Phys. **117**, 1041 (2007) [gr-qc/0702054]. 132, 133, 150, 153, 200, 202, 209

[119] N. Sago, T. Tanaka, W. Hikida, K. Ganz, and H. Nakano, *The adiabatic evolution of orbital parameters in the Kerr spacetime*, Prog. Theor. Phys. **115**, 873 (2006) [gr-qc/0511151]. 132, 148, 150, 200

[120] K. Glampedakis and D. Kennefick, *Zoom and whirl: Eccentric equatorial orbits around spinning black holes and their evolution under gravitational radiation*, Phys. Rev. D **66**, 044002 (2002) [gr-qc/0203086]. 133, 200, 209

[121] R. Fujita, W. Hikida, and H. Tagoshi, *An Efficient Numerical Method for Computing Gravitational Waves Induced by a Particle Moving on Eccentric Inclined Orbits around a Kerr Black Hole*, Prog. Theor. Phys. **121**, 843 (2009) [0904.3810]. 133, 153, 202, 203, 205, 209

[122] A. M. Samoilenko, *Elements of the Mathematical Theory of Multi-Frequency Oscillations* (Springer-Verlag, 1991). 137, 140

[123] C. Corduneanu, *Almost Periodic Functions* (Interscience Publishers, 1968). 137, 138, 140, 142

[124] S. S. F Schilder, W Vogt and H. M. Osinga, *Fourier methods for quasi-periodic oscillations*, International Journal for Numerical Methods in Engineering **67**, 629 (2006). 142

[125] Boyce and DiPrima, *Elementary Differential Equations and Boundary Value Problems* (Wiley, 2005). 146

[126] J. W. R. Kevin Beanland and C. Stevenson, *Modifications of Thomae's Function and Differentiability*, The American Mathematical Monthly **116 6**, 531 (2009)URL http://www.jstor.org/stable/40391145. 146

[127] N. Sago, T. Tanaka, W. Hikida, and H. Nakano, *Adiabatic radiation reaction to the orbits in Kerr Spacetime*, Prog. Theor. Phys. **114**, 509 (2005) [gr-qc/0506092]. 148, 150, 200

[128] W. T. V. William H. Press, Saul A. Teukolsky and B. P. Flannery, *Numerical Recipes*, third ed. (Cambridge University Press, 2007). 161

[129] P. L. Chrzanowski, *Applications of Metric Perturbations of a Rotating Black Hole: Distortion of the Event Horizon*, Phys. Rev. **D13**, 806 (1976). 162

[130] K. Belczynski, R. E. Taam, V. Kalogera, F. A. Rasio, and T. Bulik, *On the Rarity of Double Black Hole Binaries: Consequences for Gravitational-wave Detection*, astro-ph/0612032 (2007). 165

[131] R. O'Shaughnessy, J. Kaplan, V. Kalogera, and K. Belczynski, *Bounds on Expected Black Hole Spins in Inspiraling Binaries*, Ap. J. **632**, 1035 (2005)URL http://www.citebase.org/abstract?id=oai:arXiv.org:astro-ph/0503219. 165

[132] E. Ott, *Chaos in Dynamical Systems* (Cambridge University Press, 2002). 166

[133] N. J. Cornish, C. P. Dettmann, and N. E. Frankel, *Fractal basins and chaotic trajectories in multi-black hole space-times*, Phys. Rev. D **50**, 618 (1994)URL http://www.citebase.org/abstract?id=oai:arXiv.org:gr-qc/9402027. 166

[134] C. Dettmann, N. Frankel, and N. Cornish, *Fractal basins and chaotic trajectories in multi-black-hole spacetimes*, Phys. Rev. D. **50 2**, 618 (1994). 166

[135] N. J. Cornish and J. J. Levin, *The mixmaster universe is chaotic*, Phys. Rev. Lett. **78**, 998 (1997) [gr-qc/9605029]. 166

[136] S. A. Hughes, S. Drasco, E. E. Flanagan, and J. Franklin, *Gravitational radiation reaction and inspiral waveforms in the adiabatic limit*, Phys. Rev. Lett. **94**, 221101 (2005) [gr-qc/0504015]. 200

[137] S. A. Hughes, *Computing radiation from Kerr black holes: Generalization of the Sasaki-Nakamura equation*, Phys.Rev. **D62**, 044029 (2000) [gr-qc/0002043]. 203

[138] W. H. Press and S. A. Teukolsky, *Perturbations of a Rotating Black Hole. II. Dynamical Stability of the Kerr Metric*, Astrophys.J. **185**, 649 (1973). 203

[139] S. Teukolsky and W. Press, *Perturbations of a rotating black hole. III - Interaction of the hole with gravitational and electromagnet ic radiation*, Astrophys.J. **193**, 443 (1974). 203, 211, 213

[140] S. Chandrasekhar, *On the Equations Governing the Perturbations of the Schwarzschild Black Hole*, Royal Society of London Proceedings Series A **343**, 289 (1975). 203

[141] E. W. Leaver, *An analytic representation for the quasi-normal modes of Kerr black holes*, Royal Society of London Proceedings Series A **402**, 285 (1985). 203

[142] R. Haberman, *Elementary Applied Partial Differential Equations with Fourier Series and Boundary Value Problems*, third ed. (Prentice Hall, 1998). 203

[143] K. Glampedakis, *Extreme Mass Ratio Inspirals: LISA's unique probe of black hole gravity*, Class. Quant. Grav. **22**, S605 (2005) [gr-qc/0509024]. 203

[144] M. Sasaki and T. Nakamura, *A Class of New Perturbation Equations for the Kerr Geometry*, Phys. Lett. A **89A**, 68 (1982). 203

[145] R. A. Breuer, *Gravitational perturbation theory and synchrotron radiation*, vol. 44 of *Lecture notes in physics* (Springer-Verlag, the University of California, 1975), ISBN 0387075305, 9780387075303. 205

[146] R. A. Isaacson, *Gravitational Radiation in the Limit of High Frequency. II. Nonlinear Terms and the Ef fective Stress Tensor*, Phys. Rev. **166**, 1272 (1968). 210

[147] M. Maggiore, *Gravitational Waves, Volume 1: Theory and Experiments* (Oxford University Press, 2008). 210

[148] S. W. Hawking and J. B. Hartle, *Energy and angular momentum flow into a black hole*, Commun. Math. Phys. **27**, 283 (1972). 211

Appendix A

A.1 The orbital plane equations

The four equations of motion in the orbital plane are obtained by projecting Hamilton's equations onto the basis vectors, as is done in celestial mechanics. For now, consider only the projections onto the orbital basis vectors to generate the four equations,

$$\begin{aligned}
\dot{\mathbf{r}} \cdot \hat{\mathbf{n}} &= \frac{\partial H}{\partial \mathbf{p}} \cdot \hat{\mathbf{n}} \\
\dot{\mathbf{r}} \cdot \hat{\mathbf{\Phi}} &= \frac{\partial H}{\partial \mathbf{p}} \cdot \hat{\mathbf{\Phi}} \\
\dot{\mathbf{p}} \cdot \hat{\mathbf{n}} &= -\frac{\partial H}{\partial \mathbf{r}} \cdot \hat{\mathbf{n}} \\
\dot{\mathbf{p}} \cdot \hat{\mathbf{\Phi}} &= -\frac{\partial H}{\partial \mathbf{r}} \cdot \hat{\mathbf{\Phi}} \quad .
\end{aligned} \tag{A.1}$$

To break down the LHS involves

$$\begin{aligned}
\dot{\mathbf{r}} &= \dot{r}\hat{\mathbf{n}} + r\dot{\hat{\mathbf{n}}} \\
\dot{\mathbf{p}} &= \dot{P}_r\hat{\mathbf{n}} + P_r\dot{\hat{\mathbf{n}}} - \frac{L}{r^2}\dot{r}\hat{\mathbf{\Phi}} + \frac{L}{r}\dot{\hat{\mathbf{\Phi}}} \quad .
\end{aligned} \tag{A.2}$$

We will need projections of $\dot{\hat{\mathbf{n}}}$ and $\dot{\hat{\mathbf{\Phi}}}$ along $\hat{\mathbf{n}}$ and $\hat{\mathbf{\Phi}}$. Now, since $\hat{\mathbf{n}} \cdot \hat{\mathbf{n}} = 1$, it follows that $\dot{\hat{\mathbf{n}}} \cdot \hat{\mathbf{n}} = 0$ and by the same reasoning $\dot{\hat{\mathbf{\Phi}}} \cdot \hat{\mathbf{\Phi}} = 0$. Also, by orthogonality,

$$\begin{aligned}
\dot{\left(\hat{\mathbf{n}} \cdot \hat{\mathbf{\Phi}}\right)} = 0 \implies \\
\dot{\hat{\mathbf{n}}} \cdot \hat{\mathbf{\Phi}} = -\dot{\hat{\mathbf{\Phi}}} \cdot \hat{\mathbf{n}} \quad .
\end{aligned} \tag{A.3}$$

To obtain the final dot product above we expand the basis vectors $(\hat{\mathbf{n}}, \hat{\mathbf{\Phi}}, \hat{\mathbf{\Psi}})$ in terms of an intermediate basis $(\hat{\mathbf{X}}, \hat{\mathbf{Y}})$ that spans the orbital plane, and then expanding $(\hat{\mathbf{X}}, \hat{\mathbf{Y}})$ in the Cartesian basis. We proceed by defining the intersection of the orbital plane with the equatorial plane:

$$\hat{\mathbf{X}} = \frac{\hat{\mathbf{J}} \times \hat{\mathbf{L}}}{\left|\hat{\mathbf{J}} \times \hat{\mathbf{L}}\right|} = \frac{\hat{\mathbf{J}} \times \hat{\mathbf{L}}}{\sin\theta_L} \quad , \tag{A.4}$$

where $\cos\theta_L = \hat{\mathbf{L}} \cdot \hat{\mathbf{J}}$. The vector orthogonal to $\hat{\mathbf{X}}$ that lies in the orbital plane is

$$\hat{\mathbf{Y}} = \hat{\mathbf{L}} \times \hat{\mathbf{X}} \quad . \tag{A.5}$$

This intermediate orbital basis will be useful in the manipulations that follow. In terms of Cartesian components defined with $\hat{\mathbf{k}} = \hat{\mathbf{J}}$ and $\hat{\mathbf{i}}, \hat{\mathbf{j}}$ spanning the equatorial plane, we can expand

$$\begin{aligned} \hat{\mathbf{X}} &= \cos\Psi\hat{\mathbf{i}} + \sin\Psi\hat{\mathbf{j}} \\ \hat{\mathbf{Y}} &= \sin\theta_Y(-\sin\Psi\hat{\mathbf{i}} + \cos\Psi\hat{\mathbf{j}}) + \cos\theta_Y\hat{\mathbf{k}} \quad , \end{aligned} \tag{A.6}$$

where $\cos\theta_Y = \hat{\mathbf{Y}} \cdot \hat{\mathbf{J}}$. Since $\hat{\mathbf{Y}}$ is always orthogonal to $\hat{\mathbf{L}}$, again by construction, this is not really a new angle but can be recast as $\theta_Y = \pi/2 - \theta_L$.

Our non-orthogonal basis can then be expanded as

$$\begin{aligned} \hat{\mathbf{n}} &= \cos\Phi\hat{\mathbf{X}} + \sin\Phi\hat{\mathbf{Y}} \\ \hat{\mathbf{\Phi}} &= -\sin\Phi\hat{\mathbf{X}} + \cos\Phi\hat{\mathbf{Y}} \\ \hat{\mathbf{\Psi}} &= -\sin\Psi\hat{\mathbf{i}} + \cos\Psi\hat{\mathbf{j}} \quad . \end{aligned} \tag{A.7}$$

Using

$$\dot{\hat{\mathbf{X}}} = \dot{\Psi}\hat{\mathbf{\Psi}} \tag{A.8}$$

$$\dot{\hat{\mathbf{\Psi}}} = -\dot{\Psi}\hat{\mathbf{X}} \tag{A.9}$$

$$\dot{\hat{\mathbf{Y}}} = -\sin\theta_Y\dot{\Psi}\hat{\mathbf{X}} + \cos\theta_Y\dot{\theta}_Y\hat{\mathbf{\Psi}} - \sin\theta_Y\dot{\theta}_Y\hat{\mathbf{k}} \, . \tag{A.10}$$

From all of the above relations we obtain for use in the projections

$$\dot{\hat{\mathbf{n}}} \cdot \hat{\mathbf{n}} = 0 \tag{A.11}$$

$$\dot{\hat{\mathbf{\Phi}}} \cdot \hat{\mathbf{\Phi}} = 0 \tag{A.12}$$

$$\dot{\hat{\mathbf{n}}} \cdot \hat{\mathbf{\Phi}} = \dot{\Phi} + \dot{\Psi}\sin\theta_Y = \dot{\Phi} + \dot{\Psi}\cos\theta_L \tag{A.13}$$

$$\dot{\hat{\mathbf{\Phi}}} \cdot \hat{\mathbf{n}} = -\dot{\hat{\mathbf{n}}} \cdot \hat{\mathbf{\Phi}} \quad . \tag{A.14}$$

Conveniently, these are the same projections we will find in appendix B for the case in which only one black hole spins and $\dot{\theta}_Y = \dot{\theta}_L = 0$.

Now we can derive the equations of motion in the (r, Φ, Ψ) coordinates. We use the equations we explicitly construct in chapter 4

$$\begin{aligned}\dot{\mathbf{r}} &= A\mathbf{p} + B\hat{\mathbf{n}} + \frac{\mathbf{S_{eff}} \times \mathbf{r}}{r^3} \\ \dot{\mathbf{p}} &= C\mathbf{p} + D\hat{\mathbf{n}} + \frac{\mathbf{S_{eff}} \times \mathbf{p}}{r^3} + 3\frac{\mathbf{L} \cdot \mathbf{S_{eff}}}{r^4}\hat{\mathbf{n}} \quad ,\end{aligned} \tag{A.15}$$

where A, B, C, D are given by Eqs. (3.18). With the projections (Eqs. (A.1)), (A.2), and the above vector relations we have the radial equation from $\dot{\mathbf{r}} \cdot \hat{\mathbf{n}}$ in (A.15):

$$\dot{r} = AP_r + B \quad . \tag{A.16}$$

The Φ equation follows from

$$\dot{\mathbf{r}} \cdot \hat{\mathbf{\Phi}} = \frac{\partial H}{\partial \mathbf{p}} \cdot \hat{\mathbf{\Phi}} \tag{A.17}$$

$$r\left(\dot{\Phi} + \dot{\Psi}\cos\theta_L\right) = A\frac{L}{r} + \frac{(\mathbf{S_{eff}} \times \mathbf{r}) \cdot \hat{\mathbf{\Phi}}}{r^3} \quad . \tag{A.18}$$

Look at

$$(\mathbf{S_{eff}} \times \mathbf{r}) \cdot \hat{\mathbf{\Phi}} = r\left(\mathbf{S_{eff}} \cdot \hat{\mathbf{L}}\right) \quad . \tag{A.19}$$

The Φ equation is then

$$\dot{\Phi} = A\frac{L}{r^2} - \dot{\Psi}\cos\theta_L + \frac{\mathbf{S_{eff}} \cdot \hat{\mathbf{L}}}{r^3} \tag{A.20}$$

where $\hat{\mathbf{S}}_{\mathbf{eff}} \cdot \hat{\mathbf{L}}$ is constant.

The two conjugate momenta equations are next. We start with P_r:

$$\begin{aligned}\dot{\mathbf{p}} \cdot \hat{\mathbf{n}} &= \dot{P}_r - \frac{L}{r}(\dot{\Phi} + \dot{\Psi}\cos\theta_L) \\ &= CP_r + D + 2\frac{\mathbf{S_{eff}} \cdot \mathbf{L}}{r^4}\end{aligned} \tag{A.21}$$

where we have used that

$$(\mathbf{p} \times \mathbf{S_{eff}}) \cdot \hat{\mathbf{n}} = \frac{\mathbf{S_{eff}} \cdot \mathbf{L}}{r} \tag{A.22}$$

Notice if we use Eq. (A.20), we have

$$\dot{P}_r = A\frac{L^2}{r^3} + CP_r + D + 3\frac{\mathbf{S_{eff}}\cdot\mathbf{L}}{r^4}$$

and last

$$\begin{aligned}\dot{\mathbf{p}}\cdot\hat{\mathbf{\Phi}} &= P_r(\dot{\Phi}+\dot{\Psi}\cos\theta_L) - \frac{L}{r^2}\dot{r} \\ &= C\frac{P_\Phi}{r} + \frac{P_r\mathbf{S_{eff}}\cdot\hat{\mathbf{L}}}{r^3}\end{aligned} \tag{A.23}$$

where we have used that

$$(\mathbf{p}\times\mathbf{S_{eff}})\cdot\hat{\mathbf{\Phi}} = \mathbf{S_{eff}}\cdot(\hat{\mathbf{\Phi}}\times\mathbf{p}) = -P_r\mathbf{S_{eff}}\cdot\hat{\mathbf{L}} \tag{A.24}$$

Notice if we use Eq. (A.20), we have a cancellation and

$$(AP_r - \dot{r})\frac{L}{r^2} = -B\frac{L}{r} = C\frac{L}{r}$$

which confirms a true statement but does not provide any new equation of motion. The final equation of motion is simply $\dot{P}_\Phi = 0$. All four equations in the orbital basis are compiled in Eqs. (3.12).

A.2 The precession of the plane

The plane precesses in the direction $\hat{\mathbf{\Psi}}$ at a rate $\dot{\Psi}$, which can be computed from the first of Eqs. (A.10):

$$\dot{\hat{\mathbf{X}}} = \dot{\Psi}\hat{\mathbf{\Psi}} \quad .$$

We can isolate $\dot{\Psi}$ by projecting along $\hat{\mathbf{\Psi}}$,

$$\dot{\hat{\mathbf{X}}}\cdot\hat{\mathbf{\Psi}} = \dot{\Psi} \quad . \tag{A.25}$$

We take the time derivative of Eq. (A.4) and use the constancy of $\hat{\mathbf{J}}$ and the precession equation for $\dot{\hat{\mathbf{L}}}$ from Eq. (3.8) to find

$$\dot{\Psi} = \left(\frac{\hat{\mathbf{J}}\times\left(\mathbf{S_{eff}}\times\hat{\mathbf{L}}\right)}{\left|\hat{\mathbf{J}}\times\hat{\mathbf{L}}\right| r^3}\right)\cdot\hat{\mathbf{\Psi}} \quad . \tag{A.26}$$

Notice that the term that would have been proportional to $\dot{\theta}_L$ is killed since it is also proportional to $\hat{\mathbf{X}} \cdot \hat{\mathbf{\Psi}} = 0$. With some vector manipulations, including the general rule $\mathbf{A} \times (\mathbf{B} \times \mathbf{C}) = \mathbf{B}(\mathbf{A} \cdot \mathbf{C}) - \mathbf{C}(\mathbf{A} \cdot \mathbf{B})$, applied to both the term in parentheses and to $\hat{\mathbf{\Psi}} = \hat{\mathbf{J}} \times \hat{\mathbf{X}}$ with $\hat{\mathbf{X}}$ given by Eq. (A.4), this can be reduced to

$$\dot{\Psi} = \frac{\mathbf{S_{eff}} \cdot \left(\hat{\mathbf{J}} - \hat{\mathbf{L}}(\hat{\mathbf{J}} \cdot \hat{\mathbf{L}})\right)}{\sin\theta_L^2 r^3} \quad . \tag{A.27}$$

Going in the other direction with the general rule, $\mathbf{B}(\mathbf{A} \cdot \mathbf{C}) - \mathbf{C}(\mathbf{A} \cdot \mathbf{B}) = \mathbf{A} \times (\mathbf{B} \times \mathbf{C})$, we can write the right-hand-side as a triple cross product and identify the particularly compact form

$$\dot{\Psi} = \frac{\mathbf{S_{eff}} \cdot \hat{\mathbf{Y}}}{\sin\theta_L r^3} \quad . \tag{A.28}$$

As we show in appendix B,

$$P_\Psi = L_z = \mathbf{L} \cdot \hat{\mathbf{J}} \quad . \tag{A.29}$$

P_Ψ, which can also be expressed as $P_\Psi = L\cos\theta_L$, is not conserved when both black holes spin and precess, however is will be conserved in chapter 4 when we specialize to one spinning black hole.

A.3 One effective spin

The equations of motion simplify considerably if there is only one effective spin, such as the case of only black hole spinning which we explore in chapter 4:

$$\begin{aligned} \dot{r} &= AP_r + B \\ \dot{P}_r &= A\frac{L^2}{r^3} - \frac{B}{r}P_r + D + 3\delta_1\frac{\mathbf{S_1} \cdot \mathbf{L}}{r^4} \\ \dot{\Phi} &= A\frac{L}{r^2} - \delta_1\frac{L}{r^3} \\ \dot{P}_\Phi &= 0 \end{aligned} \tag{A.30}$$

The orbital plane precesses with frequency

$$\dot{\Psi} = \Omega_L = \delta_1\frac{J}{r^3} \qquad \dot{P}_\Psi = 0. \tag{A.31}$$

Consequently, the equations of motion above are independent of angles. In chapter 4, we use these purely radial equations to study several features of the dynamical system, such as a periodic table that defines the spectrum of black hole orbits.

The same simplification can be effected when the black holes are of equal mass $m_1 = m_2$. Then what we really mean by $\mathbf{S_1}$ is $\mathbf{S_1} \to \mathbf{S_1} + \mathbf{S_2}$.

Appendix B

B.1 Projection onto orbital basis

By projecting the equations of motion onto the orbital basis $(\hat{\mathbf{n}}, \hat{\mathbf{\Phi}}, \hat{\mathbf{\Psi}})$, we show here that the equations of motion depend only on the radius.

The four equations of motion in the orbital plane are obtained by projecting Hamilton's equations onto the basis vectors, as is done in celestial mechanics. For now, consider only the projections onto the orbital basis vectors to generate the four equations,

$$\begin{aligned}
\dot{\mathbf{r}} \cdot \hat{\mathbf{n}} &= \frac{\partial H}{\partial \mathbf{p}} \cdot \hat{\mathbf{n}} \\
\dot{\mathbf{r}} \cdot \hat{\mathbf{\Phi}} &= \frac{\partial H}{\partial \mathbf{p}} \cdot \hat{\mathbf{\Phi}} \\
\dot{\mathbf{p}} \cdot \hat{\mathbf{n}} &= -\frac{\partial H}{\partial \mathbf{r}} \cdot \hat{\mathbf{n}} \\
\dot{\mathbf{p}} \cdot \hat{\mathbf{\Phi}} &= -\frac{\partial H}{\partial \mathbf{r}} \cdot \hat{\mathbf{\Phi}} \quad .
\end{aligned} \tag{B.1}$$

To break down the LHS and RHS of the above projections it will be useful to write

$$\begin{aligned}
\mathbf{p} &= (\mathbf{p} \cdot \hat{\mathbf{n}})\hat{\mathbf{n}} + (\hat{\mathbf{n}} \times \mathbf{p}) \times \hat{\mathbf{n}} && \text{(B.2)} \\
&= P_r \hat{\mathbf{n}} + \frac{\mathbf{L}}{r} \times \hat{\mathbf{n}} && \text{(B.3)} \\
&= P_r \hat{\mathbf{n}} + \frac{L}{r} \hat{\mathbf{\Phi}} && \text{(B.4)}
\end{aligned}$$

where the component $p_r = P_r$ and by capitol P's we mean canonical momenta versus small case, which will mean components. To break down the LHS

involves

$$\begin{aligned}\dot{\mathbf{r}} &= \dot{r}\hat{\mathbf{n}} + r\dot{\hat{\mathbf{n}}} \\ \dot{\mathbf{p}} &= \dot{P}_r\hat{\mathbf{n}} + P_r\dot{\hat{\mathbf{n}}} - \frac{L}{r^2}\dot{r}\hat{\mathbf{\Phi}} + \frac{L}{r}\dot{\hat{\mathbf{\Phi}}} \quad .\end{aligned} \tag{B.5}$$

So, we will need $\dot{\hat{\mathbf{n}}}$ and $\dot{\hat{\mathbf{\Phi}}}$, which are most directly obtained by expanding $(\hat{\mathbf{n}}, \hat{\mathbf{\Phi}})$ in the $(\hat{\mathbf{X}}, \hat{\mathbf{Y}})$ basis and then expanding $(\hat{\mathbf{X}}, \hat{\mathbf{Y}})$ in the Cartesian basis. So, we will need

$$\begin{aligned}\hat{\mathbf{n}} &= \cos\Phi\hat{\mathbf{X}} + \sin\Phi\hat{\mathbf{Y}} \\ \hat{\mathbf{\Phi}} &= -\sin\Phi\hat{\mathbf{X}} + \cos\Phi\hat{\mathbf{Y}} \\ \hat{\mathbf{X}} &= \cos\Psi\hat{\mathbf{i}} + \sin\Psi\hat{\mathbf{j}} \\ \hat{\mathbf{Y}} &= \sin\theta_Y(-\sin\Psi\hat{\mathbf{i}} + \cos\Psi\hat{\mathbf{j}}) + \cos\theta_Y\hat{\mathbf{k}} \\ \hat{\mathbf{\Psi}} &= -\sin\Psi\hat{\mathbf{i}} + \cos\Psi\hat{\mathbf{j}} \quad .\end{aligned} \tag{B.6}$$

Using

$$\dot{\hat{\mathbf{X}}} = \dot{\Psi}\hat{\mathbf{\Psi}} = \Omega_L\hat{\mathbf{\Psi}} \tag{B.7}$$

$$\dot{\hat{\mathbf{\Psi}}} = -\dot{\Psi}\hat{\mathbf{X}} = -\Omega_L\hat{\mathbf{X}} \tag{B.8}$$

$$\dot{\hat{\mathbf{Y}}} = \sin\theta_Y\dot{\hat{\mathbf{\Psi}}} = -\sin\theta_Y\Omega_L\hat{\mathbf{X}} \quad . \tag{B.9}$$

where $\dot{\Psi} = \Omega_L = \delta_1 J/r^3$ from Eq. (4.25) so that we have $\dot{\hat{\mathbf{n}}}$:

$$\begin{aligned}\dot{\hat{\mathbf{n}}} &= \dot{\Phi}\hat{\mathbf{\Phi}} + \cos\Phi\dot{\hat{\mathbf{X}}} + \sin\Phi\dot{\hat{\mathbf{Y}}} \\ &= \dot{\Phi}\hat{\mathbf{\Phi}} + \Omega_L\left(\cos\Phi\hat{\mathbf{\Psi}} - \sin\Phi\sin\theta_Y\hat{\mathbf{X}}\right) \\ &= \dot{\Phi}\hat{\mathbf{\Phi}} + \frac{\Omega_L}{\sin\theta_Y}\left(\cos\Phi\hat{\mathbf{Y}} - \cos\Phi\cos\theta_Y\hat{\mathbf{k}} - \sin\Phi\sin^2\theta_Y\hat{\mathbf{X}}\right)\end{aligned} \tag{B.10}$$

To take the projection of Eqs. (B.1) we will also need

$$\begin{aligned}\hat{\mathbf{n}}\cdot\hat{\mathbf{X}} &= \cos\Phi & \hat{\mathbf{\Phi}}\cdot\hat{\mathbf{X}} &= -\sin\Phi \\ \hat{\mathbf{n}}\cdot\hat{\mathbf{Y}} &= \sin\Phi & \hat{\mathbf{\Phi}}\cdot\hat{\mathbf{Y}} &= \cos\Phi \\ \hat{\mathbf{n}}\cdot\hat{\mathbf{k}} &= \sin\Phi\cos\theta_Y & \hat{\mathbf{\Phi}}\cdot\hat{\mathbf{k}} &= \cos\Phi\cos\theta_Y\end{aligned} \tag{B.11}$$

In the last step we use

$$\hat{\mathbf{k}}\cdot\hat{\mathbf{n}} = \hat{\mathbf{J}}\cdot(\cos\Phi\hat{\mathbf{X}} + \sin\Phi\hat{\mathbf{Y}}) = \sin\Phi\hat{\mathbf{J}}\cdot\hat{\mathbf{Y}} \tag{B.12}$$

since $\hat{\mathbf{X}}$ lies in the equatorial plane, it is by definition perpendicular to $\hat{\mathbf{J}} = \hat{\mathbf{k}}$. From all of the above relations we obtain for use in the projections

$$\dot{\hat{\mathbf{n}}} \cdot \hat{\mathbf{n}} = 0 \tag{B.13}$$

$$\dot{\hat{\mathbf{n}}} \cdot \hat{\mathbf{\Phi}} = \dot{\Phi} + \Omega_L \sin\theta_Y = \dot{\Phi} + \Omega_L \cos\theta_L \quad . \tag{B.14}$$

Now for $\dot{\hat{\Phi}}$. Taking the derivative of $\hat{\Phi}$ as expressed in Eq. (B.6) we have

$$\begin{aligned} \dot{\hat{\mathbf{\Phi}}} &= -\dot{\Phi}\hat{\mathbf{n}} - \sin\Phi\dot{\hat{\mathbf{X}}} + \cos\Phi\dot{\hat{\mathbf{Y}}} \\ &= -\dot{\Phi}\hat{\mathbf{n}} + \Omega_L\left(-\sin\Phi\hat{\mathbf{\Psi}} - \cos\Phi\sin\theta_Y\hat{\mathbf{X}}\right) \\ &= -\dot{\Phi}\hat{\mathbf{n}} + \frac{\Omega_L}{\sin\theta_Y}\left(-\sin\Phi\hat{\mathbf{Y}} + \sin\Phi\cos\theta_Y\hat{\mathbf{k}} - \cos\Phi\sin^2\theta_Y\hat{\mathbf{X}}\right) \end{aligned} \tag{B.15}$$

and using Eqs. (B.11), we have for use in the projections of Eqs. (B.1),

$$\begin{aligned} \dot{\hat{\mathbf{\Phi}}} \cdot \hat{\mathbf{n}} &= -\left(\dot{\Phi} + \Omega_L\sin\theta_Y\right) = -\left(\dot{\Phi} + \Omega_L\cos\theta_L\right) \\ \dot{\hat{\mathbf{\Phi}}} \cdot \hat{\mathbf{\Phi}} &= 0 \quad . \end{aligned} \tag{B.16}$$

Now we can derive the equations of motion in the (r, Φ, Ψ) coordinates. From the equations we constructed in section §4.2.3,

$$\begin{aligned} \dot{\mathbf{r}} &= A\mathbf{p} + B\hat{\mathbf{n}} + \delta_1\frac{\mathbf{S}\times\mathbf{r}}{r^3} \\ \dot{\mathbf{p}} &= C\mathbf{p} + D\hat{\mathbf{n}} + \delta_1\frac{\mathbf{S}\times\mathbf{p}}{r^3} + 3\delta_1\frac{\mathbf{L}\cdot\mathbf{S}}{r^4}\hat{\mathbf{n}} \quad , \end{aligned} \tag{B.17}$$

and the projections (Eqs. (B.1)), with all of the the above vector relations we have the radial equation,

$$\dot{\mathbf{r}} \cdot \hat{\mathbf{n}} = \dot{r} = AP_r + B \quad . \tag{B.18}$$

The Φ equation is found from

$$\dot{\mathbf{r}} \cdot \hat{\mathbf{\Phi}} = \frac{\partial H}{\partial \mathbf{p}} \cdot \hat{\mathbf{\Phi}} \tag{B.19}$$

$$r\left(\dot{\Phi} + \Omega_L\cos\theta_L\right) = A\frac{L}{r} + \delta_1\frac{(\mathbf{S}\times\mathbf{r})\cdot\hat{\mathbf{\Phi}}}{r^3} \quad . \tag{B.20}$$

Look at

$$(\mathbf{S}\times\mathbf{r})\cdot\hat{\mathbf{\Phi}} \;=\; r\left(\mathbf{S}\cdot\hat{\mathbf{L}}\right) \quad . \tag{B.21}$$

The Φ equation is then

$$\dot{\Phi} \;=\; A\frac{L}{r^2}+\Omega_L\left(-\cos\theta_L+\frac{\mathbf{S}\cdot\hat{\mathbf{L}}}{J}\right) \tag{B.22}$$

where $\hat{\mathbf{S}}\cdot\hat{\mathbf{L}}$ is constant. Another helpful relation is

$$\frac{\mathbf{S}\cdot\hat{\mathbf{L}}}{J} \;=\; \hat{\mathbf{J}}\cdot\hat{\mathbf{L}}-\frac{L}{J}=\cos\theta_L-\frac{L}{J} \tag{B.23}$$

allowing us to write the Φ equation in its final form,

$$\dot{\Phi} \;=\; A\frac{L}{r^2}-\Omega_L\frac{L}{J} \quad . \tag{B.24}$$

The two conjugate momenta equations are next. We start with P_r:

$$\begin{aligned}\dot{\mathbf{p}}\cdot\hat{\mathbf{n}} \;&=\; \dot{P}_r-\frac{L}{r}(\dot{\Phi}+\Omega_L\cos\theta_L) \\ &=\; CP_r+D+2\Omega_L\frac{\mathbf{S}\cdot\mathbf{L}}{Jr}\end{aligned} \tag{B.25}$$

where we have used that

$$(\mathbf{p}\times\mathbf{S})\cdot\hat{\mathbf{n}} \;=\; \frac{\mathbf{S}\cdot\mathbf{L}}{r} \tag{B.26}$$

Notice if we use Eq. (B.22), we have

$$\dot{P}_r=A\frac{L^2}{r^3}+CP_r+D+3\Omega_L\frac{\mathbf{S}\cdot\mathbf{L}}{Jr}$$

and last

$$\begin{aligned}\dot{\mathbf{p}}\cdot\hat{\mathbf{\Phi}} \;&=\; P_r(\dot{\Phi}+\Omega_L\cos\theta_L)-\frac{L}{r^2}\dot{r} \\ &=\; C\frac{L}{r}+\Omega_L\frac{P_r\mathbf{S}\cdot\hat{\mathbf{L}}}{J}\end{aligned} \tag{B.27}$$

where we have used that

$$(\mathbf{p}\times\mathbf{S})\cdot\hat{\mathbf{\Phi}} = \mathbf{S}\cdot(\hat{\mathbf{\Phi}}\times\mathbf{p}) = -P_r\mathbf{S}\cdot\hat{\mathbf{L}} \tag{B.28}$$

Notice if we use Eq. (B.22), we have a cancellation and

$$(AP_r - \dot{r})\frac{L}{r^2} \;\; = \;\; -B\frac{L}{r} = C\frac{L}{r}$$

which confirms a true statement but does not provide any new equation of motion since we implicitly used $\dot{L}=0$. We will show in the next subsection that the canonical momentum $P_\Phi = L$ and so the last equation of motion corresponds to $\dot{P}_\Phi = 0$. All four equations in the orbital basis are compiled in Eqs. (3.12).

B.2 Conjugate momenta for Φ and Ψ

We can show that the momentum conjugate to Φ is $P_\Phi = L$ and the momentum conjugate to Ψ is $P_\Psi = L_z = L\cos\theta_L$. So the equations of motion (Φ, P_Φ) and (Ψ, P_Ψ) should be derivable from

$$\begin{aligned}\dot{\Phi} &= \frac{\partial H}{\partial P_\Phi} \quad , \qquad \dot{P}_\Phi = 0 \\ \dot{\Psi} &= \frac{\partial H}{\partial P_\Psi} \quad , \qquad \dot{P}_\Psi = 0\end{aligned} \tag{B.29}$$

This is far more elaborate than one might guess and so we spend this last subsection verifying that L and L_z are the conjugate momenta and that the equations of motion derived according to (B.29) are in fact the same as those of Eqs. (3.12).

We begin by showing that $P_\Phi = L$ and $P_\Psi = L_z$ are consistent with our equations before we explicitly rederive the equations of motion using (B.29). Bear in mind that the variables (r, Φ, Ψ) and their conjugate momenta must be linearly independent and so $\partial X^i/\partial X^j = \delta^i_j$ where $X = (r, P_r, \Phi, P_\Phi, \Psi, P_\Psi)$. We also need to be careful to rewrite everything in terms of (r, Φ, Ψ) and the conjugate momenta (P_r, L, L_z). Particularly, we will need to take the derivative of terms like $\cos\theta_L = P_\Psi/P_\Phi = L_z/L$. From Eqs. (B.29) we have

that

$$\begin{aligned}\dot{\Phi} = \frac{\partial H}{\partial P_\Phi} &= \frac{\partial H}{\partial \mathbf{p}} \cdot \frac{\partial \mathbf{p}}{\partial P_\Phi} + \frac{\partial H}{\partial \mathbf{r}} \cdot \frac{\partial \mathbf{r}}{\partial P_\Phi} \\ &= \dot{\mathbf{r}} \cdot \frac{\partial \mathbf{p}}{\partial L} - \dot{\mathbf{p}} \frac{\partial \mathbf{r}}{\partial L}\end{aligned} \tag{B.30}$$

Now

$$\begin{aligned}\dot{\mathbf{r}} &= \dot{r}\hat{\mathbf{n}} + r\dot{\hat{\mathbf{n}}} \\ \dot{\mathbf{p}} &= \dot{P}_r\hat{\mathbf{n}} + P_r\dot{\hat{\mathbf{n}}} - \frac{L\dot{r}}{r^2}\hat{\mathbf{\Phi}} + \frac{L}{r}\dot{\hat{\mathbf{\Phi}}} \quad .\end{aligned} \tag{B.31}$$

and

$$\begin{aligned}\frac{\partial \mathbf{p}}{\partial L} &= P_r \frac{\partial \hat{\mathbf{n}}}{\partial L} + \frac{L}{r}\frac{\partial \hat{\mathbf{\Phi}}}{\partial L} + \frac{1}{r}\hat{\mathbf{\Phi}} \\ \frac{\partial \mathbf{r}}{\partial L} &= r\frac{\partial \hat{\mathbf{n}}}{\partial L} \quad .\end{aligned} \tag{B.32}$$

The unit vectors $\hat{\mathbf{n}}$ and $\hat{\mathbf{\Phi}}$ depend on L and L_z through $\cos\theta_L = L_z/L$. Using Eq. (B.6) and replacing $\sin\theta_Y$ with $\cos\theta_L$ etc. we have

$$\begin{aligned}\frac{\partial \hat{\mathbf{n}}}{\partial L} &= \sin\Phi \frac{\partial \hat{\mathbf{Y}}}{\partial L} = -\sin\Phi \frac{\cos\theta_L}{L}\left(\hat{\mathbf{\Psi}} - \cot\theta_L \hat{\mathbf{k}}\right) \\ \frac{\partial \hat{\mathbf{\Phi}}}{\partial L} &= \cos\Phi \frac{\partial \hat{\mathbf{Y}}}{\partial L} = -\cos\Phi \frac{\cos\theta_L}{L}\left(\hat{\mathbf{\Psi}} - \cot\theta_L \hat{\mathbf{k}}\right)\end{aligned} \tag{B.33}$$

Using Eq. (B.10) for $\dot{\hat{\mathbf{n}}}$ and Eq. (B.14) for $\dot{\hat{\mathbf{n}}} \cdot \hat{\mathbf{\Phi}}$, Eq. (B.30) becomes

$$\begin{aligned}\dot{\Phi} = \dot{\Phi} + \dot{\Psi}\cos\theta_L + \frac{\cos\theta_L}{L}\left(\cot\theta_L\hat{\mathbf{k}} - \hat{\mathbf{\Psi}}\right) \cdot \Bigg[&\left(P_r \sin\Phi + \frac{L}{r}\cos\Phi\right)\left(\dot{r}\hat{\mathbf{n}} + r\dot{\hat{\mathbf{n}}}\right) \\ &- r\sin\Phi\left(\dot{P}_r\hat{\mathbf{n}} + P_r\dot{\hat{\mathbf{n}}} - \frac{L\dot{r}}{r^2}\hat{\mathbf{\Phi}} + \frac{L}{r}\dot{\hat{\mathbf{\Phi}}}\right)\Bigg]\end{aligned} \tag{B.34}$$

Taking the dot products, there are some fortunate cancellations and overall we find

$$\dot{\Phi} = \dot{\Phi} + \dot{\Psi}\cos\theta_L - \dot{\Psi}\cos\theta_L = \dot{\Phi} \quad . \tag{B.35}$$

As claimed, $P_\Phi = L$ is consistent. The same procedure for Ψ with $P_\Psi = L_z$ yields a similarly consistent equality.

Now, to derive the equations of motion directly from

$$\dot{\Phi} = \frac{\partial H}{\partial L} = \frac{\partial H_{PN}}{\partial L} + \frac{\partial H_{SO}}{\partial L} \tag{B.36}$$

is tedious but doable. The PN piece is straightforward if one first writes everything in terms of canonical variables; i.e., $(\hat{\mathbf{n}} \cdot \mathbf{p}) = P_r$ and $\mathbf{p}^2 = P_r^2 + P_\Phi^2/r^2 = P_r^2 + L^2/r^2$, then

$$\frac{\partial H_{PN}}{\partial L} = A\frac{L}{r^2} \qquad . \tag{B.37}$$

The partial of the spin orbit piece is

$$\begin{aligned}
\frac{\partial H_{SO}}{\partial L} &= \frac{\delta_1 \mathbf{S}}{r^3} \cdot \frac{\partial(\mathbf{r} \times \mathbf{p})}{\partial L} \\
&= \frac{\delta_1 \mathbf{S}}{r^3} \cdot \left[r\frac{\partial \hat{\mathbf{n}}}{\partial L} \times \mathbf{p} + \mathbf{r} \times \frac{\partial \mathbf{p}}{\partial L} \right] \\
&= \frac{\delta_1 \mathbf{S}}{r^3} \cdot \left[r\frac{\partial \hat{\mathbf{n}}}{\partial L} \times \mathbf{p} + \mathbf{r} \times \left(P_r \frac{\partial \hat{\mathbf{n}}}{\partial L} + \frac{L}{r}\frac{\partial \hat{\mathbf{\Phi}}}{\partial L} + \frac{\hat{\mathbf{\Phi}}}{r} \right) \right]
\end{aligned}$$

Replace $P_r\hat{\mathbf{n}}$ with $\mathbf{p} - (L/r)\hat{\mathbf{\Phi}}$ to cancel the first cross product with part of the second cross product. We then have

$$\frac{\partial H_{SO}}{\partial L} = \delta_1 \frac{\mathbf{S} \cdot \hat{\mathbf{L}}}{r^3} + \frac{\delta_1 L}{r^3} \mathbf{S} \cdot \left[\left(\hat{\mathbf{n}} \times \frac{\partial \hat{\mathbf{\Phi}}}{\partial L} \right) - \left(\hat{\mathbf{\Phi}} \times \frac{\partial \hat{\mathbf{n}}}{\partial L} \right) \right]$$

Taking the cross products we have

$$\begin{aligned}
\frac{\partial H_{SO}}{\partial L} &= \delta_1 \frac{\mathbf{S} \cdot \hat{\mathbf{L}}}{r^3} - \frac{\delta_1}{r^3} \mathbf{S} \cdot \cos\theta_L \left(\hat{\mathbf{k}} - \cot\theta_L \hat{\mathbf{\Psi}} \right) \\
&= \delta_1 \frac{\mathbf{S} \cdot \hat{\mathbf{L}}}{r^3} - \frac{\delta_1}{r^3} \cos\theta_L \left(J - L_z - \cot\theta_L \mathbf{S} \cdot \hat{\mathbf{\Psi}} \right)
\end{aligned}$$

where in the last step we have used $\mathbf{S} \cdot \hat{\mathbf{k}} = J - L_z$. Taking $\mathbf{S} \cdot \hat{\mathbf{\Psi}} = (\mathbf{J} - \mathbf{L}) \cdot \hat{\mathbf{\Psi}} = -\mathbf{L} \cdot \hat{\mathbf{\Psi}} = -L\sin\theta_L$ gives

$$\begin{aligned}
\frac{\partial H_{SO}}{\partial L} &= \delta_1 \frac{\mathbf{S} \cdot \hat{\mathbf{L}}}{r^3} - \frac{\delta_1}{r^3} \cos\theta_L \left(J - L_z - L\cos\theta_L \right) \\
&= \delta_1 \frac{\mathbf{S} \cdot \hat{\mathbf{L}}}{r^3} - \frac{\delta_1 J}{r^3} \cos\theta_L \\
&= -\Omega_L \frac{L}{J} \qquad .
\end{aligned} \tag{B.38}$$

Added together Eqs. (B.37) and (B.38) give the equation of motion for Φ in Eqs. (3.12) as claimed. The $\dot{\Psi}$ equation can be derived similarly. Since both P_Φ and P_Ψ are constants, the Hamiltonian is cyclic in Φ and Ψ.

Appendix C

C.1 Mino time vs. coordinate time Fourier coefficients

Suppose $A_{kn;t}$ is a Fourier coefficient of some biperiodic coordinate time function $f(t)$,

$$A_{kn;t} = \lim_{T\to\infty} \frac{1}{T} \int_{-\frac{T}{2}}^{\frac{T}{2}} dt\, e^{i(k\omega_\theta + n\omega_r)t} f(t) \quad . \tag{C.1}$$

Then $A_{kn;t}$ is also the knth Fourier coefficient of a different biperiodic Mino time function $g(\lambda)$,

$$\begin{aligned} A_{kn;t} &= \lim_{\Lambda\to\infty} \frac{1}{\Lambda} \int_{-\frac{\Lambda}{2}}^{\frac{\Lambda}{2}} d\lambda\, e^{i(k\Omega_\theta + n\Omega_r)\lambda} g(\lambda) \\ &\equiv A_{kn;\lambda} \quad . \end{aligned} \tag{C.2}$$

We prove equation (C.2) by constructing the function g from f explicitly. We will need the fact (see Ref. [105] for details) that $dt/d\lambda$ depends on r and θ and is thus biperiodic when evaluated on a trajectory $r(\lambda), \theta(\lambda)$. $dt/d\lambda$ also has a nonzero average value Γ defined by

$$\Gamma \equiv \lim_{\Lambda\to\infty} \frac{1}{\Lambda} \int_{-\Lambda/2}^{\Lambda/2} d\lambda \frac{dt}{d\lambda} \quad . \tag{C.3}$$

Consequently, the function $t(\lambda)$ takes the form

$$t(\lambda) = \Gamma\lambda + \Delta t(\lambda) \tag{C.4}$$

where $\Delta t(\lambda)$ is biperiodic in λ and has zero average value.

We can now construct $g(\lambda)$. Since $\Delta t(\lambda)$ is biperiodic, it is also bounded. Thus, if we define $T \equiv t(\Lambda)$, then in the limit $T \to \infty$, we get $T \to \Gamma\Lambda$. We can now change variables in the integral in (C.1):

$$\begin{aligned}\lim_{T\to\infty} \frac{1}{T} \int_{-\frac{T}{2}}^{\frac{T}{2}} dt\, e^{i(k\omega_\theta + n\omega_r)t} f(t) &= \lim_{\Gamma\Lambda\to\infty} \frac{1}{\Gamma\Lambda} \int_{-\frac{\Gamma\Lambda}{2}}^{\frac{\Gamma\Lambda}{2}} d\lambda\, e^{i(k\omega_\theta + n\omega_r)(\Gamma\lambda + \Delta t(\lambda))} \\ &\qquad \times \frac{dt}{d\lambda}(\lambda) f\left(t(\lambda)\right) \\ &= \lim_{\Lambda\to\infty} \frac{1}{\Lambda} \int_{-\frac{\Lambda}{2}}^{\frac{\Lambda}{2}} d\lambda\, e^{i(k\Omega_\theta + n\Omega_r)\lambda} e^{i(k\omega_\theta + n\omega_r)\Delta t(\lambda)} \\ &\qquad \times \frac{dt}{d\lambda}(\lambda) f\left(t(\lambda)\right) \quad . \end{aligned} \tag{C.5}$$

In the second line above, we have absorbed[1] the Γ into the Λ and used the fact that the coordinate-time and Mino-time frequencies will be related [105] by

$$\omega_r = \frac{1}{\Gamma}\Omega_r \tag{C.6a}$$

$$\omega_\theta = \frac{1}{\Gamma}\Omega_\theta \quad , \tag{C.6b}$$

to convert to Mino frequencies in the argument of the exponential.

Comparing (C.2) to (C.5), we see that due to the dependence on k and n in the argument of the exponential (the coordinate time frequencies ω_θ and ω_r appear here simply as parameters), there is actually a different function

$$g_{kn}(\lambda) = e^{i(k\omega_\theta + n\omega_r)\Delta t(\lambda)} \frac{dt}{d\lambda}(\lambda) f\left(t(\lambda)\right) \tag{C.7}$$

for each $A_{kn;\lambda}$. In other words, the $A_{kn;t}$ are Fourier coefficients of a single function f while each $A_{kn;\lambda}$ is the knth Fourier coefficient of a different function $g_{kn}(\lambda)$. But that poses no problem — we only sought to show that every t-Fourier coefficient is also the λ-Fourier coefficient of *some* function of λ. The pragmatic importance of this fact has to do with the evaluation of coefficients of torus functions, which, though stated in slightly different language, is the

[1] All we need is for the denominator of the prefactor and the size of the integration interval to agree. Since there is no preferred size for that interval (the function f is not periodic) and we are taking the infinite limit, we are free to call the size of that interval $\Gamma\Lambda$ or Λ.

crux of the original argument in Ref. [105] and which we discuss in Section C.2.

Analogous reasoning to the above in the resonant case with

$$\frac{\omega_\theta}{\omega_r} = \frac{\Omega_\theta}{\Omega_r} = \frac{p}{z} \tag{C.8}$$

and p, z relatively prime shows that each coefficient $C_{j;t}$ of $f(t)$ can likewise be considered a Mino time coefficient $C_{j;\lambda}$ of some different function

$$g_j(\lambda) = e^{ij\omega_P \Delta t(\lambda)} \frac{dt}{d\lambda}(\lambda) f\left(t(\lambda)\right) \quad . \tag{C.9}$$

The difference is that now each of $\Delta t(\lambda), dt/d\lambda(\lambda)$ and $f\left(t(\lambda)\right)$ is a singly periodic function of λ with period

$$\Lambda_P = z\Lambda_r = p\Lambda_\theta = \frac{2\pi}{\omega_P} \quad . \tag{C.10}$$

Temporal Fourier coefficients can be calculated in the resonant case without first having to convert to Mino time. We will nonetheless express and evaluate coefficients $C_{j;t}$ as coefficients $C_{j;\lambda}$ in order to parallel the non-resonant case.

C.2 λ-based vs. t-based torus coordinates

Figure 6.5 represents $\mathbb{T}^2_{\vec{\xi}}$ as a compact 2π-by-2π square in the χ_r, χ_θ angle coordinates defined in Section 6.2.2. Kerr geodesics trace out lines on this torus-square at constant velocity. With respect to any other time parameter, geodesic curves continue to be lines on the torus-square, but their parametric representations are not in general linear in time, nor are their velocities on the torus constant.

For any choice of time parameter, however, there is always some set of coordinates on the torus such that geodesic motion on that torus is linear in that time parameter and has constant velocity[2]. For instance, with respect to coordinate time t, there will be coordinates $\vec{\gamma} \equiv (\gamma_r, \gamma_\theta)$ such that

$$\gamma_r(t) = \omega_r t + \gamma_{r_0} \tag{C.11a}$$

$$\gamma_\theta(t) = \omega_\theta t + \gamma_{\theta_0} \quad . \tag{C.11b}$$

[2]Darboux's theorem guarantees that there is a way to write Hamilton's equations with respect to any evolution parameter. If the system is integrable, there will then exist a transformation to angle variables on the torus that increase linearly with respect to that evolution parameter [115].

Note that in any set of angle coordinates in which the trajectory velocities are constant with respect to some time parameter, orbit trajectories will all be lines with the same slope $1 + q_{r\theta}$. Such coordinate systems are nevertheless distinct: identical ordered pairs in two such coordinate systems will not, in general, correspond to the same point on the torus.

Though not unique, the χ_r-χ_θ coordinate system on $\mathbb{T}^2_{\vec{\mathcal{E}}}$ is nevertheless uniquely *useful*. Since each of γ_r, γ_θ would be a combination of χ_r and χ_θ, each point on the projected r-p_r curve of an orbit would be labeled by a pair of values $(\gamma_r, \gamma_\theta)$ rather than by a single value χ_r, and likewise for the projected θ-p_θ curve. This mixing of radial and polar motions in each torus coordinate makes most calculations harder than they need to be, and the impetus behind χ_r-χ_θ coordinates is precisely the convenience that flows from torus coordinates that separately shadow radial and polar motion.

Still, we sometimes are interested in values of quantities averaged over the $\vec{\gamma}$ coordinates. Luckily, by the correspondence between temporal Fourier coefficients of biperiodic functions and spatial Fourier coefficients of torus functions, equations (C.2) and (C.7) further establish that if $A_{kn;\vec{\gamma}}$ is the knth coefficient of the torus function $f(\vec{\gamma})$ associated with $f(t)$, then it is also the knth coefficient $A_{kn;\vec{\chi}}$ of the torus function $g_{kn}(\vec{\chi})$ corresponding to $g_{kn}(\lambda)$. This is important for evaluating torus coefficients in practice: it is usually very difficult to go from a function $f\left(r(t), p_r(t), \theta(t), p_\theta(t)\right)$ to a form $f(\vec{\gamma})$ explicitly while it is straightforward to go from $g\left(r(\lambda), p_r(\lambda), \theta(\lambda), p_\theta(\lambda)\right)$ to $g(\vec{\chi})$.

Appendix D

D.1 A synopsis of the Teukolsky formalism

Here we summarize some relevant aspects of the Teukolsky formalism as applied to the EMRI problem. More details of this application can be found in numerous references, including [99; 100; 118; 119; 120; 127; 136]. Our goal in this appendix is to justify the expressions for the coefficients $Z^{H/\infty}_{lmkn}$ and $Z^{H/\infty}_{lmj;\lambda}$ in equations (6.61) and (6.68), respectively.

D.1.1 The Weyl scalar, ψ_4

In 1972 Teukolsky derived the master equation [32; 33], a separable partial differential equation (PDE) whose solution describes the propagation in the Kerr spacetime of small perturbations to fields of different spin-weights s: scalar, electromagnetic and gravitational. Each solution to the master equation is a separable function which can be written as a multipole expansion. There are two computational approaches to solving the master equation for each multipole mode: the time-domain approach, which solves the resulting PDE directly, and the frequency-domain approach, which further Fourier expands the solutions. For the purposes of extracting flux information from gravitational perturbations, frequency-domain codes are the accuracy standard and the ones to which our savings proposal applies. We thus restrict our attention to the frequency-domain approaches to solving the master equation.

The combined multipole-Fourier expanded perturbations take the form

$$ {}_s\psi\left(t,r,\theta,\varphi\right) = \sum_{lm}\int_{-\infty}^{\infty} d\omega R_{lm\omega}\left(r\right) {}_sS_{lm}^{a\omega}\left(\theta\right) e^{-i\omega t+im\varphi} \quad , \quad \text{(D.1)} $$

where ω denotes the coordinate-time frequency of the perturbations at the field point due to the source. Each ${}_s\psi$ is a function of the field point (t, r, θ, φ) at which we wish to evaluate the perturbation. The s marker in equation (D.1) is a "spin-weight parameter" [32] which denotes the perturbation type. For gravitational radiation, $s=-2$, and ${}_{-2}\psi = \psi_4\rho^{-4}$ where

$$ \rho \quad = \quad -\left(r-ia\cos\theta\right)^{-1} \quad . \quad \text{(D.2)} $$

The functions $R_{lm\omega}(r)$ and ${}_{-2}S_{lm}^{a\omega}(\theta)$ (described in the next subsections) each depend on the parameter ω as a consequence of the separation of variables procedure. When the source is a geodesic, ω turns out to be a discrete variable composed of harmonics of the radial, polar and azimuthal frequencies of that geodesic. That discrete dependence can be expressed differently for non-resonant orbits,

$$ \omega = \omega_{mkn} = m\omega_\varphi + k\omega_r + n\omega_\theta \quad \text{(D.3a)} $$

and for resonant orbits,

$$ \omega = \omega_{mj} = m\omega_\varphi + j\omega_P \quad . \quad \text{(D.3b)} $$

Once ω becomes a discrete variable, we can replace the integral over all possible ω in equation (D.1) with a sum over either m,k,n or m,j for non-resonant and resonant sources, respectively.

Because everything in this paper deals with gravitational spin-weighting, we henceforth omit all the -2 subscripts. The net result is that equation (D.1) becomes

$$ \psi_4\left(t,r,\theta,\varphi\right) = \rho^4 \sum_{lmnk} R_{lm\omega_{mkn}}\left(r\right) S_{lm}^{a\omega_{mkn}}\left(\theta\right) e^{-i\omega_{mkn}t+im\varphi} \quad , \quad \text{(D.4a)} $$

for a non-resonant source and

$$ \psi_4\left(t,r,\theta,\varphi\right) = \rho^4 \sum_{lmj} R_{lm\omega_{mj}}\left(r\right) S_{lm}^{a\omega_{mj}}\left(\theta\right) e^{-i\omega_{mj}t+im\varphi} \quad \text{(D.4b)} $$

for a resonant source.

D.1.2 The Spheroidal Harmonics

The functions $S_{lm}^{a\omega}(\theta)$ with a spin-weight of $s = -2$ are the gravitational (tensor) spheriodal harmonics, a generalization of the likewise spin-weighted spherical harmonics. These functions satisfy [33]

$$\left[(a\omega)^2\cos^2\theta + 4a\omega\cos\theta - \left(\frac{m^2 - 4m\cos\theta + 4}{\sin^2\theta}\right) + \mathcal{C}_{lm}\right] S_{lm}^{a\omega}(\theta) + \frac{1}{\sin\theta}\frac{d}{d\theta}\left(\sin\theta\frac{dS_{lm}^{a\omega}(\theta)}{d\theta}\right) = 0 \quad . \tag{D.5}$$

$\mathcal{C}_{lm}$ are the eigenvalues for which equation (D.5) has solutions. Solving for $S_{lm}^{a\omega}(\theta)$ for given l, m, ω requires simultaneously determining an eigenvalue $\mathcal{C}_{lm}$ and the associated spheroidal harmonic. These eigenvalue-eigenfunction pairs can be computed in several different ways (see Refs. [99; 118; 121]).

The spheroidal harmonics satisfy several orthogonality relations. The one we will need in this paper is that, for fixed m and ω,

$$\int_0^\pi S_{lm}^{a\omega}(\theta)\,\bar{S}_{l'm}^{a\omega}(\theta)\sin\theta d\theta = \frac{1}{2\pi}\delta_{ll'} \quad , \tag{D.6}$$

where the overbar denotes complex conjugation. We have chosen a normalization of $\frac{1}{2\pi}$, as in Ref. [100].

D.1.3 The radial Teukolsky functions

Solving for the radial functions $R_{lm\omega}(r)$ is more difficult. $R_{lm\omega}(r)$ satisfy the inhomogeneous radial Teukolsky equation [33]

$$\mathcal{T}_{lm\omega}(r) = \Delta^2\frac{d}{dr}\left(\frac{1}{\Delta}\frac{dR_{lm\omega}(r)}{dr}\right) - V_{lm\omega}(r)\,R_{lm\omega}(r) \quad . \tag{D.7}$$

The potential $V_{lm\omega}(r)$ depends in part on the eigenvalue $\mathcal{C}_{lm}$ of $S_{lm}^{a\omega}(\theta)$, so equation (D.5) must be solved before the homogeneous or inhomogeneous version of equation (D.7) can be.

The source term $\mathcal{T}_{lm\omega}$ is built by, among other things, evaluating $S_{lm}^{a\omega}(\theta)$ and two homogeneous solutions[1] $R_{lm\omega}^{\text{in/up}}(r)$ to (D.7) along the geodesic source.

[1] Other basis solutions to the homogeneous equation exist, e.g. the out/down basis $R_{lm\omega}^{\text{out/down}}(r)$. For a summary, see [108] and references therein.

Two general methods are described for constructing $R^{\text{in/up}}_{lm\omega}(r)$. One approach integrates the homogeneous Teukolsky equation (or, equivalently, the better numerically behaved Sasaki-Nakamura equation [137]) outward from the horizon. The other expands $R^{\text{in/up}}_{lm\omega}(r)$ in terms of hypergeometric functions (see [121] and references therein) and evaluates $R^{\text{in/up}}_{lm\omega}(r)$ directly at certain points, possibly extrapolating its values to nearby points with series expansions. Both approaches are fairly computationally costly. For detailed explanations on these different approaches and how various numerical problems are circumvented, see [121; 137; 138; 139; 140; 141]. We elaborate a bit more on the structure of the source term below.

D.1.4 The quantities $Z^{H/\infty}_{lm\omega}$

With the homogeneous radial solutions in hand, the inhomogeneous Teukolsky equations can be solved using the method of variation of parameters[2] [142]. The radial functions $R_{lm\omega}(r)$ can be written as [32; 33; 100; 105; 143; 144]

$$R_{lm\omega}(r) = Z^{H}_{lm\omega}(r) R^{\text{up}}_{lm\omega}(r) + Z^{\infty}_{lm\omega}(r) R^{\text{in}}_{lm\omega}(r) \quad , \tag{D.8}$$

where $Z^{H}_{lm\omega}(r)$ and $Z^{\infty}_{lm\omega}(r)$ are defined as

$$\begin{aligned} Z^{H}_{lm\omega}(r) &= \int_{r_+}^{r} dr' \, \frac{R^{\text{in}}_{lm\omega}(r') \mathcal{T}_{lm\omega}(r')}{c} \\ Z^{\infty}_{lm\omega}(r) &= \int_{r}^{\infty} dr' \, \frac{R^{\text{up}}_{lm\omega}(r') \mathcal{T}_{lm\omega}(r')}{c} \quad . \end{aligned} \tag{D.9}$$

The constant c is related to the Wronskian of $R^{\text{in}}_{lm\omega}(r)$ and $R^{\text{up}}_{lm\omega}(r)$. r_+ is the larger root of Δ and is the radial coordinate of the black hole horizon (the smaller root is denoted r_-).

Because we are only interested in the radiation going into the black hole and being carried away to infinity, we are only concerned about the asymptotic behavior of $R_{lm\omega}(r)$ as $r \to r_+$ and $r \to \infty$. In fact, the homogeneous basis

[2] Most references use the method of Green functions, but variation of parameters works as well.

solutions have been chosen to have the simplifying feature that

$$\begin{aligned} Z^{\infty}_{lm\omega}(r \to r_+) &= Z^{\infty}_{lm\omega} \\ Z^{H}_{lm\omega}(r \to r_+) &= 0 \\ Z^{\infty}_{lm\omega}(r \to \infty) &= 0 \\ Z^{H}_{lm\omega}(r \to \infty) &= Z^{H}_{lm\omega} \quad . \end{aligned} \tag{D.10}$$

Note that we have used the same notation for the *functions* $Z^{H/\infty}_{lm\omega}(r)$ and for the *constants* $Z^{H/\infty}_{lm\omega}$ representing their asymptotic values at ∞ and r_+, respectively. As mentioned in Section 6.4.1, the literature seems stuck with the rather backward notational convention that $Z^{H}_{lm\omega}$ is nonvanishing at ∞ while $Z^{\infty}_{lm\omega}$ is nonvanishing at r_+.

The radial functions as $r \to \infty$ and $r \to r_+$ thus become

$$\begin{aligned} R^{\infty}_{lm\omega} &= R_{lm\omega}(r \to \infty) \\ &= Z^{H}_{lm\omega} R^{\rm up}_{lm\omega}(r \to \infty) \\ &= Z^{H}_{lm\omega} r^3 e^{i\omega r^*} \end{aligned} \tag{D.11a}$$

$$\begin{aligned} R^{H}_{lm\omega} &= R_{lm\omega}(r \to r_+) \\ &= Z^{\infty}_{lm\omega} R^{\rm in}_{lm\omega}(r \to r_+) \\ &= Z^{\infty}_{lm\omega} \Delta^2 e^{-ikr^*} \quad , \end{aligned} \tag{D.11b}$$

where and $k \equiv \omega - ma/(2r_+)$ and r^* is the Kerr tortoise coordinate defined by

$$\begin{aligned} r^*(r) &= r + \frac{2r_+}{r_+ - r_-} \ln \frac{r - r_+}{2} - \frac{2r_-}{r_+ - r_-} \ln \frac{r - r_-}{2} \\ \frac{dr^*}{dr} &= \frac{r^2 + a^2}{\Delta} \quad . \end{aligned} \tag{D.12}$$

The coefficients $Z^{H/\infty}_{lm\omega}$ are found from

$$Z^{H/\infty}_{lm\omega} = \int_{r_+}^{\infty} dr' \, \frac{R^{\rm in/up}_{lm\omega}(r') \mathcal{T}_{lm\omega}(r')}{c} \quad . \tag{D.13}$$

The source function $\mathcal{T}_{lm\omega}(r)$ in (D.13) is an integral of the form

$$\mathcal{T}_{lm\omega}(r) = \int_{-\infty}^{\infty} dt \int d\Omega \, B_{m\omega}(t, r, \theta, \varphi) S^{a\omega}_{lm} e^{i\omega t} e^{-im\varphi} \quad . \tag{D.14}$$

The source term is derived in [145], but we have written it borrowing the notation $B_{m\omega}$ from [100]. All that matters for our purposes is that $B_{m\omega}$ is built out of a series of operations on the null tetrad components of the energy-momentum tensor of the orbiting particle and thus contains delta functions and derivatives of delta functions centered on the source geodesic. Thus, the $d\Omega$ integral can be evaluated, resulting in every θ and φ in (D.14) being replaced with the source trajectories $\theta_s(t), \varphi_s(t)$ (the subscript s here denotes "source" as opposed to a spin-weight as earlier in this Appendix).

Delta functions $\delta\left(r - r_s(t)\right)$ and derivatives thereof still remain in (D.14), along with the integration over t. When we plug (D.14) into equation (D.13), we can switch the order of integration for r' and t and use those remaining delta functions in r (we rename r' to r now, for simplicity) to replace every r with $r_s(t)$. The net result is that $Z^{H/\infty}_{lm\omega}$ takes the form

$$Z^{H/\infty}_{lm\omega} = \int_{-\infty}^{\infty} dt\, e^{i\omega t} e^{-im\varphi_s(t)} \mathcal{I}^{H/\infty}_{lm\omega}\left(r_s\left(t\right), \theta_s\left(t\right)\right) \quad . \tag{D.15}$$

The functions $\mathcal{I}^{H/\infty}_{lm\omega}$ depend on r and θ both directly and via a combination of elementary functions, the spheroidal harmonics, the homogeneous radial Teukolsky functions, and various derivatives thereof. Explicit expressions can be found in several sources (see, for instance, [100; 121]).

We will now use this form for $Z^{H/\infty}_{lm\omega}$ to define the coefficients $Z^{H/\infty}_{lmkn}$ and $Z^{H/\infty}_{lmj;\lambda}$ to which the efficiency arguments of Sections 6.4 and 6.5 apply, respectively.

D.1.5 The quantities $Z^{H/\infty}_{lmkn}$

We now show that, when the source is a non-resonant orbit, the ω-dependence of $Z^{H/\infty}_{lm\omega}$ takes the form

$$Z^{H/\infty}_{lm\omega} = \sum_{kn} Z^{H/\infty}_{lmkn;\lambda} \delta\left(\omega - \omega_{mkn}\right) \quad , \tag{D.16}$$

where ω_{mkn} are the coordinate-time harmonic frequencies defined in equation (D.3a). Note that even though equation (D.16) has the form of the Fourier transform of an almost-periodic function with respect to coordinate time t, we are free to interpret the coefficients of the delta functions either as Fourier coefficients of a coordinate time function or as Fourier coefficients of a (different) Mino time function.

For the reasons stated in Appendix C, we opt for the latter and begin by rewriting (D.15) as an integral over Mino time. Treating all source coordinates as functions of λ and using equation (C.4), we get

$$Z^{H/\infty}_{lm\omega} = \int_{-\infty}^{\infty} d\lambda\, e^{i\omega(\Gamma\lambda+\Delta t(\lambda))} e^{-im\varphi_s(\lambda)} \mathcal{I}^{H/\infty}_{lm\omega}\left(r_s(\lambda), \theta_s(\lambda)\right) . \quad \text{(D.17)}$$

We now use the fact (see Ref. [105]) that, like $dt/d\lambda$, $d\varphi/d\lambda$ depends on r and θ and is thus biperiodic when evaluated on a trajectory $r(\lambda), \theta(\lambda)$. $d\varphi/d\lambda$ has a nonzero average value Ω_φ defined by

$$\Omega_\varphi \equiv \lim_{\Lambda\to\infty} \frac{1}{\Lambda} \int_{-\Lambda/2}^{\Lambda/2} d\lambda\, \frac{d\varphi}{d\lambda} \quad . \quad \text{(D.18)}$$

Consequently, the function $\varphi_s(\lambda)$ takes the form

$$\varphi_s(\lambda) = \Omega_\varphi \lambda + \Delta\varphi_s(\lambda) \quad \text{(D.19)}$$

where $\Delta\varphi_s(\lambda)$ is biperiodic in λ and has zero average value. Like its radial and polar counterparts, Ω_φ is related to the coordinate-time frequency ω_φ via

$$\omega_\varphi = \frac{1}{\Gamma}\Omega_\varphi \quad . \quad \text{(D.20)}$$

More generally, coordinate-time and Mino-time frequencies are related by

$$\omega = \frac{1}{\Gamma}\Omega \quad . \quad \text{(D.21)}$$

In light of equations (D.19)–(D.21), equation (D.17) becomes

$$Z^{H/\infty}_{lm\omega} = \int_{-\infty}^{\infty} d\lambda\, e^{i\Omega\lambda} e^{-im\Omega_\varphi\lambda} e^{i\omega\Delta t(\lambda)} e^{-im\Delta\varphi_s(\lambda)} \mathcal{I}^{H/\infty}_{lm\omega}\left(r_s(\lambda), \theta_s(\lambda)\right) . \quad \text{(D.22)}$$

Note that the coordinate-time frequency ω still appears as a parameter in both $\mathcal{I}^{H/\infty}_{lm\omega}$ and in the argument of $e^{i\omega\Delta t(\lambda)}$.

Like $\Delta t(\lambda)$ and $\Delta\varphi(\lambda)$, the functions $\mathcal{I}^{H/\infty}_{lm\omega}$ are biperiodic in λ. We define the biperiodic function

$$f^{H/\infty}_{lm\omega}(\lambda) \equiv e^{i\omega\Delta t(\lambda)} e^{-im\Delta\varphi_s(\lambda)} \mathcal{I}^{H/\infty}_{lm\omega}\left(r_s(\lambda), \theta_s(\lambda)\right) \quad \text{(D.23)}$$

and Fourier expand it as

$$f^{H/\infty}_{lm\omega}(\lambda) \equiv \sum_{k,n} Z^{H/\infty}_{lm\omega;kn;\lambda} e^{-i(k\Omega_\theta + n\Omega_r)\lambda} \quad . \tag{D.24}$$

Inserting (D.24) into equation (D.22) yields

$$\begin{aligned} Z^{H/\infty}_{lm\omega} &= \sum_{k,n} Z^{H/\infty}_{lm\omega;kn;\lambda} \int_{-\infty}^{\infty} d\lambda\, e^{i\Omega\lambda} e^{-i(m\Omega_\varphi + k\Omega_\theta + n\Omega_r)\lambda} \\ &= \sum_{k,n} Z^{H/\infty}_{lm\omega;kn;\lambda} 2\pi\delta(\omega - \omega_{mkn}) \\ &= \sum_{k,n} Z^{H/\infty}_{lm\omega=\omega_{mkn};kn;\lambda} 2\pi\delta(\omega - \omega_{mkn}) \quad . \end{aligned} \tag{D.25}$$

The multipole index m and the Fourier indices k, n all do double duty by helping to specify the value of the parameter ω in $Z^{H/\infty}_{lm\omega=\omega_{mkn};kn;\lambda}$. Consequently, each $Z^{H/\infty}_{lm\omega=\omega_{mkn};kn;\lambda}$ is fully specified by the four integers l, m, k, n and we can define

$$Z^{H/\infty}_{lmkn;\lambda} \equiv 2\pi Z^{H/\infty}_{lm\omega=\omega_{mkn};kn;\lambda} \quad . \tag{D.26}$$

We will absorb the factor of 2π into the function $f^{H/\infty}_{lm\omega}$ in the integral defining $Z^{H/\infty}_{lmkn;\lambda}$.

Since each $Z^{H/\infty}_{lmkn;\lambda}$ is a temporal Fourier coefficient, then by the arguments of Section 6.3.4, we determine it by instead computing the corresponding spatial Fourier coefficient

$$Z^{H/\infty}_{lmkn} \equiv \frac{1}{(2\pi)^2} \int_0^{2\pi} d\chi_r \int_0^{2\pi} d\chi_\theta\, e^{ik\chi_\theta} e^{in\chi_r} f^{H/\infty}_{lm\omega=\omega_{mkn}}(\chi_r, \chi_\theta) \tag{D.27}$$

of the associated torus function in the $\vec{\chi}$ torus coordinates. Despite our earlier notation, the function $\mathcal{I}^{H/\infty}_{lm\omega}$ actually depends not only on r and θ but also on their conjugate momenta (since it depends on the r and θ velocities via the energy-momentum tensor of the particle). $f^{H/\infty}_{lm\omega}$ inherits this dependence, and it is thus appropriate to write it as a function of the torus coordinates $\vec{\chi}$ that need not have any special symmetries on the torus.

As we show in Appendix D.2, the averaged fluxes required to evaluate the RHS of the adiabatic equations for $\vec{\mathcal{E}}$ depend on the $Z^{H/\infty}_{lmkn}$ defined in (D.27). Thus, equation (D.27) verifies equation (6.61), on which the savings arguments of Section 6.4.2 are based.

D.1.6 The quantities $Z^{H/\infty}_{lmj;\lambda}$

We now show that when the source is a resonant orbit, the ω-dependence of $Z^{H/\infty}_{lm\omega}$ instead takes the form

$$Z^{H/\infty}_{lm\omega} = \sum_j Z^{H/\infty}_{lmj;\lambda} \delta\left(\omega - \omega_{mj}\right) \quad , \tag{D.28}$$

where ω_{mj} are now the coordinate-time harmonic frequencies defined in equation (D.3b). As before, we are free to interpret the coefficients of the delta functions either as Fourier coefficients of a coordinate time function or as Fourier coefficients of a (different) Mino time function and take the computationally tractable latter option.

Equations (D.17)–(D.23) carry over to the resonant case with the difference that each of $\Delta t(\lambda), \Delta\varphi(\lambda), r(\lambda), \theta(\lambda)$ and thus $\mathcal{I}^{H/\infty}_{lm\omega}$ is now singly periodic with period Λ_P. Thus $f^{H/\infty}_{lm\omega}$ can be Fourier expanded in harmonics of a single fundamental frequency Ω_P,

$$f^{H/\infty}_{lm\omega}(\lambda; \vec{\chi}_0) \equiv \sum_j Z^{H/\infty}_{lm\omega;j;\lambda}(\vec{\chi}_0) e^{-ij\Omega_P\lambda} \tag{D.29}$$

with

$$Z^{H/\infty}_{lm\omega;j;\lambda}(\vec{\chi}_0) = \frac{1}{\Lambda_P}\int_0^{\Lambda_P} d\lambda\, e^{ij\Omega_P\lambda} f^{H/\infty}_{lm\omega}(\lambda; \vec{\chi}_0) \quad . \tag{D.30}$$

The functions $f^{H/\infty}_{lm\omega}(\lambda; \vec{\chi}_0)$ are induced from some torus function, so by the arguments of Section 6.3.4, both they and the coefficients $Z^{H/\infty}_{lm\omega;j;\lambda}(\vec{\chi}_0)$ depend on initial positions, which we can represent compactly as a dependence on initial position $\vec{\chi}_0$ on the phase space torus.

Inserting (D.29) into the resonant version of equation (D.22) yields

$$\begin{aligned} Z^{H/\infty}_{lm\omega} &= \sum_j Z^{H/\infty}_{lm\omega;j;\lambda} \int_{-\infty}^{\infty} d\lambda\, e^{i\Omega\lambda} e^{-i(m\Omega_\varphi + j\Omega_P)\lambda} \\ &= \sum_j Z^{H/\infty}_{lm\omega;j;\lambda} 2\pi\delta(\omega - \omega_{mj}) \\ &= \sum_j Z^{H/\infty}_{lm\omega=\omega_{mj};j;\lambda} 2\pi\delta(\omega - \omega_{mj}) \quad . \end{aligned} \tag{D.31}$$

The relevant quantities, then, are those in equation (D.30) with the parameter ω in $f^{H/\infty}_{lm\omega}$ set to ω_{mj}.

Paralleling the non-resonant case, each $Z^{H/\infty}_{lm\omega=\omega_{mj};j;\lambda}$ is fully specified by the three integers l, m, j. By absorbing the factor of 2π into the functions $f^{H/\infty}_{lm\omega}$ in the integrand of (D.30), we can define the notationally more compact coefficients

$$Z^{H/\infty}_{lmj;\lambda} \equiv 2\pi Z^{H/\infty}_{lm\omega=\omega_{mj};j;\lambda} \quad . \tag{D.32}$$

By the construction above, each such $Z^{H/\infty}_{lmj;\lambda}$ is given by

$$Z^{H/\infty}_{lmj;\lambda} = \frac{1}{\Lambda_P}\int_0^{\Lambda_P} d\lambda\, e^{ij\Omega_P\lambda} f^{H/\infty}_{lm\omega=\omega_{mj}}(\lambda;\vec{\chi}_0) \quad . \tag{D.33}$$

As we show in Appendix D.2, the time-averaged fluxes for $\vec{\mathcal{E}}$ from resonant orbits depend on the $Z^{H/\infty}_{lmj;\lambda}$ defined in (D.33). Thus, equation (D.33) verifies equation (6.68), on which the more speculative savings arguments of Section 6.5 are based.

D.2 Fluxes from the Teukolsky formalism

In this appendix, we review how the apparatus of Appendix D.1 yields fluxes of conserved quantities. Several authors [99; 100; 108; 118; 120; 121] implement this Fourier-domain formalism in TB codes to calculate the radiative $\vec{\mathcal{E}}$ fluxes at radial infinity and the horizon to determine how the inspiral evolves. We show how expressions for time-averaged (as opposed to torus-averaged) fluxes differ between non-resonant and resonant orbits.

D.2.1 Overview of flux calculation

We will not refer to the Q flux, but restrict our discussion to E and L_z. To determine the evolution of an inspiral in orbital parameter space, we use the the E and L_z fluxes at radial infinity and the horizon as proxies for the local self-force. This subsection gives an overview of the calculation for finding these fluxes.

From the Weyl scalar ψ_4, the gravitational waveform and the E, L_z and Q radiation fluxes can be calculated. Specifically, we can calculate the polarizations h_+ and $h_\times$ of the metric perturbations at infinity (i.e. the GWs) via

$$\psi_4 \;=\; \frac{1}{2}\frac{\partial^2}{\partial t^2}\left(h_+ + ih_\times\right) \quad . \tag{D.34}$$

After integrating equation (D.34) twice to get $h_+ + ih_\times$ (the integration constants are set to zero), we can calculate an effective GW stress-energy tensor at infinity [146] as

$$T^{\infty}_{\alpha\beta} = \frac{1}{16\pi}\left\langle \frac{\partial h_+}{\partial x^\alpha}\frac{\partial h_+}{\partial x^\beta} + \frac{\partial h_\times}{\partial x^\alpha}\frac{\partial h_\times}{\partial x^\beta}\right\rangle_{\substack{\text{several}\\ \text{wavelengths}}}. \tag{D.35}$$

The average over several wavelengths signifies the following [147]. The stress-energy tensor of GWs contributes to curvature in the analogous way that the stress-energy tensor of matter does. However, since GWs are fluctuations in the metric itself, we cannot define their stress-energy tensor at a field point because, with only information at one point, we cannot distinguish between the curvature of the background spacetime and the contributions to that curvature from fluctuations on the spacetime. To distinguish between the background and the effect of the fluctuations, there needs to be either a length or frequency scale separation between the two. In our case, as $r \to \infty$, the background curvature scale is much greater than the wavelength of the fluctuations. Therefore, we average over several gravitational wavelengths in order to smooth out the fluctuations and determine only the secular contribution of such GWs to the curvature.

While the background curvature scale is much greater than the GW wavelength, GW detectors look not for spatial fluctuations to the metric but rather temporal ones. Therefore, in the spirit of applicability to actual experiments, it is more useful to distinguish between a background frequency (i.e. a reciprocal of a curvature scale in the timelike direction) and the much larger frequency of the fluctuations. Therefore, rather then average over several wavelengths, we average over several periods to isolate the net effect of the GWs [147].

The energy and angular momentum fluxes carried to radial infinity by GWs are related to the components of $T^{\infty}_{\alpha\beta}$ by,

$$\begin{aligned} T^{\infty}_{tt} &= \frac{dE}{dtdA} \\ T^{\infty}_{t\varphi} &= \frac{dL_z}{dtdA} \quad . \end{aligned} \tag{D.36}$$

The E and L_z fluxes are calculated by integrating equation (D.36) over a

2-sphere of radius r on a constant t spacelike hypersurface

$$\begin{aligned}\left(\frac{dE}{dt}\right)^{\infty} &= \int T^{\infty}_{tt} r^2 d\Omega \\ \left(\frac{dL_z}{dt}\right)^{\infty} &= \int T^{\infty}_{t\varphi} r^2 d\Omega \quad .\end{aligned} \tag{D.37}$$

The time-averaged fluxes from a given geodesic can then be calculated by

$$\begin{aligned}\left\langle \frac{dE}{dt} \right\rangle^{\infty}_{t} &= \lim_{T\to\infty} \frac{1}{T} \int_{-\frac{T}{2}}^{\frac{T}{2}} \left(\frac{dE}{dt}\right)^{\infty} dt \\ \left\langle \frac{dL_z}{dt} \right\rangle^{\infty}_{t} &= \lim_{T\to\infty} \frac{1}{T} \int_{-\frac{T}{2}}^{\frac{T}{2}} \left(\frac{dL_z}{dt}\right)^{\infty} dt \quad .\end{aligned} \tag{D.38}$$

Alternatively, we can calculate the torus-averaged fluxes by taking the average of the time-averages for all geodesics with a given set of orbital parameters over all possible initial conditions,

$$\begin{aligned}\left\langle \frac{dE}{dt} \right\rangle^{\infty}_{\vec{\gamma}} &= \frac{1}{(2\pi)^2} \int_0^{2\pi} d\gamma_{r_o} \int_0^{2\pi} d\gamma_{\theta_o} \left\langle \frac{dE}{dt} \right\rangle^{\infty}_{t} \\ \left\langle \frac{L_z}{dt} \right\rangle^{\infty}_{\vec{\gamma}} &= \frac{1}{(2\pi)^2} \int_0^{2\pi} d\gamma_{r_o} \int_0^{2\pi} d\gamma_{\theta_o} \left\langle \frac{dL_z}{dt} \right\rangle^{\infty}_{t} \quad .\end{aligned} \tag{D.39}$$

An analogous procedure can be performed to calculate the fluxes at the horizon [139; 148].

D.2.2 Fluxes from ψ_4

Combining equations (D.4) with (D.11) we find that

$$\psi_4^{\infty} = \rho^{-4} \sum_{lmkn} Z^H_{lmkn;\lambda} r^3 e^{i\omega_{mkn} r^*} S^{a\omega_{mkn}}_{lm}(\theta)\, e^{-i\omega_{mkn} t + im\varphi} \tag{D.40a}$$

for non-resonant orbits, and

$$\psi_4^{\infty} = \rho^{-4} \sum_{lmj} Z^H_{lmj;\lambda} r^3 e^{i\omega_{mj} r^*} S^{a\omega_{mj}}_{lm}(\theta)\, e^{-i\omega_{mj} t + im\varphi} \quad . \tag{D.40b}$$

Similar expressions can be found for ψ_4^H, but for brevity, we will only proceed with the detailed computations for $r \to \infty$. Also, we only work out the details for the E flux, but the L_z flux follows exactly the same prescription.

Following the prescription laid out in section D.2.1 we find that

$$\left(\frac{dE}{dt}\right)^{\infty} = \frac{1}{4\pi}\left\langle \sum_{lm\omega}\sum_{l'm'\omega'} \frac{1}{\omega\omega'} Z^H_{lm\omega;\lambda}\bar{Z}^H_{l'm'\omega';\lambda} e^{i(\omega-\omega')r^*} e^{-i(\omega-\omega')t} \right. \tag{D.41}$$
$$\left. \times \int_0^{\pi} \sin\theta S^{a\omega}_{lm}(\theta)\bar{S}^{a\omega'}_{l'm'}(\theta)\, d\theta \int_0^{2\pi} d\varphi e^{i(m-m')\varphi} \right\rangle_{\substack{\text{several}\\ \text{periods}}} ,$$

where ω, ω' denote the discrete variables that are two-indexed for resonant orbits and three-indexed for non-resonant orbits. Performing the φ integration in equation (D.41) yields $2\pi\delta_{mm'}$. We thus set $m = m'$ everywhere.

For non-resonant orbits, equation (D.41) becomes

$$\left(\frac{dE}{dt}\right)^{\infty} = \frac{1}{2}\left\langle \sum_{lmkn}\sum_{l'k'n'} \frac{1}{\omega_{mkn}\omega_{mk'n'}} Z^H_{lmkn;\lambda}\bar{Z}^H_{l'mk'n';\lambda} e^{-i\{(n-n')\omega_r+(k-k')\omega_\theta\}(t-r^*)} \right. \tag{D.42}$$
$$\left. \times \int_0^{\pi} d\theta \sin\theta S^{a\omega_{mkn}}_{lm}\bar{S}^{a\omega_{mk'n'}}_{l'm} \right\rangle_{\substack{\text{several}\\ \text{periods}}} .$$

We are interested in an infinite time-average of equation (D.42). Therefore, we can drop the average over several periods because the time-averaging process will smooth out the fluxes so that the period averaging will have no further effect once we have time-averaged. The time-average of a function corresponds to the constant term in a Fourier expansion, so the argument of the exponential in t will need to be zero. Therefore, performing the infinite time-average yields the added conditions $k = k'$ and $n = n'$. This equates the frequencies everywhere, including in the spheroidal harmonics. We can therefore now perform the θ integration using (D.6) and get $l = l'$. The result is that the infinite time average in the non-resonant case is

$$\left\langle \frac{dE}{dt} \right\rangle_t^{\infty} = \sum_{lmkn} \frac{1}{4\pi\omega^2_{mkn}} \left| Z^H_{lmkn;\lambda} \right|^2 . \tag{D.43}$$

In Section 6.3.4, we saw that infinite time averages over non-resonant orbits are the same as torus averages over non-resonant tori with respect to the

corresponding torus coordinates. The time average over t on the LHS of (D.43) thus corresponds to a torus average over the $\vec{\gamma}$ torus coordinates. We also saw that $\left|Z^H_{lmkn;\lambda}\right|^2 = \left|Z^H_{lmkn}\right|^2$, where the Z^H_{lmkn} are spatial Fourier coefficients (for fixed l, m) with respect to the $\vec{\chi}$ torus coordinates. Therefore, the torus averaged energy flux is

$$\left\langle \frac{dE}{dt} \right\rangle^{\infty}_{\vec{\gamma}} = \sum_{lmkn} \frac{1}{4\pi\omega^2_{mkn}} \left|Z^H_{lmkn}\right|^2 \quad . \tag{D.44}$$

This expression is true for all tori, as torus averages are insensitive to whether the orbits on that torus are resonant or non-resonant.

Analogous arguments lead to the angular momentum flux at infinity. Similar arguments to those above then lead to the corresponding fluxes at the horizon. The upshot is that all the torus-averaged fluxes are given by

$$\begin{aligned} \left\langle \frac{dE}{dt} \right\rangle^{H/\infty}_{\vec{\gamma}} &= \sum_{lmkn} \frac{\alpha^{H/\infty}_{lmkn}}{4\pi\omega^2_{mkn}} \left|Z^{H/\infty}_{lmkn}\right|^2 \\ \left\langle \frac{dL_z}{dt} \right\rangle^{H/\infty}_{\vec{\gamma}} &= \sum_{lmkn} \frac{\alpha^{H/\infty}_{lmkn} m}{4\pi\omega^3_{mkn}} \left|Z^{H/\infty}_{lmkn}\right|^2 \quad , \end{aligned} \tag{D.45}$$

where $\alpha^{\infty}_{lmkn} \equiv 1$ and the details of α^H_{lmkn} can be found in reference [139]. We note that there is no residual dependence on the initial conditions $\vec{\chi}_0$.

We return to equation (D.42) and evaluate it for a resonant orbit,

$$\begin{aligned} \left(\frac{dE}{dt}\right)^{\infty} = \frac{1}{2} \Bigg\langle \sum_{lmj} \sum_{l'j'} \frac{1}{\omega_{mj}\omega_{mj'}} Z^H_{lmj;\lambda} Z^{*H}_{lmj';\lambda} e^{-i(j-j')\omega_P(t-r^*)} \\ \times \int_0^{\pi} d\theta \sin\theta S^{a\omega_{mj}}_{lm} \bar{S}^{a\omega_{mj'}}_{l'm} \Bigg\rangle_{\substack{\text{several} \\ \text{periods}}} \quad . \end{aligned} \tag{D.46}$$

As was the case with the non-resonant infinite time average, we can drop the averaging over several periods. Additionally, the resonant time-average picks out the constant term in the Fourier expansion, which results when $j = j'$. Therefore,

$$\left\langle \frac{dE}{dt} \right\rangle^{\infty}_{t} = \sum_{lmj} \frac{1}{4\pi\omega^2_{mj}} \left|Z^H_{lmj;\lambda}\right|^2 \quad . \tag{D.47}$$

The rest of the E and L_z time-averaged fluxes can be found similarly and are,

$$\left\langle \frac{dE}{dt} \right\rangle_t^{H/\infty} = \sum_{lmj} \frac{\alpha_{lmj}^{H/\infty}}{4\pi\omega_{mj}^2} \left| Z_{lmj;\lambda}^{H/\infty} \right|^2 \tag{D.48}$$

$$\left\langle \frac{dL_z}{dt} \right\rangle_t^{H/\infty} = \sum_{lmj} \frac{\alpha_{lmj}^{H/\infty} m}{4\pi\omega_{mj}^3} \left| Z_{lmj;\lambda}^{H/\infty} \right|^2 \quad .$$

We remark that unlike the torus-averaged fluxes, the time-averaged fluxes of resonant orbits clearly depend on the initial conditions of the orbit, since as we saw in Section D.1.6, $\left| Z_{lmj;\lambda}^{H/\infty} \right|^2$ is not the same for all initial conditions.

Alternatively, we can write the time-averaged fluxes of equation (D.48) explicitly in terms of the torus coefficients $Z_{lmkn}^{H/\infty}$. From section 6.3.4 we know that

$$Z_{lmj;\lambda}^{H/\infty} = \sum_{\substack{kn: \\ pn+zk=j}} Z_{lmkn}^{H/\infty} e^{-in\chi_{r_0}} e^{-ik\chi_{\theta_0}} \quad . \tag{D.49}$$

Therefore, we can rewrite equation (D.48) as

$$\left\langle \frac{dE}{dt} \right\rangle_t^{H/\infty} = \sum_{lmkn} \sum_{\substack{k'n': \\ zn+pk= \\ zn'+pk'}} \frac{\alpha_{lmkn}^{H/\infty}}{4\pi\omega_{mkn}^2} Z_{lmkn}^{H/\infty} Z_{lmk'n'}^{*H/\infty} e^{-i\{(n-n')\chi_{r_o}+(k-k')\chi_{\theta_o}\}} \tag{D.50}$$

$$\left\langle \frac{dL_z}{dt} \right\rangle_t^{H/\infty} = \sum_{lmkn} \sum_{\substack{k'n': \\ zn+pk= \\ zn'+pk'}} \frac{\alpha_{lmkn}^{H/\infty} m}{4\pi\omega_{mkn}^3} Z_{lmkn}^{H/\infty} Z_{lmk'n'}^{*H/\infty} e^{-i\{(n-n')\chi_{r_o}+(k-k')\chi_{\theta_o}\}} \quad .$$

The explicit initial condition dependence is now evident. Notice that if we average the time-averaged flux expressions of equation (D.50) over all possible initial conditions, we reproduce the torus-averaged fluxes of equation (D.44)

$$\left\langle \frac{dE}{dt} \right\rangle_\gamma^{H/\infty} = \frac{1}{(2\pi)^2} \int_0^{2\pi} d\chi_{r_o} \int_0^{2\pi} d\chi_{\theta_o} \left\langle \frac{dE}{dt} \right\rangle_t^{H/\infty} \tag{D.51}$$

$$= \sum_{lmkn} \frac{\alpha_{lmkn}^{H/\infty}}{4\pi\omega_{mkn}^2} \left| Z_{lmkn}^{H/\infty} \right|^2 \quad .$$